Quenching and morphological evolution of galaxies at high redshift

Peter Lustig

München 2022

Quenching and morphological evolution of galaxies at high redshift

Peter Lustig

Dissertation
an der Fakultät für Physik
der Ludwig–Maximilians–Universität
München

vorgelegt von
Peter Lustig
aus Wuppertal

München, den 23.03.2022

Erstgutachter: Prof. Dr. Joseph J. Mohr
Zweitgutachter: Prof. Dr. Volker Springel
Tag der mündlichen Prüfung: 4. Mai 2022

Zusammenfassung

Im lokalen Universum gibt es eine klare Korrelation zwischen Morphologie von Galaxien und Eigenschaften ihrer Sternpopulationen: Early-type Galaxien sind dominiert durch ihren Bulge und beinhalten alte Sternpopulationen mit wenig Entstehung neuer Sterne, während late-type Galaxien von ihrer Scheibe dominiert sind und Sterne produzieren. Allerdings ist es immer noch unklar wann und wie diese Korrelation entsteht. In dieser Dissertation untersuchen wir die Morphologie sowie Eigenschaften von Sternpopulationen passiver Galaxien bei Rotverschiebung $z \sim 3$ mittels Beobachtungen und Simulationen. Dafür analysieren wir strukturelle Eigenschaften einer der ersten statistischen Stichproben spektroskopisch bestätigter massiver passiver Galaxien bei $z \sim 3$ und finden einen hohen Anteil von Bulge dominierten Galaxien. Unsere Messung ihrer Größe erweitert existierende Messungen der Relation zwischen Größe und stellarer Masse von passiven Galaxien in den Bereich der massivsten und seltensten Galaxien bei $z \sim 3$. In Übereinstimmung mit der Extrapolation früherer Messungen deuten unsere gemessen Kompaktheiten der Galaxien auf eine Größenentwicklung passiver Galaxien bei konstanter Masse von fast einer Größenordnung seit $z \sim 3$ hin.

Da bei niedriger Rotverschiebung die massivsten, ältesten passiven Galaxien typische Signaturen von Galaxienhaufen sind suchen wir in der Umgebung bestätigter massiver passiver Galaxien bei $z \sim 3$ nach erhöhter Galaxiendichte die potentiell auf das Vorhandensein einer Vorstufe von Galaxienhaufen hinweisen könnte. Um den Zusammenhang zwischen früher Unterdrückung der Sternentstehung und dichter Umgebung zu untersuchen vergleichen wir die Dichte an Orten massiver, passiver und sternbildender Galaxien bei vergleichbarer Rotverschiebung. Wir finden dass die Mehrheit passiver Galaxien in Umgebungen mit leicht erhöhter Dichte lokalisiert ist, in 25 Prozent der Fälle mit deutlich erhöhter Dichte.

Um die Natur massiver passiver Galaxien bei hoher Rotverschiebung besser zu verstehen führen wir eine ergänzende Analyse in hydrodynamischen Simulationen von Galaxienentwicklung bei $z \sim 3$ durch. Während die stellare Massenfunktion in allen untersuchten Simulationen bei $z \sim 3$ weitgehend mit Beobachtungen übereinstimmt, ist der Anteil passiver Galaxien in einigen Simulationen höher als observiert. In allen Simulationen sind Sternpopulationen von Galaxien bei dieser Rotverschiebung um den Faktor ~ 2 älter als observierte spektroskopisch bestätigte Gegenstücke. Es ist noch nicht klar in welchem Ausmaß diese Diskrepanz auf Unterschiede im Verlauf der Sternentstehungsaktivität in Simulationen im Vergleich zu observierten Galaxien oder auf Verzerrungen in Beobachtungen aufgrund einer höheren Sensitivität für die jüngste Sternentstehungsaktivität zurückzuführen sind. Wir untersuchen die standardmäßige photometrische Selektion passiver Galaxien bei dieser Rotverschiebung und finden Hinweise auf potentiell starke Kontamination und Unvollständigkeit photometrisch selektierter Stichproben. Eine Analyse der Morphologie passiver und sternbildender Galaxien in Simulationen zeigt bereits bei hoher Rotverschiebung Entwicklung von Unterschieden zwischen passiven und sternbildenden Galaxien in Bezug auf Galaxiengröße, Konzentration, Axenverhältnisse und Drehimpuls. Qualitativ sind die Unterschiede analog zu beobachteten, allerdings gibt es quantitative Unterschiede.

Abstract

In the local Universe a clear correlation is seen between morphological and stellar population properties of galaxies: early-type, bulge dominated galaxies have quenched their star-formation and host old stellar populations while late-type, disk dominated galaxies are actively star forming. However, it is still unclear when and how this correlation was established. In this thesis we investigate morphology and stellar population properties of quiescent galaxies at redshift $z \sim 3$ by means of observations and simulations. To this aim we analyse the structural properties of one of the very first statistical samples of spectroscopically confirmed massive quiescent galaxies at $z \sim 3$. We find that a large fraction of the studied sample is already largely bulge dominated at this redshift. Our galaxy size measurements extend previous determinations of the quiescent galaxy mass-size relation at $z \sim 3$ to the rarest, most massive galaxies. In agreement with extrapolations from previous measurements, the observed compact sizes point towards size evolution of massive, quiescent galaxies at fixed mass by nearly an order of magnitude since $z \sim 3$.

Because at lower redshift the most massive oldest quiescent galaxies are a typical signature of cluster environments, we investigate the surroundings of confirmed, massive quiescent galaxies at $z \sim 3$ to search for over-densities that could potentially indicate the presence of proto-clusters. To probe the potential relation between early quenching and early dense environments, we compare the galaxy density around massive quiescent vs. star-forming galaxies at similar redshift, finding that the majority of quiescent galaxies is located in marginally overdense environments, with 25 percent exhibiting significant overdensities.

To better understand the nature of massive high redshift quiescent galaxies we perform a complementary analysis using hydrodynamical simulations of galaxy evolution at $z \sim 3$. While the stellar mass function at $z \sim 3$ in all studied simulations is in broad agreement with observations, quiescent fractions in some simulations are higher than observed. In all simulations at this redshift, quiescent galaxies contain stellar populations older by a factor of ~ 2 than observed, spectroscopically confirmed counterparts. It is not yet clear to what extent this tension depends on intrinsically different star formation histories between observed and simulated galaxies, or on potential observational biases that favor more recent star formation. We investigate the performance of routinely used photometric selection of quiescent galaxies at this redshift, finding evidence of potentially significant contamination and incompleteness of photometrically selected samples. A morphological study of quiescent vs. star-forming galaxies in simulations shows the development already at high redshift of differences between these populations in terms of galaxy sizes, concentrations, axis ratios and angular momenta. These differences are qualitatively analogous to those found in observations, but quantitative differences remain.

Contents

List of Figures

List of Tables

Chapter 1

Introduction

The subject of this thesis is the investigation of galaxy evolution with a focus on quenching of star formation at high redshift. Galaxies are gravitationally bound systems consisting of dark matter, gas, stars (and their remnants) and dust. Our Galaxy for example, the Milky Way, has a total stellar mass of $M_\star \sim 5-7\times10^{10}\,M_\odot$ (e.g., Licquia and Newman, 2015; Bland-Hawthorn and Gerhard, 2016), and it is embedded in a dark matter halo with a virial mass of $0.8-1.3\times10^{12}\,M_\odot$ (e.g., Kafle et al., 2014; McMillan, 2017). However, the Milky Way is only one representative of the population of galaxies that is diverse in many properties like (stellar) mass, morphology and star formation. In this chapter we want to highlight important aspects directly relevant to this work on how these large structures form, what determines their evolution and how we can observe them.

1.1 Formation and evolution of galaxies

The cause for the formation of structures in the Universe are initial perturbations in the otherwise homogeneous and isotropic universe. Because of the solely attractive nature of the gravitational force, regions with a density higher than the average attract material from regions with lower density, amplifying the density contrast. However, the early Universe was hot and dense, so that ordinary matter that interacts electromagnetically was ionised and coupled to the photons. Concentrations of ordinary matter were therefore washed out by radiation pressure. A crucial role for structure formation is here played by dark matter that does not interact electromagnetically. Overdensities of dark matter can grow without being impacted by radiation pressure. About 380 000 years after the Big Bang the Universe cooled to $\sim 2700\,\mathrm{K}$ and electrons and protons recombined to form neutral Hydrogen. From this moment on photons could freely propagate without being scattered. Today they can be observed as the cosmic microwave background (CMB) that provides information about the density contrast at recombination. After recombination the neutral atoms were attracted by the gravitational potential of dark matter overdensities, called dark matter halos. For the formation of galaxies this gas has to cool to collapse and eventually form stars, which can be achieved by different processes. In massive halos with a high virial temperature of $T_{\mathrm{vir}} \gtrsim 10^7\,\mathrm{K}$ gas is collisionally ionized and cools via bremsstrahlung emission. At $10^4 < T_{\mathrm{vir}} < 10^6$ (de-)excitation processes can significantly contribute to cooling. Ions can recombine with electrons and emit photons. Also neutral atoms can cool through collisional excitation and subsequent emission of photons when de-exciting. At lower temperatures gas is pre-

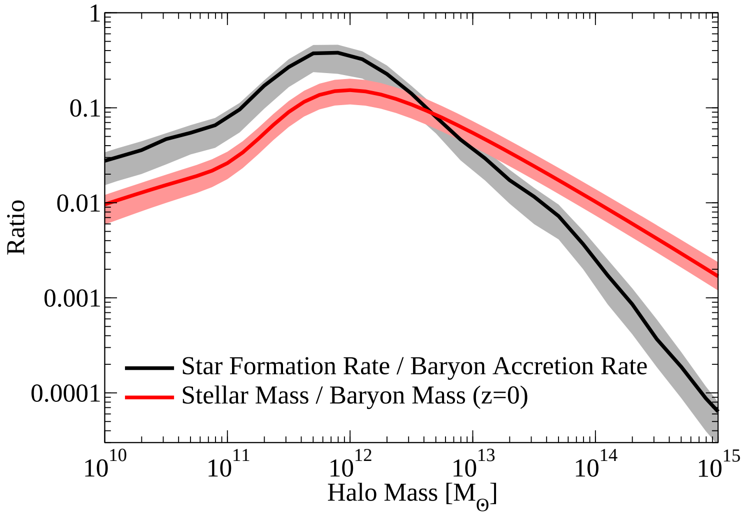

Figure 1.1: Star formation efficiency vs. halo mass at $z = 0$ (reproduced from Behroozi, Wechsler, and Conroy, 2013). The black line shows the instantaneous star formation efficiency (star formation rate / baryon accretion rate), the red line the integrated star formation efficiency (stellar mass / baryon mass). Halos with masses of $\sim 10^{12}\,M_{\odot}$ where the star formation efficiency reaches a maximum typically host spiral galaxies, while lower (higher) mass halos are typically populated by dwarf (elliptical) galaxies.

dominately neutral. Cooling is then still possible through collisional (de-)excitation. These aforementioned processes all involve two body interactions and are therefore more effective in dense environments. An additional cooling process effective at high redshift is inverse Compton scattering of CMB photons by energetic electrons in the halo (Mo, van den Bosch, and White, 2010).

1.1.1 Star formation

In most galaxies the visible light is predominantly produced by stellar emission. When cooling in a proto-galaxy is efficient and the gas density is higher than the dark matter density, the gas can collapse catastrophically under its own gravity. These cold gas clouds then fragment into cores with a very high density in which star formation takes place. The star formation rate of a galaxy therefore not only depends on the availability of gas, but also on the efficiency with which the gas is cooled to eventually form stars. While the first models of galaxy formation predicted that most of the baryonic material is turned into stars, observations show that the star formation efficiency is actually very low and the ratio of stellar to baryonic mass in galaxies is $\lesssim 0.1$ (e.g., Fukugita and Peebles, 2004; Shull, Smith, and Danforth, 2012; Bluck et al., 2020, see also Figure 1.1). Therefore there must be processes that prevent gas from forming stars. This can happen when cooling is inefficient or gas is reheated. An important role is believed to be played by feedback processes, either by stellar feedback (e.g., Dekel and Silk, 1986; Ciotti et al., 1991), especially in low-mass galaxies, or from active galactic nuclei (AGN, e.g., Ciotti and Ostriker, 2007; Alexander and Hickox, 2012; Fabian, 2012), especially in high-mass galaxies.

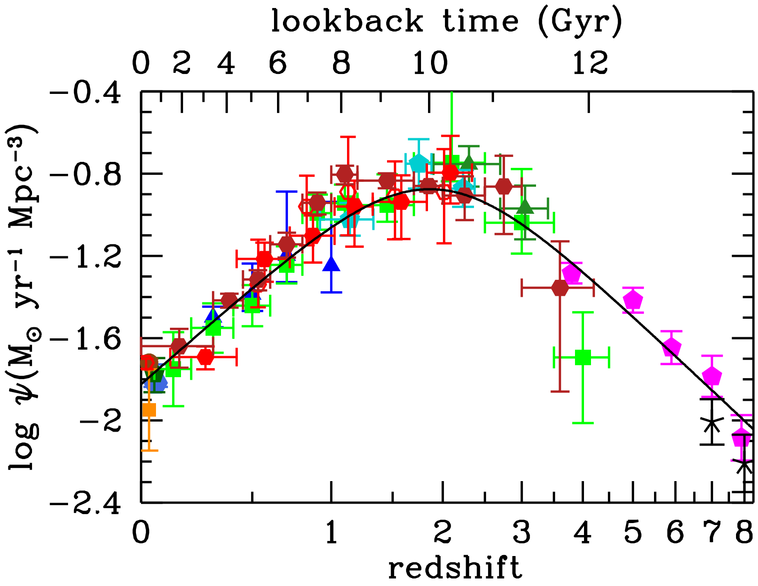

Figure 1.2: Cosmic star formation history as measured from UV and IR data (reproduced from Madau and Dickinson, 2014)

Investigations of the cosmic star formation history have shown that the cosmic star formation rate density peaked at $z \sim 2$ (3.5 Gyr after the Big Bang) with values higher than today by a factor of ~ 10 and about half of the stellar mass in the Universe today formed before $z = 1.3$ (at the age of the Universe of 5 Gyr, Madau and Dickinson, 2014, see Figure 1.2).

Observations have identified a correlation between star formation rate (SFR) and stellar mass of actively star-forming galaxies, producing the so-called main sequence of star-forming galaxies in the SFR vs. $M_\star$ diagram. An example of the main sequence is shown in Figure 1.3. It can be identified up to at least $z \approx 4$ (e.g., Noeske et al., 2007; Daddi et al., 2007; Pannella et al., 2009a; Rodighiero et al., 2011; Wuyts et al., 2011; Schreiber et al., 2015; Renzini and Peng, 2015; Tacchella et al., 2016b). The scatter of the main sequence at fixed mass is ≈ 0.3 dex, independent of redshift and stellar mass up to as least $z \approx 3$ (Whitaker et al., 2012b; Speagle et al., 2014; Tomczak et al., 2016; Pearson et al., 2018). It has been argued that galaxies with a steady balance between gas infall and SFR should lie on the main sequence with a slope of 1, however observed slopes are between 0.4 and 1.0. It is assumed that this difference is caused by quenching processes that are especially effective at high stellar masses. Galaxies with a star formation rate significantly lower than galaxies on the main sequence are called quiescent, quenched or passive galaxies. Different mechanisms have been discussed to explain why star formation in these galaxies is either not efficient or why they contain less gas available for star formation.

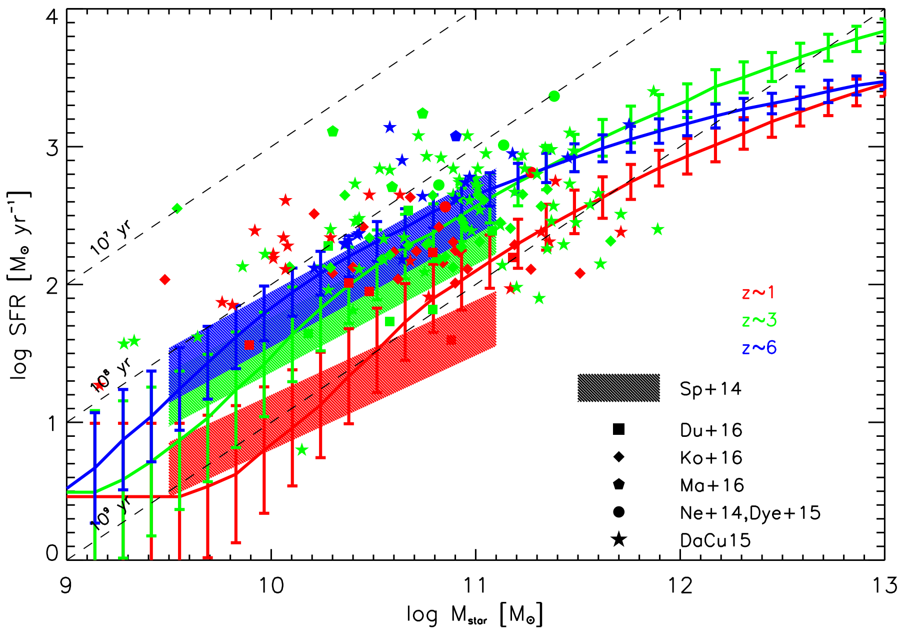

Figure 1.3: The main sequence of star-forming galaxies from $z \sim 1$ to $z \sim 6$ (reproduced from Mancuso et al., 2016). The solid lines show the main sequence as estimated by Mancuso et al. (2016) at $z \sim 1$ (red), 3 (green) and 6 (blue). Errorbars show the 2σ scatter.

Quenching of star formation

The observed baryon conversion efficiencies and old stellar populations in the most massive galaxies at low redshift require formation of the bulk of their stellar population already at $z \gtrsim 2$. Especially the most massive galaxies were expected to host younger stellar populations than lower mass galaxies in the first theoretical expectations from hierarchical structure formation models, because of their later assembly. Mechanisms are therefore needed to efficiently suppress star formation at later times. Although different mechanisms have been proposed, quenching of star formation is not yet fully understood. Concerning the timescales of quenching, two types of mechanisms exist: those that operate on short timescales and suppress star formation in a previously star-forming galaxy and those that operate on longer timescales, being able to maintain quenching even if new cold gas accretes onto the galaxy (even though the timescales can be very different some mechanisms could possibly also be responsible for both, quenching and maintaining of quenching). As previously discussed, stars form from collapsing cold gas. Quenching can therefore be achieved if either no gas is available for star formation or if it cannot cool (Man and Belli, 2018).

To have gas available for star formation it has to accrete onto the galaxy. This can be prevented by cosmological starvation, which is the reduction of the gas supply from the cosmic web (Feldmann and Mayer, 2015). As a consequence of the lack of accretion only gas from stellar evolution, mainly stellar winds and core collapse supernovae, can provide new fuel for galaxy formation. A lack of gas can also arise if it is rapidly consumed in bursts of star formation or if already accreted gas is

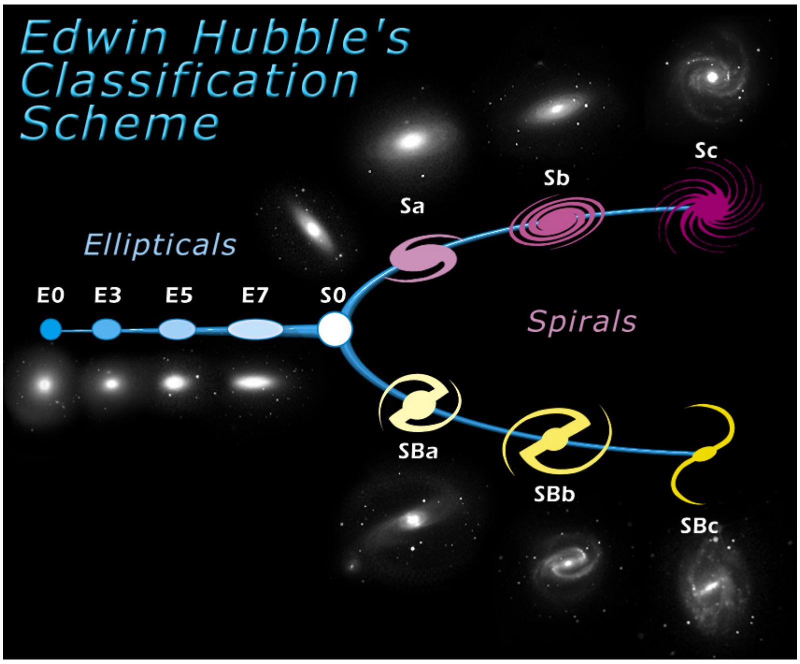

Figure 1.4: The Hubble tuning fork (reproduced from esahubble.org[1]).

expelled by AGN feedback. Both, star formation bursts and AGN activity can be triggered by major mergers and violent disk instabilities that drive cold gas toward the galaxy center.

In massive halos shocks can form and heat the infalling gas to the virial temperature (e.g., Birnboim and Dekel, 2003; Dekel and Birnboim, 2006). Additional heating can come from radio mode feedback of AGN or stellar feedback from Type Ia supernovae and asymptotic giant branch stars.

Another way to quench star formation is morphological quenching: because star formation happens in fragmented clouds that form in gravitationally unstable disks, star formation can be suppressed if the disks becomes stable against fragmentation. Martig et al. (2009) have shown that the transition from a stellar disk to a spheroid can sufficiently stabilize the gas disk to quench star formation even in halos less massive than $\log(M_\star/M_\odot) \approx 12$ and even if gas accretion continues. A similar effect can be caused by a stellar bar (Khoperskov et al., 2018).

1.1.2 Morphological properties of galaxies

Galaxies span a wide range of morphologies. One of the oldest and still commonly used morphological classification schemes for galaxies is the so-called Hubble sequence (or tuning-fork; Hubble, 1926) that arranges galaxies into a sequence of different morphological types. A schematic view of the Hubble sequence together with example images is shown in Figure 1.4. On the left-hand side Hubble arranged elliptical galaxies in the order of increasing flattening. The different types are called En, where the integer $n, n \in [0, 1, ..., 7]$ depends on the ellipticity and is calculated as $10 \times (a - b)/a$, where a (b) is the length of the semi-major (-minor) axis of the galaxy. On the right-hand side of the diagram two series of spiral galaxies are found. The class of normal spirals is divided into the types Sa, Sb and Sc, going from systems with a more prominent central, dense spheroidal component named "bulge"

[1] https://esahubble.org/images/heic9902o/

and closely wound spiral arms, to those with a smaller bulge component and looser spiral arms. The second series of spiral galaxies are barred spiral galaxies showing a bar across the central region with spiral arms emerging at the end of these bars. Analogously to normal spirals they are classified as SBa, SBb and SBc. Disk galaxies without spiral arms are intermediate between spirals and ellipticals and denoted S0. According to Hubble's assumption on morphological evolution of galaxies, galaxies on the left-hand side of the Hubble-fork are called early-type galaxies, those on the right late-type galaxies. Galaxies that do not fit in this classification scheme are called irregular galaxies.

The morphology of galaxies correlates also with their dynamical properties. In massive elliptical galaxies stars move on random orbits in three dimensions while stars in disk galaxies have circular orbits within the disk. At fixed mass the Hubble sequence can be considered as a sequence of increasing angular momentum (Sandage, Freeman, and Stokes, 1970).

A more quantitative way to describe morphology of galaxies is surface brightness modeling. An empirical law for the description of the surface brightness profile of elliptical galaxies was proposed by de Vaucouleurs (1948):

$$\log\left[\frac{I(r)}{I(r_{\mathrm{e}})}\right] = -3.331\left[\left(\frac{r}{r_{\mathrm{e}}}\right)^{1/4} - 1\right], \tag{1.1}$$

where r_{e} is the effective radius of the galaxy, containing half of its total luminosity and $I(r)$ the surface brightness at radius r. The surface brightness distribution of disks can be approximated by an exponential profile:

$$I(r) = I_0 \exp(-r/h), \tag{1.2}$$

where h is the disk scale length. A more general profile to model the surface brightness of galaxies was introduced by Sérsic (1963, 1968). The Sérsic profile is defined as:

$$I(r) = I(r_{\mathrm{e}}) \exp\left\{-b_{\mathrm{n}}\left[\left(\frac{r}{r_{\mathrm{e}}}\right)^{1/n} - 1\right]\right\} \tag{1.3}$$

with $\gamma(2n, b_{\mathrm{n}}) = \frac{1}{2}\Gamma(2n)$, where Γ (γ) is the (lower incomplete) Gamma function. For $n = 4$ the Sérsic profile corresponds to the de Vaucouleurs profile, for $n = 1$ to the exponential profile (Longair, 2008). For this reason Sérsic profile fitting has often been used to roughly separate bulge vs. disk dominated galaxies. To describe the observed image of galaxies with Sérsic profiles the ellipticity and the rotation angle have to be taken into account additionally. While the ellipticity of an individual galaxy depends strongly on the inclination angle, it is on average higher for disk galaxies.

1.1.3 Nuclear activity

The visible light of a galaxy is not necessarily only emitted by stars. Some galaxies have a very bright central region that can, in some cases, even exceed the emission of the stellar component of the galaxy by up to more than a factor of thousand. In contrast to what would be expected if the light from this central region came from stellar emission, spectra of these galaxies are characterised by strong emission lines and also show strong emission in radio and X-ray bands. The emission from this central region, the AGN, is powered by the accretion of material onto a central supermassive black hole. Feedback from the AGN emission is believed to have a potentially important impact on star formation and possibly morphology of galaxies (e.g., Alexander and Hickox, 2012; Fabian, 2012). The central supermassive black hole is surrounded by a luminous accretion disk. The temperature of the disk is not high enough to account for the observed X-ray emission; however, it can be generated by inverse Compton scattering by relativistic electrons. Synchrotron radiation contributes to the emission in radio bands. Broad emission lines are produced in inner regions above the disk characterised by high velocities and high densities. They only contain allowed transitions. In the outer regions where velocities are smaller, narrow lines are produced. Because of the lower density in these regions they also contain forbidden transitions. The accretion disk is surrounded by a dusty torus that can block – depending on the inclination angle – the light from the broad line region (Mo, van den Bosch, and White, 2010; Alexander and Hickox, 2012; Fabian, 2012).

1.2 Galaxies and their environment

Because of the gravitational attraction galaxies are not uniformly distributed. Regions with a high density attract even more matter from regions with lower density, amplifying the density contrast. This leads to the formation of the large scale structure of the Universe that is characterised by high-density regions with groups or clusters of galaxies connected by filaments and low-density regions (so-called voids). Clusters of galaxies are the largest virialized structures in the Universe. They can contain more than thousand galaxies embedded in massive dark matter halos ($M > 10^{14}\,M_\odot$) with sizes of several Mpc. The space between galaxies in a cluster is filled with the intracluster medium consisting of hot gas with temperatures up to $\sim 10^8$ K. Clusters can therefore be detected through the X-ray emission of their intracluster medium or through interaction of electrons of the intracluster medium with photons from the CMB (Loewenstein, 2004; Sunyaev and Zeldovich, 1972).

Galaxies interact with their environment and the presence of higher fractions of quiescent early-type galaxies in denser regions shows that galaxy evolution is significantly impacted by the environment (Hubble and Humason, 1931; Dressler, 1980; Baldry et al., 2006; Peng et al., 2010b). As discussed in Section 1.1.1 gas accreted from the cosmic web can fuel star formation in galaxies, and the higher availability of gas in denser environments can accelerate galaxy evolution at early cosmic times. Furthermore, interaction between galaxies can significantly impact star formation and morphological properties. A satellite galaxy encountering a massive galaxy can experience stripping of matter in the outer parts if tidal forces from the massive galaxy overcome the binding forces from the satellite. The subsequent lack of fuel for star formation can significantly reduce the SFR. Close encounters of galaxies can lead to merging if their orbital energy is low enough. Generally, galaxies in bound orbits will eventually always merge because their orbital energy in transferred into internal energy due to tidal interaction. However, the timescales can be very different depending on their orbital energy and angular momentum. The actual properties of the resulting galaxy depend mainly on the mass ratio, morphology, gas fraction and orbital properties of the merging progenitors. Mergers in which the more massive galaxy is at most 4 times more massive than the lower mass galaxy are typically called major mergers, others minor mergers. Major mergers can significantly impact the morphology of the merger remnant and are often considered an important channel to produce massive elliptical galaxies from disky progenitors (e.g., White, 1978; van der Wel et al., 2009a). Gas poor (so-called dry) mergers mainly change the stellar mass of the resulting galaxy and potentially increase its size, which is often invoked as a potentially important contribution to the evolution of the galaxy stellar mass vs. size relation (Khochfar and Silk, 2006; Bell et al., 2006; Naab, Khochfar, and Burkert, 2006). Gas rich (wet) mergers can significantly trigger star formation and AGN activity through gas inflow to the center as a consequence of tidal torques that remove its angular momentum (e.g., Mihos and Hernquist, 1996). The impact of the environment is further discussed in Chapter 4 and references therein.

1.3 Observations of galaxies

Galaxies emit a broad spectrum of light, originating from different processes, and characterised by the properties of the galaxy components. The spectrum consists of a continuum and of emission and absorption lines. The continuum from UV to the near infrared is mainly produced by ionization in the photosphere of stars. From mid- to far-infrared the continuum is dominated by thermal emission from dust. At radio wavelengths the emission is produced by relativistic and thermal electrons, while X-ray emission can be produced by gas accretion onto an AGN, X-ray binary stars, and inverse Compton scattering of the CMB. Lines in galaxy spectra are produced by transitions in atoms, ions and molecules in the photosphere of stars and in the interstellar gas. Emission lines provide information about density, chemical composition and temperature of the interstellar gas, while absorption lines are mainly produced in the atmospheres of stars and are routinely used to gather information about age and metallicity of stellar populations (Mo, van den Bosch, and White, 2010).

Galaxies contain dust grains that are produced in stellar atmospheres and supernovae (Draine, 2011). The dust interacts with the stellar light and significantly impacts the observed spectral energy distribution (SED) of a galaxy due to attenuation and emission processes. Dust attenuation includes the extinction of light due to absorption processes or scattering of light away and into the line of sight and contributions by unobscured stars (Salim and Narayanan, 2020). Dust extinction is generally stronger at shorter wavelength, so that the presence of dust causes reddening of the stellar SED. Given the intrinsic intensity $I_{0,\lambda}$, the intensity I_λ accounting for dust extinction can be written as $I_\lambda = I_{0,\lambda}\exp(-\tau_\lambda)$, where τ_λ is the optical depth. Given a dust attenuation law that describes the relative dependence of attenuation as a function of wavelength, the strength of the dust attenuation (or normalisation) is usually expressed by the resulting magnitude change at a specific wavelength $A_\lambda = 2.5\log(e)\tau_\lambda$. Traditionally the V band at $\sim 5500\,\mathrm{\AA}$ is chosen as reference band, although the actual choice of the reference is arbitrary (Mo, van den Bosch, and White, 2010; Salim and Narayanan, 2020).

To analyse galaxy properties it is therefore necessary to sample the SED at different wavelengths. Spectroscopy allows one to sample the galaxy SED with high resolution, enabling the investigation of distinct absorption and emission lines. To obtain galaxy optical spectra the observed light is dispersed by a slit, grating or a prism. However, spectroscopy is expensive and limited to the brightest objects. With much lower resolution the SED of a galaxy can also be sampled with broad band photometry, where the received flux of a galaxy is measured limited to a certain wavelength range by a filter. Given the intrinsic luminosity per unit wavelength L_λ of a galaxy at redshift z the observed flux (corrected by atmospheric and Galactic absorption) can be calculated as:

$$f_\lambda = \int_{-\infty}^{\infty} \mathrm{d}\lambda\, \lambda \frac{L_\lambda[\lambda(1+z)^{-1}, t(z)]}{(1+z)4\pi d_L^2(z)} R(\lambda), \tag{1.4}$$

where $R(\lambda)$ is the filter response function and $d_L(z)$ the luminosity distance (e.g., Bruzual and Charlot, 2003). The observed flux can be converted into the apparent magnitude, defined as:

$$m_{\mathrm{AB}} = -2.5 \log\left(f_\nu \times \frac{\mathrm{cm^2\,s\,Hz}}{\mathrm{erg}}\right) - 48.60, \tag{1.5}$$

where $f_\nu = \frac{\lambda^2}{c} f_\lambda$ is the observed flux per unit frequency (e.g., Oke, 1974).

To infer properties of the underlying stellar populations the observed SED has to be compared with physically motivated models of stellar emission, so-called stellar population synthesis models. A stellar population that forms at the same time with the same chemical compositions is called simple stellar population (SSP). Galaxies have complex star formation histories (star formation rate as a function of time), and thus their stellar emission can be described by so-called composite stellar populations, that have formed over long time with varying intensity of star formation and evolving chemical composition. These composite stellar populations can be seen as the superposition of many SSPs. Three ingredients are necessary to derive the spectrum of an SSP: the initial mass function (IMF) that describes the distribution of initial masses of born stars (e.g., Salpeter, 1955; Kroupa, 2001; Chabrier, 2003), a stellar spectral library that describes the spectra of stars at any position in the Hertzsprung-Russel diagram (e.g., Lejeune, Cuisinier, and Buser, 1997, 1998) and isochrones that assign the location in the Hertzsprung-Russel diagram given the age and metallicity of the star (e.g., Girardi et al., 2000). To calculate the spectrum of a composite stellar population additionally the star formation history (SFH) and chemical enrichment law have to be known (e.g., Bruzual and Charlot, 2003; Tinsley, 1980). In Figure 1.5 we show the spectra of an SSP with ages of 0, 0.1 and 0.5 Gyr derived with Bruzual and Charlot, 2003 models, assuming solar metallicity and a Chabrier, 2003 IMF.

1.3.1 Measuring star formation rates

Current star formation rates can be estimated by measuring light directly emitted by stars or by indirect light from dust emission. Massive stars have significantly shorter lifetimes than low-mass stars. In recently formed stellar populations where the massive O and B stars have not yet exceeded their lifetime most of the star light is emitted in the UV. This emission can then be observed and converted into a SFR, although assumptions on the IMF and star formation timescales are required to obtain the conversion factor. Because most galaxies contain dust that absorbs the UV emission and re-emits it in the infrared, corrections for dust attenuation have to be applied. Alternatively this re-emitted light can also be used as a tracer of star formation. The luminosity of the dust emission depends mainly on the dust temperature (and therefore on the composition of the stellar population because

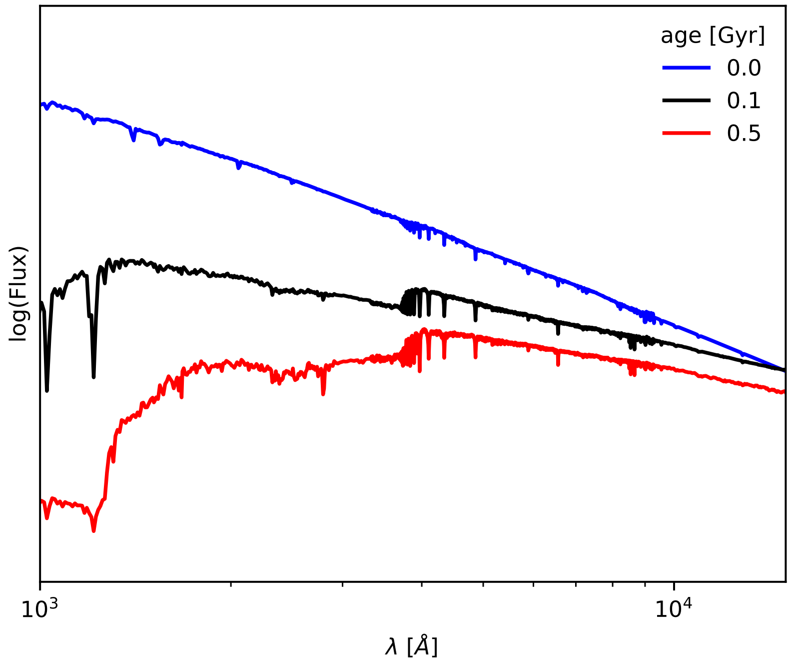

Figure 1.5: The emitted flux as a function of wavelength of a simple stellar population with solar metallicity and ages as indicated, assuming Bruzual and Charlot, 2003 models and a Chabrier, 2003 initial mass function.

younger stars heat the dust to higher temperatures, e.g., Helou 1986) and on the amount of dust. Another indirect tracer of star formation is ionised gas. The emission of massive stars can ionise the gas in the star forming region which can then be detected through various transitions, like the often used $H\alpha$ line at ~ 656 nm (e.g., Kennicutt, 1998).

1.3.2 Identifying quiescent and star-forming galaxies

To classify galaxies into star-forming and quiescent sources different methods have been developed that do not require expensive observations to estimate the SFR but rely on broad band photometry and can therefore be applied to large photometric surveys. Colors of galaxies, defined as the magnitude difference between two passbands, correlate with the specific star formation rate (star formation rate per unit stellar mass), with quiescent galaxies being redder than star-forming galaxies due to the lack of young stars emitting in the UV, and can thus be used to classify galaxies. The spectrum of evolved stellar populations shows a break at 4000 Å resulting from metal absorption lines, with the strength of the break being a good indicator of the stellar population age (Kauffmann et al., 2003). However, reddening of stellar populations can also be caused by dust, and samples of quiescent galaxies selected by a single (typically optical) color may potentially be significantly contaminated with dusty star forming sources. For this reason, galaxies are often photometrically classified by means of their position in a two-color space, with colors carefully chosen to break the degeneracy between age and dust reddening, like observed $B-z$ vs. $z-K$ colors (Daddi et al., 2004), restframe $U-V$ vs. $V-J$ colors (Williams et al., 2009) or restframe NUV$-r^+$ vs. r^+-J colors (Ilbert et al., 2013). In Figure 1.6 we show as an example UVJ color-color diagrams of galaxies in four different redshift bins.

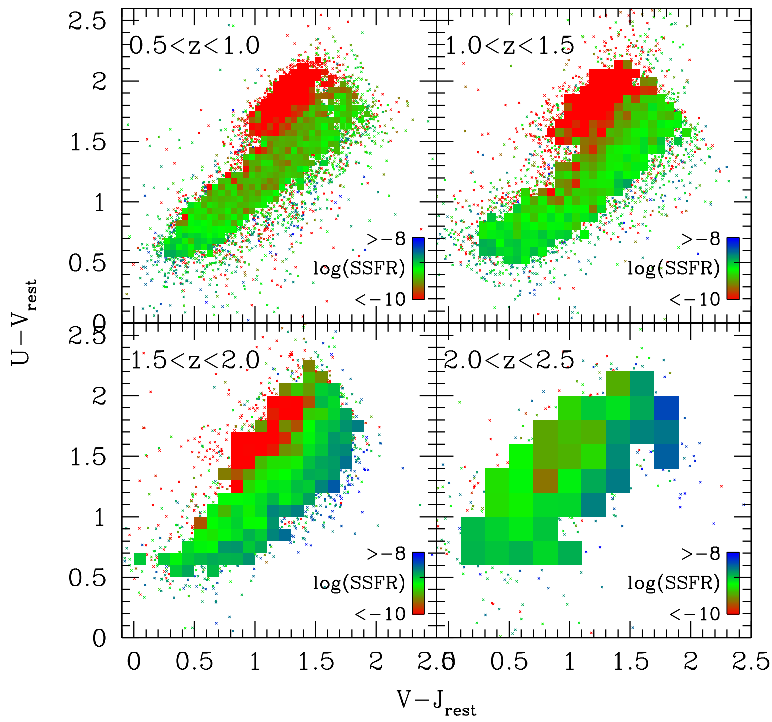

Figure 1.6: The UVJ restframe colors in four redshift bins as indicated (reproduced from Williams et al., 2009). The histogram is color coded by the median specific star formation rate in each bin.

1.4 Theoretical simulation of galaxy evolution

Because of the long timescales of galaxy evolution we typically only see a static picture of individual galaxies. In this respect simulations of galaxy evolution are a useful tool, allowing us to verify if our cosmological models can explain what we observe and providing further information that is difficult to access from observations alone. Increasing computing power has significantly increased the number of resolution elements in simulations, allowing one to simulate large volumes with high resolution and increased complexity of the models (Genel et al., 2014).

Nevertheless, simulations cannot be performed with unlimited precision and approximations are necessary. Close encounters of particles can lead to a divergence of the gravitational potential due to the numeric treatment, so that gravitational softening is introduced that replaces the $1/r$ dependence of the gravitational potential by $1/\sqrt{(}r^2+\epsilon^2)$ with the gravitational softening length ϵ (Dehnen, 2001). Furthermore it is computationally too expensive to calculate the gravitational potential between all particles, so that different methods have been developed to reduce the computational cost. In Barnes-Hut or tree simulations only close particles are considered individually, and more distant particles grouped together and treated as a single particle (Barnes and Hut, 1986). In particle mesh codes a density grid is calculated and the potential is solved for this grid using Fourier transformation (Klypin and Holtzman, 1997). A combination of these methods are tree particle-mesh codes that use a tree approach for close particles and a particle mesh for distant particles.

In hydrodynamical simulations the gaseous component is treated as a fluid. Different algorithms exist to discretise it into individual elements. The three most used methods are grid, particle and moving mesh codes. Grid codes divide the fluid into volume elements and the fluid is evolved by calculating the forces on the fluid in each element. Material can be moved between neighbours and the grid can be fixed or adaptive. In smoothed particle hydrodynamics the fluid is represented by many particles, and the evolution of the fluid can be calculated by the forces acting on each individual particle. Physical properties are obtained as the sum over all particles. Moving mesh codes combine both methods and use a moving grid to discretise the fluid, with particles within the cells that follow the flow of the fluid (Dale, 2015).

Hydrodynamical simulations are not the only numerical method to study galaxy evolution. Another numerical approach employs semi-analytic models that focus mainly on global galaxy properties by describing galaxies as unresolved objects with physical properties like stellar mass and morphology represented by single numbers. These properties change while the galaxy evolves following laws for star formation, cooling, feedback, interaction and more. Semi-analytic models are computationally less expensive, allowing the investigation of larger samples and a larger parameter space (Neistein et al., 2012; Hou, Lacey, and Frenk, 2019).

In this thesis we use hydrodynamical simulations of galaxy evolution to investigate properties of massive quiescent galaxies at $z \sim 3$ in simulations on a particle basis, allowing us to mimic observational effects like projection and the application of apertures, to compare current galaxy evolution models with observational findings. Owing to the large volume necessary to contain a decent amount of intrinsically very rare massive quiescent galaxies at high redshift (see Section 1.5) and at the same time high resolution necessary for a morphological analysis we focus on box 3 of the Magneticum simulations, that are based on the smoothed particle hydrodynamic tree particle mesh code Gadget (Springel, 2005), and boxes TNG100 and TNG300 of IllustrisTNG simulations that are based on the moving mesh tree particle mesh code AREPO (Springel, 2010). Further details about the simulations are given in Chapter 3 and the references therein.

1.5 Galaxies at high redshift

The long timescales of astronomical processes do not allow one to observe galaxy evolution in individual objects, however, galaxies at higher redshift are assumed to be the progenitors of lower-redshift galaxies, so that we can study galaxy evolution on a statistical basis by comparing galaxy populations at different cosmic times.

In the local Universe the bulk of the stellar mass is contained in elliptical galaxies and spiral bulges (e.g., Baldry et al., 2004) that have quenched their star formation and host old stellar populations, requiring the formation of the bulk of their stars already at much higher redshift.

Higher redshift studies have shown that the fraction of galaxies with quenched star formation decreases significantly at high redshift and the population of quiescent galaxies dominates the stellar mass density growth (e.g., Muzzin et al., 2013b). However, galaxies with quenched star-formation have also been discovered at high redshift (Glazebrook et al., 2017), challenging models of galaxy evolution that where not able to reproduce the oberserved numbers of quenched galaxies at these early cosmic epochs. In Figure 1.7 we show the evolution of the stellar mass functions (the number of galaxies per mass interval per volume) from $z = 0.2$ to $z = 4.0$, showing that the number density of quiescent galaxies is dramatically suppressed beyond $z \sim 2$, and that at the same time quiescent galaxies exist up to $z \sim 4$,

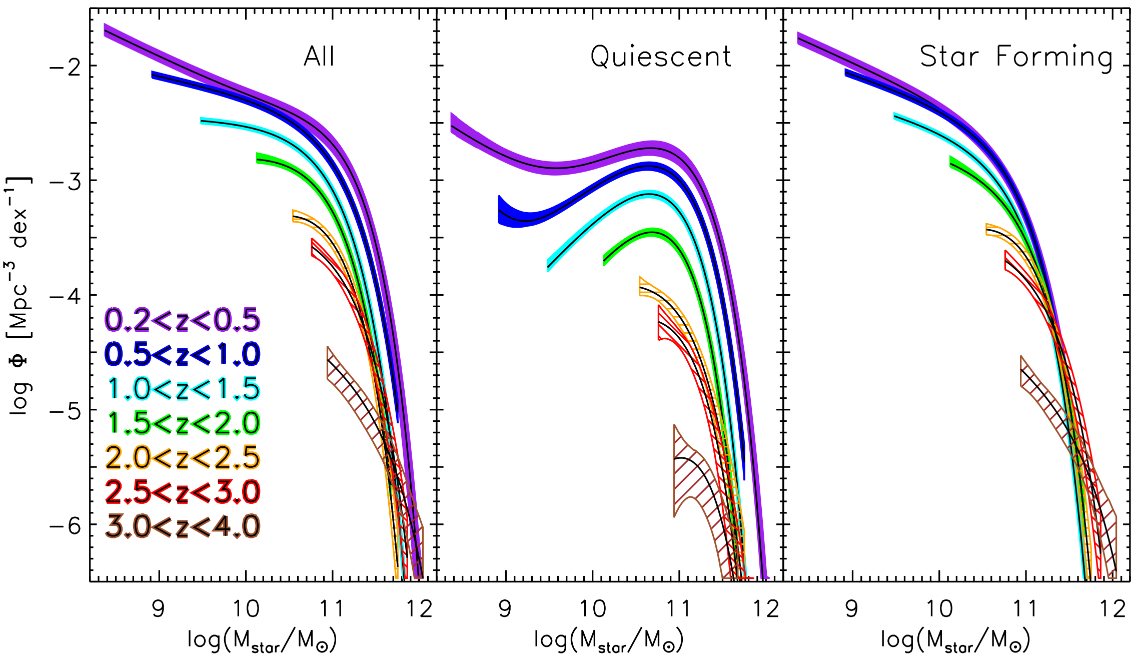

Figure 1.7: Stellar mass functions in the redshift range $0.2 < z < 4.0$ for all, quiescent and star-forming galaxies as indicated (reproduced from (Muzzin et al., 2013b)).

although they are very rare. Today AGN feedback is assumed to be an important contribution to quenching at high redshift and current simulations are now able to explain the existence of quenched galaxies at early cosmic times, although it is still challenging to quantitatively reproduce all their observed properties.

To understand what drives quenching at high redshift it is important to analyse properties of early quenched galaxies and compare them with our models of galaxy evolution. The previously mentioned strong correlation between galaxy quiescence and early-type morphology suggests that processes driving these two properties might be related. This has led to evolution scenarios of early quenched sources involving the formation of a compact, highly star forming core through cold gas inflow to the center, triggering AGN and star formation, and subsequent quenching due to feedback processes, morphological quenching and further mechanisms as discussed in Section 1.1.1.

However, while these models may be able to explain the correlation between quenching and morphological transformation, it is not yet clear if this correlation actually exists in the high redshift universe. Observing quenched galaxies at high redshift is challenging. While star-forming galaxies host bright massive stars and have been discovered and spectroscopically confirmed up to $z \sim 11$ (e.g., Oesch et al., 2016), galaxies with old stellar populations lack these stars and are significantly fainter, and do not have strong emission lines in their spectra that instead typically characterise star-forming galaxy spectra. The analysis of quiescent galaxy properties is therefore restricted to small sample sizes and obtaining similar signal-to-noise ratios to observations of star-forming galaxies requires much longer observation times. Although spectroscopy is very expensive due to the longer required integration times, it is crucial especially for these faint objects to have well constrained redshifts and a secure confirmation of quiescence. Indeed, because of the increasing photometric uncertainties of very distant, faint galaxies and of the small number of high-redshift quiescent sources, contamination with dusty star-forming galaxies in photometrically selected samples can become very significant, potentially biasing derived properties.

Given these complications, it is not astonishing that morphological studies of quiescent galaxies at high redshift have produced in some cases inconsistent results: The study of the mass size relation of quiescent vs. star-forming galaxies up to $z \sim 3$ with data from the CANDELS survey shows a constant slope of the mass vs. size relation for both, star-forming and quiescent galaxy populations, steeper for quiescent galaxies with more compact average sizes at a given stellar mass up to very high masses. The increase in the average size of massive $\log(M_\star/M_\odot) \gtrsim 11$ quiescent galaxy samples since $z \sim 3$ is found to be nearly one order of magnitude (e.g., van der Wel et al., 2014; Kubo et al., 2018). However, recent studies suggest that the most massive quiescent galaxies at high redshift are larger than expected from previous studies of the size vs. mass relation (Patel et al., 2017; Marsan et al., 2019). The strong evolution of the mass vs. size relation of quiescent galaxies is assumed to be driven by two main components: galaxies grow in mass and size, with a potentially significant impact of gas poor minor mergers on the evolution of the average mass-size relation (Khochfar and Silk, 2006; Bell et al., 2006; Naab, Khochfar, and Burkert, 2006, see Section 1.2). Additionally, progenitor bias may contribute to the evolution: When comparing quiescent galaxy samples at different redshift we assume that the higher redshift quiescent galaxies are the progenitors of those at lower redshift. However, quiescent galaxies at low redshift may have been star-forming galaxies at higher redshift. Because of the correlation between galaxy sizes and formation redshift of their stellar populations, this sample mismatch may contribute to producing a different mass-size relation at different redshifts (e.g., Cassata et al., 2013; Carollo et al., 2013).

While some morphological investigations find evidence of quiescent galaxies showing evolved, bulge-dominated morphologies already at high redshift (Bell et al., 2012; Mowla et al., 2019; Esdaile et al., 2020), thus supporting evolution scenarios that are able to explain a concomitant or quickly following transformation of morphology and suppression of star formation, others find that high-redshift quiescent galaxies seem to be rather flat, disk-dominated systems (e.g., Stockton, Canalizo, and Maihara, 2004; van Dokkum et al., 2008; van der Wel et al., 2011; Bezanson et al., 2018; Hill et al., 2019).

To better constrain models of galaxy evolution, and specifically quenching and morphological transformation and their connection, it is necessary to observe larger samples of high redshift quiescent galaxies, also in particular with spectroscopic follow-up to confirm their quiescent nature to better constrain their stellar population properties.

1.6 Structure of this thesis

This thesis is structured as follows: In Chapter 2 we investigate morphological properties of one of the first statistical samples of spectroscopically confirmed massive quiescent galaxies at high redshift by means of targeted Hubble Space Telescope observations. In Chapter 3 we compare observed stellar population and morphological properties of massive quiescent galaxies at high redshift with their counterparts in the hydrodynamical simulations IllustrisTNG (boxes TNG100, TNG300) and Magneticum (box 3) to investigate whether current galaxy formation models agree with recent observations, and to further explore the performance of the photometric selection of massive quiescent galaxies at high redshift exploiting additional information from simulations that is instead difficult to obtain in observations. In Chapter 4 we investigate the local environment at positions of spectroscopically confirmed massive quiescent galaxies at high redshift, to investigate potential signposts of dense protocluster cores that might evolve into massive galaxy clusters at lower redshift. In Chapter 5 we summarise the conclusions of this work and outline ongoing follow-up studies.

Chapter 2

Compact, bulge dominated structures of spectroscopically confirmed quiescent galaxies at $z \approx 3$

Lustig, Peter; Strazzullo, Veronica; D'Eugenio, Chiara; Daddi, Emanuele; Pannella, Maurilio; Renzini, Alvio; Cimatti, Andrea; Gobat, Raphael; Jin, Shuowen; Mohr, Joseph J.; Onodera, Masato, 2021, *Monthly Notices of the Royal Astronomical Society*, 501.2, 2659-2676

ABSTRACT

We study structural properties of spectroscopically confirmed massive quiescent galaxies at $z \approx 3$ with one of the first sizeable samples of such sources, made of ten $10.8 < \log(M_\star/M_\odot) < 11.3$ galaxies at $2.4 < z < 3.2$ in the COSMOS field whose redshifts and quiescence are confirmed by HST grism spectroscopy. Although affected by a weak bias toward younger stellar populations, this sample is deemed to be largely representative of the majority of the most massive and thus intrinsically rarest quiescent sources at this cosmic time. We rely on targeted HST/WFC3 observations and fit Sérsic profiles to the galaxy surface brightness distributions at $\approx 4000\,\text{Å}$ restframe. We find typically high Sérsic indices and axis ratios (medians ≈ 4.5 and 0.73, respectively) suggesting that, at odds with some previous results, the first massive quiescent galaxies may largely be already bulge-dominated systems. We measure compact galaxy sizes with an average of $\approx 1.4\,\mathrm{kpc}$ at $\log(M_\star/M_\odot) \approx 11.2$, in good agreement with the extrapolation at the highest masses of previous determinations of the stellar mass - size relation of quiescent galaxies, and of its redshift evolution, from photometrically selected samples at lower and similar redshifts. This work confirms the existence of a population of compact, bulge dominated, massive, quiescent sources at $z \approx 3$, providing one of the first statistical estimates of their structural properties, and further constraining the early formation and evolution of the first quiescent galaxies.

2.1 Introduction

Structural properties of galaxies in the nearby universe correlate with their stellar population properties. Early-type galaxies are characterised by a higher central concentration and typically lower apparent ellipticity than late-type galaxies, and generally have a low specific star formation rate (sSFR). Up to a stellar mass of $\log(M_\star/M_\odot) \approx 11$ early-type galaxies are more compact than late-type galaxies and show a steeper stellar mass vs. size relation (e.g., Shen et al., 2003; Guo et al., 2009).

Up to $z \approx 1$, high axis ratios are largely ubiquitous in the most massive $\log(M_\star/M_\odot) \gtrsim 11$ quiescent galaxies, although larger fractions of lower mass galaxies show lower axis ratios; this suggests that the mechanisms forming the most massive quiescent sources also result in the formation of bulge-dominated, spheroidal structures (van der Wel et al., 2009a; Holden et al., 2012). In fact, integral field spectroscopy showed that the vast majority of early-type galaxies in the nearby universe are fast rotators, with slow rotators dominating the early-type galaxy population only at the high mass end ($M_\star \gtrsim 2 \times 10^{11} M_\odot$; e.g., Emsellem et al., 2011; Cappellari, 2016).

Structural properties of massive galaxies at higher redshift are more sparsely investigated and have produced more controversial results. Stockton, Canalizo, and Maihara (2004) and Stockton et al. (2008) provided the first constraints on the structure of massive quiescent galaxies at $z \approx 2.5$ and revealed a higher fraction of quiescent galaxies with low Sérsic index profiles and smaller axis ratios with respect to low-redshift samples. Such scenario has been strengthened by following works with larger samples (van Dokkum et al., 2008; van der Wel et al., 2011; Bezanson et al., 2018; McGrath et al., 2008; Bundy et al., 2010; Chang et al., 2013; McLure et al., 2013; Hsu, Stockton, and Shih, 2014). Recently Hill et al. (2019) investigated the axis ratio evolution of star-forming and quiescent galaxies over the redshift range $0.2 < z < 4.0$, finding that massive ($\log(M_\star/M_\odot) > 11$) quiescent galaxies at $2.5 < z < 3.5$ are as flat as star-forming galaxies. Limited measurements of rotation curves indeed provide evidence for the existence of rotationally supported massive quiescent galaxies at high redshift (Newman, Belli, and Ellis, 2015; Newman et al., 2018; Toft et al., 2017). Nonetheless, the coupling of structural and stellar population properties of galaxies at higher redshifts remains debated, as other studies find that the correlation between early-type structure and low sSFR holds at least up to $z \approx 3$, suggesting that morphological transformation towards bulge-dominated systems is tightly related to quenching of star formation already at high redshift (Bell et al., 2012; Mowla et al., 2019; Esdaile et al., 2020; Lang et al., 2014; Tacchella et al., 2015). It has in fact been shown that galaxies beyond a given stellar mass or central stellar mass density threshold are largely quiescent (e.g., Peng et al., 2010b; Kauffmann et al., 2003; Brinchmann et al., 2004; Franx et al., 2008; van Dokkum et al., 2015; Whitaker et al., 2017), and that - although it remains unclear whether mass or density is the actual driver (Lilly and Carollo, 2016) - the most massive star-forming galaxies that at high redshift approach such density threshold are very likely to rapidly quench, given the drop in their number density at lower redshifts (Mowla et al., 2019).

A possible mechanism to explain the correlation between structural and stellar population properties is the compaction of a star-forming disk in a first step, followed by quenching (possibly also as a consequence of the morphological transformation). The compaction of the disk can be a result of gas inflow from filaments or mergers (e.g., Birnboim and Dekel, 2003; Dekel and Birnboim, 2006; Kereš et al., 2005a; Dekel et al., 2009), causing violent disk instabilities that drive dissipative gas inflow in the center. This leads to a compact galaxy with a high star formation rate (e.g., Dekel, Sari, and Ceverino, 2009; Burkert et al., 2010; Dekel et al., 2013; Dekel and Burkert, 2014; Zolotov et al., 2015; Gómez-Guijarro et al., 2019; Wu et al., 2020). Multiple mechanisms can then quench star formation, as suggested by simulations: gas consumption by star formation, stellar and AGN feedback as well as morphological quenching can produce fast quenching at high redshift, while virial shock heating, gravitational infall and AGN feedback can maintain quenching at lower redshift (e.g., Dekel and Silk, 1986; Ciotti and Ostriker, 2007; Birnboim and Dekel, 2003; Dekel and Birnboim, 2006; Martig et al., 2009; Kereš et al., 2005a; Dekel et al., 2009; Dekel and Birnboim, 2008; Khochfar and Ostriker, 2008; Tacchella et al., 2016a). Bulges embedded in star-forming disks can remain starved from accreted gas and maintain quenching if the infalling gas has a too high angular momentum to reach the bulge (Renzini et al., 2018).

Many studies have shown that the average size of distant quiescent galaxies at a given stellar mass is lower than for lower-redshift counterparts (e.g., Kubo et al., 2018; Cassata et al., 2013; Carollo et al., 2013; Mowla et al., 2019; Daddi et al., 2005; Trujillo et al., 2006; Toft et al., 2007; Cimatti et al., 2008; Cimatti, Nipoti, and Cassata, 2012, among many others). Although an evolution in the average size at fixed mass is also observed for late-type galaxies, it is milder than for early-types. With a large sample drawn from the CANDELS/3D-HST survey (Grogin et al., 2011; Koekemoer et al., 2011; Momcheva et al., 2016), van der Wel et al. (2014) studied morphologies of quiescent and star-forming galaxies with redshifts $0 < z < 3$. They find a redshift independent slope of the mass-size relation that is steeper for quiescent than for star-forming galaxies, and a size growth of massive quiescent galaxies of nearly an order of magnitude since $z \approx 3$, compared to a factor ≈ 3 for star-forming sources. Using measurements from the COSMOS-DASH survey, Mowla et al. (2019) extended the van der Wel et al. (2014) sample to higher stellar masses (162 galaxies at $1.5 < z < 3.0$ with $\log(M_\star/M_\odot) > 11.3$), which are poorly probed in the CANDELS/3D-HST survey due to the intrinsically very low number density of such sources, and find consistent results. However, even this survey only adds two quiescent galaxies to the van der Wel et al. (2014) sample at $z > 2.5$. As an alternative to overcome the problem of small sample sizes of the most distant, massive quiescent galaxies in deep fields, targeted imaging has been used to study these objects up to $z \approx 4$ (Kubo et al., 2018; Straatman et al., 2015), supporting the findings of strong average size growth of the quiescent galaxy population.

The observed redshift evolution of the mass-size relation of quiescent galaxies can be explained by a combination of different effects. Although gas rich mergers, resulting in central starbursts, are not an efficient way to increase galaxy size (Lin et al., 2007, 2008; Perez, Michel-Dansac, and Tissera, 2011; Athanassoula et al., 2016), gas poor minor mergers are often considered a viable and potentially significant channel for size growth of quiescent galaxies (Khochfar and Silk, 2006; Bell et al., 2006; Naab, Khochfar, and Burkert, 2006; Lin et al., 2008; Naab, Johansson, and Ostriker, 2009; Bezanson et al., 2009; Oser et al., 2010, 2012; Trujillo, Ferreras, and de La Rosa, 2011; Bédorf and Portegies Zwart, 2013). Progenitor bias is also often considered as an important contribution to the evolution of the mass-size relation, because of the significant drop of the quiescent galaxy population towards higher redshifts, implying a progenitor-descendant mismatch when comparing quiescent galaxy samples at different redshifts (Cassata et al., 2013; Carollo et al., 2013; van Dokkum and Franx, 1996; van Dokkum and Franx, 2001; Poggianti et al., 2013). To minimise the effect of progenitor bias, Belli, Newman, and Ellis (2014) and Stockmann et al. (2020) investigated size evolution at constant velocity dispersion (which is found to remain approximately unchanged for quiescent systems, van der Wel et al., 2009b; Bezanson, van Dokkum, and Franx, 2012), finding that size growth of individual galaxies may in fact have a significant role in the observed mass-size evolution. The observed evolution is thus likely produced by a combination of both galaxy growth and progenitor bias. Additional complications come from the use of light as a tracer of stellar mass. Radial color – and thus mass-to-light ratio – gradients can lead to significant differences between half-light and half-mass radii. Suess et al. (2019a,b) find that color gradients of quiescent galaxies are nearly flat at $z \gtrsim 2$, increase with decreasing redshift and are stronger in massive, larger and redder galaxies. Stellar mass vs. half-mass size relations of quiescent galaxies are shallower than stellar mass vs. (restframe optical) half-light size relations, and the growth of half-mass sizes towards lower redshifts is milder than for optical half-light sizes.

In most studies of the highest redshift quiescent sources, relying on purely photometric observations, the classification of star-forming vs. quiescent galaxies is performed by exploiting the correlation between sSFR and galaxy colors in properly chosen passbands (Daddi et al., 2004; Williams et al., 2009; Labbé et al., 2005; Ilbert et al., 2010). Especially at high redshift, where the number density of massive quiescent galaxies and the quiescent galaxy fraction decrease significantly (Ilbert et al., 2013; Muzzin et al., 2013b; Mowla et al., 2019; Whitaker et al., 2010a; Marchesini et al., 2010; Brammer et al., 2011a) and the bimodality in color sequences is less pronounced (Muzzin et al., 2013a; Laigle et al., 2016), misclassification can lead to a significant contamination of quiescent galaxy samples from star-forming objects. Spectroscopic confirmation of quiescence can help securing higher-purity samples of quiescent galaxies. However, spectroscopically confirming very distant quiescent sources is difficult and observationally expensive compared to star-forming galaxies at similar redshifts because of the lack of strong emission lines. Direct spectroscopic confirmation of quiescent sources currently reaches out to $z \approx 4$, and is based on the 4000 Å break, overall continuum shape, and/or weaker features as Fe and Mg absorption lines (Glazebrook et al., 2017; Esdaile et al., 2020; Newman, Belli, and Ellis, 2015; Newman et al., 2018; Glazebrook et al., 2004; Cimatti et al., 2004; Kriek et al., 2006; Gobat et al., 2012; Onodera et al., 2012, 2015; Marsan et al., 2015; Hill et al., 2016; Marsan et al., 2017; Gobat et al., 2017; Schreiber et al., 2018; Tanaka et al., 2019; Forrest et al., 2020a,b; Valentino et al., 2020). The morphological properties of sizeable samples of spectroscopically confirmed quiescent galaxies have only been analysed up to $z < 2.3$ (van Dokkum et al., 2008; Cimatti et al., 2008; Stockmann et al., 2020; Belli, Newman, and Ellis, 2017). At higher redshifts investigations are limited to a handful of galaxies at most (Esdaile et al., 2020; Gobat et al., 2012; Marsan et al., 2015; Hill et al., 2016; Tanaka et al., 2019). In this work we investigate structural properties of a spectroscopically confirmed sample of 10 quiescent galaxies at $2.4 < z < 3.2$ with stellar masses of $\log(M_\star/M_\odot) \gtrsim 11$, relying on targeted Hubble Space Telescope (HST) WFC3/F160W imaging and G141 grism observations. This sample contains $\approx 1/4$ of all spectroscopically confirmed quiescent galaxies at $z > 2.4$. Our sample is presented in Section 2.2. In Section 2.3 we explain our analysis and methods. In Section 2.4 we present and discuss our results.

Section 2.5 summarizes our findings and conclusions.

We assume a ΛCDM cosmology with $H_0 = 71$, $\Omega_{\rm M} = 0.27$ and $\Omega_\Lambda = 0.73$. Magnitudes are given in the AB system.

2.2 The quiescent galaxy sample

2.2.1 Sample selection

We selected high-redshift quiescent galaxy candidates for HST grism follow-up from the McCracken et al. (2010) photometric catalog of the 2 deg^2 COSMOS field. Initially we selected passive BzK (pBzK) galaxies (Daddi et al., 2004) that satisfy the conditions:

$$\mathrm{BzK} = (z_{\rm AB} - K_{\rm AB}) - (B_{\rm AB} - z_{\rm AB}) > -0.2 \tag{2.1}$$

$$\mathrm{zK} = (z_{\rm AB} - K_{\rm AB}) > 2.5. \tag{2.2}$$

These criteria select high-redshift (typically $z \gtrsim 1.4$) passive galaxies purely based on observed colors, without relying on photometric redshift estimation or SED analysis to identify quiescent sources. Given the low signal-to-noise ratio (SNR) of even massive quiescent galaxies at $z > 2$ in the available B and z band imaging, leading to large uncertainties in the formal passive vs. star-forming BzK classification of such sources, we also retained galaxies with SNR < 5 in these bands, independent of their classification as quiescent or star-forming BzK galaxies. We then considered photometric redshifts ($z_{\rm phot}$) for the selected galaxies estimated with the software EAZY (Brammer, van Dokkum, and Coppi, 2008) and specifically calibrated to better estimate photometric redshifts of high-redshift quiescent galaxies (see details in Strazzullo et al., 2015a). These photometric redshifts are listed in Table 2.1. We removed from the sample all galaxies with $z_{\rm phot} < 2.5$, as well as galaxies classified as star-forming from their restframe UVJ colors (Williams et al., 2009) as estimated by EAZY assuming the galaxy photometric redshift. We performed SED fitting with FAST (Kriek et al., 2009) with different model libraries, including 1) a generic setup with delayed exponential SFH and dust attenuation up to $A_{\rm V} = 5$ mag, assuming a Calzetti (2001) dust attenuation law, 2) constant SFR with $A_{\rm V}$ up to 5 mag, 3) only quiescent (including very young quiescent, given the redshift of our targets) models (age/$\tau > 4$, age > 0.5 Gyr). Based on this analysis, we discarded all candidates with an SED suggesting a possible star-forming solution. To further reduce potential contamination of the HST follow-up target sample from star-forming sources, we also deprioritised candidates with a SNR ≥ 4 at 24 µm in the Le Floc'h et al. (2009) catalog, except if they had a well probed, convincingly quiescent SED with no plausible star-forming solution, suggesting that the 24 µm emission could be powered by an AGN. We then selected from these candidates suitable targets for HST grism follow-up observations. In order to observe a first, sizeable sample of $z \approx 3$ quiescent candidates, we focused on massive galaxies for which a sufficiently high SNR spectrum to measure a reliable redshift could be obtained in $1-2$ orbits. To this aim, we simulated for each candidate the grism spectrum that could be obtained within this observing time, assuming the source photometric redshift and best-fit SED model, modelling the simulated spectrum to estimate the redshift. This observational constraint largely limited the viable targets to sources brighter than $H_{\rm AB} \approx 22$, leading to a sample of 23 sources that are shown in Figure 2.1. Owing to the low number density of such massive, quiescent galaxies at $z \approx 3$, none of these objects is found in the CANDELS/3D-HST COSMOS field (Grogin et al., 2011; Koekemoer et al., 2011; Momcheva et al., 2016). Although such bright ($H_{\rm AB} < 22$) targets were favoured because of the observational reasons discussed above, as well as of higher SNR photometry resulting in a more robust characterization of the galaxy SED, we also explored fainter candidates that potentially allow us to probe higher redshift galaxies. We thus included in the final target sample a fainter ($H_{\rm AB} \approx 23$) source at $z_{\rm phot} = 3.2$ for which - in contrast to most similarly faint candidates - the SED modeling discussed above was able to reject star-forming solutions at high confidence. The final target sample of 10 sources with photometric redshifts between 2.5 and 3.2 is listed in Table 2.1 and shown in Figure 2.1.

The selected targets have been observed with the G141 grism and direct imaging in the F160W band with the Wide Field Camera 3 (WFC3) on board of HST (program ID 15229, PI: E. Daddi). D'Eugenio et al. (D'Eugenio et al., 2020, 2021) have estimated spectroscopic redshifts from the grism spectra, which are shown in Table 2.1. They combined the grism spectra with photometric measurements from the Laigle et al. (2016) catalog and performed a stellar population analysis. By comparing the goodness-of-fit of constant SFR vs. passive templates with exponentially declining SFHs, star-forming solutions could be rejected for all galaxies in the sample (see full details and discussion in D'Eugenio et al. in preparation).

From the analysis of the stacked spectrum of all galaxies in the sample (except ID 7) D'Eugenio et al. (2020) derived a sSFR of $4.35 \pm 2.47 \times 10^{-11}\,\rm yr^{-1}$, which is 60 times below the main sequence of star-forming galaxies at the median redshift of $z = 2.8$ (Schreiber et al., 2015). The lookback time where 50 percent of the stellar mass of the stacked sample was formed is $t_{50} = 300^{+200}_{-50}$ Myr.

We note that the median and NMAD (normalised mean absolute difference) scatter of $(z_{\rm spec} - z_{\rm phot})/(1 + z_{\rm spec})$ for the sample studied here, using the grism redshifts from D'Eugenio et al. (2020) and the Strazzullo et al. (2015a) photometric redshifts used for the sample selection, are 0.03 and 0.06; we thus assume that no significant biases are introduced in the sample studied here by uncertainties in the photometric redshifts used for the sample selection.

2.2.2 SED modeling and stellar mass estimates

We perform SED fitting to estimate stellar masses of the targets from multi-band photometry from the COSMOS2015 catalog (Laigle et al., 2016) adopting the spectroscopic redshifts measured in D'Eugenio et al. (2020). We use FAST++[1] to fit Bruzual and Charlot (2003) population synthesis models to 29 photometric bands[2] from 0.42 µm to 8 µm (including narrow bands). We assume a Chabrier (2003) IMF, a Calzetti (2001) dust attenuation law and a delayed exponentially declining SFH with $7 \leq \log(\tau/\rm yr) \leq 10$. To allow for a more direct comparison with van der Wel et al. (2014, see Section 2.4) we also estimate stellar masses assuming an exponentially declining SFH, finding no systematics and individual stellar mass estimates differing by at most 0.05 dex for this specific sample, having no impact on our analysis. The metallicity is fixed to solar; leaving it free affects the mass estimates by at most

[1] https://github.com/cschreib/fastpp

[2] For sources that are observed in the H and Ks band by both UltraVISTA and WIRCam we have checked that there is no impact on the stellar mass estimates if the shallower WIRCAM data is removed.

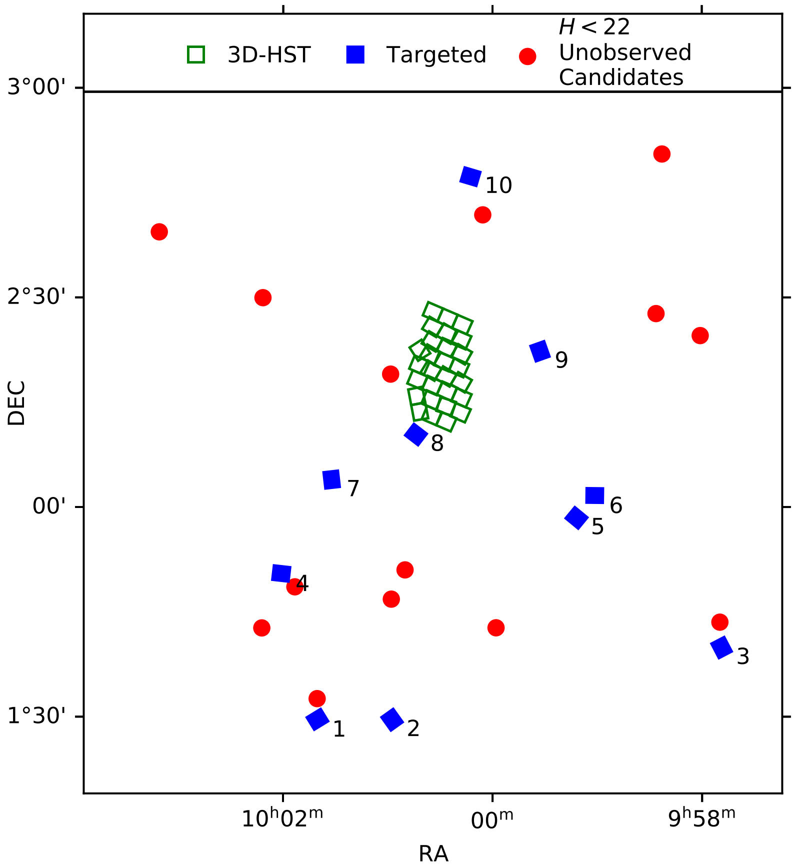

Figure 2.1: Selection of targets for HST follow-up observations in the $2\,\mathrm{deg}^2$ COSMOS field. Blue rectangles show the WFC3 footprint of the observations acquired for this project. Red symbols show the remaining quiescent galaxies from our $H < 22$, $z > 2.5$ candidate sample that were not included in the target list. Green rectangles show the footprint of the 3D-HST survey field in COSMOS.

0.07 dex. The best fit SED models are shown in Figure 2.2. The formal uncertainties on the estimated stellar masses with the given SED fitting setup are $\lesssim 0.06$ dex; we stress that these uncertainties do not include known sources of statistical and systematic errors (e.g., Maraston et al., 2006; Longhetti and Saracco, 2009; Muzzin et al., 2009; Conroy, 2013; Pacifici et al., 2015), and that more realistic absolute uncertainties on the individual mass estimates are likely around a factor ≈ 2.

IDs 2, 4, 7 and 10 have close neighbours in our F160W imaging that are undetected in the Laigle et al. (2016) catalog (see Section 2.3). For these targets we scale the estimated stellar masses by the fraction of the target flux to the total flux including the undetected neighbours within the 3 arcsec aperture used in Laigle et al. (2016), assuming the F160W fluxes measured in Section 2.3. This correction decreases the masses of IDs 2, 4, 7 and 10 by 0.01, 0.11, 0.02 and 0.01 dex, respectively. The resulting stellar masses are listed in Table 2.1[3].

The median estimated stellar mass of our sample is $\log(M_\star/M_\odot) = 11.16$ with individual masses in the range $10.8 < \log(M_\star/M_\odot) < 11.3$. To ensure that no systematics affect our comparisons with van der Wel et al. (2014, see Section 2.4), who use stellar mass estimates from Skelton et al. (2014), we estimate stellar masses with the same setup for sources from the Skelton et al. (2014) catalog using Laigle et al. (2016) photometry and redshifts from Skelton et al. (2014). By comparison of the two estimates we find a statistical scatter on the estimated stellar masses of 0.1 dex and no systematics[4].

2.2.3 Sample Characterisation and Representativeness

For sources at $z \approx 3$ the observed H band probes the galaxy SED at ≈ 4000 Å restframe, where the mass-to-light (M/L) ratio is sensitive to the age of the stellar population. Selecting H band bright sources as discussed in Section 2.2.1 may therefore bias the sample towards younger and/or less dust attenuated stellar populations. Depending on quenching mechanisms, and at least at lower redshifts on progenitor bias effects, sizes of younger vs. older quiescent sources at fixed stellar mass may differ on average (e.g., Saracco, Longhetti, and Andreon, 2009; Belli, Newman, and Ellis, 2015; Yano et al., 2016; Williams et al., 2017; Zahid and Geller, 2017; Almaini et al., 2017; Wu et al., 2018). Our $H < 22$ selection could thus potentially result in a bias on the average quiescent galaxy size at a given mass inferred from this sample. In this Section we thus discuss the representativeness of this H-selected sample with respect to the parent (mass-selected) sample of massive quiescent galaxies at this redshift.

To address the relevance of the potential bias in the quiescent sample caused by the H band selection, we compare the UVJ restframe colors of the $H < 22$ quiescent population with those of the full massive galaxy population at $2.5 < z < 3$. For

[3]We note that these masses reflect the total fluxes reported in the Laigle et al. (2016) catalog. We have verified that the total flux estimated by GALFIT on the F160W imaging is fully consistent with the total flux in the H band from the Laigle et al. (2016) catalog (the average flux ratio for these targets is 0.96 with a dispersion of ≈ 0.15, accounting for the small color term between the two filters).

[4]We do not use stellar mass estimates from Laigle et al. (2016) because: 1) we re-estimate stellar masses adopting the grism redshift (see also related discussion in Section 2.2.3 and Appendix 2.6.1), and 2) as also reported in Mowla et al. (2019) the stellar mass estimates from Laigle et al. (2016) are systematically higher than those from Skelton et al. (2014) by $\gtrsim 0.1$ dex for sources with $\log(M_\star/M_\odot) > 10.75$.

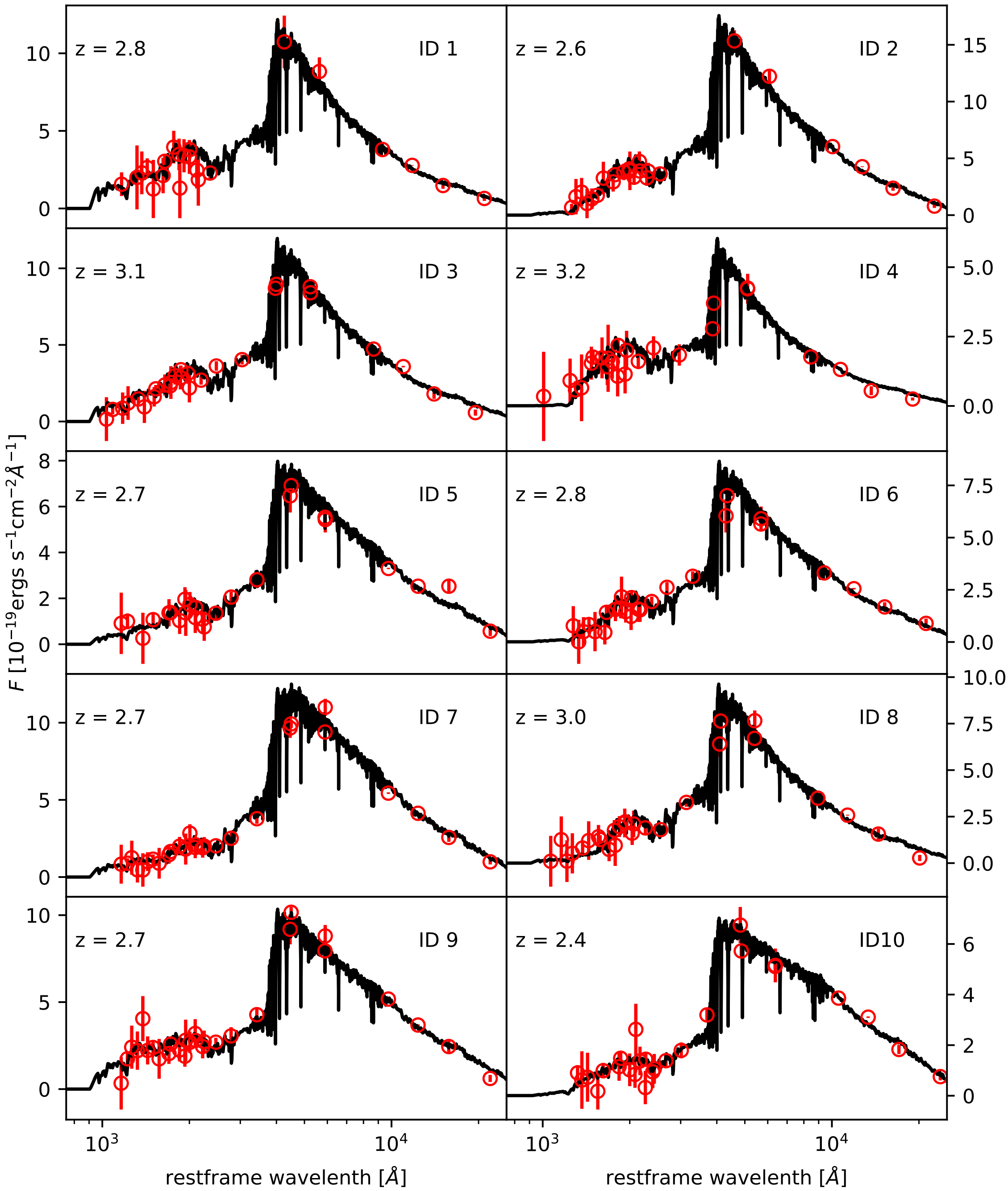

Figure 2.2: Observed SED's from 0.42 µm to 8 µm (Laigle et al., 2016) and best fit stellar population models (see Section 2.2.2).

the full parent sample, we match the Laigle et al. (2016) and Muzzin et al. (2013a) catalogs in order to fit the Laigle et al. (2016) photometry assuming the Muzzin et al. (2013a) photometric redshifts and spectroscopic redshifts from D'Eugenio et al. (2020) for our targets. We choose this approach in order to make use of the deeper photometry in the Laigle et al. (2016) catalog (that we use throughout in the analysis of our target sample in Section 2.2.2) and at the same time of the more accurate Muzzin et al. (2013a) photometric redshifts for massive quiescent sources at this redshift, as inferred by comparison with spectroscopic samples as shown in Appendix 2.6.1. We use the same FAST++ setup as in Section 2.2.2 to estimate stellar masses and EAZY to estimate restframe UVJ colors. We consider galaxies more massive than the mass completeness limit of $\log(M_\star/M_\odot) = 11.1$ at $z = 3$ from Muzzin et al. (2013a), providing a sample of 43 UVJ quiescent galaxies at $2.5 < z < 3.0$.

The location of quiescent galaxies in the UVJ plane correlates with the age of their stellar populations (e.g., Belli, Newman, and Ellis, 2019). We thus investigate in Figure 2.3 the distribution of our targets in the UVJ plane, and more generally of sources brighter than $H = 22$, with respect to the parent population, to constrain possible biases in our sample. All of our targets are well within the UVJ-quiescent region (Williams et al., 2009) except ID 10, which is anyway consistent with being UVJ-quiescent.

Belli, Newman, and Ellis (2019) parametrise the relation between stellar population age and UVJ colors by adopting t_{50} as an age estimate. We use this parametrization to investigate the impact of the H band selection on the fraction of post-starburst ($t_{50} < 800\,\mathrm{Myr}$) to old passive galaxies in the full sample of $\log(M_\star/M_\odot) > 11.1$ quiescent galaxies. As it may be expected given the high redshift, a large fraction of the quiescent galaxy sample is made of relatively young sources which at lower redshift are typically classified as post-starburst based on their colors (see also e.g., Whitaker et al., 2012a; Marchesini et al., 2014; Merlin et al., 2018; Maltby et al., 2018). To account for the uncertainties on the photometric measurements and redshift estimates we perturbe the source photometry and photometric redshift within the uncertainties and estimate restframe UVJ colors accordingly for 10000 realizations. The inferred median distribution of UVJ color combination which translates to t_{50} in the Belli, Newman, and Ellis (2019) parametrization is shown in the bottom panel of Figure 2.3. With this approach the estimated fraction of post-starburst galaxies in the full massive quiescent sample is 50 ± 9 percent. Considering only galaxies with $H < 22$ this fraction increases to 77 ± 9 percent, consistent with our sample in which 9 of 10 galaxies have $t_{50} < 800\,\mathrm{Myr}$, according to the relation from Belli, Newman, and Ellis (2019). Indeed D'Eugenio et al. (2020) found $t_{50} \leq 800\,\mathrm{Myr}$ for all galaxies in the sample. Therefore, at face value the average stellar age of galaxies in the $\log(M_\star/M_\odot) > 11.1$, $H < 22$ sample is indeed younger than in the whole $\log(M_\star/M_\odot) > 11.1$ sample, suggesting that our sample may be more representative of younger, post-starburst quiescent systems (see Figure 2.3), and likely biased against the oldest quiescent galaxies at this redshift. If significant morphological transformations happen on longer time scales than the typical age of this sample we would not be able to see it in our analysis because our sample does not contain these older sources. On the other hand, we stress that the uncertainties on the estimated restframe UVJ colors are significantly higher - as expected given the quality of the available photometry - for older quiescent galaxies, possibly resulting in a more significant contamination from dusty star-forming sources. To investigate this further, we also highlight in Figure 2.3 sources that are detected at 24 µm (≈ 6 µm restframe) with a SNR > 5 in the Jin et al. (2018) catalog. The fraction of 24 µm detected sources is higher for old quiescent galaxies than for "post-starburst" systems. Out of the six oldest UVJ quiescent sources in the sample shown in Figure 2.3, five are detected at 24 µm. However the 24 µm emission could also originate from nuclear activity (see D'Eugenio et al. in preparation for a discussion of 24 µm emissions of our targets), considering the large photometric uncertainties for the oldest sources, this suggests that a significant fraction of the full massive sample considered in Figure 2.3 might be star-forming contaminants. We thus re-estimate the fraction of post-starburst galaxies excluding all galaxies that are both 24 µm detected and UVJ quiescent with a probability lower than $p(\text{UVJ-Q}) = 0.997$ (3σ) and find that 65 ± 10 percent of the full $\log(M_\star/M_\odot) > 11.1$ sample have $t_{50} < 800$ Myr compared to 77 ± 10 percent of the galaxies of the full sample with $H < 22$. Although some of the 24 µm detections could be due to nuclear activity, the distribution of 24 µm detections across the UVJ plane and the estimated uncertainties in UVJ colors strongly suggest that a possibly significant fraction of the oldest quiescent galaxies are actually contaminants, and that the impact of the $H < 22$ selection on the age distribution of our target sample is smaller than would be suggested by face-value comparison of UVJ colors alone. Indeed, the independent estimate of the selection bias for this sample presented in D'Eugenio et al. (2020) consistently concludes that our target sample is representative of $\gtrsim 70$ percent of the overall quiescent population in the probed mass and redshift range. A specific - and currently very expensive - follow-up of a sample of the highest M/L ratio candidates would be necessary to conclusively address the picture of the potentially oldest massive quiescent galaxies at this redshift.

2.3 Morphological analysis

We investigate morphological properties of our targets by means of parametric modeling of the surface brightness distribution in the F160W band images. For each target we have 3 to 5 dithered observations with total exposure times ranging from 980 s to 1130 s at an observed wavelength of ≈ 16 000 Å. We reduce the preprocessed flat-fielded single exposures retrieved from the STSci archive in 2 different ways to investigate the robustness and sensitivity of the fit results to the reduction procedure. For the first reduction we use DrizzlePac release 2.2.6[5] to subtract the background, remove cosmic rays and for each source use a square kernel to drizzle the exposures to a pixel scale of 0.06 arcsec before median stacking them to the final image. Each image covers an area of ≈ 4.8 arcmin^2. For reference, the estimated 90 percent point-source completeness of the images is ≈ 26.7 mag.

We use SExtractor (Bertin and Arnouts, 1996) to detect sources in the F160W band images. We select point-like sources in each image by means of a magnitude (MAG_AUTO) vs. half-light radius (FLUX_RADIUS 50 percent) diagram. The comparison of point-like sources across the images of the 10 different fields and at different positions on the detector suggests that the point spread function (PSF) is relatively stable with no significant variations for the purposes relevant to this work. This allows us to create a single PSF by stacking high SNR ($H \lesssim 21$) point-like sources from all ten fields with SWarp (Bertin et al., 2002), improving the SNR

[5]https://github.com/spacetelescope/drizzlepac/blob/master/doc/source/index.rst

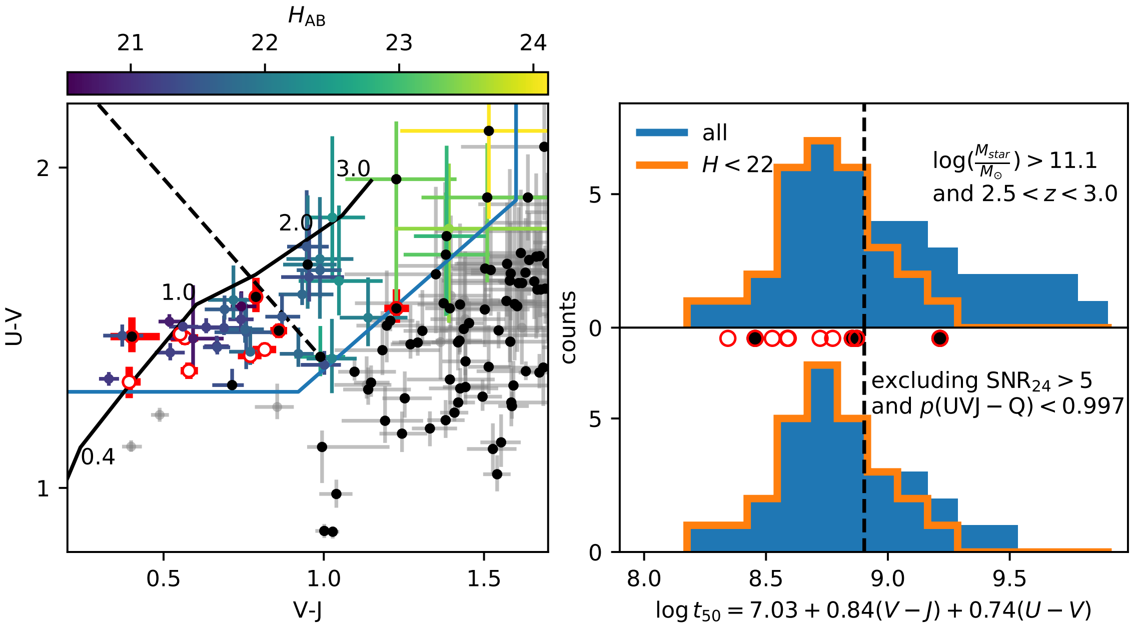

Figure 2.3: *Left panel*: restframe UVJ colors of massive ($\log(M_\star/M_\odot) > 11.1$) galaxies in the UltraVISTA COSMOS field (see Section 2.2.3) in the redshift range $2.5 < z < 3$. For UVJ-quiescent sources, the colors of the symbols scale with the H band magnitude, as indicated by the color bar. The sources studied in this work are overplotted as red circles, with colors computed assuming the spectroscopic redshift. The 1 sigma color uncertainties account for photometric and redshift uncertainties. 24 µm detections from Jin et al. (2018) are marked with a black dot. The blue line shows the adopted separation between star-forming and quiescent galaxies (Williams et al., 2009). The black solid line shows for reference the evolution of a simple stellar population (numbers along the line show ages in Gyr). The dashed line shows the location in the diagram corresponding to an average stellar age of $t_{50} = 800$ Myr based on the empirical relation between restframe UVJ colors and t_{50} from Belli, Newman, and Ellis (2019). *Right panel*: histograms of the UVJ color combination translating into t_{50} with the Belli, Newman, and Ellis (2019) relation (see Section 2.2.3), for the full $\log(M_\star/M_\odot) > 11.1$ UVJ-quiescent sample (top) and for the UVJ-quiescent sample excluding 24 µm detections with a probability of being quiescent < 0.997 (see text). In both cases orange histograms refer to the $H < 22$ subsample. Red symbols show the ten targets of this work.

of the model. To estimate the effect of possible systematics of the PSF modeling on our results (see discussion in Section 2.3.1), we vary the point-like source selection criteria to create a set of PSFs from our observations. We also compare these PSFs with a synthetic model, created with TinyTim, and with the hybrid model from van der Wel et al. (2014). Both are more peaked than our models and, if fitted to point sources in our images, subtract systematically too much flux in the center, while our PSF models do not cause systematic features in the residuals, confirming that they are appropriate descriptions of the PSF of our images. A possible reason why our PSF is less sharp is the low number (3-5) of dithered exposures per target.

For the second reduction we use the grizli pipeline[6] (Brammer, 2018) to produce science ready images from the single exposures, detect sources and create a PSF for each image. The science images produced with the grizli pipeline are slightly sharper and have less residual cosmic rays compared to the images from the former procedure. Nonetheless, the results of our analysis are largely independent of the reduction method as discussed in detail later in this section. Cutouts of all targets are shown in Figure 2.4.

We use GALFIT (Peng et al., 2002, 2010a) to fit PSF convolved Sérsic (1963, 1968) profiles to the F160W band images of the sources from both reductions. We create uncertainty maps by quadratically adding Poisson source noise to the background root mean square (RMS), estimated in $9 \times 9\,\mathrm{arcsec}^2$ boxes across the images. We fit sources in cutouts with a sidelength of 9 arcsec, allowing GALFIT to fit a constant background simultaneously with the Sérsic profiles. Estimating the local background and subtracting it from the image, rather than fitting it, has no significant impact on the estimated parameters for the targets considered here. For cutouts containing multiple galaxies, we simultaneously fit Sérsic profiles for all sources. We do not set prior constraints on any of the fit parameters (postition, magnitude, effective radius r_e, Sérsic index n, axis ratio q, position angle). Starting values for the fitted parameters are estimated based on the SExtractor output except for the Sérsic index for which we use a starting value of 1. We verified that varying the initial parameters in a reasonable range has no impact on the results for our targets. Estimated effective radii and axis ratios are stable against the use of the different reductions and corresponding PSFs, being entirely consistent within the estimated uncertainties with no systematic biases. Sérsic indices are systematically lower by 20 percent in the grizli reduction. In the following we always refer to the measurements obtained on the grizli reductions unless otherwise stated. We stress again that all conclusions would be unchanged if referring to the other reduction, and that all results would be fully consistent except Sérsic indices which would be on average larger, thus resulting in even stronger conclusions on the typically high Sérsic indices of these sources as discussed in Section 2.4. The target images, best fit models and corresponding residuals, together with HST ACS F814W imaging (Koekemoer et al., 2007; Massey et al., 2010, only available for IDs 4-10), are shown in Figure 2.4. The resulting profile parameters are presented in Table 2.1. Radii in this paper refer to effective radii along the semi major axis.

Some of our targets have faint close neighbouring sources with unknown redshifts (see also Stockmann et al., 2020), in particular ID 7 has a very close neighbour ($d \approx 0.8$ arcsec, corresponding to 6 kpc if at the target redshift). With the available data, we do not see evidence of interaction between these sources. Furthermore, after subtracting the best fit model the residuals of a single Sérsic profile

[6] https://github.com/gbrammer/grizli/

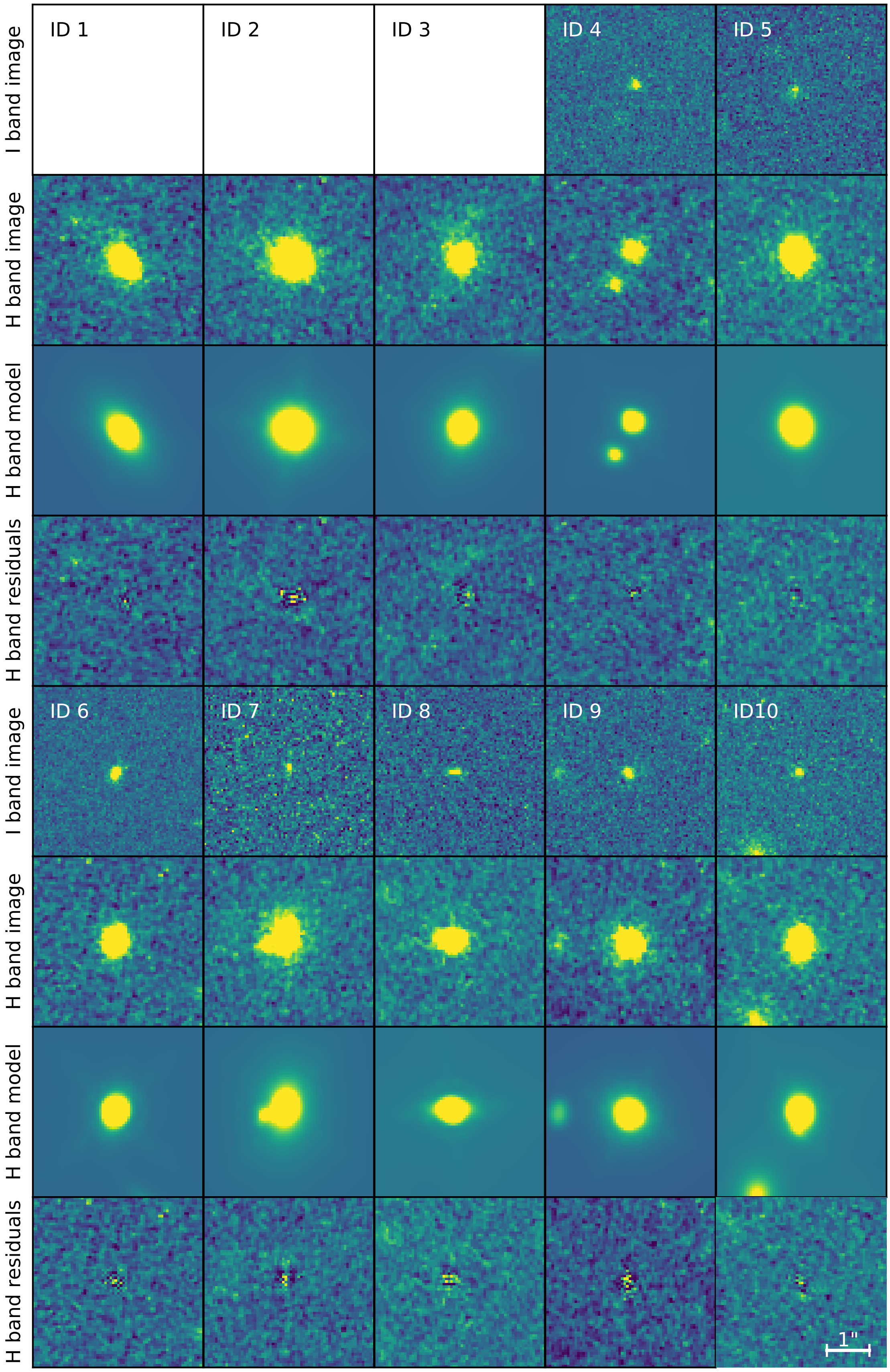

Figure 2.4: HST F160W (H band) images of the ten observed targets, the best fit models (see Section 2.3) and the corresponding residuals. For IDs 4-10 F814W (I band) imaging is available and also shown. The cutouts have a size of 4 arcsec (≈ 32 kpc) by side.

Table 2.1: Main properties and estimated morphological parameters of the ten targets. The column $\mathrm{ID_C}$ lists for convenience the IDs from the COSMOS Laigle et al. (2016) catalog. The z_{phot} column lists the photometric redshifts used for target selection, while z_{spec} lists the spectroscopic redshifts from D'Eugenio et al. (2020). The column $\log(M_\star/M_\odot)$ lists stellar mass estimates (see Section 2.2.2 for details, including a discussion of the uncertainties). The columns mag, r (sky), n, q list the GALFIT best fit values for the Sérsic profile; radii are effective radii along the semimajor axis. Uncertainties are estimated as explained in Section 2.3.1. The physical radii in kpc, r_{e} (5000 Å), are inferred sizes at 5000 Å, derived as explained in Section 2.4.2.

ID	$\mathrm{ID_C}$	R.A. (h:m:s)	Dec (d:m:s)	z_{phot}	z_{spec}	$\log\left(\frac{M_\star}{M_\odot}\right)$	mag	r_{e} (sky) (arcsec)	r_{e} (5000 Å) (kpc)	n	q
1	135730	10:01:39.98	01:29:34.49	2.6	$2.841^{+0.021}_{-0.018}$	11.14	$21.99^{+0.10}_{-0.09}$	$0.40^{+0.07}_{-0.06}$	$3.07^{+0.57}_{-0.47}$	$4.7^{+0.8}_{-0.8}$	$0.50^{+0.03}_{-0.03}$
2	137182	10:00:57.35	01:29:39.46	2.7	$2.557^{+0.005}_{-0.005}$	11.27	$21.32^{+0.02}_{-0.03}$	$0.15^{+0.01}_{-0.01}$	$1.18^{+0.04}_{-0.04}$	$3.0^{+0.3}_{-0.2}$	$0.96^{+0.02}_{-0.02}$
3	252568	09:57:48.57	01:39:57.82	2.8	$3.124^{+0.003}_{-0.003}$	11.32	$21.88^{+0.10}_{-0.10}$	$0.33^{+0.08}_{-0.05}$	$2.37^{+0.58}_{-0.37}$	$6.2^{+1.2}_{-1.1}$	$0.78^{+0.04}_{-0.04}$
4	361413	10:02:00.97	01:50:24.28	3.2	$3.230^{+0.007}_{-0.006}$	10.75	$23.37^{+0.08}_{-0.11}$	$0.07^{+0.01}_{-0.01}$	$0.46^{+0.08}_{-0.07}$	$4.8^{+2.9}_{-1.3}$	$0.86^{+0.11}_{-0.11}$
5	447058	09:59:11.77	01:58:32.96	2.5	$2.665^{+0.003}_{-0.007}$	11.11	$22.20^{+0.02}_{-0.02}$	$0.21^{+0.01}_{-0.01}$	$1.63^{+0.05}_{-0.05}$	$1.2^{+0.1}_{-0.1}$	$0.79^{+0.03}_{-0.03}$
6	478302	09:59:01.31	02:01:34.15	2.6	$2.801^{+0.005}_{-0.002}$	11.13	$22.23^{+0.02}_{-0.02}$	$0.109^{+0.004}_{-0.004}$	$0.84^{+0.03}_{-0.03}$	$2.3^{+0.3}_{-0.3}$	$0.56^{+0.04}_{-0.04}$
7	503898	10:01:31.86	02:03:58.79	2.6	$2.674^{+0.005}_{-0.009}$	11.32	$21.60^{+0.13}_{-0.11}$	$0.57^{+0.13}_{-0.11}$	$4.45^{+1.04}_{-0.89}$	$6.3^{+1.0}_{-1.2}$	$0.60^{+0.03}_{-0.03}$
8	575436	10:00:43.76	02:10:28.71	2.8	$2.998^{+0.002}_{-0.003}$	11.17	$22.30^{+0.03}_{-0.04}$	$0.10^{+0.01}_{-0.01}$	$0.75^{+0.05}_{-0.04}$	$4.3^{+0.8}_{-0.7}$	$0.33^{+0.03}_{-0.03}$
9	707962	09:59:32.52	02:22:21.99	2.6	$2.667^{+0.015}_{-0.002}$	11.3	$21.66^{+0.15}_{-0.17}$	$0.29^{+0.16}_{-0.07}$	$2.27^{+1.24}_{-0.58}$	12[a]	$0.87^{+0.05}_{-0.05}$
10	977680	10:00:12.65	02:47:23.47	2.5	$2.393^{+0.011}_{-0.000}$	11.1	$22.39^{+0.03}_{-0.03}$	$0.15^{+0.01}_{-0.01}$	$1.19^{+0.06}_{-0.05}$	$2.6^{+0.4}_{-0.3}$	$0.67^{+0.04}_{-0.04}$

[a] If the Sérsic index is fixed to 4, the effective radius decreases to 0.14 arcsec (2.1σ), see Section 2.3.

fit for IDs 2 and 10 also show faint neighbours close to the targets (0.56 arcsec and 0.1 arcsec, respectively, corresponding to 4.6 kpc and 1.0 kpc if they are at the targets redshift). For these sources an additional Sérsic component is thus used in the following to simultaneously model the faint neighbours. The models and residuals in Figure 2.4 show the modeling accounting for these sources. Estimated parameter values (r_e, n, q) change by $\lesssim 10$ percent, except for the estimated effective radius of ID 10 which decreases by 19 percent and its axis ratio which increases by 25 percent.

For several sources, namely IDs 6, 7, 8, 9 and 10 the residual images show a central residual. For ID 8 about 4 percent of the pixels associated with the source have a significance of more than 3σ in the residuals. For all other sources this fraction is $\lesssim 2$ percent. This is also shown in the Appendix in Figure 2.10. We verified that this is not a PSF effect by fitting the targets with different PSF models, including the more peaked TinyTim and van der Wel et al. (2014) models and examining a larger number of residuals from fits of other sources in the images. We also verified that adding an additional point-like component to the fit does not produce an appreciable improvement on the residuals for any of these targets. We note that 3 of these sources (IDs 6, 7 and 10) are detected in both the Jin et al. (2018) 24 µm catalog and the Marchesi et al. (2016) catalog of X-ray sources. Therefore, some level of star formation (in the galaxy center) and/or nuclear activity might possibly cause the central excess. By comparing the 24 µm and X-ray luminosities, D'Eugenio et al. (in preparation) suggest that in at least two out of these three sources the IR and X-ray emission is likely AGN dominated. The flux of the central residual for these sources is smaller than 10 percent of the image flux in any pixel.

2.3.1 Uncertainties

The precision and accuracy of our measurements are limited by noise and by uncertainties in the PSF model, which are analysed in the following.

To estimate the impact of PSF uncertainties on the parameter estimates we create on empty images without noise artificial sources with effective radius ranging from 0.03 to 0.72 arcsec ($0.2\,\mathrm{kpc} \leq r_\mathrm{e} \leq 5.8\,\mathrm{kpc}$ at $z = 2.75$) and with Sérsic indices from 0.5 to 8, spanning a reasonably wide range of Sérsic parameters for quiescent galaxies in the mass and redshift range of our targets. We then fit these artificial sources with the same procedure used for our targets, using different PSF models (see Section 2.3) for the convolution in the creation and in the fitting process. The deviations of the retrieved parameters (effective radius, Sérsic index, axis ratio) from the input ones are generally smaller than 5 percent; for very small radii ($r_\mathrm{e} \lesssim 0.05$ arcsec or $r_\mathrm{e} \lesssim 0.4$ kpc in the probed redshift range) they can exceed 10 percent. All of our targets except one (ID 4, $r_\mathrm{e} \approx 0.07$ arcsec) are significantly larger than this size. The uncertainties on the PSF model are therefore expected to have a subdominant impact on our results.

To investigate the uncertainties due to noise we create Sérsic models with Poisson noise in different empty areas of the observed images. We first create sources with the approximate magnitude of our targets, $H \approx 22$, and effective radius and Sérsic index in the same range as discussed above for the evaluation of systematic uncertainties. In this case we use the same PSF for the creation of the artificial sources and for their modeling.

In Figure 2.5 we show the deviation of the retrieved best-fit values for the Sérsic index, effective radius and axis ratio with respect to the input values. The estimated

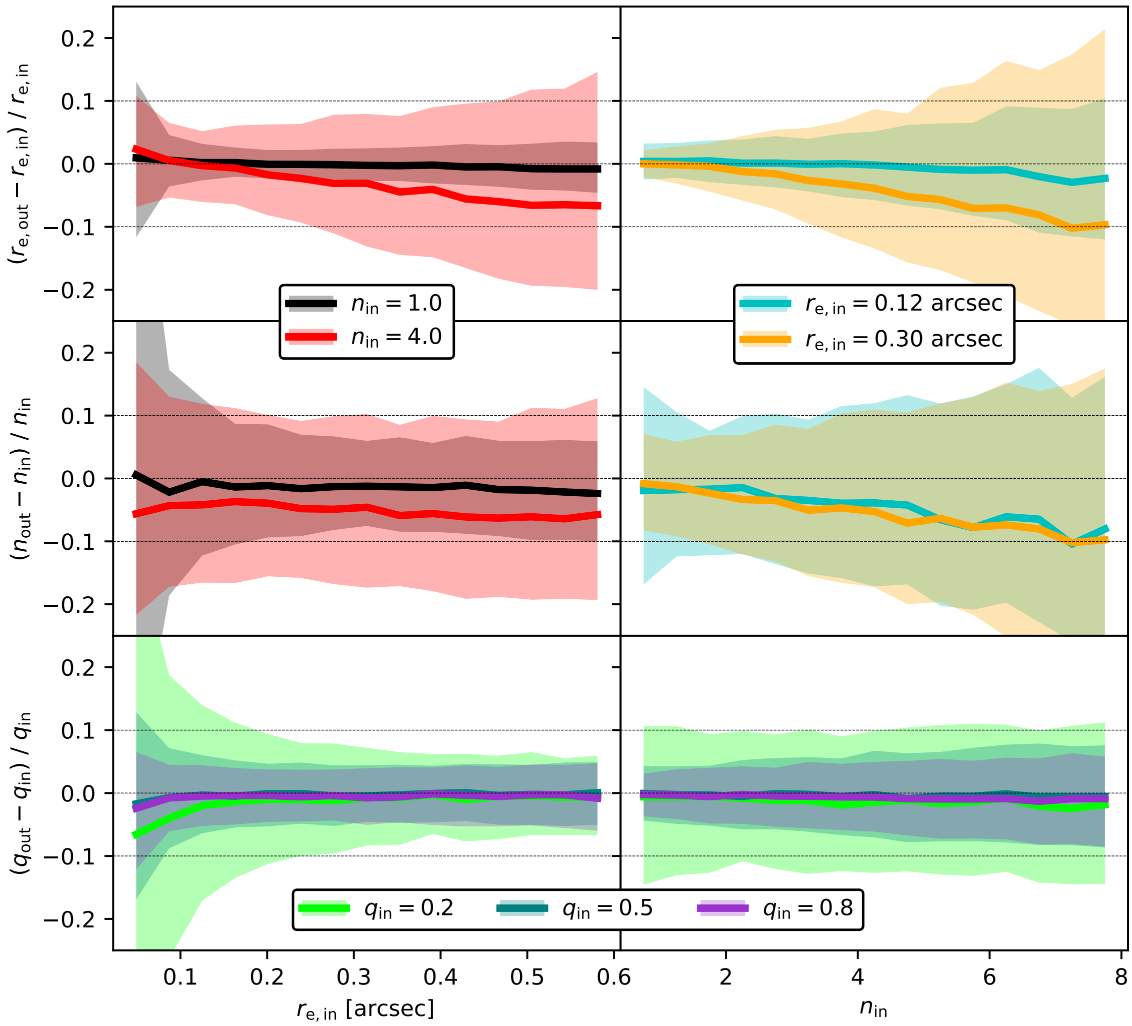

Figure 2.5: Relative uncertainties on the estimated effective radius, Sérsic index and axis ratio from the simulations (Section 2.3.1), defined as $(p_{\mathrm{out}} - p_{\mathrm{in}})/p_{\mathrm{in}}$ where p_{in} is the input parameter value of the artificial source and p_{out} the retrieved value from the fit. Left and right-hand panels show, respectively, the deviation of the retrieved vs. input parameters as a function of effective radius and Sérsic index of the source. The solid lines represent the median deviation from the input value, the shaded areas show the scatter estimated from the $16 - 84$ percentile range. We show as an example in the upper two panels results for a Sérsic index of 1 (black) and 4 (red) in the left panels and for $r_{\mathrm{e}} = 0.06\,$arcsec (cyan) and $r_{\mathrm{e}} = 0.12\,$arcsec (orange) in the right panels, both with axis ratios $0.5 \leq q_{in} \leq 1$. In the lower panels we show uncertainties on the retrieved axis ratio for input axis ratios of $0.2, 0.5$ and 0.8, as indicated.

scatter in r_e and n is of the order of 10 percent but depends on the actual values of r_e and n. The scatter of the axis ratio is of the order of 5 percent except for very small ratios of ≈ 0.2 where it reaches ≈ 10 percent. Models with larger Sérsic indices have generally larger uncertainties on the retrieved parameters and the Sérsic index tends to be underestimated, because of the extended tails and low SNR in the outskirts (see also e.g., Marleau and Simard, 1998; Pignatelli, Fasano, and Cassata, 2006; Sargent et al., 2007; Pannella et al., 2009b). This underestimation, $\Delta n \approx 5$ percent for $n \approx 4$ and $\Delta n \approx 10$ percent for very high Sérsic indices of $n \approx 8$, is about 4 times smaller than the statistical uncertainty. Sources with very small radii, close to the resolution limit, are affected by larger uncertainties, as well as those with very large radii because of the lower SNR per pixel at fixed magnitude. Sources with $n \approx 1$ and with $r_\mathrm{e} \gtrsim 0.15$ arcsec have uncertainties $\sigma_{r_\mathrm{e}} < 5$ percent and $\sigma_n < 10$ percent. The effective radius of models with large n and r_e is also affected by a systematic underestimation of r_e. For large sources with $r_\mathrm{e} = 0.3$ arcsec and $n \approx 4$, r_e is underestimated by ≈ 5 percent, for $n = 8$ by ≈ 10 percent. These systematics are small compared to the statistical uncertainties for the same models.

To properly estimate statistical uncertainties on the measured Sérsic parameters for each target, we then create artificial sources with parameters in a 10 percent range around the best fit models, motivated by the previous results, adding as usual Poisson noise. We add them to different empty areas of the observed images and fit them again with the same PSF as used for the creation. Since the estimated systematics are typically small compared to the statistical uncertainties we do not apply any correction for the described systematics in the following.

2.4 Results and discussion

2.4.1 Broad structural properties

Sérsic indices of our sources range from 1.2 to 6.3 with median statistical uncertainties of 16 % except for source ID 9, which formally has a best-fit Sérsic index of 12. The median Sérsic index of all targets is $4.5^{+0.3}_{-1.4}$. The high Sérsic index of ID 9 has no strong influence on the median Sérsic index, excluding it leads to a median of $n = 4.3^{+0.5}_{-1.2}$. The low Sérsic index $n = 1.2^{+0.1}_{-0.1}$ of ID 5 is also reinforced by the diffuse appearance in the F814W image compared to the other sources (see Figure 2.4).

In Figure 2.6 we show the median Sérsic index of massive quiescent galaxy samples as a function of redshift. For comparison to lower redshift quiescent and star forming galaxies we show median Sérsic indices of galaxies with stellar masses of $11 < \log(M_\star/M_\odot) < 11.5$ from the morphological analysis of van der Wel et al. (2014). At all redshifts, median Sérsic indices of quiescent galaxies are significantly larger than those of star-forming galaxies. The median Sérsic indices of quiescent galaxies from the van der Wel et al. (2014) sample decrease from $n = 4.5^{+0.2}_{-0.3}$ at $z = 0.4$ to $n = 3.3^{+1.0}_{-0.4}$ at $z = 2.7$. Our results are consistent with no significant evolution in the median Sérsic index of quiescent galaxies up to $z \approx 3$, in agreement with other studies from Patel et al. (2017), Mowla et al. (2019), Marsan et al. (2019), Stockmann et al. (2020) and Esdaile et al. (2020), although some investigations have reported lower Sérsic indices at $z \gtrsim 1.5$ (e.g., van Dokkum et al., 2008; van der Wel et al., 2011).

Axis ratios of our targets range between 0.33 and 0.96 with a median of $0.73^{+0.06}_{-0.12}$. The only source with $q < 0.5$ is ID 8 having $q = 0.33^{+0.03}_{-0.03}$ in spite of a high Sérsic index of $4.3^{+0.8}_{-0.7}$. The source also appears rather flat in the F814W image, which could be explained by a combination of an older bulge with redder colors and a younger and bluer disc that is seen edge-on.

Hill et al. (2019) find a redshift and stellar mass independent linear relation between Sérsic index and apparent axis ratio with a slope of $\mathrm{d}q/\mathrm{d}n = 0.062$, yielding an axis ratio of 0.71 at our median Sérsic index of 4.5, in perfect agreement with our measurement and reinforcing our conclusions on the generally high Sérsic indices of these sources.

In Figure 2.6 we also show the median axis ratio of massive quiescent galaxies as a function of redshift from Hill et al. (2019), comparing with measurements from our work and other studies at $z \gtrsim 1.5$. While at $z < 2$ median axis ratios of quiescent galaxy samples are larger than those of star-forming galaxies, at $z \gtrsim 2$ no clear difference can be seen, although uncertainties become large and quiescent galaxy sample contamination from starforming sources is likely more significant. Our measurement of the average axis ratio is in agreement with typical axis ratios of quiescent galaxies at low redshift (e.g., Hill et al., 2019; Holden et al., 2012). Consistent with our measurements, Patel et al. (2017) and Marsan et al. (2019) also find high axis ratios and Sérsic indices for massive ($\log(M_\star/M_\odot) > 11.26$) quiescent galaxies at $z \approx 2.6$ as well as Esdaile et al. (2020) at $z \approx 3.3$, suggesting that already at $z \approx 3$ a large fraction of quiescent galaxies are bulge dominated. On the other hand van Dokkum et al. (2008) investigated morphologies of 9 spectroscopically confirmed massive ($\log(M_\star/M_\odot) > 11.1$) quiescent galaxies at $z \approx 2.3$. The median Sérsic index of their sample is $2.3^{+0.5}_{-0.0}$ and the median apparent axis ratio $0.63^{+0.08}_{-0.24}$. In agreement with these results, van der Wel et al. (2011) analysed a color selected sample of 14 massive ($\log(M_\star/M_\odot) > 10.8$) quiescent galaxies at $1.5 < z < 2.5$ finding a median Sérsic index of $2.45^{+0.15}_{-0.40}$ and a median axis ratio of $0.67^{+0.10}_{-0.06}$. Belli, Newman, and Ellis (2017) find a median Sérsic index of $3.25^{+0.45}_{-0.30}$ and a median axis ratio of $0.69^{+0.05}_{-0.04}$ in the same redshift range. Hill et al. (2019) investigated the median flattening of galaxies in the redshift range $0.2 < z < 4.0$, based on the structural analysis from van der Wel et al. (2014) and also find that, for quiescent galaxies with $\log(M_\star/M_\odot) > 11.0$, the apparent axis ratio decreases to $q = 0.60 \pm 0.07$ at $z = 2.7$. In contrast to results from this work and other previous investigations as discussed above, these studies suggest that massive quiescent galaxies at high redshift are flatter than low-redshift counterparts, with a large fraction of disk-dominated systems. Considering at face value our results on both Sérsic indices and axis ratios, our measurements do not lend support to this picture. Nonetheless, concerning axis ratios, we note that given the large statistical uncertainties our median axis ratio is still consistent with results from van Dokkum et al. (2008), van der Wel et al. (2011), and Hill et al. (2019). Furthermore, one of our targets has $q < 0.5$ and three have $n < 3$, suggesting that some sources in our sample might indeed be disk-dominated or have a significant disk component. We note that differences in results and conclusions from the studies discussed above may partly derive from different sample selection criteria (in particular van der Wel et al. (2011) and Hill et al. (2019) rely on different flavours of photometrically selected samples).

2.4.2 The mass-size relation

The estimated effective radii of the galaxies in our sample are between 0.07 and 0.57 arcsec, corresponding to physical sizes of 0.5 to 4.5 kpc at restframe wavelengths

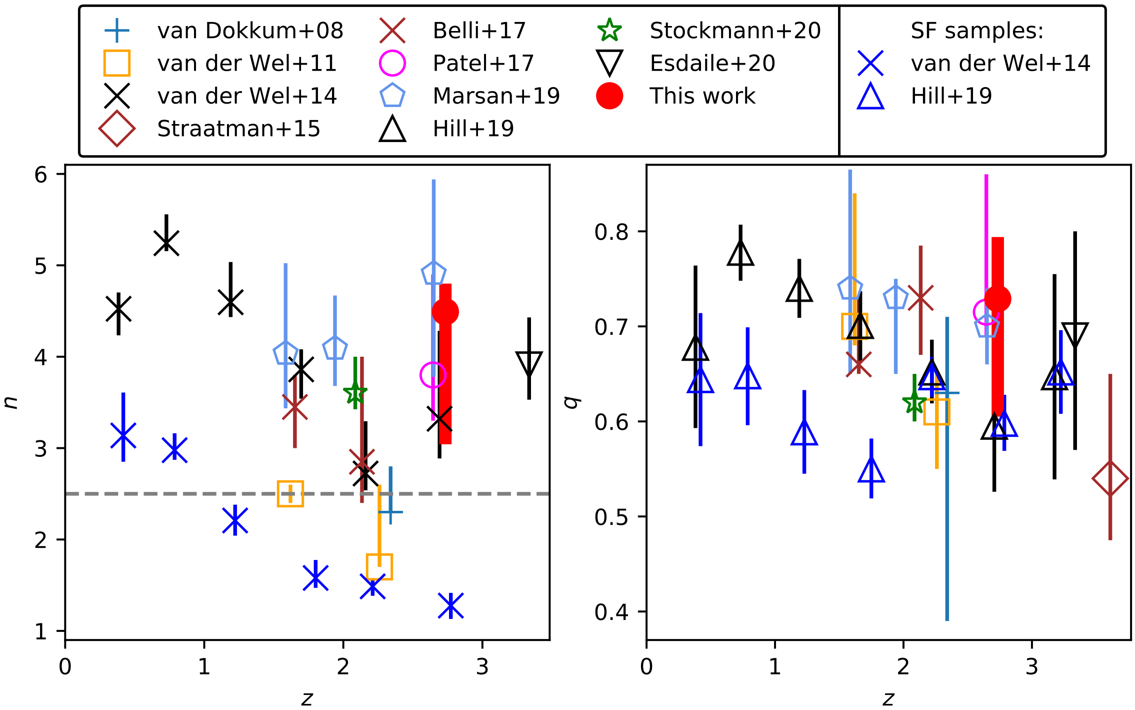

Figure 2.6: Median Sérsic indices (left panel) and axis ratios (right panel) of massive quiescent galaxy samples as a function of redshift. For comparison, we also show the evolution of the Sérsic index for star-forming galaxies from van der Wel et al. (2014, left) and of the axis ratios from the same sample analysed by Hill et al. (2019, right). Sources from van der Wel et al. (2014) have stellar masses of $11 < \log(M_{\star}/M_{\odot}) < 11.5$ and sources from Hill et al. (2019) have $\log(M_{\star}/M_{\odot}) > 11$. Results from other works are reported as published, with no further mass selection applied. If the same mass selection is applied to the other samples, measurements change within the uncertainties with no systematics. Uncertainties for the samples of van der Wel et al. (2014) and Hill et al. (2019) are taken from the papers while we use bootstrapping for the calculation for the other samples.

from 3800 to 4700 Å. Fitting ID 9 with the Sérsic index fixed to a typical value for bulge dominated systems of $n = 4$ (close to the sample median of $n = 4.5^{+0.3}_{-1.4}$) leads to a decrease of the estimated effective radius by 50 percent.

Because of - mostly negative - color gradients of galaxies (van der Wel et al., 2014; Suess et al., 2019a,b; Szomoru et al., 2011; Wuyts et al., 2012), galaxy sizes inferred from light profiles depend on the probed wavelength with sizes being larger at shorter wavelengths. For a proper comparison with previous works we convert all measured sizes to the same restframe wavelength of 5000 Å, adopting the correction appropriate for quiescent galaxies from van der Wel et al. (2014):

$$r_{\mathrm{e}}(5000\,\text{Å}) = r_{\mathrm{e}}(\lambda_{\mathrm{obs}}) \left(\frac{1+z}{\lambda_{\mathrm{obs}}/5000\,\text{Å}} \right)^{\frac{\Delta \log r_{\mathrm{e}}}{\Delta \log \lambda}} \tag{2.3}$$

with

$$\frac{\Delta \log r_{\mathrm{e}}}{\Delta \log \lambda} = -0.35 + 0.12z - 0.25 \log \left(\frac{M_\star}{10^{10} M_\odot} \right), \tag{2.4}$$

where λ_{obs} is the observed wavelength of 16 000 Å. This results in a very small correction decreasing the measured sizes of our targets by about 5 percent; the final sizes adopted in the following are between 0.5 and 4.4 kpc with a median size of $1.4^{+0.9}_{-0.2}$ kpc. Uncertainties on the median are obtained by bootstrapping. These sizes are reported in Table 2.1.

In Figure 2.7 we compare our results for the stellar mass-size relation of quiescent galaxies at $z \approx 3$ with previous measurements of photometrically (UVJ) selected quiescent and star-forming galaxies from van der Wel et al. (2014), as well as quiescent galaxies from Patel et al. (2017) and Mowla et al. (2019), in the same redshift range. To ensure that no systematics on stellar masses affect our comparison with size estimates from van der Wel et al. (2014), we fit Sérsic profiles to all galaxies in our fields and estimate their stellar masses as explained in Section 2.2.2. Their mass size relations are consistent with results from van der Wel et al. (2014) at the corresponding redshifts, indicating no significant systematics between the mass and size measurements in the two studies. For a more proper comparison of the mass-size relation within the probed $2.4 < z < 3.2$ range, and given the small sample size of the plotted samples from this work, Patel et al. (2017) and Mowla et al. (2019), we scale individual sizes for galaxies from these samples to a pivot redshift of 2.75 using the size evolution dependence on the Hubble parameter from van der Wel et al. (2014). This scaling leads to a maximum decrease of sizes by 17 percent at the lowest redshift $z = 2.4$ and a maximum increase by 25 percent at the highest redshift $z = 3.2$ [7]. The median sizes of our, Patel et al. (2017) and Mowla et al. (2019) samples decrease by ≈ 7, 8 and 10 percent, respectively.

Our sources specifically probe the mass-size relation at the highest stellar masses, for the first time with a statistical, homogeneously analysed, spectroscopically confirmed quiescent galaxy sample at this redshift. Our measurements thus extend towards the highest masses the determination of the mass-size relation of quiescent sources at $z \approx 3$, which in deep fields is typically dominated by lower-mass galaxies because of the intrinsically low number density of very massive quiescent sources. Our measurement of the median quiescent galaxy size at the tip of the mass-size

[7] If rather than using the size evolution dependence on the Hubble parameter we use the dependence on $1 + z$, always from van der Wel et al. (2014), the maximum increase (decrease) is 14 percent (20 percent) which does not impact the results of this analysis.

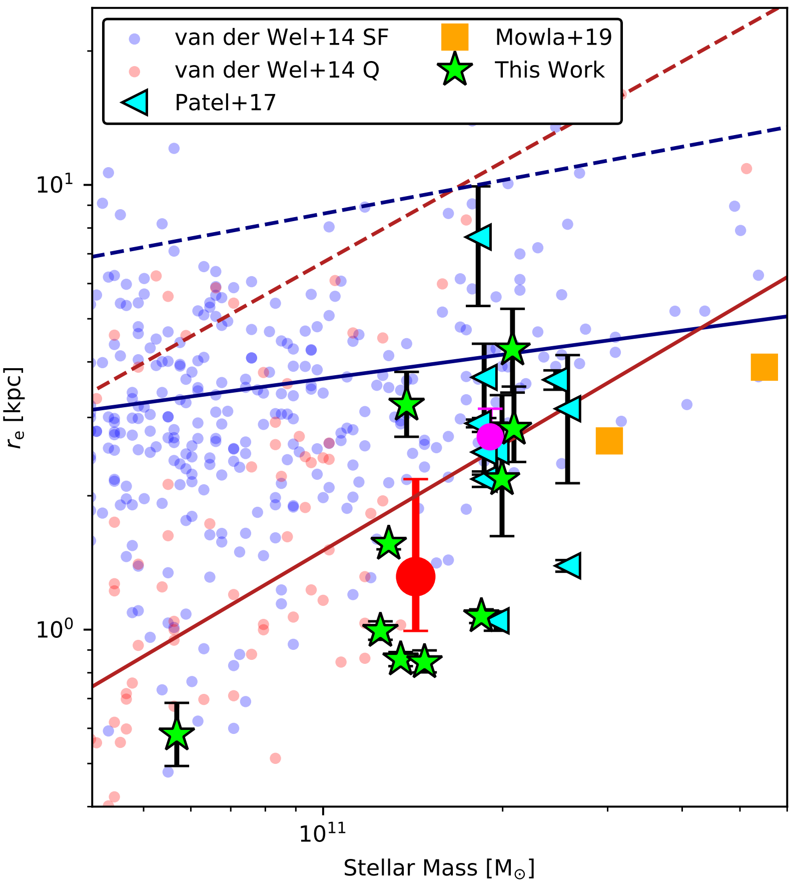

Figure 2.7: Estimated effective radii as a function of stellar mass. Sizes of individual galaxies from this work (stars), Patel et al. (2017, triangles) and Mowla et al. (2019, squares) are scaled to a pivot redshift of 2.75 (see Section 2.4.2). The red and purple dots show the median size and median mass from our sample and from Patel et al. (2017), respectively. Red (blue) dots are quiescent (star-forming) galaxies with $2.5 < z < 3.0$ from van der Wel et al. (2014), with red and blue solid lines showing the corresponding best-fit mass-size relations. For comparison, the best-fit relations for $z < 0.5$ from the same work are shown with dashed lines.

relation ($\log(M_\star/M_\odot) \gtrsim 11$) at $z \approx 3$ is nonetheless consistent with the relation measured in van der Wel et al. (2014).

Central Stellar Mass Densities

Although with the available data we can only probe the projected surface brightness distribution of our targets in the F160W band, we attempt a conversion of the observed light profile to a stellar mass density profile, to estimate central densities of these galaxies for the purpose of comparing with other similar studies. This conversion relies in particular on the assumption that the observed F160W light traces stellar mass across the galaxy: we stress that, also given the restframe wavelength probed by the F160W imaging at the redshift of these sources, this assumption has in fact significant limitations which are neglected in the following calculations.

We deproject the observed surface brightness distributions of our targets and calculate their central densities within 1 kpc following the procedure in Whitaker et al. (2017). Briefly, we calculate a circularized density profile from the best-fit structural parameters derived in Section 2.3 by performing an Abel transform as descibed in Bezanson et al. (2009). In the assumption that light traces mass the central stellar mass density within 1 kpc is then given by:

$$\rho_1 = \frac{\int_0^{1\,\mathrm{kpc}} \rho(r) r^2 \mathrm{d}r}{\int_0^{\infty} \rho(r) r^2 \mathrm{d}r} \frac{M_\star}{\frac{4}{3}\pi(1\,\mathrm{kpc})^3}, \tag{2.5}$$

where $\rho(r)$ is the spherical density profile as a function of radius. We estimate uncertainties coming from the measurement of structural parameters by perturbing r_e, n and q within their estimated uncertainties and recalculating the central densities 1000 times. These uncertainties are at most 0.09 dex; the uncertainties on the central densities are therefore dominated by the uncertainties on the stellar mass estimates (see Section 2.2.2) as well as by the limitations of the adopted assumptions to convert the observed surface brightness distribution to a stellar mass density profile. The central densities of the targets are $9.8 \lesssim \log(\rho_1\,\mathrm{kpc}^3/M_\odot) \lesssim 10.4$ with a median of $\log(\rho_1\,\mathrm{kpc}^3/M_\odot) = 10.1 \pm 0.1$. Such central densities translate in circular velocities at $r = 1\,\mathrm{kpc}$ of $330\,\mathrm{km/s} \lesssim v_1 \lesssim 640\,\mathrm{km/s}$ (median $480^{+50}_{-60}\mathrm{km/s}$), as obtained by $v_1 = \sqrt{\frac{4\pi}{3}(1\,\mathrm{kpc})^2 \rho_1 \mathrm{G}}$, where G is the gravitational constant, by balancing gravitational and centrifugal forces (see e.g., Whitaker et al., 2017).

These high inferred central densities - and implied circular velocities - are in line with previous determinations for high-redshift massive, quiescent sources (e.g., Mowla et al., 2019; Whitaker et al., 2017; van Dokkum et al., 2014).

2.4.3 Size evolution

To constrain the redshift evolution of massive quiescent galaxies at early times we compare sizes from our work with measurements from van der Wel et al. (2014), Straatman et al. (2015), Patel et al. (2017), Kubo et al. (2017), Belli, Newman, and Ellis (2017), Kubo et al. (2018), Marsan et al. (2019), Stockmann et al. (2020) and Esdaile et al. (2020) in Figure 2.8. Sources from Belli, Newman, and Ellis (2017), Stockmann et al. (2020), Esdaile et al. (2020) and from this work are spectroscopically confirmed quiescent galaxies, while the other studies we compare with rely on photometrically selected quiescent sources.

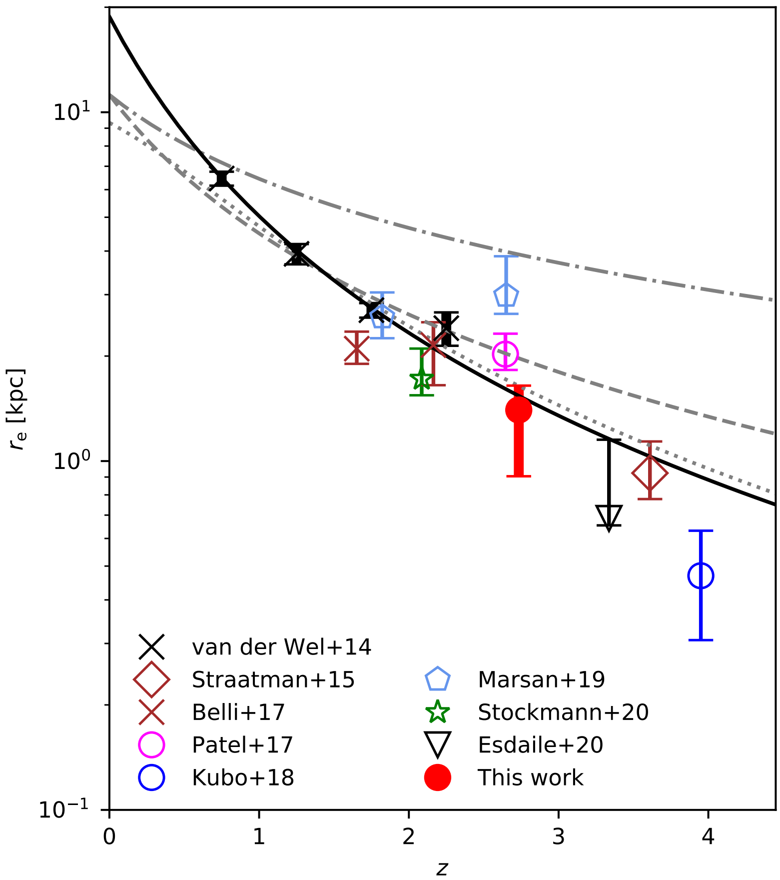

Figure 2.8: Median effective radii of quiescent galaxy samples with $10.6 < \log(M_\star/M_\odot) < 11.8$ as function of redshift. Sizes are scaled to a pivot mass of $\log(M_\star/M_\odot) = 11.1$ as explained in section 2.4.2. The Marsan et al. (2019) (Belli, Newman, and Ellis, 2017) sample is split into two subsamples with $1.5 < z < 2.1$ ($1.5 < z < 1.9$) and $2.6 < z < 3$ ($2.1 < z < 2.4$). The dotted line shows the best fit model from van der Wel et al. (2014) assuming a $r_e \propto h(r)^\beta$ relation, while the dashed and solid lines show best fit models assuming $r_e \propto (1+z)^\beta$ from van der Wel et al. (2014) and Kubo et al. (2018), respectively. The dashed-dotted line shows for reference the median evolution for star-forming galaxies from van der Wel et al. (2014).

Sources from van der Wel et al. (2014) in this figure have masses between $11.0 < \log(M_\star/M_\odot) < 11.5$ with a median mass of $\log(M_\star/M_\odot) \approx 11.1$ in each redshift bin. We use the redshift independent slope of the mass size relation from van der Wel et al. (2014) ($\mathrm{d}\log(r_\mathrm{e})/\mathrm{d}\log(M_\star) = 0.7$) to scale sizes of individual galaxies of all other samples (with masses in the range $10.6 < \log(M_\star/M_\odot) < 11.8$) to $\log(M_\star/M_\odot) = 11.1$. We then calculate median sizes and uncertainties for all samples by bootstrapping. The aforementioned scaling to a common mass of $\log(M_\star/M_\odot) = 11.1$ has a very limited impact on our measurement of the median size of our sample being $1.4^{+0.2}_{-0.5}$ kpc at the pivot mass, basically affecting only the uncertainties. For the least massive sample (Straatman et al., 2015) this correction increases the median size by ≈ 0.1 dex, while for the most massive sample (Marsan et al., 2019) the median size decreases by ≈ 0.25 dex. For the study of Kubo et al. (2018) the size and uncertainty of the stack is shown. All points are plotted at the median redshift of the respective sample[8].

Our measurements are in line with previous determinations indicating that sizes of quiescent galaxies at fixed stellar mass have increased by nearly one order of magnitude since $z = 3$. The different models from van der Wel et al. (2014) and Kubo et al. (2018), that parametrise the redshift evolution of the mass-size relation either as a function of the Hubble parameter, that is related to halo properties, or as a function of the scale factor, differ by a maximum of 0.1 dex at the median target redshift of 2.73. The median of our size measurements is consistent with the van der Wel et al. (2014) evolution as a function of $h(z)$ and the Kubo et al. (2018) evolution as a function of $1+z$. Our measurement is 2 sigma smaller than expected from the van der Wel et al. (2014) evolution as a function of $1+z$, which suggests, together with the higher redshift measurements by Straatman et al. (2015), Kubo et al. (2018) and Esdaile et al. (2020) that size evolution is steeper than in this relation.

At redshifts closest to our measurements, the median sizes from Patel et al. (2017) and especially from the highest redshift sources in Marsan et al. (2019) tend to be larger than our estimate as well as than extrapolations from most of the other high-redshift measurements discussed above. Both measurements are largely based on the same sample of galaxies with a median mass of $\log(M_\star/M_\odot) \approx 11.3$. Based on these measurements, Patel et al. (2017) and Marsan et al. (2019) suggest that very massive galaxies with $\log(M_\star/M_\odot) > 11.25$ are systematically larger than expected from the mass-size relation determined at lower masses, and thus that the size evolution factor may be different at the highest masses. On the other hand, results from the very massive samples with $\log(M_\star/M_\odot) \approx 11.5$ from Marsan et al. (2019) at $z \approx 1.8$ and from Stockmann et al. (2020) at $z \approx 2$ – the latter likely affected by minimal contamination from star-forming sources, due to spectroscopic confirmation – do not seem to support such a scenario. From the four most massive galaxies in our sample with $\log(M_\star/M_\odot) > 11.25$ we see excellent agreement with the extrapolation of the van der Wel et al. (2014) mass-size relation, although the statistics are very limited due to the small sample size.

[8] We do not use any size vs. redshift relation to scale individual galaxy sizes to the median redshift before calculating the median size. However, if any of the relations shown in Figure 2.8 is adopted to do so, the impact on the median size is smaller than 0.03 dex for any sample and does not affect our discussion.

2.5 Summary and Conclusions

We have analysed structural properties of a first sizeable sample of spectroscopically confirmed, massive, quiescent galaxies at $z \approx 3$ (D'Eugenio et al., 2020). Due to the rarity of these objects, we relied on targeted HST/WFC3 imaging of 10 robust candidates.

We estimate structural properties by fitting Sérsic profiles to the F160W images and obtain half light radii of about $r_{\rm e} \approx 1\,{\rm kpc}$ at stellar masses of $\log(M_\star/M_\odot) \approx 11.2$, in agreement with photometrically selected samples at this redshift. The comparison with sizes of massive quiescent galaxies at different redshifts shows substantial agreement with the expected evolution of the mass-size relation of quiescent galaxies as determined in previous work, pointing towards a size evolution factor at fixed stellar mass of almost a factor 10 from $z \approx 3$ to today.

Although our observations are consistent with a fraction of our sample being made of disk-dominated galaxies, and a larger sample would be needed to better quantify the prevalence of such sources, our measurements of both axis ratios and Sérsic indices suggest that massive, quiescent galaxies are already largely bulge dominated at $z \approx 3$. Based on a sample of massive galaxies in the redshift range $0.5 < z < 3$, Barro et al. (2017) find a redshift and mass independent relation between the offset of a galaxy's star formation rate from the main sequence and the central mass density, that strongly correlates with Sérsic index. This implies that star forming galaxies first grow inside out while increasing the radius and the central mass density, followed by a phase of enhanced bulge growth that increases the Sérsic index. Star formation is then suppressed and galaxies become quiescent. This picture is also in line with other studies by e.g. Lang et al. (2014), van Dokkum et al. (2015, 2014), Gobat et al. (2017), Whitaker et al. (2017) and Gómez-Guijarro et al. (2019) and is consistent with the large fraction of bulge dominated systems in our sample. The presence of bulge-dominated, quiescent galaxies already at $z \approx 3$ constraints the timescales of quenching and of morphological transformations at early times. Although merging is believed to be a critical process to explain the size and structural evolution of quiescent high redshift progenitors into local massive ellipticals, the combination of young ages and dense, compact structures of the most distant quiescent galaxies such as those studied here suggest different mechanisms for the fast formation of the stellar core. Matching number densities and high SFRs at high redshift have suggested an evolutionary path linking the intense bursts of star formation in high-redshift sub-mm galaxies to the high stellar densities and old stellar populations of massive elliptical galaxies at lower redshifts down to the nearby universe (e.g., Cimatti et al., 2008; Lilly et al., 1999; Genzel et al., 2003; Tacconi et al., 2008b; Simpson et al., 2014, 2017), including in particular the most distant massive, dusty star-forming galaxies being likely progenitors of (at least some of) the first massive, compact quiescent galaxies at $z > 2$ (e.g., Forrest et al., 2020a; Valentino et al., 2020; Toft et al., 2014). High resolution ALMA imaging of $z \sim 4-6$ dusty, massive, highly star-forming sources confirms the existence of possible star-forming progenitors with already compact morphologies (Oteo et al., 2017; Jin et al., 2019). The majority of bright sub-mm galaxies in simulations (Dekel, Sari, and Ceverino, 2009; Zolotov et al., 2015; Hopkins et al., 2008; Wellons et al., 2015; Lagos et al., 2020) are experiencing central starbursts driven by two main channels, gas-rich major mergers and disk instabilities, that increase the central density forming a compact remnant. Such remnants may still have disks and disk-dominated kinematics (e.g., Newman et al., 2018; Toft et al., 2017; Belli, Newman, and Ellis, 2017, and references therein), suggesting that the morphological transformations creating dispersion-supported ellipticals are not necessarily coincident with quenching. The mechanism by which star formation would stop in the compact star-forming progenitors is still unclear, with proposed processes including dynamical heating (morphological quenching, Martig et al., 2009), stellar and AGN feedback (Hopkins et al., 2006), shock heating (Dekel and Birnboim, 2006), cosmological starvation (Feldmann and Mayer, 2015), starvation by the circumgalactic medium having too high angular momentum to be accreted by the central galaxy (Peng and Renzini, 2020) (see also e.g., Man and Belli, 2018, and references therein). Some observations (Nelson et al., 2014; Gilli et al., 2014) have identified possible compact star-forming progenitors suggestive of dense stellar cores in their formation phase (see also Patel et al., 2013; Stefanon et al., 2013; Barro et al., 2013; Barro et al., 2014a; Barro et al., 2014b; Williams et al., 2015) or quenching progenitors suggestive of the transition stage to compact quiescent remnants (Marsan et al., 2015). Recent and upcoming efforts to secure samples of very distant quiescent galaxies and of their immediate progenitors, their observation with state-of-the art and new instruments to probe their stellar population, gas content, and structural and kinematical properties, and the detailed comparison with state-of-the-art simulations, will soon provide new constraints on the early formation of massive quiescent galaxies.

Acknowledgements

We thank the anonymous referee for a constructive report that improved the presentation of this work. PL and VS acknowledge support from the Deutsches Zentrum für Luft- und Raumfahrt Verbundforschung grant 50OR1805. VS and MP acknowledge support from the ERC-StG ClustersXCosmo grant agreement 716762. AC acknowledges support from grant PRIN MIUR 2017 - 20173ML3WW_001. S.J. acknowledges financial support from the Spanish Ministry of Science, Innovation and Universities (MICIU) under AYA2017-84061-P, co-financed by FEDER (European Regional Development Funds). This research is based on observations made with the NASA/ESA Hubble Space Telescope obtained from the Space Telescope Science Institute, which is operated by the Association of Universities for Research in Astronomy, Inc., under NASA contract NAS 5–26555. These observations are associated with program ID 15229. Partly based on data products from observations made with ESO Telescopes at the La Silla Paranal Observatory under ESO programme ID 179.A-2005 and on data products produced by TERAPIX and the Cambridge Astronomy Survey Unit on behalf of the UltraVISTA consortium. This study is partly based on a K_s-selected catalog of the COSMOS/UltraVISTA field from Muzzin et al. (2013a). The catalog contains PSF-matched photometry in 30 photometric bands covering the wavelength range 0.15 µm → 24 µm and includes the available *GALEX* (Martin et al., 2005), CFHT/Subaru (Capak et al., 2007), UltraVISTA (McCracken et al., 2012), S-COSMOS (Sanders et al., 2007), and zCOSMOS (Lilly et al., 2009) datasets.

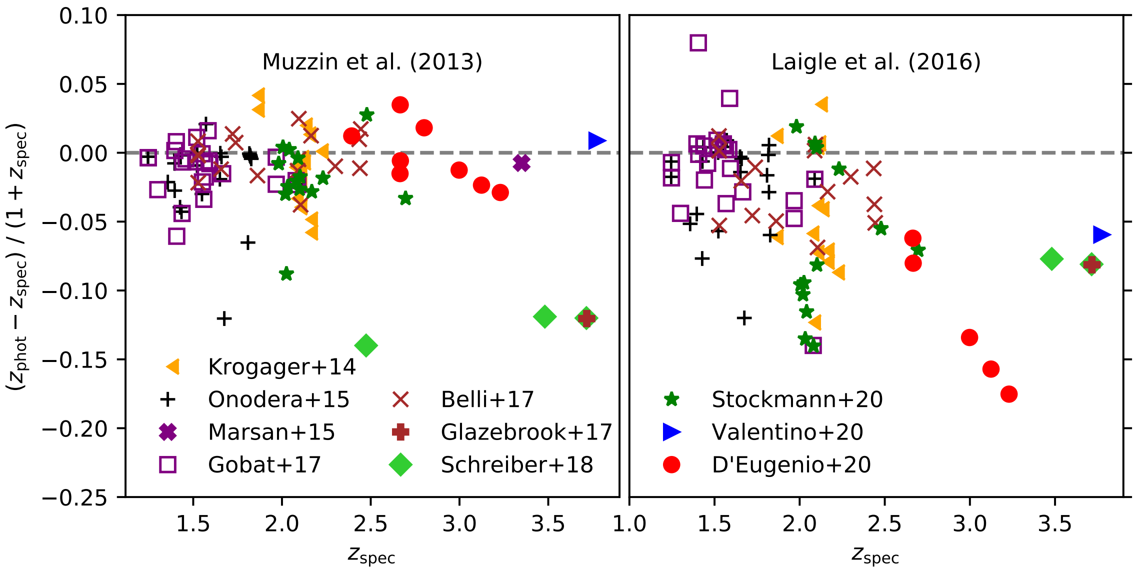

Figure 2.9: Comparison of spectroscopic redshifts of quiescent galaxies with photometric redshifts from Muzzin et al. (2013a, left panel) and Laigle et al. (2016, right panel). Sources from Schreiber et al. (2018) at $z \approx 2.5$ and (Marsan et al., 2015) at $z \approx 3.4$ have a photometric redshift estimates in Laigle et al. (2016) of 4.9 and $z = 0.3$, respectively and are not shown in the right panel. The sources from Glazebrook et al. (2017) and Schreiber et al. (2018) at $z = 3.7$ are the same.

Data Availability

The data of the HST program underlying this article are available in the HST archive[9]. References for additional data are given in the text.

2.6 Appendix

2.6.1 Comparison of spectroscopic and photometric redshifts

In section 2.2.3 we compare restframe UVJ colors of our sample with the full massive parent sample at $2.5 < z < 3.0$. To derive UVJ colors and stellar masses for the parent sample we make use of photometric redshifts. To investigate how reliable the photometric redshifts are we compare in Figure 2.9 spectroscopic redshifts of quiescent galaxies at $z_{spec} \gtrsim 1.2$ with photometric redshifts from Muzzin et al. (2013a) and Laigle et al. (2016). Redshifts from Krogager et al. (2014) and D'Eugenio et al. (2020) rely on HST grism data while redshifts from Onodera et al. (2015), Marsan et al. (2015), Gobat et al. (2017), Belli, Newman, and Ellis (2017), Glazebrook et al. (2017), Schreiber et al. (2018), Valentino et al. (2020) and Stockmann et al. (2020) rely on spectroscopic observations from ground-based telescopes. Photometric redshifts from Laigle et al. (2016) have a larger scatter and are systematically underestimated in this redshift range, especially at $z_{spec} \gtrsim 2.5$. We therefore use redshifts from Muzzin et al. (2013a) together with the deeper photometry from Laigle et al. (2016) for our analysis in Section 2.2.3.

[9] https://archive.stsci.edu/hst/

2.6.2 Significance of the central residuals

In Figure 2.10 we show the F160W images and residuals after subtracting the best fit Sérsic profiles (see Figure 2.4 and Section 2.3) together with a plot of the significance of the residuals that we define as the absolute value of the residuals divided by the noise in each pixel. Considering only pixels of the F160W images with a flux higher than 3 times the root mean square of the background we find that the fraction of pixels in the residual images with a significance higher than 3 is $\lesssim 2$ percent for all sources except for ID 8, where we find 4 percent.

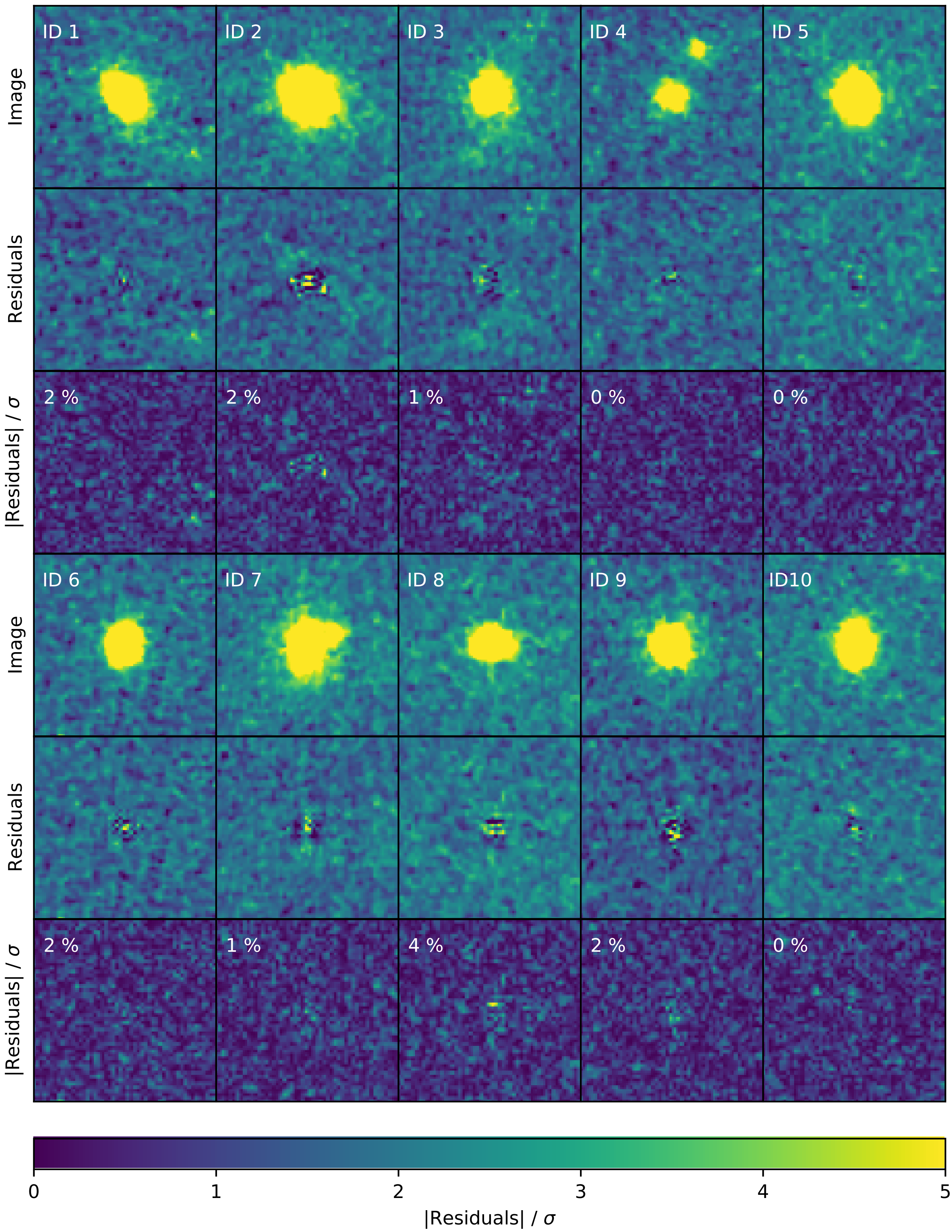

Figure 2.10: HST F160W images of the targets, residuals and their significance, defined as $|\text{residuals}|/\sigma$. For each source the fraction of pixels associated with the sources that have $|\text{residuals}|/\sigma > 3$ is indicated.

Chapter 3

Massive quiescent galaxies at $z \approx 3$: a comparison of selection, stellar population and structural properties with simulation predictions

Lustig, Peter; Strazzullo, Veronica; Remus, Rhea-Silvia; D'Eugenio, Chiara; Daddi, Emanuele; Burkert, Andreas; De Lucia, Gabriella; Delvecchio, Ivan; Dolag, Klaus; Fontanot, Fabio; Gobat, Raphael; Mohr, Joseph J.; Onodera, Masato; Pannella, Maurilio; Pillepich, Annalisa; Renzini, Alvio,
submitted to *Monthly Notices of the Royal Astronomical Society*

ABSTRACT

We study stellar population and structural properties of massive $\log(M_\star/M_\odot) > 11$ galaxies at $z \approx 2.7$ in the Magneticum (box 3) and IllustrisTNG (TNG100, TNG300) hydrodynamical simulations. We find stellar mass functions broadly consistent with observations, with no scarcity of massive, quiescent galaxies at $z \approx 2.7$, but with a higher quiescent galaxy fraction at high masses in IllustrisTNG. Average ages of simulated quiescent galaxies are between ≈ 0.8 and 1.0 Gyr, older by a factor ≈ 2 than observed in spectroscopically-confirmed quiescent galaxies at similar redshift. Besides being potentially indicative of issues with star-formation recipes in simulations, this discrepancy might also be partly explained by limitations in the estimation of observed ages. We investigate the purity of simulated UVJ rest-frame color-selected massive quiescent samples with photometric uncertainties typical of deep surveys (e.g., COSMOS). We find evidence for significant contamination (up to 60 percent) by dusty star-forming galaxies in the UVJ region that is typically populated by older quiescent sources. Furthermore, simulations suggest that the completeness of UVJ-selected quiescent samples at this redshift may be reduced by ≈ 30 percent due to a high fraction of young quiescent galaxies not entering the UVJ quiescent region. Massive, quiescent galaxies in simulations have on average lower angular momenta and higher projected axis ratios and concentrations than star-forming counterparts. Average sizes of simulated quiescent galaxies are relatively close to observed ones, and broadly consistent within the

uncertainties. The average size ratio of quiescent and star-forming galaxies in the probed mass range is formally consistent with observations, although this result is partly affected by poor statistics.

3.1 Introduction

In the local Universe spheroids contain about 75 percent of the total stellar mass (including ellipticals, E0s and bulges in spirals, Renzini, 2006). At the same time, about 10 times more quiescent than star-forming galaxies are found at $\log(M_\star/M_\odot) \gtrsim 11.5$ (e.g., Baldry et al., 2004). Indeed, there is a long-known strong correlation between morphology and stellar populations of nearby galaxies, where early-type, bulge-dominated systems have suppressed star-formation and generally host older stellar populations, whereas younger, actively star-forming galaxies typically have late-type, disk-like morphologies. Morphologically early-type galaxies have higher central concentrations and lower apparent ellipticity. It is established that they are more compact than star-forming galaxies up to stellar masses $\log(M_\star/M_\odot) \approx 11$ (e.g., Shen et al., 2003; Guo et al., 2009) and have lower specific angular momentum at fixed stellar mass (e.g., Fall, 1983; Romanowsky and Fall, 2012; Fall and Romanowsky, 2018).

Studies of massive galaxies at higher redshift have revealed a much lower quiescent fraction, reduced by up to a factor of ≈ 10 at $z \approx 3$ at the same stellar mass (e.g., Muzzin et al., 2013b; Martis et al., 2016; Davidzon et al., 2017). Morphological studies of massive quiescent galaxies at higher redshift have produced conflicting results. Some studies find quiescent galaxies with low Sérsic indices and smaller axis ratios than at lower redshift (van Dokkum et al., 2008; van der Wel et al., 2011; Bezanson et al., 2018; McGrath et al., 2008; Bundy et al., 2010; Chang et al., 2013; McLure et al., 2013; Hsu, Stockton, and Shih, 2014), suggesting that the strong correlation between morphology and SFR is not as pronounced in the early Universe. However, other studies (e.g., Bell et al., 2012; Mowla et al., 2019; Esdaile et al., 2020; Lang et al., 2014; Tacchella et al., 2015) find evidence that the correlation already exists at high redshift. The investigation of the relation between morphology and star formation properties is crucial to understanding quenching processes and is more generally a critical aspect of galaxy evolution.

The most famous morphological classification scheme for galaxies is the Hubble sequence (Hubble, 1926). Sandage, Freeman, and Stokes (1970) suggested that the Hubble sequence is at fixed mass a sequence of increasing angular momentum. The angular momentum of galaxies is obtained by primordial tidal torques (Peebles, 1969). Fall (1983) found that the specific angular momentum at fixed stellar mass of nearby spiral galaxies is larger than for ellipticals. This result was later confirmed by Romanowsky and Fall (2012), Obreschkow and Glazebrook (2014) and Cortese et al. (2016). The lower specific angular momentum of elliptical galaxies has been investigated from a theoretical perspective in a number of studies (e.g., Barnes and Efstathiou, 1987; Navarro and White, 1994; Heyl, Hernquist, and Spergel, 1996; Zavala, Okamoto, and Frenk, 2008; Lagos et al., 2018, 2017). By measuring stellar kinematics with integral field spectroscopy it has been shown that in the local Universe the vast majority of early type galaxies are fast rotators and slow rotators dominate only on the high-mass end ($M_\star \gtrsim 2 \times 10^{11}\, M_\odot$, Emsellem et al., 2011; Cappellari, 2016). Another contribution to the evolution of the specific angular momentum with time comes from cosmic expansion for which Obreschkow et al.

(2015) derive that for a spherical halo the specific angular momentum evolves with $(1+z)^{-1/2}$.

Concerning star formation properties, many studies over more than a decade have shown a close correlation between the SFR and the stellar mass of star-forming galaxies, the so-called star-forming main-sequence (MS) that exists up to at least $z \approx 4$ (e.g., Noeske et al., 2007; Daddi et al., 2007; Pannella et al., 2009a; Rodighiero et al., 2011; Wuyts et al., 2011; Schreiber et al., 2015; Renzini and Peng, 2015; Whitaker et al., 2012b; Tacconi, Genzel, and Sternberg, 2020). It has been argued that galaxies with a steady balance between gas infall and SFR lie on the MS with a slope of 1, however, observations find lower values between 0.4 and 1.0, which is assumed to be a result of quenching processes and smaller cold gas fractions at higher stellar mass (Pearson et al., 2018; Pan, Zheng, and Kong, 2017). The scatter of the MS is estimated to be approximately 0.3 dex, independent of mass and at least up to $z \approx 3$ (Whitaker et al., 2012b; Speagle et al., 2014; Tomczak et al., 2016; Pearson et al., 2018). This is believed to be a result of a cyclic process in which galaxies achieve a higher SFR as a consequence of compactification of the gas in their center that triggers star-formation. This is followed by depletion of the gas and reduced SFR until new infalling gas fuels the star-formation again. When the replenishment time becomes longer than the depletion time the galaxy becomes quiescent (Tacchella et al., 2016b; Pearson et al., 2018). The normalization of the MS increases at higher redshift (e.g., Schreiber et al., 2015; Speagle et al., 2014; Tomczak et al., 2016; Johnston et al., 2015) as expected due to the higher amount of cold gas available for star formation (Pearson et al., 2018; Tacconi et al., 2008a; Dunne et al., 2011; Genzel et al., 2015; Scoville et al., 2016).

While at low redshift a specific star formation rate (sSFR = SFR/$M_\star$) threshold of $\log(\mathrm{sSFR} \times \mathrm{yr}) = -11$ is often used to classify galaxies as star-forming or quiescent (e.g., Brinchmann et al., 2004; Fontanot et al., 2009), the evolving MS can be used at higher redshift to define a threshold for quiescence to account for the generally higher SFR at earlier cosmic times. However, since robust SFR estimates require unbiased SFR tracers rarely available over large, mass-limited samples, especially at high redshift the quiescent vs. star-forming classification of galaxies is often done by means of observed or restframe colors that are able to separate quiescent and star-forming galaxies accounting for the impact of dust attenuation (e.g., Daddi et al., 2004; Williams et al., 2009; Ilbert et al., 2013; Arnouts et al., 2013). At higher redshift increasing photometric uncertainties lead to larger uncertainties on the classification and to potentially strong contamination of quiescent samples by star-forming sources that may bias derived properties of quiescent galaxies. Additionally, quiescent samples at high redshift contain a larger fraction of relatively young sources that would be classified as post-starburst galaxies at lower redshift (e.g., D'Eugenio et al., 2020; Whitaker et al., 2012a; Marchesini et al., 2014; Merlin et al., 2018; Maltby et al., 2018; Lustig et al., 2021). As shown in some studies (e.g., Schreiber et al., 2018; Forrest et al., 2020b; Merlin et al., 2018) a potentially significant population of such young quiescent galaxies might be missed by using standard photometric classification criteria.

The comparison of galaxy properties in observations and simulations allows a more detailed investigation and improvement of our theoretical understanding of the evolution of galaxies, at the same time enhancing our capabilities of interpreting observations disentangling different aspects. Indeed, the discovery of massive quiescent galaxies in the early Universe has shown a tension with simulations that predicted too low quiescent fractions at the time (e.g., Glazebrook et al., 2017; Schreiber et al., 2018; Forrest et al., 2020a; Straatman et al., 2014; Merlin et al., 2019; Guarnieri et al., 2019; Alcalde Pampliega et al., 2019). It has been shown that this problem might at least partly be solved by better physical descriptions of AGN which can quench star formation and eject gas from the host galaxy. AGN feedback could increase the fraction of quiescent galaxies to approach agreement with observations and is potentially also an important contribution for morphological evolution (e.g., McCarthy et al., 2011; Dubois et al., 2016; Remus et al., 2017; Kaviraj et al., 2017; Weinberger et al., 2018). In addition, the number of resolution elements in hydrodynamical simulations has increased significantly in recent years, allowing simulations with larger volume and higher resolution to investigate spatially resolved properties of galaxies (e.g., Genel et al., 2014).

To reduce model ambiguities and provide conclusive evidence of the high redshift and quiescence of candidate quiescent galaxies, spectroscopic observations are necessary: current spectroscopic confirmations of quiescent galaxies reach out to $z \approx 4$ (Glazebrook et al., 2017; Esdaile et al., 2020; Newman, Belli, and Ellis, 2015; Newman et al., 2018; Glazebrook et al., 2004; Cimatti et al., 2004; Kriek et al., 2006; Gobat et al., 2012; Onodera et al., 2012, 2015; Marsan et al., 2015; Hill et al., 2016; Marsan et al., 2017; Gobat et al., 2017; Schreiber et al., 2018; Tanaka et al., 2019; Forrest et al., 2020a,b; Valentino et al., 2020). In D'Eugenio et al. (2020, 2021) and Lustig et al. (2021) we presented an analysis of stellar population and structural properties of one of the first sizeable samples of $z \approx 3$ spectroscopically confirmed quiescent galaxies, with the homogeneous investigation of 10 massive sources at $2.4 < z < 3.2$, extending previous work on spectroscopically confirmed samples (van Dokkum et al., 2008; Cimatti et al., 2008; Stockmann et al., 2020; Belli, Newman, and Ellis, 2017) to higher redshift.

In this paper we use Magneticum and IllustrisTNG (hereafter TNG) cosmological simulations to compare observational findings on morphology and stellar population properties of massive quiescent galaxies at $z \approx 3$ with current models of galaxy evolution. We also take advantage of the simulation framework to investigate the performance, limitations and biases of the routinely adopted photometric selection of quiescent galaxies at this redshift. In Section 3.2 we introduce the simulations used in this paper, and present the investigated simulated galaxy samples and main observational studies used here for comparison. In Section 3.3 we present stellar mass functions (SMFs) at $z \approx 3$ as predicted in the simulations in the context of observational determination and in Section 3.4 we discuss stellar ages of galaxies. In Section 3.5 we discuss photometric selection of quiescent galaxies at high redshift and in Section 3.6 we present a morphological analysis of simulated galaxies. We summarize our findings and conclusions Section 3.7. Despite some small differences the cosmology adopted in all the different parts contributing to this analysis is a flat ΛCDM cosmology with $\Omega_{\mathrm{M}} \approx 0.3$ and $h \approx 0.7$ (see more specific details in Section 3.2.3 and Table 3.1). We assume a Chabrier (2003) IMF. Magnitudes are given in the AB system.

3.2 High-redshift quiescent galaxies in simulations and observations

In this work we use the IllustrisTNG and Magneticum suites of hydrodynamical simulations. We focus on simulations with a large enough volume to host a decent amount of quiescent galaxies at $z \approx 2.7$ and a high enough resolution for a morphological analysis. In the following we briefly introduce the simulations. Their most important parameters are listed in Table 3.1 and we refer to the relevant publications listed below for a more throughout description.

3.2.1 Simulation data

IllustrisTNG

IllustrisTNG[1] (Springel et al., 2018; Nelson et al., 2018; Marinacci et al., 2018; Pillepich et al., 2018a; Naiman et al., 2018) is a set of hydrodynamical cosmological simulations with different physical sizes and mass resolutions. In this work we use the public data release (Nelson et al., 2019) of the simulations TNG100 and TNG300, with box sizes of 100 and 300 Mpc, at the highest available resolution. Baryonic particle masses in TNG300 and TNG100 are $1.1 \times 10^7\,M_\odot$ and $1.4 \times 10^6\,M_\odot$, respectively. A Planck Collaboration et al. (2016) cosmology is used in both simulations with $\mathrm{h} = 0.677, \Omega_\Lambda = 0.691, \Omega_\mathrm{M} = 0.309$ and $\Omega_\mathrm{B} = 0.049$. The comoving softening length for stellar particles is 2.0 kpc/h in TNG300 and 1.0 kpc in TNG100. Details of the galaxy formation models can be found in Weinberger et al. (2017) and Pillepich et al. (2018b).

Magneticum Pathfinder

The Magneticum Pathfinder[2] simulations are a suite of fully hydrodynamical cosmological simulations, covering different box volumes and resolutions (see Hirschmann et al., 2014; Teklu et al., 2015). Here, we use the Magneticum Pathfinder simulation box 3 (hereafter M3) with the highest available resolution (Steinborn et al., 2016). The simulated box has a comoving side length of 128 Mpc/h containing initially 2×1536^3 particles (dark matter and gas) with a resolution of $m_\mathrm{DM} = 3.6 \times 10^7\,M_\odot$ and $m_\mathrm{gas} = 7.3 \times 10^6\,M_\odot$ with each gas particle spawning up to 4 stellar particles, resulting in an average particle mass of $\approx 1.8 \times 10^6\,M_\odot$. The comoving softening length for stellar particles is $\epsilon_\mathrm{star} = 0.7\,\mathrm{kpc/h}$. A WMAP7 ΛCDM cosmology (Komatsu et al., 2011) is used for the simulation with $\sigma_8 = 0.809, \mathrm{h} = 0.704, \Omega_\Lambda = 0.728, \Omega_\mathrm{M} = 0.272$ and $\Omega_\mathrm{B} = 0.045$. M3 provides a refined black hole accretion and AGN feedback model with respect to the implementation from Springel (2005) that results in a better agreement with the observed black hole mass - stellar mass relation due to faster black hole growth at higher redshifts. The stronger feedback is able to suppress star formation in galaxies earlier, leading to more quenched galaxies at higher redshift in agreement with observations. For further details we refer to Steinborn et al. (2015).

[1] www.tng-project.org
[2] www.magneticum.org

3.2.2 Observational studies used for comparison

In this work, simulation results are compared to a range of observational properties of distant quiescent galaxies drawn from several studies. We focus in particular on the number density of quiescent galaxies and quiescent fractions at $z \approx 3$ as estimated in deep fields from Ilbert et al. (2013), Muzzin et al. (2013b), Martis et al. (2016), Davidzon et al. (2017) and Sherman et al. (2020), and on structural and stellar population properties both from statistical photometric samples from deep-field photometric studies (van der Wel et al., 2014; Laigle et al., 2016) and more specifically from our dedicated follow-up of a spectroscopically confirmed sample of massive (median stellar mass $\log(M_\star/M_\odot) \approx 11.2$) quiescent galaxies at $z \approx 3$ (D'Eugenio et al., 2020, 2021; Lustig et al., 2021).

Indeed, this work is partly intended as a simulation analysis counterpart to our previous observational studies of this sample, which is one of the first sizeable samples of spectroscopically confirmed quiescent galaxies at this redshift (see discussion in the introduction). Therefore, we use results from D'Eugenio et al. (2020, 2021) and Lustig et al. (2021) as a preferential observational counterpart in the following, specifically commenting on relevant results from other studies as needed. We summarise here the main aspects of these observations.

The sample was targeted with the Wide Field Camera 3 on the Hubble Space Telescope with the F160W filter (H band) and the G141 grism. Targets were selected as $z > 2.5$ quiescent galaxy candidates based on photometric classification, excluding potential star-forming contaminants and focusing on the brightest sources with $H \lesssim 22$ for observational reasons (for full details on sample selection see D'Eugenio et al., 2021; Lustig et al., 2021). D'Eugenio et al. (2020, 2021) measured spectroscopic redshifts from grism data between $z = 2.4$ and $z = 3.2$ (median $z = 2.7$) and confirmed quiescence for all targets. They found young stellar ages between 300 and 800 Myr, consistent with an average formation redshift of $z \approx 3.5$. In Lustig et al. (2021) we analysed the morphology of galaxies in this sample and found high Sérsic indices and axis ratios (medians ≈ 4.5 and 0.73, respectively), pointing towards a largely bulge dominated population among quiescent galaxies already at $z \approx 3$. For further details we refer to the aforementioned papers.

3.2.3 Sample selection of simulated galaxies

We use the available simulation snapshots closest to the median redshift of our main observed comparison sample (D'Eugenio et al., 2020, 2021; Lustig et al., 2021), which is $z = 2.73$ in both TNG simulations and $z = 2.79$ in M3. Halo structures in all simulations are identified with SUBFIND (Springel et al., 2001; Dolag et al., 2009). To compare with the massive galaxies in our observed sample (median stellar mass $\log(M_\star/M_\odot) \approx 11.2$) we focus on the most massive galaxies with $\log(M_\star/M_\odot) \geq 11.0$ and initially select all galaxies above this mass threshold considering all gravitationally bound particles according to SUBFIND. This yields a parent sample of 196 galaxies in M3, 1077 in TNG300 and 78 in TNG100.

The comparison between stellar masses from observations and simulations is not trivial. Statistical and systematic uncertainties on stellar masses from SED fitting are estimated to be a factor of ≈ 2 (e.g., Maraston et al., 2006; Longhetti and Saracco, 2009; Muzzin et al., 2009; Conroy, 2013; Pacifici et al., 2015). On the simulation side, stellar masses assigned to simulated galaxies rely anyway on assumptions (and are thus not necessarily directly comparable to the observational estimates). Furthermore, from a more practical point of view, because of the limited SNR in observations, the inclusion of all bound stellar particles is not comparable to what occurs in the analysis of observed galaxies Pillepich et al. (see also e.g., 2018a), Genel et al. (2018), and Donnari et al. (2019, 2021). For a more realistic comparison we define different subsamples that only include bound particles within a certain distance from the center of the host galaxy. Because of the complex behaviour of the SNR of observed galaxies and of the corrections applied to estimate the total galaxy light, it is not trivial to find an aperture that matches those used in observations. We therefore use a range of 2-dimensional apertures (by projecting the galaxies along random lines of sight) to estimate the systematic uncertainties implied by the aperture choice and the impact on our analysis. We carry out the analyses in the following for four different aperture choices: 30 kpc apertures (corresponding to ≈ 3.7 arcsec at $z = 2.7$) around both the center of mass and center of light (in the observed H-band, see Section 3.2.4 for the calculation of the adopted synthetic luminosities for simulated galaxies), and apertures equal to 2 times the half-mass and half-light radii. The average offset between the mass and light-weighted center is less than 0.2 kpc in the considered simulations, the choice between the two has no impact on our results. The half-light and half-mass radii are in the order of $1 - 4$ kpc for the kind of galaxies studied here (see Section 3.6). The large range of sizes covered by these apertures brackets typical sizes of apertures in observations (see also e.g., Donnari et al., 2019, 2021). We therefore obtain 4 different subsamples of massive galaxies by applying again the mass cut of $\log(M_\star/M_\odot) \geq 11$ to the same simulated parent galaxy sample by accounting for particles within the 4 different apertures considered.

To calculate the centers (of mass and light) of simulated galaxies for defining apertures, we project the particle positions along random lines of sight and iteratively calculate the average position of particles weighted by either their stellar mass or H-band luminosity, excluding particles at > 2 kpc from the center[3] until convergence. Identifying as the galaxy center the position of the local (mass or light) density maximum within 10 kpc of the above-defined center - possibly a better definition for a minor fraction of asymmetric galaxies - results in an average shift of the assumed center of the aperture by 0.16 kpc, and has no impact on the results presented here.

3.2.4 Estimation of luminosities for simulated galaxies

For some analyses we use restframe U, V, J and observed H band luminosities. To calculate luminosities for simulated galaxies we assign to each stellar particle a SED corresponding to its age using Bruzual and Charlot (2003) stellar population synthesis models with a Chabrier (2003) IMF, linearly interpolating the models to match the metallicity of the given particle. We then calculate global SED's as the sum of the individual particle SED's within the considered apertures.

We adopt an empirical approach to model the impact of dust on the global galaxy SED's. For quiescent galaxies we adopt results from D'Eugenio et al. (2021) for our sample of 10 quiescent galaxies at $2.4 < z < 3.2$, finding $0.1 < A_{\rm V} < 1.6$ with a median $A_{\rm V} = 0.5$ (other spectroscopic studies at similar redshift find $A_{\rm V}$ in good agreement, e.g., Esdaile et al., 2020; Schreiber et al., 2018; Valentino et al.,

[3]Visual inspection confirms that a threshold of 2 kpc gives the best estimate of the halo centers for most of the subhalos.

2020). For each simulated quiescent galaxy we randomly choose an $A_{\rm V}$ from this distribution and consequently apply dust reddening to its SED assuming a Calzetti (2001) attenuation law modified by a power law with slope (Noll et al., 2009; Salim, Boquien, and Lee, 2018) $\delta = -0.4$. Since all galaxies in the D'Eugenio et al. (2021) sample are relatively young with $t_{50} < 0.8\,{\rm Gyr}$ (where t_{50} is the lookback time when half of the stellar mass of the galaxy was formed, see Section 3.4) and a median $t_{50} = 0.45^{+0.05}_{-0.10}\,{\rm Gyr}$, adopting the attenuation values estimated by D'Eugenio et al. (2021) might overestimate the attenuation for older quiescent galaxies. To gauge the impact of this effect on our results, we also calculate luminosities by applying dust attenuation with D'Eugenio et al. (2021) $A_{\rm V}$ only to quiescent galaxies with $t_{50} < 0.8\,{\rm Gyr}$, while for older sources, due to the lack of measurements at this redshift, we adopt a Calzetti (2001) dust attenuation law with an $A_{\rm V}$ typical of quiescent galaxies with stellar ages $1-2\,{\rm Gyr}$ - as appropriate for old populations at $z \approx 3$ - from lower redshift work (González Delgado et al., 2015). We therefore assume for simulated quiescent galaxies with $t_{50} > 0.8\,{\rm Gyr}$ a randomly selected $A_{\rm V}$ from a Gaussian distribution with mean 0.25 mag and standard deviation 0.15 mag. As this estimate is based on low-redshift quiescent sources (likely affected by, if anything, less dust attenuation than $z \sim 3$ counterparts of similar mass and age) we assume that our two empirical approaches should bracket the actual dust attenuation affecting $z \sim 3$ quiescent galaxies in the probed mass range. In the following we quote as a default results assuming this prescription for dust attenuation of quiescent galaxies, and discuss as needed the dependence of the results on this choice.

For star-forming galaxies we use a Calzetti (2001) dust attenuation law with stellar mass dependent $A_{\rm V}$ from McLure et al. (2018) and Pannella et al. (2015), giving $A_{\rm V} = 1.8 - 1.6\,{\rm mag}$ for a $\log(M_\star/M_\odot) = 11$ galaxy, with a scatter of $0.4 - 0.2\,{\rm mag}$, respectively. Given the similarity of the attenuation estimated from the work of McLure et al. (2018) and Pannella et al. (2015), for the sake of simplicity results presented in the following for star-forming galaxies are quoted only assuming $A_{\rm V}$ from Pannella et al. (2015). Using $A_{\rm V}$ from McLure et al. (2018) does not affect our results unless otherwise noted.

For some purposes of our analysis we need to mimic photometric uncertainties. We quantify these based on the uncertainties (as a function of magnitude) on the photometry of galaxies at $2.5 < z < 3$ in the COSMOS2015 (Laigle et al., 2016) catalog, whose data have been used for several observational work on high-redshift quiescent galaxies and in particular for studies we directly compare with in the following.

3.2.5 Selection of quiescent galaxies in simulations

Galaxies are often classified - and especially so at high redshift - as star-forming or quiescent based on their position in rest-frame or observed color diagrams (e.g., Daddi et al., 2004; Williams et al., 2009; Ilbert et al., 2013; Arnouts et al., 2013). In simulations, different sSFR criteria are used to separate quiescent and star-forming galaxies throughout the literature. If a MS of star-forming galaxies (e.g., Noeske et al., 2007) can be identified in the simulated sample, galaxies with a SFR significantly lower than the MS can be defined as quiescent (e.g., Genel et al., 2018; Donnari et al., 2019, 2021). Alternatively, an absolute sSFR threshold, typically depending on redshift (e.g., Franx et al., 2008) can be defined to separate star-forming and quiescent sources. In this section we compare the impact of such different criteria on the selection of high-redshift massive quiescent galaxies in the TNG and Magneticum simulations investigated here.

We estimate the MS following Donnari et al. (2019); briefly, we bin galaxies in 0.2 dex stellar mass bins and iteratively calculate the median SFR in each bin, excluding galaxies with a SFR more than 1 dex below the median until convergence. The uncertainty on the derived MS is estimated by bootstrapping over 1000 samples.

In Figure 3.1 we show the estimated MS of star-forming galaxies at $z \approx 2.7$ for the three simulations used in this paper and for different apertures (see Section 3.2.3). In this figure we include for clarity lower mass galaxies down to $\log(M_\star/M_\odot) = 10.6$. Differences between the estimates adopting different apertures are consistent within the uncertainties, as shown in the figure. The MS in M3 rises linearly from $\log(\mathrm{SFR}/M_\odot\,\mathrm{yr}^{-1}) \approx 1.4$ at $\log(M_\star/M_\odot) \approx 10.6$ to $\log(\mathrm{SFR}/M_\odot\,\mathrm{yr}^{-1}) \approx 2.1$ at $\log(M_\star/M_\odot) \approx 11.5$. At low masses the main sequence in TNG300 is about 0.2 dex higher than in M3; it rises with a similar slope as in M3 but bends at $\log(M_\star/M_\odot) \approx 11.1$ (≈ 11.3 for the two smallest apertures) reaching down to $\log(\mathrm{SFR}/M_\odot\,\mathrm{yr}^{-1}) \approx 1.3$ at $\log(M_\star/M_\odot) = 11.5$. This is because a large fraction of massive galaxies in TNG300 is already quenched and no sequence of star-forming galaxies can be clearly identified. The MS in TNG100 is flat over the full mass range considered here with a value of $\log(\mathrm{SFR}/M_\odot\,\mathrm{yr}^{-1}) \approx 1.6$.

MS determinations from observations at similar redshift (e.g., Schreiber et al., 2015; Sargent et al., 2014, see brown and red lines in the upper panels in Figure 3.1) have slopes in overall good agreement with our measurements in M3 and TNG300 at lower masses. However, observed MSs show higher SFRs by ≈ 0.6 dex with respect to both M3 and TNG300 simulations.

An often used SFR threshold for defining quiescence is 1 dex below the main sequence (see e.g., Sherman et al., 2020; Donnari et al., 2019; Morselli et al., 2019) which we show for measurements in an aperture of 30 kpc in Figure 3.1 together with the Franx et al. (2008) criterion $\mathrm{sSFR} < 0.3 \times H(t)$ (see also Lotz et al., 2021, in particular on a study in Magneticum), that is $\log(\mathrm{sSFR} \times \mathrm{yr}) \approx -10.0$ at $z = 2.75$. As the figure shows, in M3 the MS-based quiescence threshold is 0.3 dex lower than the Franx et al. (2008) sSFR threshold over the full mass range. For TNG300 both criteria are consistent for galaxies with $\log(M_\star/M_\odot) \lesssim 11.1$; in TNG100 the two criteria imply the same SFR threshold at $\log(M_\star/M_\odot) \approx 10.7$ but deviate at higher masses.

The broadly similar threshold defined by both criteria in M3 and in TNG300 at masses where the main sequence can be robustly estimated suggests that the Franx et al. (2008) criterion is appropriate to classify star-forming and quiescent galaxies in the simulated samples considered here. The discrepancy between the two criteria in TNG100 can be explained by a combination of small sample size and an also high fraction of quenched galaxies at high masses in this simulations. In the following we therefore denote galaxies as quiescent if they fulfil the Franx et al. (2008) criterion.

Leja, Tacchella, and Conroy (2019) investigate the correlation between the location of galaxies at $0.5 < z < 2.5$ in a UVJ restframe color plane and their sSFR and calibrate the separation in the UVJ plane for different thresholds of sSFR. According to this calibration, the often used UVJ criterion from Williams et al. (2009) roughly corresponds to a sSFR threshold of $-9.5 < \log(\mathrm{sSFR} \times \mathrm{yr}) < -10.0$, similar at face value to the sSFR threshold adopted here.

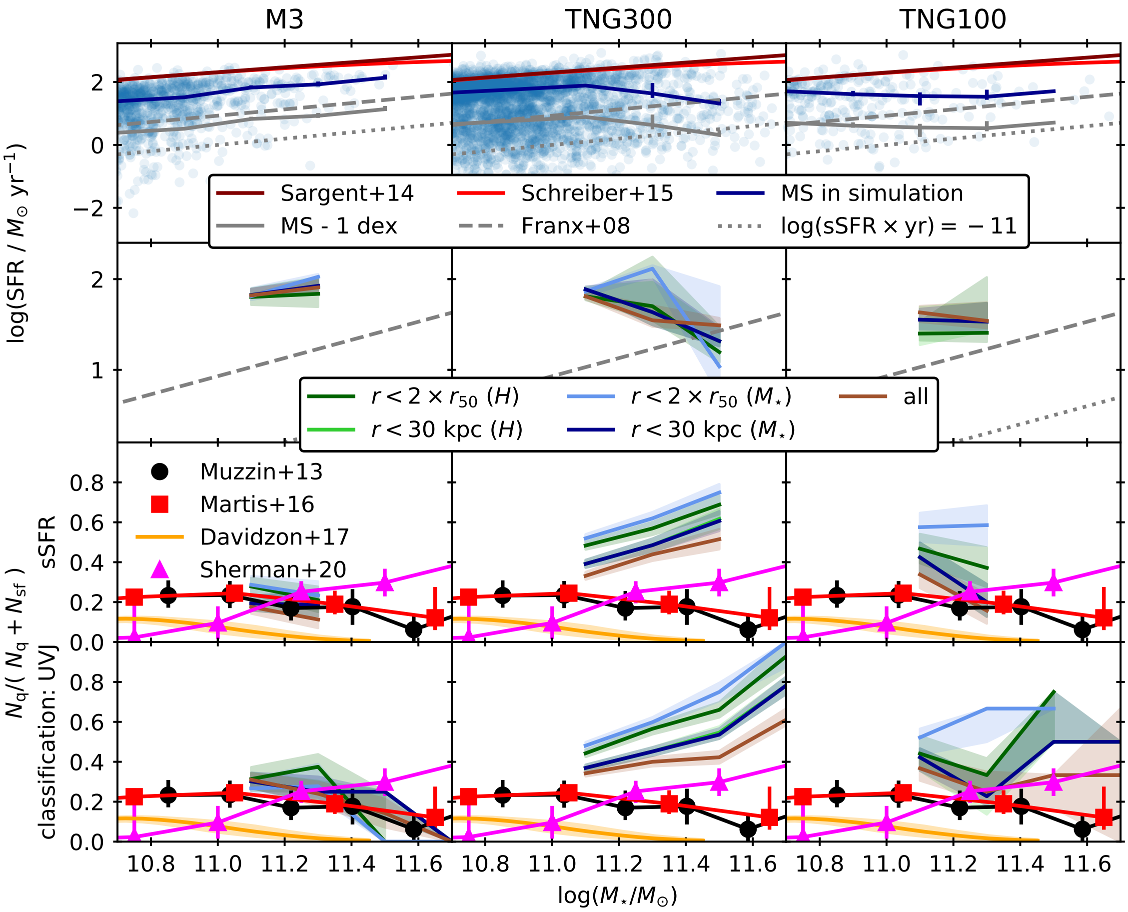

Figure 3.1: The main sequence and quiescent galaxy fraction at $z \approx 2.7$ in the studied simulations. *First row*: the MS of star-forming galaxies (blue solid line) as determined in the M3 (left), TNG300 (middle) and TNG100 (right) simulations at $\log(M_\star/M_\odot) > 10.6$ (stellar masses and SFRs measured in 30 kpc apertures, see Section 3.2.3). Blue circles show individual galaxies. The gray solid line shows the MS offset to lower SFR by 1 dex. The dashed gray line shows the Franx et al. (2008) criterion for quiescence. Dotted gray line shows a $\log(\mathrm{sSFR} \times \mathrm{yr}) = -11$. Observational determinations of the MS at the same redshift are shown, as indicated. *Second row:* the dependence of the estimated MS at high masses on the aperture used to compute galaxy stellar mass and SFR, as indicated (see Section 3.2.3). Dashed and dotted lines are the same as in top panels. *Third row:* the estimated quiescent fraction in the simulations as a function of stellar mass, and its dependence on the adopted aperture as indicated. Quiescent fractions shown here are defined based on the Franx et al. (2008) criterion for quiescence. Observational estimates of the quiescent fraction at the same redshift are shown, as indicated (see Section 3.2.6 for full details). *Fourth row:* Same as third row, but quiescent fractions in the simulations are estimated from UVJ color diagrams (see Section 3.5).

3.2.6 Quiescent fractions in simulations

In Figure 3.1 we show quiescent fractions at $\log(M_\star/M_\odot) > 11$, as estimated from the Franx et al. (2008) criterion as discussed above, as a function of stellar mass for different apertures, and compare with observational results at $2.5 < z < 3.0$ from Ilbert et al. (2013), Muzzin et al. (2013b), Martis et al. (2016), Davidzon et al. (2017) and Sherman et al. (2020). Uncertainties are obtained by calculating the binomial confidence intervals following Cameron (2011). The quiescent fraction for all $\log(M_\star/M_\odot) > 11$ galaxies in M3 is 19 ± 3 percent with no significant dependence on the adopted aperture (among the choices discussed in Section 3.2.3). Quiescent fractions for the same mass range in TNG are higher with 44 ± 2 percent in TNG300 and 34 ± 5 percent in TNG100, and more sensitive to the chosen aperture with larger apertures leading to smaller quiescent fractions. In TNG300 the difference between estimates with the smallest ($2 \times r_{50}$) vs. the largest (including all particles) apertures is constant at ≈ 20 percentage points over the full mass range, indicating that star formation is stronger in the galaxy outskirts (see also Merlin et al., 2019; Donnari et al., 2019). TNG300 quiescent fractions strongly increase with mass also in the $\log(M_\star/M_\odot) > 11$ mass range investigated here, reaching values of $50 - 70$ percent at $\log(M_\star/M_\odot) \approx 11.5$. In TNG100 quiescent fractions decrease with increasing stellar stellar mass except for the smallest aperture ($2 \times r_{50}^{\rm mass}$).

Observed quiescent fractions from Ilbert et al. (2013), Muzzin et al. (2013b), Martis et al. (2016) and Sherman et al. (2020) are in good agreement with those estimated for M3 and lower than in both TNG simulations. The quiescent fraction estimated in Davidzon et al. (2017) is significantly lower than other observations[4]. Based on SED fitting on optical (DES) and NIR (NEWFIRM, VISTA, CFHT, IRAC) data, Sherman et al. (2020) estimate quiescent fractions with three different criteria to select quiescent galaxies: UVJ color classification, $\log(\mathrm{sSFR} \times \mathrm{yr}) < -11$ and SFR > 1 dex below the MS. They find consistent results with all criteria, which also agree with quiescent fractions from Muzzin et al. (2013b), Tomczak et al. (2016) and Martis et al. (2016) and in M3 (see Figure 3.1). However, in contrast to their result, applying a quiescence threshold of $\log(\mathrm{sSFR} \times \mathrm{yr}) = -11$ in the simulations (corresponding to ≈ 2 dex below the MS) results in quiescent fractions of $5 - 15$ percent (depending on the adopted aperture) in M3, and $2 - 45$ percent (strongly depending on aperture) in both TNG boxes (see Figure 3.8).

In the following for the sake of brevity and readability we will present by default only results obtained with 30 kpc apertures around the center of mass, and explicitly comment as needed on results that depend on this choice.

[4]Davidzon et al. (2017) explain such lower quiescent fractions as likely due to their use of the NUV$-r-J$ classification method (Ilbert et al., 2013) rather than UVJ, resulting in different sSFR thresholds. To investigate this we consider the COSMOS2015 (Laigle et al., 2016) catalog on which Davidzon et al. (2017) study is based. While Davidzon et al. (2017) re-estimate photometric redshifts and stellar masses, we take the original masses and NUV-$r - J$ classification from Laigle et al. (2016) to compute quiescent fractions. These fractions are in good agreement with those from Muzzin et al. (2013b), Martis et al. (2016) and Sherman et al. (2020), so we conclude that the lower quiescent fractions in Davidzon et al. (2017) might in fact also depend on the different redshift and stellar mass estimates.

Table 3.1: Properties of the simulations used for this work.

	Magneticum 3	TNG300	TNG100
$m_\mathrm{b}\,[10^6\,M_\odot]$	7.3	11.0	1.4
$m_\mathrm{DM}\,[10^6\,M_\odot]$	36.0	59.0	7.5
$\epsilon_\star$ [comoving kpc/h]	0.7	2.0	1.0
Box size [comoving Mpc]	182	303	111
Cosmology			
Ω_M	0.272	0.309	
Ω_Λ	0.728	0.691	
Ω_B	0.046	0.049	
h	0.704	0.677	
σ_8	0.809	0.816	
The sample			
z_snap	2.79	2.73	
$\epsilon_{\star,z_\mathrm{snap}}$ [physical kpc]	0.26	0.8	0.4
Number of $\log(M_\star/M_\odot) > 11$ galaxies (30 kpc aperture)			
All	166	993	73
Star-forming	136	549	47
Quiescent	30	444	26

3.3 Stellar mass functions and number densities

In the upper panel of Figure 3.2 we compare observed SMFs at $2.5 < z < 3.0$ from Ilbert et al. (2013), Muzzin et al. (2013b) and Davidzon et al. (2017) for all, quiescent and star-forming galaxies with those that we obtain for the simulations at $z \approx 2.73$. Uncertainties are obtained by bootstrapping. At $\log(M_\star/M_\odot) > 11$ the total SMFs of all simulations are in reasonably good agreement. The SMF of quiescent galaxies at $\log(M_\star/M_\odot) > 11$ is significantly lower in M3 than in both TNG boxes (reflecting the high quiescent fraction in TNG already discussed in Section 3.2.6). At lower masses instead, the SMF of quiescent galaxies in both TNG boxes declines while it continues to increase towards lower masses in M3 where a large fraction of galaxies at low masses is quenched. The best agreement between all simulations is seen in the SMFs of star-forming galaxies at $\log(M_\star/M_\odot) > 11$ where the lower fraction of star-forming galaxies in TNG is compensated by the slightly larger total SMF.

At $\log(M_\star/M_\odot) \gtrsim 11$ the observed SMFs for all and star-forming galaxies from Ilbert et al. (2013) and Muzzin et al. (2013b) are in perfect agreement with TNG100 and also reasonably close to TNG300 and M3 results. The total SMF from Davidzon et al. (2017) is a bit lower than in TNG100, Ilbert et al. (2013) and Muzzin et al. (2013b) but still in very good agreement with M3 at $\log(M_\star/M_\odot) > 11$. The star-forming SMF from Davidzon et al. (2017) matches perfectly TNG300 and M3 (because of their very high fraction of star forming galaxies compensating the lower total SMF). The strongest differences in Figure 3.2 can be seen for the SMFs for quiescent galaxies, where results from Ilbert et al. (2013) and Muzzin et al. (2013b) lie between (and broadly consistent with) those from the TNG boxes and M3, while the SMF from Davidzon et al. (2017) is much lower than in all simulations (reflecting their low quiescent fraction, as discussed in Section 3.2.6).

For quiescent galaxies with $\log(M_\star/M_\odot) \geq 11$ we find number densities of $\eta = 5.0 \pm 0.9,\ 16.0 \pm 0.8$ and $19.2 \pm 3.81 \times 10^{-6}\mathrm{Mpc}^{-3}$ for M3, TNG300 and

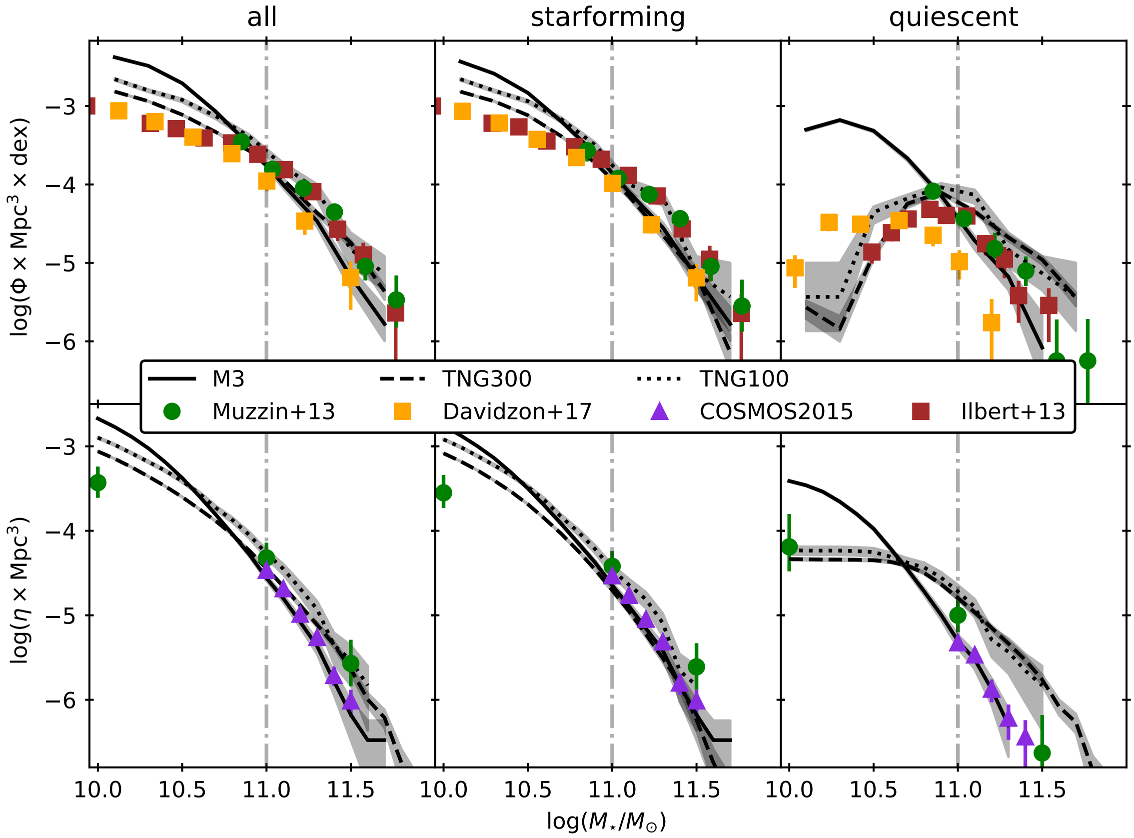

Figure 3.2: Stellar mass functions and cumulative number densities at $z \approx 2.7$ in the studied simulations. *Top panels*: The SMF of all (left), star-forming (middle) and quiescent (right) galaxies from M3, TNG300 and TNG100. Observational estimates are shown for comparison, as indicated. *Bottom panels:* The corresponding cumulative number densities of all, star-forming and quiescent galaxies compared with observational estimates as indicated. In all panels the grey shaded areas show poisson uncertainties. Total SMFs and number densities in the simulations are in overall good agreement with observations. Higher SMFs and number densities for quiescent galaxies in TNG simulations with respect to M3 and observations reflect the higher quiescent fraction in TNG. See Section 3.3 for full details.

TNG100, respectively. In the bottom panels of Figure 3.2 we show cumulative number densities from all simulations and compare these results again with observational estimates from Muzzin et al. (2013b). The agreement between the number densities reflects the agreement for the SMFs shown in the upper panels. Because Davidzon et al. (2017) do not estimate cumulative number densities we estimate them from the original COSMOS2015 redshifts and NUV-r^+ vs. $r^+ - J$ from Laigle et al. (2016), finding perfect agreement with M3 for all number densities (all, quiescent and star-forming galaxies), and relatively good agreement also with TNG with the significant exception of the quiescent galaxy number density.

3.4 Stellar ages

The age of the Universe at $z \approx 3$ is only ≈ 2 Gyr, but short star formation timescales at high redshift allow the existence of quiescent galaxies older than 1 Gyr. However, spectroscopic studies confirming the most distant quiescent galaxies, at $3 < z < 4$, find with very few exceptions only young galaxies (partly because of observational reasons, see below) with ages significantly below 1 Gyr (Schreiber et al., 2018; Forrest et al., 2020a,b; Valentino et al., 2020; Saracco et al., 2020). For our observed sample at $2.4 < z < 3.2$, ages are also young with a median t_{50}, the lookback time when 50 percent of the stellar mass of the galaxies was formed, of $0.45^{+0.05}_{-0.10}$ Gyr (D'Eugenio et al., 2021).

To compare observed stellar ages of quiescent galaxies with those of galaxies in the simulations we also calculate t_{50} for the simulated galaxies as the lookback time when half of the stellar mass of the galaxy was formed not accounting for mass losses, i.e. we consider the initial masses of the stellar particles. As previously discussed we consider all particles within an aperture of 30 kpc at the snapshot redshift. Ages estimated in smaller apertures are slightly older but average ages are consistent within the uncertainties, and the aperture choice does not impact the results of the discussion. Histograms of t_{50} for quiescent and star-forming galaxies together with the results for our observed quiescent sample are shown in Figure 3.3. The average ages for quiescent galaxies in M3, TNG300 and TNG100 are $1.03^{+0.11}_{-0.15}$, $0.78^{+0.01}_{-0.01}$ and $0.91^{+0.02}_{-0.10}$ Gyr and for star-forming galaxies $0.71^{+0.03}_{-0.01}$, $0.67^{+0.01}_{-0.01}$ and $0.64^{+0.04}_{-0.02}$ Gyr. The median age of our observed sample $t_{50} = 0.45^{+0.05}_{-0.10}$ Gyr is significantly younger than those of the simulated galaxies.

There may be several reasons for such age discrepancy on both the simulation and observation sides. We note first of all that age determinations from spectroscopic samples are expected to be biased towards younger ages, because the oldest galaxies are extremely difficult to observe even at very high masses with current instruments. Indeed, based on photometric observations older quiescent galaxies may actually exist (e.g., Straatman et al., 2014; Carnall et al., 2020; Kalita et al., 2021), but while they may be elusive even in photometric studies, obtaining spectra to robustly confirm their nature and measure their ages is currently too expensive or unfeasible. Indeed, in Lustig et al. (2021) and D'Eugenio et al. (2020) we have analysed our selection criteria for the observed sample and found a mild bias towards younger ages due to the applied H band cut. However, applying the same $H < 22$ mag cut to galaxies in the simulated sample has a negligible effect (see dashed lines in Figure 3.3), and thus we conclude that the expected age bias of spectroscopic samples cannot be a main explanation for the age discrepancy between observed and simulated quiescent galaxies. Star formation histories in the simulations might be intrinsically different from those of real galaxies, resulting in too old ages with respect to observations. Furthermore, our specific analysis of the simulation might affect this result: we investigate the impact of our sSFR criterion to select the quiescent sample on the age distribution of quiescent galaxies. The scatter of the MS is approximately 0.3 dex, independent of stellar mass at least up to $z \approx 3$ (e.g., Whitaker et al., 2012b; Speagle et al., 2014; Tomczak et al., 2016; Pearson et al., 2018). The Franx et al. (2008) criterion discussed above thus identifies as quiescent only galaxies much below the MS ($\gtrsim 3$ times the intrinsic scatter). This might limit our simulated quiescent samples to older ages. We therefore investigate this by reselecting quiescent galaxies including all sources with a SFR already significantly below the MS but that have not yet reached formal quiescence according to the Franx et al. (2008) criterion by relaxing the SFR threshold for quiescence to 2σ (0.6 dex) below the MS. More specifically, following the discussion in Section 3.2.3, in particular with respect to the uncertainties in defining the MS at high masses and the location of the Franx et al. (2008) threshold $\approx 10\times$ below the MS, for the purpose of this check we define as quiescent those galaxies having a sSFR of at most 2.5× higher than the Franx et al. (2008) threshold. As expected the average age of the selected quiescent population becomes younger with this relaxed cut, however, the change is marginal in both TNG boxes and about 20 percent in M3, not strong enough to explain the discrepancy with the observed results. For a significant effect on the average age a much larger fraction of young star-forming galaxies would have to be classified as quiescent. In fact, Figure 3.3 shows that the bulk of the star-forming population is anyway older than the average t_{50} estimated in the observational sample by D'Eugenio et al. (2021).

To investigate this discrepancy further we show in Figure 3.4 the average SFH of quiescent and star-forming galaxies in the three simulations, that we obtain by averaging the fraction of formed mass in an interval of look-back time $t_{\rm LB}$ for all galaxies. It can be seen that most of the star formation in the quiescent population happens at $t_{\rm LB} > 0.5$ Gyr, reflecting the relatively old ages. To estimate the t_{50} of the observed galaxies from spectro-photometric modeling, D'Eugenio et al. (2021) marginalize over a set of constant, truncated constant, exponentially declining and delayed exponentially declining SFHs. The average onset of star formation estimated in D'Eugenio et al. (2021) occurs much later than in the simulations (only ≈ 0.6 Gyr before observation epoch, see Figure 3.4). To more specifically compare SFHs of quiescent galaxies we also show in Figure 3.4 the average SFH of simulated quiescent galaxies in different age bins. Generally, in all three simulations the maximum of star formation in quiescent galaxies is reached at larger lookback times than in star-forming galaxies. In the TNG simulations about 8 percent of the galaxies have $t_{50} \leq 0.5$ Gyr, 80 percent have $0.5 < t_{50} \leq 1.0$ Gyr, the remaining galaxies are older. On average their star-formation rate peaks ≈ 0.3, 0.7 and 1.1 Gyr before observation epoch, respectively. Except for galaxies in the oldest age bin, 50 percent of the total stellar mass of the galaxies is already formed before the peak of star formation. Quiescent galaxies in M3 are on average older (see Figure 3.3), with all quiescent galaxies being older than 0.5 Gyr and about 60 percent older than 1 Gyr. In this respect, we note that the t_{50} estimated from spectro-photometric fitting, being estimated from galaxy light, is anyway preferentially biased towards younger stellar populations, and especially so for complex SFHs with a significant fraction of stellar mass formed at early times but with a significant recent burst, which are often not properly accounted for by the adopted SFH libraries. As a limiting case we therefore also show in Figure 3.3 observed H band light-weighted ages (≈ 4300 Å restframe). Although we stress that ages estimated as t_{50} from spectro-photometric modeling (e.g., D'Eugenio et al., 2021) formally aim at estimating mass-weighted ages, we consider here light-weighted ages as a limiting case where the impact of the recent SFH on the age estimate is strongest. The resulting ages are younger with a median of ≈ 0.6 Gyr for quiescent and 0.3 Gyr for star-forming galaxies in all simulations. Therefore, although at face value there is a discrepancy in the ages of quiescent galaxies in observed samples and in simulations, a quantitative estimate of the actual significance of this discrepancy is limited by potential observational biases (in sample selection as well as in the estimation of stellar ages) as well as in possible inconsistencies in the analysis of the simulated galaxies with respect to the observed ones (including star formation histories and dust attenuation prescriptions).

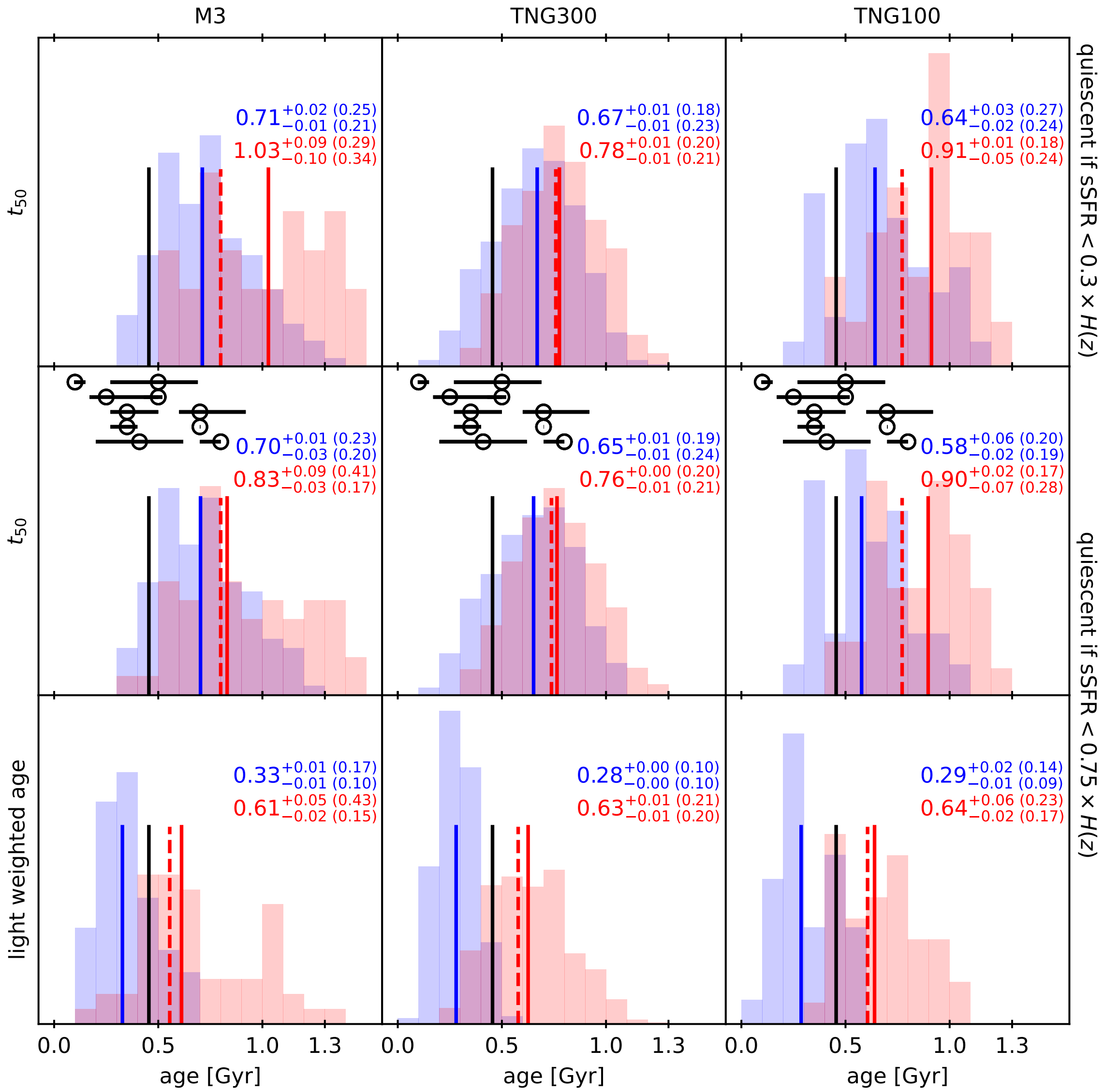

Figure 3.3: Histograms of stellar ages of quiescent (red) and star-forming (blue) galaxies in the studied simulations, as indicated. Median ages (shown by solid vertical lines) are given in each panel, together with their uncertainty and with the RMS of the age distribution. Dashed vertical lines show the median age of quiescent galaxies with $H < 22$ (see Section 3.4). Black lines and circles show the median age and individual galaxy stellar ages for the observed sample of quiescent galaxies at $z \approx 2.7$ from D'Eugenio et al. (2021). Top and middle panels show ages defined as t_{50}, and classify galaxies as star-forming vs. quiescent based on the Franx et al. (2008) and on the relaxed sSFR threshold criteria, respectively. Bottom panels show observed H-band light-weighted ages, and galaxies are classified according to the relaxed sSFR threshold. Full details in Section 3.4.

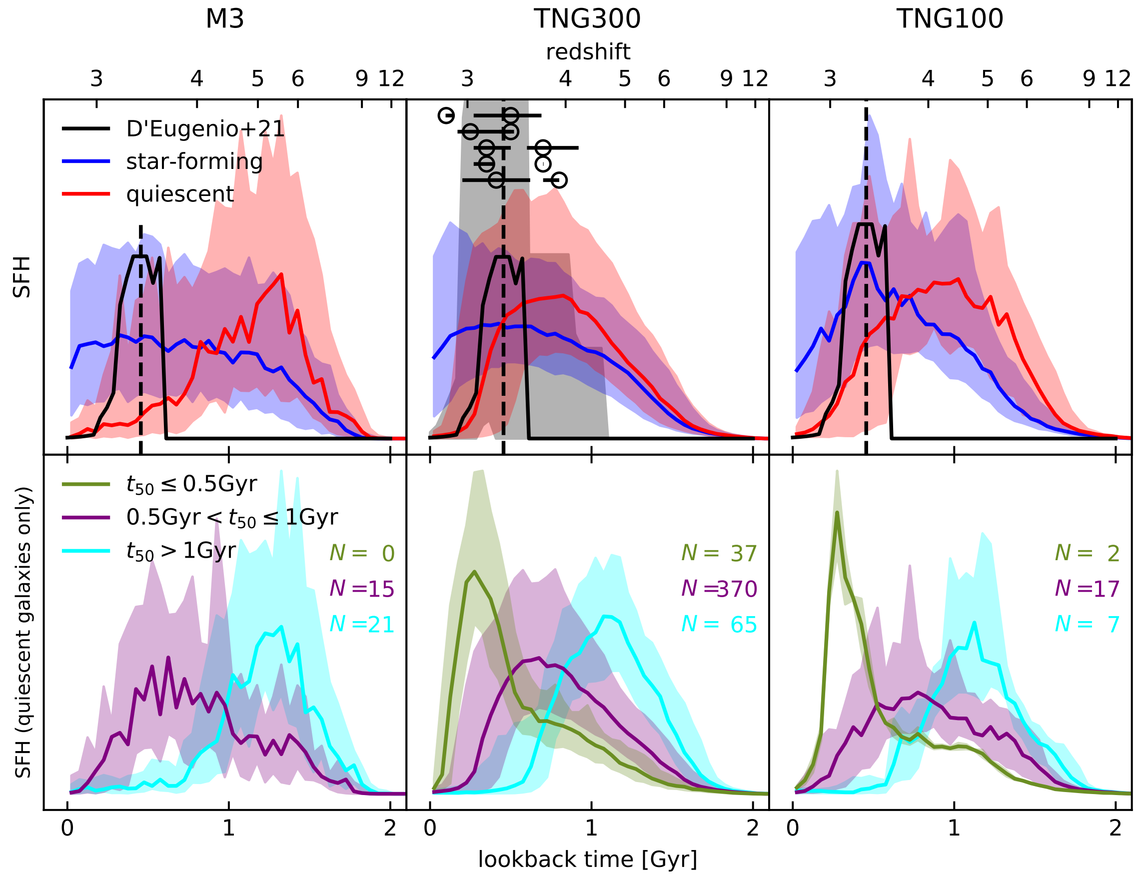

Figure 3.4: SFHs as fraction of formed mass per lookback-time interval in the studied simulations (as indicated), as a function of look-back time, for galaxies selected at $z \approx 2.7$. Top panels: average SFH of all quiescent (red) and star-forming (blue) galaxies. The black solid line shows the average SFH of 10 observed quiescent galaxies from spectro-photometric modeling from D'Eugenio et al. (2021), and the black dashed line their median age (t_{50}). In the top-middle panel the black circles show individual ages for the same sample. Bottom panels: average SFH of quiescent galaxies with $t_{50} \leq 0.5\,$Gyr (green), $0.5 < t_{50} \leq 0.5\,$Gyr (violet) and $t_{50} > 0.5\,$Gyr (cyan). In each panel, the number of galaxies in each age bin is reported in the corresponding color. Shaded areas around SFHs (including black line in top-middle panel) show the RMS of the corresponding distribution.

3.5 UVJ selection of high-redshift quiescent galaxies

In Lustig et al. (2021) we analysed the UVJ restframe color plot of massive ($\log(M_\star/M_\odot) > 11.1$) galaxies at $2.5 < z < 3.0$ from the Muzzin et al. (2013a) and COSMOS2015 (Laigle et al., 2016) catalogs. The combination of photometric uncertainties across the UVJ diagram and the distribution of 24 µm-detected sources suggested a potentially significant contamination of UVJ-quiescent samples by dusty star-forming sources. According to our analysis potential contaminants amount to ≈ 20 percent of the $\log(M_\star/M_\odot) > 11.1$ UVJ quiescent galaxy sample at this redshift, preferentially affecting the UVJ region typically populated by older quiescent galaxies (for full details see Lustig et al., 2021). In this section we investigate the purity and completeness of a UVJ selected quiescent galaxy sample as identified in the simulations mimicking the selection criteria and photometric uncertainties as in the observed case. We note already here that in the attempt to reproduce the observed selection we need to rely on assumptions concerning dust attenuation of star-forming and quiescent populations (see Section 3.2.4), and we will neglect the impact of AGN on the galaxy SED's. We also note that by construction the following results apply for photometric uncertainties typical of the COSMOS2015 catalog.

We calculate 1000 realisations of UVJ restframe colors for all simulated galaxies, in each step we randomly assign dust attenuation to the galaxies according to their classification based on the Franx et al. (2008) sSFR criterion as explained in Section 3.2.4 accounting for the scatter in A_V for both star-forming and quiescent populations, and perturb the photometry to match the photometric uncertainties of the COSMOS2015 catalog (see Section 3.2.4). We then divide the UVJ plane into bins of $V - J$ and $U - V$ and calculate for each bin and realization the fraction of quiescent galaxies according to the Franx et al. (2008) criterion. The average quiescent fraction as a function of the location in the UVJ diagram and a random single realisation of the diagram are shown in Figure 3.5. If considering the impact of the different dust attenuation prescriptions considered in Section 3.2.4 we find absolute differences for purity, completeness and overall UVJ quiescent fractions of at most 5, 4, and 3 percentage points, respectively.

In the lower panel in Figure 3.1 we show quiescent fractions in the simulations according to pure UVJ classification with the considered photometric uncertainties. For an aperture of 30 kpc (see Section 3.2.3) the overall UVJ quiescent fraction of $\log(M_\star/M_\odot) > 11$ galaxies in M3 is ≈ 30 percent (about 10 percentage points higher than according to the sSFR classification) and 40 percent in the TNG simulations (consistent with sSFR classification). Quiescent fractions in TNG simulations strongly depend on the considered aperture and are between ≈ 35 percent (considering all bound particles) and ≈ 55 percent (considering particles within $2 \times r_{50}$, see Section 3.2.3). Quiescent fractions for different apertures in M3 differ by at most 4 percentage points.

However, there are significant differences between the sSFR- and UVJ-selected quiescent samples, that reflect in the completeness and purity of the UVJ-selected sample by comparison to the sSFR-based quiescence definition. The quiescent part of the UVJ diagram shows strong contamination from star-forming galaxies at $V - J \gtrsim 1$ in all simulations. In M3 the overall purity with respect to the Franx et al. (2008) sSFR criterion of a UVJ selected quiescent galaxy sample with $\log(M_\star/M_\odot) > 11$ is only ≈ 41 percent and the completeness (with respect to the full sSFR-selected quiescent sample) is $\approx$ 67 percent (see further discussion below). As expected due to the intrinsic higher quiescent fraction (see Section 3.2.6), the contamination in the TNG simulations is lower with a purity of the overall UVJ-quiescent sample of $\approx$ 80 percent in TNG300 and 70 percent in TNG100. The completeness is $\approx$ 75 percent in both TNG boxes. We stress again that this only reflects the higher intrinsic quiescent fraction in TNG with respect to M3. Differences in the purity between the simulations at fixed quiescent fraction are an estimate of the systematic uncertainty originating from different age distributions. At a quiescent fraction of 19 percent the difference in purity between the sample with the highest (TNG300) and lowest purity (M3) is $\approx$ 10 percentage points.

Following our discussion in Section 3.4 we also repeat the calculation applying the relaxed sSFR cut (SFR 4 times below the MS) for the classification of quiescent galaxies. The corresponding UVJ color plots are shown in Figure 3.8. While the UVJ-derived quiescent fraction does not significantly change (within 4 percentage points with no systematic shifts), the purity of the UVJ quiescent sample increases by $10-16$ percentage points, reaching 57 percent in M3 and $82-90$ percent in TNG, because of an overall increase of the quiescent population due to young quenched sources with sSFR between 4 and 10 times below the MS now being classified as quiescent (this result is stable against the adopted dust attenuation prescription from Section 3.2.4). This might suggest that a non-negligible fraction of the observed UVJ-quiescent population (within the typically adopted UVJ-quiescent region, e.g., Williams et al., 2009) is made of intrinsically very young sources spread throughout the UVJ quiescent region by dust attenuation.

From our analysis of the UVJ diagram of $\log(M_\star/M_\odot) > 11.1$ galaxies at $2.5 < z < 3$ in Lustig et al. (2021), considering photometric uncertainties and 24 µm detections, we estimated the purity of a UVJ selected quiescent sample to be in the order of 80 percent with an increasing contamination towards the region typically populated by older quiescent galaxies, the latter in qualitative agreement with our findings from simulations.

As discussed above, our modelling of the UVJ diagram for simulated galaxies with both considered sSFR thresholds would suggest a higher purity of the UVJ-quiescent sample for TNG, in better agreement with purity estimates derived from observations, with respect to M3. This higher purity results from the substantially higher intrinsic quiescent fraction in TNG with respect to M3 (see Figure 3.1). In this respect we note that in TNG simulations the "observationally estimated" UVJ-derived quiescent fractions at $\log(M_\star/M_\odot) > 11$ are $\approx$ 40 percent and differ by at most 3 percentage points from intrinsic (sSFR-based) quiescent fractions, while in M3 UVJ-derived quiescent fractions are $\approx$ 30 percent ($\approx$ 10 percentage points higher than intrinsic quiescent fractions, see bottom panels of Figure 3.1).

Independent of the exact sSFR classification criterion and for all dust attenuation parametrizations that we considered (see Section 3.2.4), the UVJ classification criterion in its standard form adopted at lower redshifts (e.g., Williams et al., 2009) might not be ideal for a high completeness and purity sample of massive high redshift galaxies (with the photometric uncertainties considered here, see also e.g., Merlin et al., 2018). Investigating a sample of spectroscopically confirmed quiescent galaxies at $3 < z < 4$, Schreiber et al. (2018) find that an increasing fraction of massive quiescent galaxies at high redshift with a SFR reduced by at least 90 percent with respect to their main formation phase has not yet entered the quiescent part of the standard UVJ selection. For more complete samples of massive quiescent galaxies at high redshift they suggest to adjust the selection criteria by removing the $U - V > 1.3$ constraint that is used to avoid contamination with star-forming galaxies but is less relevant for massive samples where photometric uncertainties are smaller and star-forming sources are typically more dusty. Also Forrest et al. (2020b) find that a standard UVJ diagram does not provide a pure or complete selection of quiescent galaxies for massive samples at high redshift. Figure 3.5 shows the UVJ diagram for all three simulations according to the model described above. Our findings support the suggestion of removing the $U - V > 1.3$ constraint. Furthermore, with the photometric depth of the COSMOS2015 catalog our modeling (and we stress again the caveats deriving from making assumptions on dust attenuation, neglecting AGN contribution, and relying on SFHs from the considered simulations) suggests that strong contamination from dusty star-forming sources in the UVJ quiescent region at $V - J \gtrsim 1$ may reduce significantly the purity of such a selected sample, potentially biasing derived properties for this population. If in our analysis we remove the $U - V > 1.3$ constraint and we only consider the quiescent population at $V - J < 1$, the purity of the selected samples increase from $\lesssim 50$ to $80 - 90$ percent while completeness remains at the ≈ 90 percent level.

3.6 Morphologies

In Lustig et al. (2021) we have analysed the morphologies of our observed quiescent sample by fitting Sérsic (1963, 1968) profiles to the Wide Field Camera 3 H-band images of our targets. We found compact structures with a median radius of $r_{\mathrm{e}} = 1.4^{+0.9}_{-0.2}$ kpc, consistent with previous work suggesting size evolution by nearly an order of magnitude for massive quiescent galaxies across the redshift range $0 < z < 3$. We found high Sérsic indices with an average of $n = 4.5^{+0.3}_{-1.4}$, indicating that massive quiescent galaxies are typically already bulge dominated at $z \approx 3$. In this Section we investigate from the simulations whether structural properties are correlated with quiescence, and thus morphological differences exist between star-forming and quiescent galaxy populations at $z \approx 2.7$.

Because of the different inherent properties and statistical and systematic uncertainties of the probe of galaxy structure in observations and simulations, we cannot analyse the morphologies of simulated galaxies as we do with actual observations. Indeed the strongest constraints on the profiles of observed galaxies come from the inner part of the surface brightness profile with the highest SNR, while the outskirts are progressively more and more dominated by noise. In simulations the gravitational softening length modifies particle-particle interactions at small scales to avoid too close encounters of particles. This smooths out the distribution of particles in the central part of simulated galaxies where the density is very high and, from a modeling perspective, is not analogous to the smoothing by the PSF occurring in actual images. When analysing galaxies much larger than the softening length the central part can be excluded to fit Sérsic profiles (e.g., Remus and Forbes, 2021). However, at higher redshift, where galaxies are at fixed mass much smaller than in the local Universe, this kind of fit may be very sensitive to the size of the masked part. Following a range of tests to explore the impact of this effect, we therefore decided to use non-parametric descriptions of the morphologies that we describe in the following. We stress here that results discussed in the following are thus, by construction, not based on the direct, quantitative comparison of similarly estimated properties on observed and simulated galaxies. We rather attempt to investigate

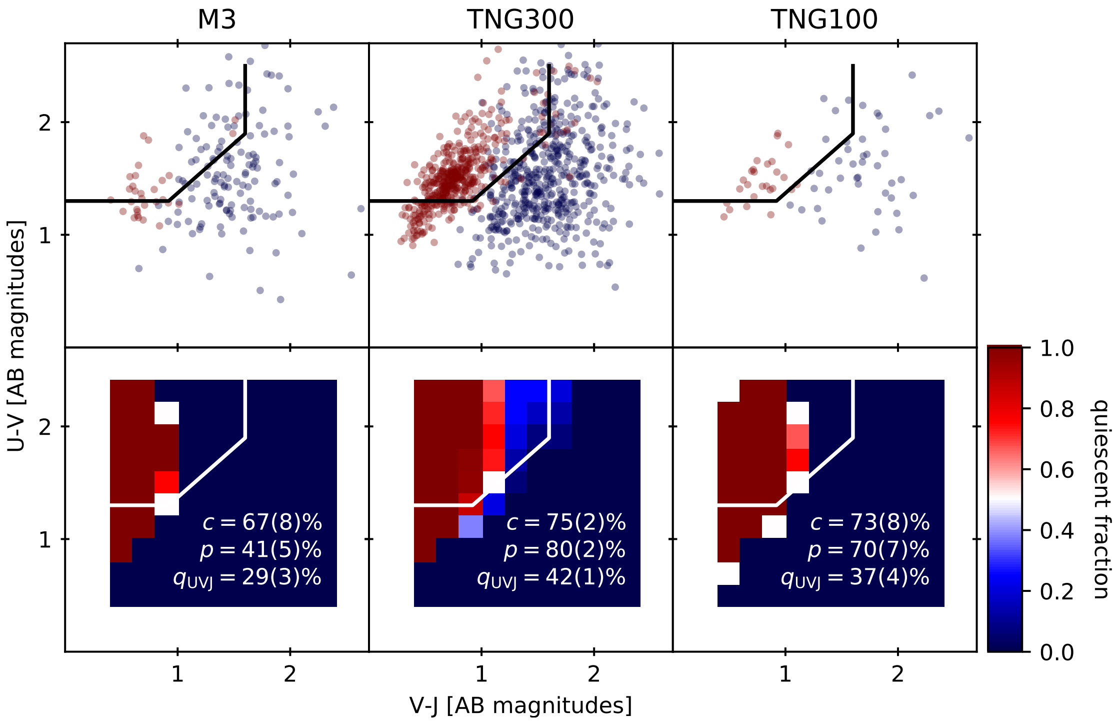

Figure 3.5: The restframe $U-V$ vs. $V-J$ color diagram for simulated galaxies at $z \approx 2.7$, adopting prescriptions for dust attenuation and photometric uncertainties corresponding to the COSMOS2015 (Laigle et al., 2016) catalog. See Section 3.2.4 for full details. Top panels: a random realization of the diagram for the studied simulations, as indicated including scatter in dust attenuation and photometric uncertainties as detailed in Section 3.2.4. Quiescent and star-forming galaxies according to the Franx et al. (2008) criterion are shown with red and blue dots, respectively. Bottom panels: the average fraction of quiescent galaxies (according to the Franx et al. (2008) criterion) over 1000 realizations, as a function of the position across the diagram, as indicated by the color bar. In each of the bottom panels, the corresponding estimated completeness (c) and purity (p) of the UVJ-selected quiescent sample are given, together with the UVJ-derived quiescent fraction q_{UVJ} (error bars give the RMS across the different realizations).

with a range of probes whether we can find structural differences between star-forming and quiescent populations in the simulated samples at this redshift.

Axis ratios

In a first step we iteratively calculate axis ratios for the projected galaxies following the equations in Bertin and Arnouts (1996) modified for our purpose where the positions and emitted light of individual particles are known. Briefly, in each step we calculate the second moments of the projected particle positions, weighted by their simulated observed H band emission:

$$\overline{x_j x_k} = \frac{\sum_i m_i x_{i,j} x_{i,k}}{\sum_i m_i} - \left(\frac{\sum_i m_i x_{i,j}}{\sum_i m_i}\right)\left(\frac{\sum_i m_i x_{i,k}}{\sum_i m_i}\right), \tag{3.1}$$

where $x_{i,j}$ is the j-th component of the position of particle i and m_i the weight. The semimajor (A_+) and semiminor axes (A_-) can then be calculated as:

$$A_\pm{}^2 = \frac{\overline{x_1^2} + \overline{x_2^2}}{2} \pm \sqrt{\left(\frac{\overline{x_1^2} - \overline{x_2^2}}{2}\right)^2 + \overline{x_1 x_2}^2}. \tag{3.2}$$

The position angle θ is given by the following equation:

$$\tan 2\theta = 2\frac{\overline{xy}}{\overline{x^2} - \overline{y^2}}. \tag{3.3}$$

We then define for a particle i its distance r_i^{e} from the center of the galaxy accounting for the ellipticity as:

$$r_i^{\mathrm{e}} = \left|\begin{pmatrix} 1 & 0 \\ 0 & q^{-1} \end{pmatrix} R(-\theta)(\mathbf{x}_i - \mathbf{x}_{\mathrm{c}})\right| \tag{3.4}$$

where $q = A_-/A_+$ is the axis ratio of the galaxy, $\mathbf{x}_{\mathrm{c}}$ its center, $\mathbf{x}_i$ the position of particle i and the matrix $R(-\theta)$ rotates the positions by $-\theta$.

Given the typical depth of images we used for the modeling of observed galaxies, the surface brightness profiles of the observed targets is equal to the background RMS at distance of on average 6 kpc from the center. For this reason, to more closely probe the axis ratios estimated for the observed galaxies, we exclude all particles with $r_i^{\mathrm{e}} > 6$ kpc and repeat the calculation of the axis ratio and the rotation angle until convergence (considering only particles with $r_i^{\mathrm{e}} < 3$ kpc rather than 6 kpc increases the axis ratios only marginally by 0.02 on average).

Sizes and Concentration

The effective radius of a Sérsic profile contains 50 percent of the total light of the galaxy. To compare with the measured sizes for our observed quiescent sample and with results from van der Wel et al. (2014) on a larger statistical galaxy sample though with limited statistics for massive quiescent galaxies at this redshift, we measure from the simulated data half-light radii of the semimajor axis within an elliptical 30 kpc aperture for the simulated galaxies using the definition of the radius accounting for ellipticities from equation 3.4. As a measure of the concentration we use the definition:

$$C = 5 \times \log(r_{\mathrm{o}}/r_{\mathrm{i}}) \tag{3.5}$$

from Kent (1985). In most works the outer (r_o) and inner (r_i) radii are defined as r_{80} and r_{20} (containing 80 and 20 percent of the total light, respectively). Since for about half of the galaxies in the TNG300 simulation at $z = 2.73$ the estimated r_{20} are smaller than the softening length these radii may be biased by the softening and we therefore use instead as inner radius the half-light radius, which is larger than the softening length for more than 95 percent of the relevant sample. We include in the further analysis also the 5 percent galaxies with a half-light radius smaller than the softening length, removing them has no significant impact on estimated average properties. Both radii are measured along the semi-major axis. All galaxy sizes defined above clearly depend on the aperture chosen as representative of the total galaxy flux (or mass). If measuring r_{50} (r_{80}) within an aperture of 2 times the half-light radius rather than in 30 kpc apertures as discussed above, sizes of individual galaxies would be on average smaller by 35 percent (60 percent). The concentration of individual galaxies would decrease by ≈ 1 on average, however, the significance of the difference of average concentrations between star-forming and quiescent galaxies is not affected.

For a closer comparison between observations and simulations, we compute concentrations corresponding to the r_{80}/r_{50} ratio also for our observed quiescent sample, based on Sérsic profiles from Lustig et al. (2021). If only the central 30 kpc of the Sérsic profiles are considered rather than the full profile, concentrations are lower by < 0.01 for 6 galaxies out of 10. For 4 galaxies with Sérsic index $\gtrsim 5$ the concentration decreases by $0.24 - 0.86$.

Specific angular momentum and b-value

We calculate the 2-dimensional specific angular momentum within elliptical apertures for all galaxies as:

$$j = \left| \frac{\sum_i m_i \, \mathbf{x}_i \times \mathbf{v}_i}{\sum_i m_i} \right| \tag{3.6}$$

where m_i is the emitted light of particle i in the observed H band, $\mathbf{x}_i$ its projected position with respect to the center of light and $\mathbf{v}_i$ its velocity with respect to the global light-weighted velocity of the galaxy. Specific angular momenta estimated within $2 \times r_{50}$ instead of 30 kpc are on average 45 percent smaller. However, the significance of the average angular momentum difference between star-forming and quiescent galaxy populations is not impacted by the choice of the aperture.

In addition we calculate for all galaxies the b-value, defined as the logarithmic specific angular momentum at a pivot stellar mass of $1\,M_\odot$, assuming $j \propto M_\star^{2/3}$ (Teklu et al., 2015):

$$b = \log(j \times \mathrm{s}\,/\,\mathrm{km}\,/\,\mathrm{kpc}) - 2/3 \times \log(M_\star/M_\odot). \tag{3.7}$$

3.6.1 Structural properties in relation to quiescence

The morphological parameters discussed above are shown as a function of stellar mass in Figure 3.6. The average morphological parameters for $\log(M_\star/M_\odot) > 11$ quiescent and star-forming galaxies are listed in Table 3.2. In Figure 3.7 we show b-values as a function of sSFR. Uncertainties on the average properties and on the difference between both populations are obtained with bootstrapping. The median mass of quiescent and star-forming galaxies in the considered simulations differs by at most 0.06 dex and does not impact the comparison. Due to the small sample size

Table 3.2: Average half-light radii (r_{50}), specific stellar angular momentum (j), concentration (C_{58}) and axis ratio (q) for the $\log(M_\star/M_\odot) > 11$ samples of quiescent (Q) and star-forming (SF) galaxies and their ratio.

		M3	TNG300	TNG100
	Q	$3.2^{+0.2}_{-0.4}$	$1.8^{+0.1}_{-0.1}$	$1.6^{+0.2}_{-0.5}$
r_{50}	SF	$1.9^{+0.2}_{-0.2}$	$2.20^{+0.07}_{-0.04}$	$2.2^{+0.2}_{-0.4}$
[kpc]	ratio	$1.7^{+0.2}_{-0.3}$	$0.81^{+0.04}_{-0.03}$	$0.7^{+0.2}_{-0.2}$
	Q	172^{+64}_{-35}	227^{+18}_{-20}	272^{+84}_{-50}
j	SF	219^{+11}_{-23}	411^{+32}_{-15}	405^{+49}_{-26}
[km kpc / s]	ratio	$0.8^{+0.3}_{-0.2}$	$0.5^{+0.1}_{-0.1}$	$0.7^{+0.3}_{-0.1}$
	Q	$2.6^{+0.2}_{-0.1}$	$2.40^{+0.05}_{-0.04}$	$2.8^{+0.1}_{-0.1}$
C_{58}	SF	$2.4^{+0.1}_{-0.1}$	$1.94^{+0.02}_{-0.04}$	$2.1^{+0.1}_{-0.1}$
	difference	$0.3^{+0.2}_{-0.2}$	$0.47^{+0.05}_{-0.05}$	$0.7^{+0.2}_{-0.2}$
	Q	$0.76^{+0.04}_{-0.03}$	$0.66^{+0.01}_{-0.01}$	$0.73^{+0.07}_{-0.05}$
q	SF	$0.72^{+0.02}_{-0.04}$	$0.57^{+0.01}_{-0.01}$	$0.58^{+0.03}_{-0.05}$
	ratio	$1.1^{+0.1}_{-0.1}$	$1.15^{+0.03}_{-0.03}$	$1.3^{+0.2}_{-0.1}$

in the TNG100 simulations the uncertainties on the average parameters are very large. Because of the consistency with TNG300 results we only comment the latter and M3 in the following.

Radii

In all simulations half-light radii of star-forming and quiescent galaxies are very similar, with a difference of the average size of at most 0.2 dex. The median size of $\log(M_\star/M_\odot) > 11$ quiescent and star-forming galaxies in TNG300 is $1.79^{+0.05}_{-0.07}$ kpc and $2.20^{+0.06}_{-0.04}$ kpc, respectively, with no significant dependence on stellar mass. Quiescent galaxies in M3 have sizes of $3.16^{+0.23}_{-0.39}$, larger than those of star-forming galaxies with $1.87^{+0.18}_{-0.18}$ kpc, though average sizes of star-forming and quiescent galaxies are consistent when estimated in 2 times the half-light radius apertures. The increase of average sizes of star-forming galaxies with stellar mass visible in M3 in Figure 3.6 is actually only seen for 30 kpc aperture based sizes. If classifying galaxies based on UVJ restframe colors (see Section 3.5) average sizes of $\log(M_\star/M_\odot) > 11$ quiescent and star-forming galaxy populations change by at most 0.05 dex.

van der Wel et al. (2014) study morphologies of star-forming and quiescent galaxies at $0 < z < 3$ based on data from the 3D-HST (Brammer et al., 2012) and CANDELS (Grogin et al., 2011; Koekemoer et al., 2011) survey. In their analysis, massive ($11.0 < \log(M_\star/M_\odot) < 11.5$) quiescent galaxies at $2.5 < z < 3.0$ are smaller than star-forming galaxies, with average sizes of $2.5^{+0.5}_{-0.4}$ kpc and $3.55^{+0.2}_{-0.2}$ kpc, respectively (although with a large scatter, see Figure 3.6). The best-fit mass-size relations of quiescent and star-forming sources cross at $\log(M_\star/M_\odot) \approx 11.6$ because of their different slopes of $d \log r\,[\mathrm{kpc}]/d \log M_\star\,[M_\odot] = 0.79 \pm 0.07$ and 0.18 ± 0.02, respec-

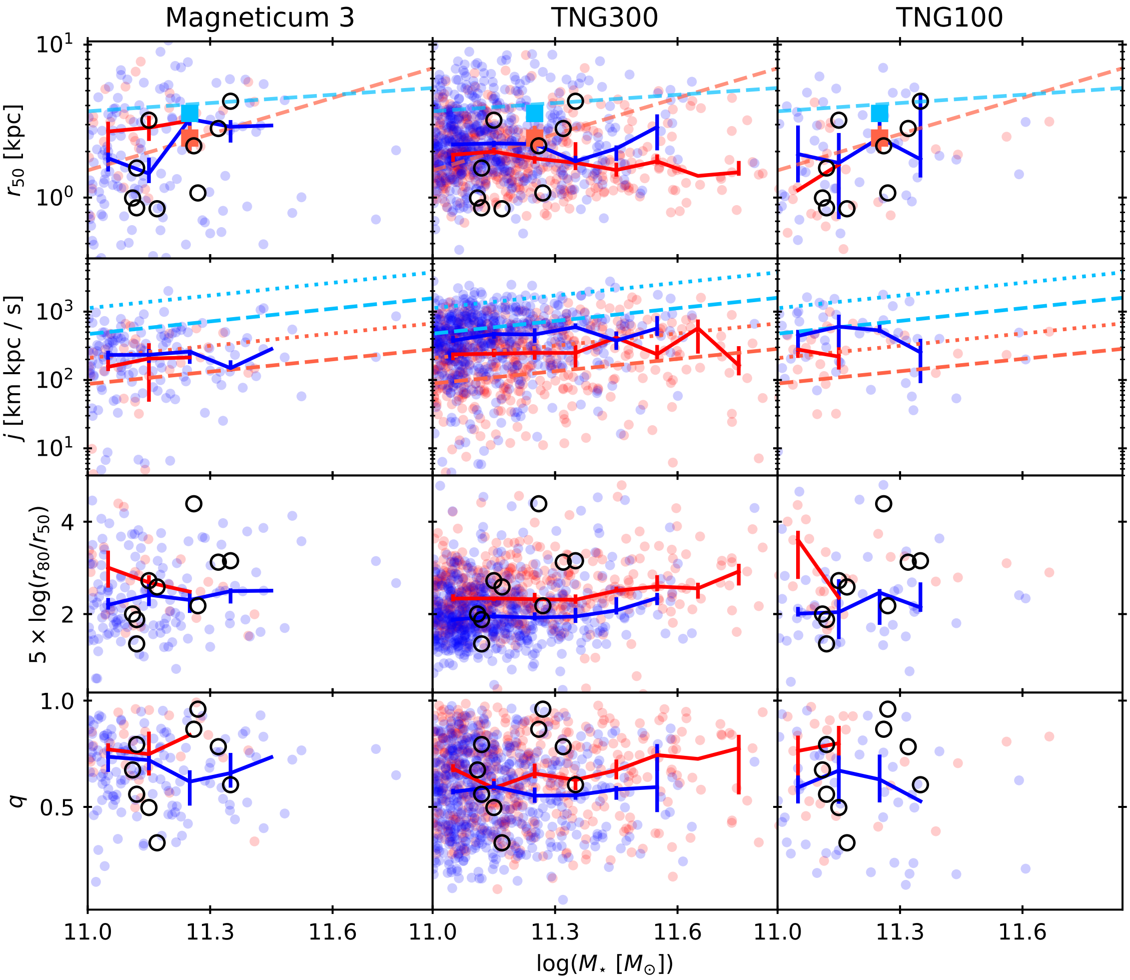

Figure 3.6: Morphological properties (projected) of quiescent (red) and star-forming (blue) galaxies at $z \approx 2.7$ as a function of stellar mass in the studied simulation as indicated. Individual galaxies are shown with filled circles, solid lines indicate median values estimated in 0.1 dex bins of stellar mass if at least 5 galaxies fall in the bin. Black open circles show observational results for quiescent galaxies from Lustig et al. (2021). In the first-row panels we show half-light (observed H band) radii along the semi-major axis. The dashed red (blue) line and square show the best-fit mass-size relation and average size in the $11.0 < \log(M_\star/M_\odot) < 11.5$ bin for observed quiescent (star-forming) galaxies at $2.5 < z < 3.0$ from van der Wel et al. (2014). In the second-row panels we show specific angular momenta. Light blue (light red) lines are references for quiescent (star-forming) galaxies from Romanowsky and Fall (2012) scaled to the redshift of the simulation by j vs. z relations from Swinbank et al. (2017, dashed lines) and Lagos et al. (2017, dotted lines). In the third-row panels we show the concentration of the galaxies. In the fourth-row panels we show projected axis ratios.

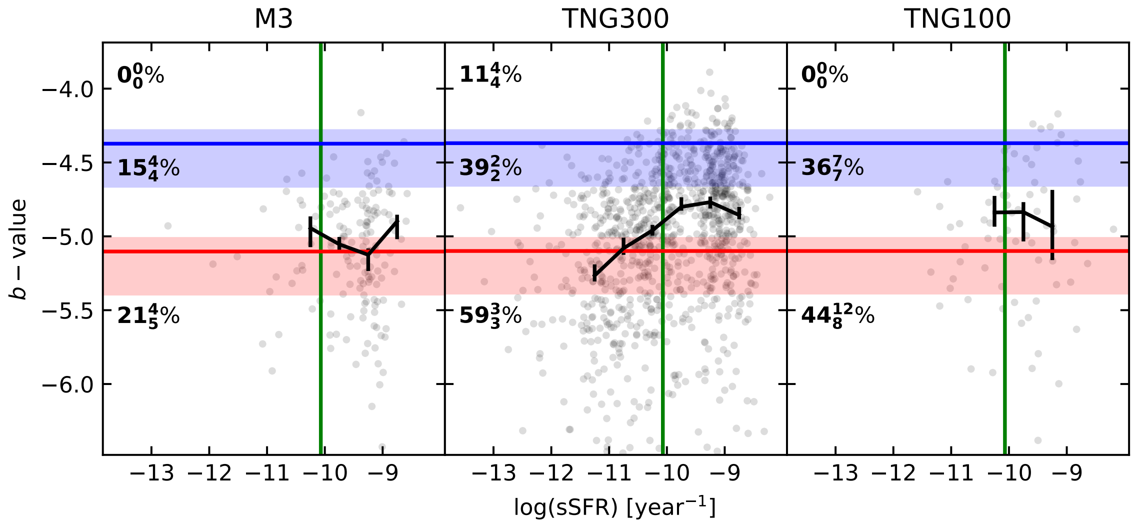

Figure 3.7: The b-value (specific angular momentum scaled to a pivot mass of $1\,M_\odot$ assuming $j \propto M^{2/3}$) for all galaxies at $z \approx 2.7$ as a function of sSFR in the studied simulations as indicated. Grey dots show individual galaxies. Blue (red) lines show the average b-value of observed nearby spiral (elliptical) galaxies from Romanowsky and Fall (2012) scaled to $z \approx 2.7$ assuming $j \propto (1+z)^{-1/2}$ (Obreschkow et al., 2015). The lower (upper) limit of the shaded areas indicates the b-value if scaled to $z \approx 2.7$ adopting the relation from Swinbank et al. (2017) (Lagos et al., 2017). Green vertical lines show the sSFR threshold for quiescence adopting the Franx et al. (2008) criterion. The black solid lines show the median b-value in bins of sSFR. Numbers indicate the quiescent fractions in the three ranges below the red solid line / above the blue solid line / in between.

tively. In M3 quiescent galaxies have sizes consistent with observed ones from van der Wel et al. (2014). However, although at face value quiescent galaxy sizes in M3 are similar in size to, or larger than, star-forming galaxies (depending on aperture choice), because of the large statistical uncertainties they are still consistent with having the same ratio of star-forming and quiescent galaxy sizes estimated by van der Wel et al. (2014). In TNG300 quiescent galaxies have on average significantly smaller sizes than star-forming galaxies with a ratio of $0.7-0.8$ (depending on the considered aperture), in good quantitative agreement with measurements from van der Wel et al. (2014). The larger sample size in TNG300 also allows to investigate the size-stellar mass relation which is consistent with being flat in the probed $\log(M_\star/M_\odot) > 11$ range for both populations.

Genel et al. (2018) investigate the mass-size relation of star-forming and quenched galaxies with $\log(M_\star/M_\odot) > 9$ in TNG100 up to $z = 3$. At masses higher than $\log(M_\star/M_\odot) \approx 10.5$ and up to $z \approx 2$, they find for both populations that the mass-size relation increases with a constant slope, in good quantitative agreement with determinations of the mass-size relation from Shen et al. (2003), Bernardi et al. (2014) and van der Wel et al. (2014). However, at $z = 3$ Genel et al. (2018) find flat mass-size relations for both populations up to $\log(M_\star/M_\odot) = 11$, in agreement with our results for TNG300 at higher masses.

Remus et al. (2017) investigated the mass-size relation for early-type galaxies in Magneticum up to $z = 2$. At all redshifts they find good agreement with van der Wel et al. (2014) as well, down to stellar masses of $\log(M_\star/M_\odot) = 10.7$, clearly showing that the observed evolution in the mass-size relation of early-type galaxies in Magneticum is reproduced successfully as well. However, from Teklu et al. (2015) it is known that some of these early-type galaxies have still large gas fractions and thus are likely not quiescent.

Specific angular momentum

The average light-weighted projected angular momenta of $\log(M_\star/M_\odot) > 11$ quiescent galaxies in M3 and TNG300 are 170^{+50}_{-40} and 230^{+20}_{-20}, respectively. In all simulations it is larger for star-forming than for quiescent galaxies, but the difference is only significant in TNG300 with a ratio of 0.55 ± 0.06.

In Figure 3.6 we compare the angular momenta from the simulations with results from Romanowsky and Fall (2012) for observed disks of nearby spiral galaxies and elliptical galaxies. To account for the evolution of the specific angular momentum with redshift we extrapolate the Romanowsky and Fall (2012) relations to $z \approx 2.7$ based on results from Swinbank et al. (2017) and Lagos et al. (2017). Swinbank et al. (2017) analyse observed star-forming galaxies at $0.3 \lesssim z \lesssim 1.7$ and find that their angular momentum evolves with $(z+1)^{-1}$ ($\approx 0.6\,$dex decrease between $z = 0$ to $z = 2.7$). To date observational statistical measurements of angular momenta of quiescent galaxies do not reach $z \approx 2$ and their redshift evolution is less constrained. However, by analysing galaxies in the EAGLE simulations, Lagos et al. (2017) find evidence for a weaker evolution of the angular momentum of quiescent galaxies of only $0.2\,$dex between $z = 0$ and 3 while star-forming galaxies show an evolution of $0.3-0.4\,$dex in the same redshift range. For an isolated spherical halo Obreschkow et al. (2015) find that the specific angular momentum evolves with $(1+z)^{-1/2}$ (increase by $\approx 0.3\,$dex between $z = 2.7$ and $z = 0$) due to cosmic expansion. Teklu et al. (2015) showed that the evolution of the specific angular momentum in Magneticum is consistent with the relation from Obreschkow et al. (2015). To account for the uncertainties in the redshift evolution of the angular momentum we therefore show the low redshift results from Romanowsky and Fall (2012) scaled by 0.2 and 0.6 dex. In TNG300 and M3 the angular momentum increases with stellar mass with a slope similar to that estimated in the parametrization of Romanowsky and Fall (2012) up to at least $\log(M_\star/M_\odot) \approx 11.3$. In TNG300 quiescent galaxies match the angular momenta of elliptical galaxies scaled by the evolution for quiescent galaxies from Lagos et al. (2017). The average angular momenta of star-forming galaxies in TNG300 are slightly lower than findings from Romanowsky and Fall (2012) for disk galaxies scaled by the relation for star-forming galaxies from Swinbank et al. (2017).

b-value

By analysing the specific angular momentum of galaxies in Magneticum up to $z \approx 2$ Teklu et al. (2015) and Teklu, Remus, and Dolag (2016) found that disk and spheroidal galaxies populate different regions in the $M_\star - j$ plane which therefore is an excellent tracer for morphology. Assuming the relation $j \propto M_\star^{2/3}$ (e.g., Romanowsky and Fall, 2012) a single parameter, the b-value (Teklu et al., 2015), can be used to separate between different morphological types.

In Figure 3.7 we show the estimated b-values of massive ($\log(M_\star/M_\odot) > 11$) galaxies at $z \approx 2.7$ for all considered simulations, as a function of sSFR. The solid red and blue lines split the diagram in regions exclusively populated by early- and late-type galaxies (bottom and top part of the plot, according to Teklu et al. (2015) based on the Obreschkow et al. (2015) scaling to $z = 2.7$). Shaded areas around the blue and red solid lines show the impact of adopting a different scaling of angular momentum with redshift, from Lagos et al. (2017) and Swinbank et al. (2017).

In all simulations, the median b-values of quiescent galaxy populations are in broad agreement with expectations for bulges from Romanowsky and Fall (2012) scaled to $z \approx 2.7$ (with scalings from Lagos et al., 2017; Obreschkow et al., 2015; Swinbank et al., 2017). However, star-forming galaxies have a median b-value which is lower by $0.4 - 0.8$ in M3 and $0.1 - 0.5$ in TNG simulations (depending on the adopted scaling) than expected for spirals.

Figure 3.7 clearly shows that in all simulations the low-b-value region (below the solid red line), which is expected to be populated by morphologically early-type galaxies, actually contains sources over a broad range of sSFR, with a significant fraction of actively star-forming sources (only ≈ 20 percent of these low-b-value galaxies are classified as quiescent in M3 and $\approx 40 - 60$ percent in TNG100 and TNG300.

Axis ratios and concentration

In all simulations we find that average projected axis ratios and concentrations of quiescent galaxies are larger than for star-forming galaxies (see lowest panels of Figure 3.6), however, due to the small sample sizes in M3 and TNG100 these differences are only significant in TNG300. Average axis ratios of quiescent galaxies in M3 and TNG300 are $0.76^{+0.04}_{-0.03}$ and $0.66^{+0.01}_{-0.01}$, which is higher than for star-forming galaxies by a factor of $1.08^{+0.07}_{-0.06}$ and $1.15^{+0.03}_{-0.03}$. In Lustig et al. (2021) we found for our observed sample of 10 quiescent galaxies an average axis ratio of $0.73^{+0.06}_{-0.12}$. The uncertainties on the average axis ratios of observed galaxies at high redshift are relatively large because of the small sample sizes and the additional dependence of the axis ratio on the inclination angle. We could therefore not see a significant difference between axis ratios of observed quiescent and star-forming galaxies.

The concentration of the profiles of quiescent galaxies is larger than that of star-forming galaxies by 0.28 ± 0.19 and 0.47 ± 0.05 in M3 and TNG300, respectively (see second lowest panels of Figure 3.6). Although the differences in average axis ratio and concentration between quiescent and star-forming galaxies in the simulations are relatively small they suggest that the evolution of quiescent galaxies towards a spheroidal, bulge dominated structure is already in progress at this redshift. For comparison we calculate concentrations for galaxies from van der Wel et al. (2014) with the same definition relying on results of their morphological analysis. We find a difference of the concentration of star-forming and quiescent galaxies of ≈ 0.8, larger than found in the simulations, with no significant redshift trend.

3.7 Summary and conclusions

We have analysed massive ($\log(M_\star/M_\odot) > 11$) galaxies at $z \approx 2.7$ in the Magneticum (M3) and IllustrisTNG (TNG100 and TNG300) hydrodynamical simulations and compared with observational results on stellar population and structural properties at similar redshift. For all of our analyses we considered a range of apertures, different prescriptions for dust attenuation for quiescent and star-forming galaxy populations and different criteria for defining quiescence, to estimate the impact of such assumptions on the comparison of simulations and observations carried out in this work.

We investigate the main sequence of star-forming galaxies in the studied simulations and find that in M3 the SFR increases constantly with stellar mass with a slope close to unity (at constant $\log(\mathrm{sSFR} \times \mathrm{yr}) \approx -9.3$) over the full mass range. In both TNG simulations at $\log(M_\star/M_\odot) \gtrsim 11.1$ a large fraction of galaxies is quenched and we can only identify a MS in TNG300 at lower masses. Observed main sequences from Sargent et al. (2014) and Schreiber et al. (2015) have a slope in agreement with our determination for M3 and TNG300 at lower masses but are offset to higher SFR by ≈ 0.6 dex. Following inspection of the star formation rate vs. mass diagram in the different simulations (see Section 3.2.3) we thus adopt the Franx et al. (2008) criterion to identify quiescent galaxies in all studied simulations, which turns out to be roughly equivalent to defining quiescent galaxies as those with a SFR 1 dex below the MS.

Based on this selection, as shown in Figure 3.1, for M3 the quiescent fraction (19 percent at $\log(M_\star/M_\odot) > 11$) is anyway largely consistent with most observations (except Davidzon et al., 2017, see Section 3.2.6) for all considered apertures, while quiescent fractions at $\log(M_\star/M_\odot) > 11$ in TNG simulations are larger than observed by a factor of ≈ 2. If quiescent galaxies are identified by UVJ colors instead, quiescent fractions at $\log(M_\star/M_\odot) > 11$ in M3 increase to 30 percent while quiescent fractions in TNG simulations differ by < 5 percentage points from the ones estimated with the Franx et al. (2008) sSFR criterion for defining quiescence.

Average ages in terms of t_{50} for the quiescent galaxy population in all simulations are $\gtrsim 0.8$ Gyr, significantly older than the average t_{50} of 0.5 Gyr estimated for our observed comparison sample in D'Eugenio et al. (2021) (as well as from studies of stellar ages as e.g., Schreiber et al., 2018; Forrest et al., 2020a,b; Valentino et al., 2020; Saracco et al., 2020). In Lustig et al. (2021) and D'Eugenio et al. (2021) we analysed the massive parent sample of quiescent galaxies at $2.5 < z < 3.0$ in the

Muzzin et al. (2013a) and COSMOS2015 (Laigle et al., 2016) catalogs and found a potential mild bias of the studied spectroscopically confirmed sample towards younger stellar ages, due to the selection of quiescent candidates for the spectroscopic follow-up. However, this selection effect alone cannot explain the discrepancy between the ages in the simulations and the observations (see Section 3.4). By analysing the SFHs of quiescent galaxies in the simulations we find that a significant fraction of their stellar mass is already formed at early times during a relatively slow increase of the SFR. The age discrepancy between observed vs. simulated quiescent galaxies might therefore partly be produced also by observational biases in the age estimation for observed sources due to a higher sensitivity to the most recent SFH and more generally model dependence of the spectro-photometric modeling as discussed in Section 3.4.

We investigate the restframe UVJ color plane of the simulated galaxies adopting recipes for dust attenuation of both quiescent and star-forming sources, and photometric uncertainties typical of deep field surveys used for studies at this redshift. We find that UVJ quiescent samples are strongly contaminated by dusty star-forming sources in the UVJ region typically populated by the oldest quiescent galaxies, reducing the overall purity of a UVJ selected sample to $\approx 40 - 50$ percent according to our modeling and with photometric uncertainties typical for the COSMOS2015 catalog. In agreement with results from previous studies (e.g., Schreiber et al., 2018; Merlin et al., 2018; Santini et al., 2021) we find that the UVJ selection with the routinely adopted criteria (Williams et al., 2009) leads to incomplete samples since a non negligible fraction of recently quenched quiescent galaxies with significantly suppressed SFR (and in this case e.g. $\log(\mathrm{sSFR} \times \mathrm{yr}) < -10$) has not yet entered the UVJ quiescent region due to the $U - V > 1.3$ constraint.

Because of the relatively small sample size in TNG100 and M3 we can detect structural differences between quiescent and star-forming populations at a significant level only in TNG300. We find that simulated quiescent galaxies are on average more centrally concentrated and have higher stellar axis ratios than star-forming galaxies, indicating that morphological differences as seen in observations at lower redshift (e.g., Hill et al., 2019) are already emerging at $z \approx 3$. In all simulations the ratio of quiescent and star-forming galaxy sizes in the observed H-band at $\log(M_\star/M_\odot) > 11$ is formally in agreement with observations at similar redshift (van der Wel et al., 2014, but note poor statistics affecting M3 and TNG100 results). With the larger sample size in TNG300 we also investigate the dependence of sizes on stellar mass and find the size-mass relation consistent with being flat for both populations in the probed $\log(M_\star/M_\odot) > 11$ range. The slope of the specific angular momentum vs. mass relation in the studied simulations is in agreement with observations from Romanowsky and Fall (2012). Specific angular momenta of quiescent (star-forming) galaxies at $\log(M_\star/M_\odot) > 11$ in TNG300 are by a factor of ≈ 1.3 (2) larger than in M3. Considering the large uncertainties on the evolution of angular momenta with redshift, the average specific angular momenta of both simulations are in agreement with our extrapolation of the low-redshift observed specific angular momentum-stellar mass relation (see Section 3.6.1).

Due to the complications hampering a proper, direct and fair comparison of structural properties in observations vs. simulations in our analysis (see full discussion in Section 3.6), it is not trivial to establish in absolute terms whether the correlation between structural and stellar population properties already seen at this redshift in several studies (see Bell et al. 2012; Mowla et al. 2019; Esdaile et al.

2020; Lang et al. 2014; Tacchella et al. 2015; Lustig et al. 2021, but see also van Dokkum et al. 2008; van der Wel et al. 2011; Bezanson et al. 2018; McGrath et al. 2008; Bundy et al. 2010; Chang et al. 2013; McLure et al. 2013; Hsu, Stockton, and Shih 2014 for a different picture) is actually quantitatively reflected in simulated galaxies. In fact, based on the analysis of b-values, that have been shown to correlate with galaxy morphology (Teklu et al., 2015; Teklu, Remus, and Dolag, 2016), early-type morphology and quiescence do not seem to be necessarily tightly related in the studied simulations with a significant fraction of morphologically early-type sources being still actively star forming (see Section 3.6.1). A more specific investigation of the early paths of structural evolution in connection with quenching in the studied simulations will be discussed in a future work.

Acknowledgements

The IllustrisTNG simulations were undertaken with compute time awarded by the Gauss Centre for Supercomputing (GCS) under GCS Large-Scale Projects GCS-ILLU and GCS-DWAR on the GCS share of the supercomputer Hazel Hen at the High Performance Computing Center Stuttgart (HLRS), as well as on the machines of the Max Planck Computing and Data Facility (MPCDF) in Garching, Germany. KD acknowledges support by the COMPLEX project from the European Research Council (ERC) under the European Union's Horizon 2020 research and innovation program grant agreement ERC-2019-AdG 882679 as well as support by the Deutsche Forschungsgemeinschaft (DFG, German Research Foundation) under Germany's Excellence Strategy - EXC-2094 - 390783311. The Magneticum Simulations were carried out at the Leibniz Supercomputer Center (LRZ) under the project pr86re. This work was supported by JSPS KAKENHI Grant Number JP21K03622.

Data availability

The IllustrisTNG simulations are publicly available and accessible at
www.tng-project.org/data (Nelson et al., 2019). The Magneticum simulations and data directly related to this publication and its figures are available upon request from the corresponding author.

3.8 Appendix

3.8.1 Impact of sSFR threshold for quiescence on quiescent fractions

In Section 3.2.3 we discuss different sSFR thresholds for defining quiescence in simulations. To take into account the evolution of the normalisation of the MS with redshift (e.g., Schreiber et al., 2015; Speagle et al., 2014; Tomczak et al., 2016; Johnston et al., 2015) we adopt for the analyses in this work a redshift dependent sSFR threshold (sSFR $\approx 1 \times 10^{-10}\,\mathrm{yr}^{-1}$ at $z = 2.7$) to define quiescence. In Figure 3.8 we show quiescent fractions if a sSFR threshold of $1 \times 10^{-11}\,\mathrm{yr}^{-1}$, often used for classification at low redshift, is used instead and compare with observational results from Muzzin et al. (2013b), Martis et al. (2016), Davidzon et al. (2017) and

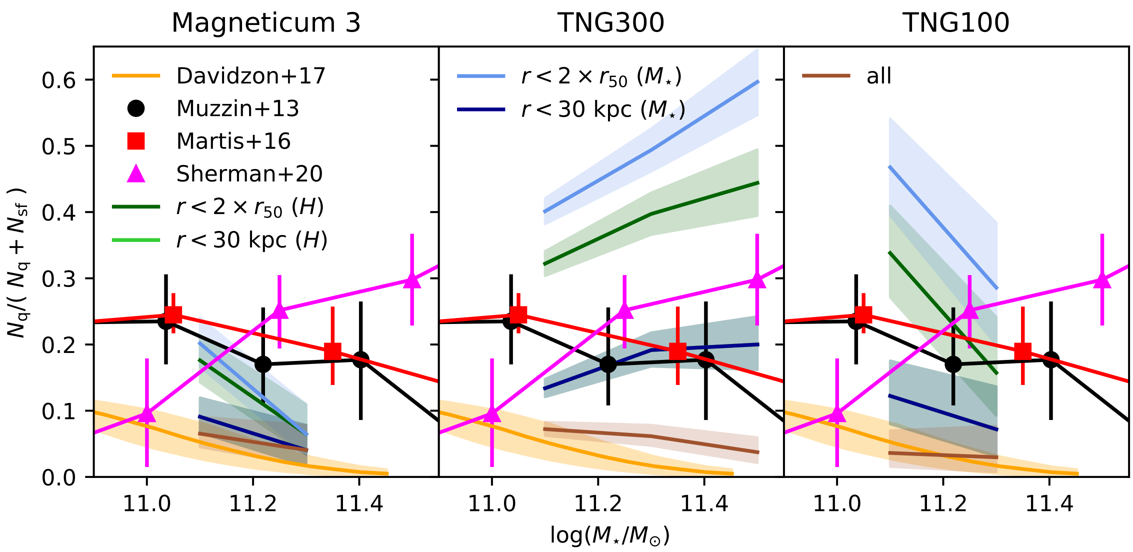

Figure 3.8: Quiescent fractions in the simulations for all apertures considered in this work (see Section 3.2.3) adopting a threshold of $\log(\mathrm{sSFR} \times \mathrm{yr}) = -11$ to define quiescence. We compare with observational results from Muzzin et al. (2013b), Martis et al. (2016), Davidzon et al. (2017) and Sherman et al. (2020) as indicated in the legend.

Sherman et al. (2020). At $\log(M_\star/M_\odot) > 11$ we find overall quiescent fractions between 5 and 15 percent for M3, lower than found by Muzzin et al. (2013b), Martis et al. (2016) and Sherman et al. (2020) but still higher than in Davidzon et al. (2017). Quiescent fractions in both TNG simulations in the same mass range show a very strong aperture dependence with overall quiescent fractions between 7 and 45 percent in TNG300 and 2 and 43 percent in TNG100. The highest quiescent fractions are measured for an aperture of 2 times the half-mass radius, the lowest if all bound particles are considered.

3.8.2 Impact of a higher sSFR threshold for defining quiescence on estimated purity and completeness of UVJ selected samples

In Section 3.5 we analyse purity, completeness and UVJ-derived quiescent fractions for a UVJ selected sample of quiescent galaxies. In Figure 3.9 we show UVJ diagrams for simulated massive galaxy samples where we adopted a relaxed sSFR threshold for defining quiescence ($\mathrm{ssfr} = 0.75 \times H(z)$, see Section 3.4). The different threshold for quiescence affects the implementation of dust attenuation for the individual galaxies, and thus the galaxy distribution in the UVJ diagram. Ultimately, the adopted definition of quiescence affects by construction the purity and completeness of the UVJ-selected quiescent samples as determined in Section 3.5. We find overall UVJ-derived quiescent fractions of 28 percent in M3 and ≈ 40 percent in the TNG simulations, consistent with UVJ-derived quiescent fractions obtained adopting the Franx et al. (2008) criterion (as in Section 3.5). The estimated completeness of UVJ-selected quiescent samples in the considered mass range decreases by $10 - 20$ percentage points with respect to our results in Section 3.5 because a significant fraction of galaxies classified as quiescent with the relaxed threshold are very young and have not yet entered the UVJ quiescent region. The purity increases by $10 - 15$

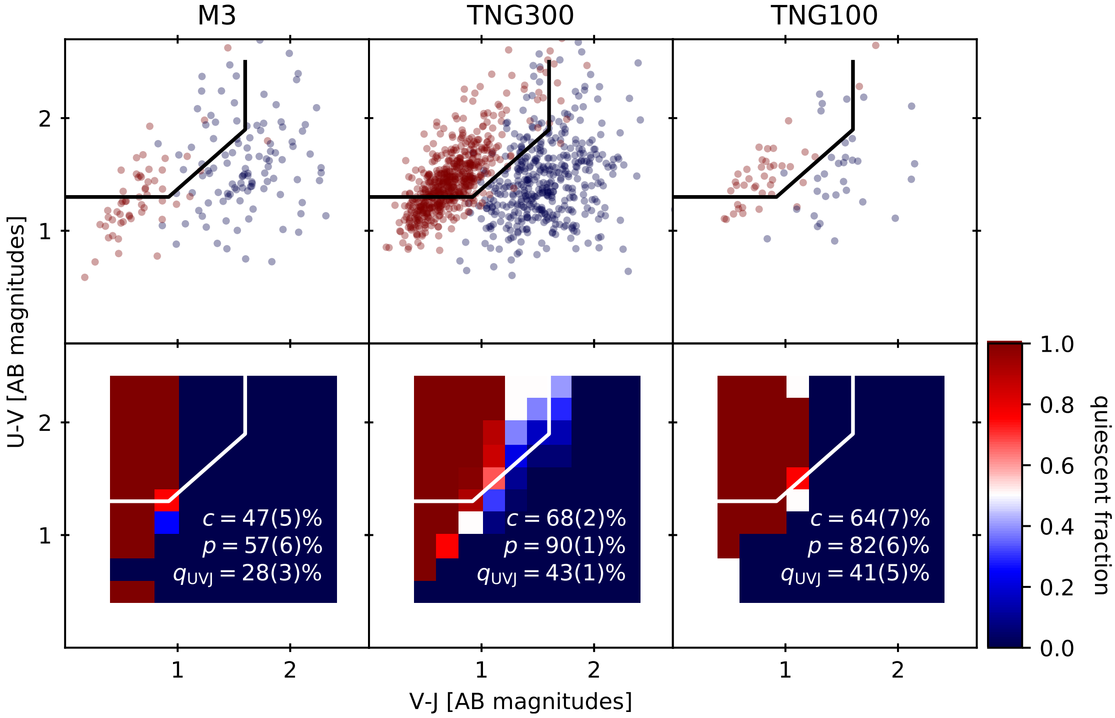

Figure 3.9: Restframe $U-V$ vs. $V-J$ colors for simulated galaxies. In the upper panel we show a random single realisation of the colors after applying dust attenuation. In the middle panel we show the average fraction of quiescent galaxies from 1000 realisations as a function of the position in the UVJ diagram as indicated by the colorbar if a threshold of sSFR $= 0.75 \times H(z)$ is adopted. The numbers show completeness (c) and purity (p) of the overall UVJ-quiescent sample and the quiescent fraction according to UVJ selection (q_{UVJ}) together with the scatter across the different realizations.

percentage points because a larger fraction of galaxies in the UVJ quiescent region is defined as quiescent with the relaxed sSFR threshold.

Chapter 4

Redshift calibration and environmental analysis of $z \approx 3$ quiescent galaxies

ABSTRACT
Dense environments like galaxy clusters are known to host a high fraction of quenched galaxies. In this work we search for overdensities of $\log(M_\star/M_\odot) > 10.8$ galaxies at positions of quiescent galaxies at $2.2 < z < 3.5$ in the COSMOS field as potential tracers of proto-clusters. For our analysis we estimate photometric redshifts of quiescent galaxies using a sample of 20 spectroscopically confirmed quiescent galaxies in the same redshift range as the calibration sample, improving significantly the photometric redshift accuracy for this specific population compared to current catalogs. We then compare the density at positions of quiescent and star-forming galaxies in redshift slices centered at the redshifts of quiescent galaxies. We find that 8-10 out of 12 quiescent galaxies are located in at least mild overdensities. In three cases the density is higher than for 90 percent of the positions of star-forming galaxies, suggesting that these galaxies might be located in proto-clusters that evolve into massive clusters at lower redshift.

4.1 Introduction

In the low redshift universe quiescent galaxies dominate the high mass end and outnumber star-forming galaxies at $\log(M_\star/M_\odot) > 11.5$ by a factor ≈ 10 (e.g., Baldry et al., 2004). There is a strong correlation between star formation and morphology, with quiescent galaxies at low redshift appearing typically as bulge-dominated early-type galaxies while star-forming galaxies mostly have disk-dominated late-type morphologies. Several ways to quench star formation have been proposed, such as gas consumption, stellar- and AGN feedback and morphological quenching (e.g., Dekel and Silk, 1986; Ciotti and Ostriker, 2007; Martig et al., 2009). These mechanisms can partly also explain the observed correlation between star-formation and morphology. Observations show that dense environments host significantly higher fractions of quiescent, bulge-dominated galaxies (e.g., Dressler, 1980; Peng et al., 2010b; Tanaka et al., 2004; Postman et al., 2005; Cooper et al., 2006; Poggianti et al., 2008; Pannella et al., 2009c; Muzzin et al., 2012; Mok et al., 2013; Woo et al., 2013; Kovač et al., 2014; Strazzullo et al., 2019; Old et al., 2020). Quenching mechanisms that are especially effective in dense environments have been proposed as an explanation. Examples include the truncation of gas accretion from the cosmic web when a satellite is accreted by a massive halo (called strangulation, e.g., Dekel and Birnboim, 2006; Larson, Tinsley, and Caldwell, 1980; Balogh and Morris, 2000; Balogh, Navarro, and Morris, 2000; Kereš et al., 2005b; van den Bosch et al., 2008; Peng, Maiolino, and Cochrane, 2015). Furthermore, if the pressure of the external medium is high enough, ram pressure stripping can remove cold gas from galaxies (e.g., Gunn and Gott, 1972; Abadi, Moore, and Bower, 1999; Quilis, Moore, and Bower, 2000). Also, accelerated evolution of galaxies in dense environments and preprocessing may significantly contribute to the larger fraction of more evolved galaxies in dense environments (e.g., Werner et al., 2022; van der Burg et al., 2020).

For the study of environmental effects on galaxy evolution, the investigation of dense environments like (proto-)clusters across a broad redshift range is crucial. Today, detections of (proto-)clusters reach out to $z \gtrsim 5$ (e.g., Andreon et al., 2009; Henry et al., 2010; Gobat et al., 2011; Capak et al., 2011; Stanford et al., 2012; Zeimann et al., 2012; Yuan et al., 2014; Newman et al., 2014; Cucciati et al., 2014; Wang et al., 2016; Mantz et al., 2018; Toshikawa et al., 2020; Shi et al., 2021b; Shi et al., 2021a; Shen et al., 2021; McConachie et al., 2021; Polletta et al., 2021; Calvi et al., 2021). A variety of approaches have been adopted to identify clusters and proto-clusters up to high redshift. Massive clusters can be detected through their intracluster medium via the Sunyaev-Zeldovich effect or their diffuse X-ray emission, with such searches reaching out to $z \approx 1.5$ (Foley et al., 2011; Bleem et al., 2015; Rosati et al., 1999; Adami et al., 2011; Fassbender et al., 2011; Klein et al., 2021). In contrast to X-ray emission, the strength of the Sunyaev-Zeldovich effect is not affected by cosmological dimming and thus may offer the advantage of a roughly constant cluster mass detection threshold as a function of redshift (e.g., Bocquet et al., 2019).

The search for less massive (proto-)clusters can employ galaxy-based methods. Overdensities of star-forming galaxies can be found via narrow-band surveys targeting Lyα or Hα emission (e.g., Steidel et al., 2000; Ouchi et al., 2003, 2005; Lemaux et al., 2009; Hatch et al., 2011; Zheng et al., 2021) and red galaxy overdensities have also been used to identify distant clusters and proto-clusters (e.g., Kodama et al., 2007; Spitler et al., 2012). Thanks to deep multi-band surveys that allow the estimation of photometric redshifts in large fields, dense environments have also been identified as galaxy overdensities in redshift slices (e.g., Castellano et al., 2007; Salimbeni et al., 2009; Scoville et al., 2013; Chiang, Overzier, and Gebhardt, 2014; Strazzullo et al., 2015b; Cucciati et al., 2018).

When estimating redshifts from broad band photometry the very coarse spectral resolution and limited number of clearly identifiable, distinct features in the probed SED implies larger uncertainties on the estimated redshifts compared to spectroscopic redshifts. However, strong features as for instance the 4000 Å break in red galaxies if properly probed with carefully chosen passbands can provide strong constraints on the photometric redshift (e.g., Gladders and Yee, 2000; Eisenstein et al., 2001; Padmanabhan et al., 2005). Large photometric multi-wavelength surveys in deep fields like COSMOS, GOODS-S and GOODS-N have sufficiently extended wavelength coverage to probe the stellar SED from UV to NIR, securing high-quality photometric redshifts (photo-z's) over a very broad redshift range (Barro et al., 2019; Whitaker et al., 2019; Weaver et al., 2022). Different techniques have been developed to map between observed fluxes and redshift, and these can be considered to fall into two different classes: template fitting (e.g., Brammer, van Dokkum, and Coppi, 2008; Arnouts et al., 1999; Bolzonella, Miralles, and Pelló, 2000; Ilbert et al., 2006; Feldmann et al., 2006) and machine learning (e.g., Tagliaferri et al., 2003; Collister and Lahav, 2004; Hoyle, 2016; Eriksen et al., 2020; Schmidt et al., 2020; Schuldt et al., 2021). While machine learning algorithms require a large training sample matching the expected redshift distribution, template fitting methods provide in principle also the possibility to estimate photometric redshifts of galaxies without reference redshifts thanks to the use of physically motivated SED templates. However, the accuracy of photometric redshifts can here also be significantly improved by calibrating the calculation with spectroscopic redshifts of galaxies with similar stellar population properties at similar redshift. Such calibration can compensate systematic offsets in different photometric bands resulting from uncertainties in the photometric zero-point calibration and transmission curves of instruments, systematics in the photometric measurements or inadequacies of spectral synthesis models (Ilbert et al., 2006; Brodwin et al., 2006).

In this work we analyse the galaxy density in redshift slices at $2.2 < z < 3.5$ in the COSMOS field to search for potential overdensities around massive, quiescent galaxies that may point toward the presence of a proto-cluster. For this analysis and more generally for the selection and investigation of targets for spectroscopic follow-up observations to improve the statistical significance of high redshift quiescent galaxy properties, we also improve the accuracy of photo-z's for high redshift quiescent galaxies at $z > 2.2$ using spectroscopic redshifts of quiescent galaxies as a calibration set. In Section 4.2 we calibrate photometric redshifts for high-redshift quiescent galaxies and estimate stellar masses for galaxies in the COSMOS field.

In Section 4.3 we analyse the source density in the COSMOS field and in Section 4.4 we summarise our findings. We assume a ΛCDM cosmology with $H_0 = 71\,\frac{\mathrm{km}}{\mathrm{s\,Mpc}}$, $\Omega_\mathrm{M} = 0.27$ and $\Omega_\Lambda = 0.73$. A Chabrier (2003) IMF is assumed. Magnitudes are given in the AB system.

4.2 Photometric redshift and stellar mass estimation

For our analysis we use the COSMOS2015 multi-band photometric catalog (Laigle et al., 2016) containing. It contains photometry for sources in the $2\,\mathrm{deg}^2$ COSMOS field (Scoville et al., 2007) in up to 32 bands (18 broad bands and 14 narrow bands). The catalog provides photometric redshift estimates with a precision of $\sigma_{\Delta z/(1+z_\mathrm{s})} = 0.007$ and a catastrophic outlier fraction of $\eta = 0.5$ percent, where catastrophic outliers are defined as sources for which $|(z_\mathrm{phot} - z_\mathrm{spec})/(1 + z_\mathrm{spec})| > 0.15$. At $3 < z < 6$ these values increase to $\sigma_{\Delta z/(1+z)} = 0.021$ and $\eta = 13.2$ percent. While these estimates apply generically to the whole galaxy population in the COSMOS2015 catalog, we compare in Figure 4.1 spectroscopic redshifts of recently confirmed quiescent galaxies in the COSMOS field in the redshift range $2.2 < z < 3.5$ from Marsan et al. (2015), Belli, Newman, and Ellis (2017), Schreiber et al. (2018, only robust redshifts), Stockmann et al. (2020), and D'Eugenio et al. (2021) with photometric redshifts from the COSMOS2015 catalog. We find that photo-z's for these sources are systematically underestimated, by on average $(z_\mathrm{phot} - z_\mathrm{spec})/(1 + z_\mathrm{spec}) = -0.06$ (-0.08 if considering only galaxies with $z_\mathrm{spec} > 2.5$). Formally the normalized median absolute deviation (NMAD, Hoaglin, Mosteller, and Tukey 1983) scatter for this sample is

$\sigma_{\rm NMAD} = 0.09$ and the catastrophic outlier fraction 4.5 percent. Considering only the 13 sources with $z_{\rm spec} > 2.5$ these values increase to 0.12 and 23 percent (3 catastrophic outliers).

4.2.1 Calibration of photometric redshifts for high-redshift quiescent galaxies

To improve the accuracy of photometric redshifts for quiescent galaxies at $2.2 < z < 3.5$ for our further analysis, we re-estimate photometric redshifts using 20 spectroscopically confirmed quiescent galaxies as a calibration set (see Table 4.1) with SED fitting. We use a combination of two template sets: the EAZY (Brammer, van Dokkum, and Coppi, 2008) standard template set[1] and a second template set specifically suited for the description of the SED's of high redshift quiescent galaxies. The EAZY template set is best suited for the bulk of the galaxy population across a broad redshift range, spanning a wide range of galaxy colors. It is composed of five templates calibrated with synthetic photometry from semi-analytical models, plus additionally a young dusty template and an old, red SED describing the oldest, most massive galaxies at $z < 1$, that were introduced to compensate for the lack of these specific kinds of SED's in the original template set (Brammer, van Dokkum, and Coppi, 2008; Brammer et al., 2011b; Whitaker et al., 2010b, 2011). Specific minority populations like high-redshift galaxies that quenched at early times may be less accurately described due to the small number of templates that can be combined to reproduce their SED's. For this reason we also add specific young quiescent templates to the EAZY template set for the photo-z calibration (as well as for the SED modelling carried out in Section 4.2.2). This young quiescent template set consists of 34 templates created with Bruzual and Charlot (2003) stellar synthesis models assuming a Chabrier (2003) IMF. The templates are created for unobscured SSPs with ages ranging between 0.5 and 3.5 Gyr (the age of the universe at $z = 1.9$) and metallicities $Z = 0.02$ (solar) and 0.008.

To carry out our photo-z calibration we use EAZY to fit combinations of SED templates to photometry of the 20 galaxies in the calibration set in 15 passbands from the COSMOS2015 catalog, ranging from 0.45 µm to 8 µm, fixing the redshift to the spectroscopic redshift. We iteratively repeat this procedure, in each step calculating, for each band, the photometric offset, that is the median ratio between best-fit model flux and observed flux in the given band over all galaxies in the calibration sample. We then multiply the observed photometry by the offsets in all bands and repeat the procedure until convergence (see e.g., Muzzin et al., 2013a; Capak et al., 2007; Ilbert et al., 2009). The obtained offsets are in the $0.88 - 1.18$ range.

We then re-estimate photo-z's for all galaxies with $z_{\rm phot} > 1.6$ or without redshift estimate in the COSMOS2015 catalog after applying these photometric offsets. In the right panel of Figure 4.1 we compare our estimated photometric redshifts for galaxies in the calibration sample with their spectroscopic redshift (because of the low number of spectroscopically confirmed quiescent galaxies at $z > 2$ we use the same sample of galaxies for calibration and verification of the photometric redshift quality). We find an NMAD scatter of 0.02 and no catastrophic outliers.

In Figure 4.2 we compare our calibrated photo-z's of quiescent galaxies with $\log(M_\star/M_\odot) > 10.8$ (for the estimation of stellar masses and classification see Sec-

[1] EAZY_v1.1_lines, http://www.astro.yale.edu/eazy/internal/index.html

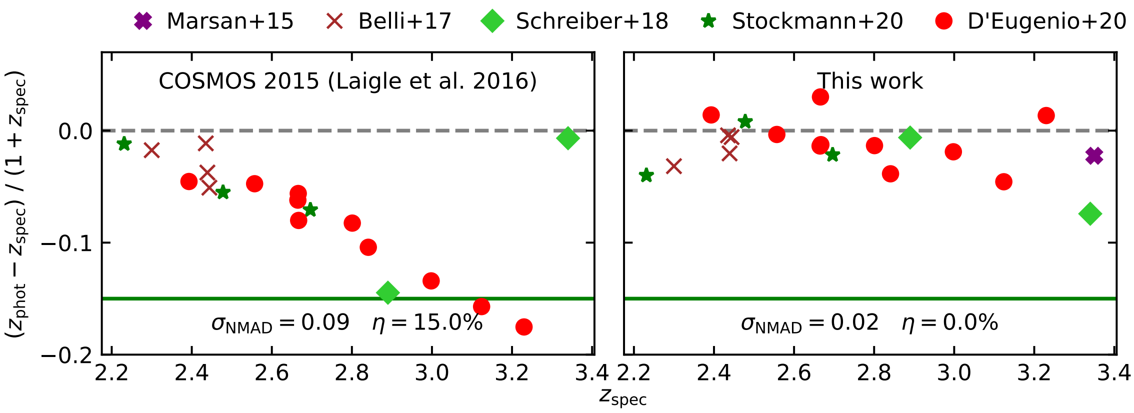

Figure 4.1: Difference between photometric and spectroscopic redshift for quiescent galaxies in the calibration set as a function of spectroscopic redshift from the literature (as indicated). In the left panel we compare spectroscopic redshifts with photometric redshifts from the COSMOS2015 (Laigle et al., 2016) catalog, in the right panel with photometric redshifts estimated in this work. By comparing the spectroscopic redshift from Marsan et al. (2015) with the corresponding photo-z in the COSMOS2015 catalog we find $(z_{\rm phot} - z_{\rm spec})/(1 + z_{\rm spec}) = -0.7$, exceeding the range of the plot. Galaxies below the green line are considered as catastrophic outliers. In both panels we show the corresponding NMAD scatter and the fraction of catastrophic outliers (η). The median systematic underestimation of photo-z's in the left panel is $(z_{\rm phot} - z_{\rm spec})/(1 + z_{\rm spec}) = -0.06$.

tion 4.2.2) in the range $2.0 < z < 3.3$ with photo-z's from several sources (Muzzin et al., 2013a; Laigle et al., 2016; Weaver et al., 2022). In the entire redshift range photometric redshifts from this work are on average higher than in all other published catalogs. By comparison with photo-z's from Laigle et al. (2016) we find $\sigma_{\rm NMAD} = 0.09$ and a catastrophic outlier fraction of $\eta = 13$ percent, in perfect agreement with what we obtain in our comparison with spectroscopic redshifts of galaxies from the calibration sample (see Figure 4.1). The agreement with photo-z's from Muzzin et al. (2013a) is better ($\sigma_{\rm NMAD} = 0.05$, $\eta = 8$ percent), as expected due to better agreement with spectroscopic redshifts in this redshift range (see Chapter 2 and Lustig et al., 2021). By comparing with photo-z's from Weaver et al. (2022), we find $\sigma_{\rm NMAD} = 0.10$ and $\eta = 19$ percent.

4.2.2 Classification and stellar mass estimation

The photometric redshifts estimated in Section 4.2.1 are calibrated for high-redshift quiescent galaxies. For the following analyses we estimate stellar masses for all galaxies in the COSMOS2015 catalog using FAST++[2] to fit stellar population synthesis models to the COSMOS2015 photometry, assuming a Chabrier (2003) IMF, a Calzetti (2001) dust attenuation law and a delayed exponentially declining SFH. We assume for quiescent galaxies the calibrated photo-z's from this work and for star-forming galaxies photo-z's from the COSMOS2015 catalog.

To identify quiescent vs. star-forming galaxies we estimate redshifts for all galaxies with $z > 1.6$ for which we calculated calibrated photo-z's again, considering two

[2]https://github.com/cschreib/fastpp

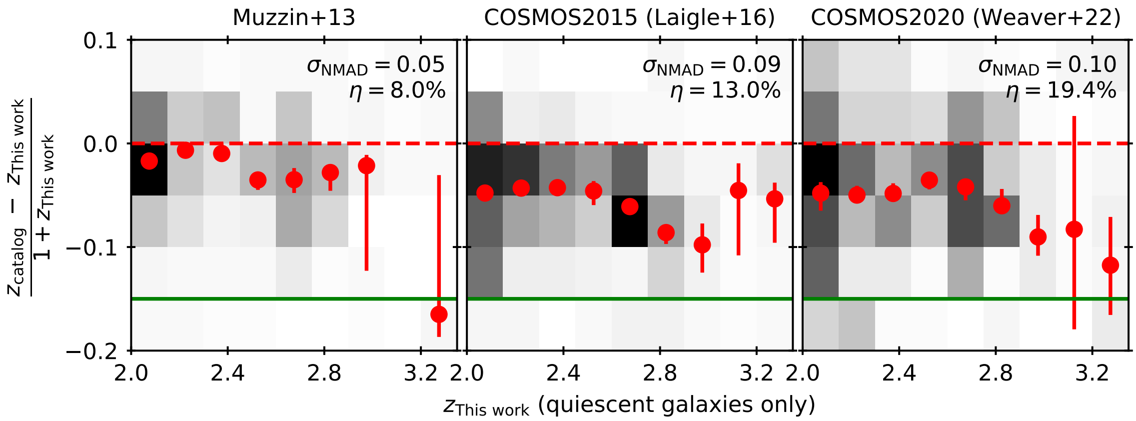

Figure 4.2: Comparison of photometric redshifts of quiescent galaxies from Muzzin et al. (2013a), Laigle et al. (2016) and Weaver et al. (2022) with estimates from this work. In all panels we show histograms of the redshift difference as a function of the redshift estimated in this work. Red circles show the median difference if at least 10 galaxies fall in the specific bin. The green line shows the threshold for catastrophic outliers (±0.15).

Table 4.1: Spectroscopically confirmed quiescent galaxies in the redshift range $2.2 < z < 3.5$ used as calibration sample for the re-estimation of photometric redshifts specifically tuned for high-redshift quiescent galaxies. The column ID lists the ids of the sources in the COSMOS2015 catalog. The columns RA and DEC list the right ascension and declination of the sources. The $z_{\rm spec}$ column lists the spectroscopic redshifts estimated in the works listed in the reference column.

ID	RA (h:m:s)	DEC (d:m:s)	$z_{\rm spec}$	reference
834299	10:00:27.81	2:33:49.10	3.35	Marsan et al. (2015)
592130	10:00:13.17	2:11:53.47	2.30	
616542	10:00:13.40	2:14:09.92	2.44	Belli, Newman, and Ellis (2017)
623536	10:00:12.60	2:14:44.16	2.44	
666180	10:00:23.93	2:18:42.53	2.44	
652048	10:00:17.15	2:17:28.32	3.34	Schreiber et al. (2018)
683969	10:00:29.83	2:20:14.64	2.89	
501158	10:00:42.38	2:03:39.22	2.23	
368191	10:00:50.13	1:51:00.91	2.70	Stockmann et al. (2020)
640744	10:01:57.00	2:16:12.11	2.48	
135730	10:01:39.98	1:29:34.45	2.84	
137182	10:00:57.35	1:29:39.54	2.56	
252568	9:57:48.58	1:39:57.76	3.12	
361413	10:02:00.97	1:50:24.32	3.23	
447058	9:59:11.77	1:58:32.97	2.67	D'Eugenio et al. (2021)
478302	9:59:01.31	2:01:34.17	2.80	
503898	10:01:31.86	2:03:58.72	2.67	
575436	10:00:43.76	2:10:28.70	3.00	
707962	9:59:32.52	2:22:22.07	2.67	
977680	10:00:12.66	2:47:23.56	2.39	

SED fitting setups: 1) only SED templates appropriate for young quiescent galaxies (see Section 4.2.1) and applying photometric offsets as derived in the previous section, specifically calibrated for high-redshift quiescent galaxies and 2) considering only EAZY_v1.1_lines templates without additional photometric offsets applied. Galaxies with a lower χ^2 in the fit with quiescent templates are defined as quiescent and our calibrated photo-z's are adopted. The remaining sources are considered to be star-forming, and we adopt the COMSOS2015 photo-z. Adopting this criterion, we find a quiescent fraction of 12 percent at $\log(M_\star/M_\odot) > 10.8$.

4.3 Mapping the number density of high redshift galaxies in the COSMOS field

In this section we search for potential overdensities preferentially associated with massive quiescent galaxies. For this purpose we compare the source density in the COSMOS field at redshifts and positions of confirmed quiescent galaxies from the combined spectroscopic sample (see Table 4.1) with the density at positions of star-forming galaxies in the same stellar mass and redshift range. We consider galaxies with $\log(M_\star/M_\odot) > 10.8$ because both the estimated uncertainties on photo-z's for quiescent galaxies increase significantly at lower masses and this threshold is close to the expected 95 percent mass completeness threshold of $\log(M_\star/M_\odot) \approx 10.9$ at $z = 3.5$ of the COSMOS2015 photometric catalog that we use, as inferred by scaling the empirically motivated mass completeness threshold of the photometric catalog from Muzzin et al. (2013a), based on the UltraVista data release 1, to the photometric depth of the data release 2, which is the basis for the COSMOS2015 catalog. For each galaxy in the spectroscopic quiescent sample we select from the COSMOS2015 catalog, adapted with our calibrated redshifts for quiescent galaxies (see Section 4.2.2), all galaxies in a photo-z range around the spectroscopic redshift. To choose an appropriate photo-z range we compare the scatter of the photometric vs. spectroscopic redshifts estimated for the calibration sample with the photometric redshift uncertainties estimated by EAZY. We find:

$$\frac{\chi^2}{n} = \frac{1}{n}\sum_i^n \left(\frac{z_{\mathrm{phot},i} - z_{\mathrm{spec},i}}{\sigma_{\mathrm{phot}_i}}\right)^2 \approx 0.6 \tag{4.1}$$

(where $n = 20$ is the size of the calibration sample), suggesting that the photo-z uncertainties estimated by EAZY broadly reflect the empirically observed uncertainties and if anything might be possibly overestimated by ≈ 25 percent. The median calibrated photo-z uncertainty for quiescent galaxies with $\log(M_\star/M_\odot) > 10.8$ is 0.2 (and if assuming that photo-z uncertainties from EAZY are overestimated by 25 percent, 64 percent of the galaxies have $\sigma_z < 0.2$). Therefore in the following we consider for the calculation of source densities around the quiescent targets all $\log(M_\star/M_\odot) > 10.8$ galaxies in a photo-z range ± 0.2 around the spectroscopic redshift of the quiescent galaxy.

We follow two different approaches to map the source density in the COSMOS field as detailed below. With both methods we calculate the density at positions in the field on a grid with a step size of 2 arcsec (≈ 16 kpc at $z = 2.75$), accounting for masked areas (see Figure 4.3, for more details see Laigle et al. 2016; Capak et al. 2007). The first estimator for source density that we use is the n-th nearest neighbour density Σ_n, that is the average density in the circle of radius equal to the

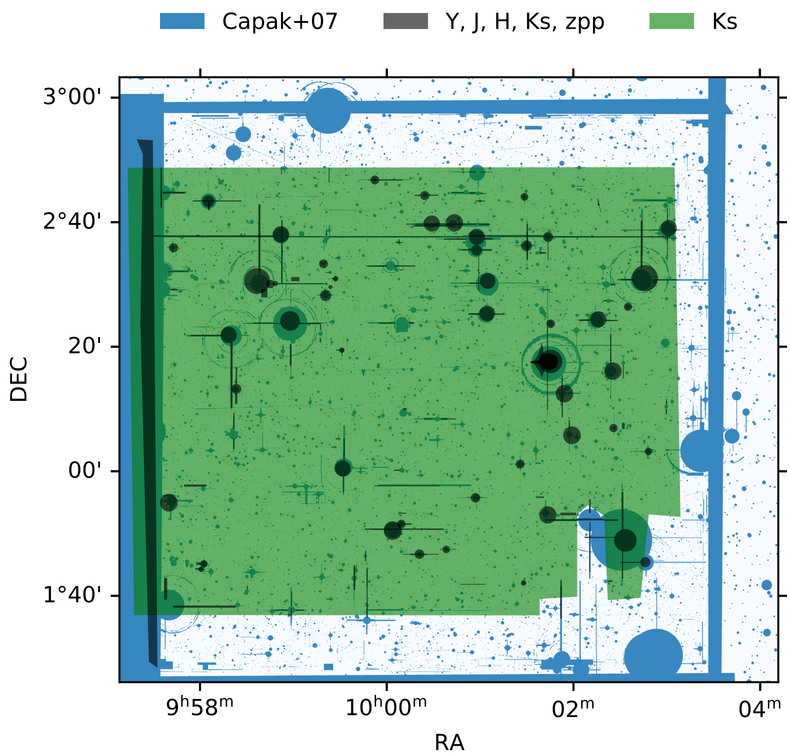

Figure 4.3: Masked areas in the COSMOS2015 catalog (Laigle et al., 2016). Blue areas are flagged in Capak et al. (2007), the green area is probed with the Ks band by the UltraVISTA-DR2 survey, grey areas are flagged in either of the Y, J, H, Ks or z^{++} band.

distance of the n-th nearest neighbour (e.g., Wang et al., 2016; Daddi et al., 2017). In this analysis, for a grid point i, j it is defined as:

$$\Sigma_n^{i,j} = \frac{n}{A_{r_n}^{i,j}}, \tag{4.2}$$

where $A_{r_n}^{i,j}$ is the unmasked surface of a circle with radius r_n, the distance to the n-th neighbour, around the grid point. Given the mass completeness threshold our search is limited to massive proto-cluster cores, that are expected to have a size of $\lesssim 200$ kpc at $2 < z < 4$ (e.g., Wang et al., 2016; Oteo et al., 2018; Strazzullo et al., 2018; Willis et al., 2020). Given the density of massive tracers in the cores we choose $n = 2$.

For our second density estimator we convolve the positions of sources in the COSMOS field with a Gaussian kernel k, accounting for masked areas as described below. The density is then given by:

$$D = \frac{M * k}{I * k} = \frac{d}{f}, \tag{4.3}$$

where the value of $M^{i,j}$ corresponds to the number of galaxies at position i, j, and $I^{i,j} = 1$ at unmasked positions and 0 elsewhere. For the following analysis we only consider grid points with $f^{i,j} \geq 0.8$. We choose Gaussian kernels with standard deviations of 20 arcsec (160 kpc at $z = 2.7$).

4.3.1 Massive galaxy density around quiescent vs. star-forming galaxies

In Figure 4.4 (Figure 4.5) we show cutouts of Σ_2 (Gaussian convolution) maps at the position of spectroscopically confirmed quiescent galaxies. We only consider the 12 galaxies for which at most 20 percent of the surface within a radius equal to the distance to the second neighbour is masked. The bottom sub-panel for each quiescent target shows for comparison the histogram of the density estimator at the position of star-forming galaxies with $z_{\text{spec}} - 0.05 < z_{\text{phot}} < z_{\text{spec}} + 0.05$, where z_{spec} is the spectroscopic redshift of the corresponding quiescent galaxy that defines the central redshift of the map. Our results do not significantly change if we consider galaxies within a range of $z_{\text{spec}} - 0.1 < z_{\text{phot}} < z_{\text{spec}} + 0.1$. For all studied quiescent galaxies we calculate the fraction of star-forming counterparts located in denser environments as a measure of the relative density difference. The uncertainty on the fraction is calculated with binomial confidence intervals following Cameron (2011) and is ≤ 4 percent.

Figures 4.4 and 4.5 show that 8 out of the 12 quiescent galaxies are located in regions that are denser than the average location of star-forming counterparts, though generally only marginally, with consistent results obtained by the two adopted density estimators. However, in three cases (IDs 575436, 616542 and 623536) the source density excess is not strongly pronounced with still $\gtrsim 30$ percent of star-forming counterparts being located in denser environments. The source density at the position of IDs 368191, 592130 and 666180 is higher than for $\gtrsim 90$ percent of the positions of star-forming counterparts, which might suggest the presence of a protocluster environment.

The strongly pronounced overdensities for three out of the twelve studied quiescent galaxies with respect to star-forming counterparts, and the typically higher source density of 8 of them, even though these sources were not selected based on environmental criteria, suggests that quiescent galaxies at $2.2 < z < 3.5$ may be preferentially found in dense environments that might potentially evolve into massive clusters at lower redshift. Especially the three targets located in significant overdensities are potentially interesting targets for follow-up observations for the study of the evolution of massive clusters and the environmental impact on the evolution of their galaxies.

4.4 Summary and conclusion

In this work we analyse the source density at positions of quiescent vs. star-forming galaxies in the same stellar mass ($\log(M_\star/M_\odot) > 10.8$) and redshift ($2.2 < z < 3.5$) range, to investigate potential differences in the environments of quiescent vs. star-forming galaxies at fixed mass at this cosmic time. Because photometric redshifts in the current photometric catalogs are systematically underestimated, for this analysis we first calibrate photo-z's specifically for quiescent galaxies at $2.2 < z < 3.5$ (see Section 4.2.1). For this purpose we use spectroscopically confirmed quiescent galaxies as a calibration sample to improve the photo-z accuracy specifically for this population. By comparison with spectroscopic redshifts from the calibration sample we find a scatter of $\sigma_{\text{NMAD}} = 0.02$ and no catastrophic outliers, although the small number of spectroscopically confirmed quiescent galaxies in this redshift range does not allow one to estimate these numbers on an independent sample.

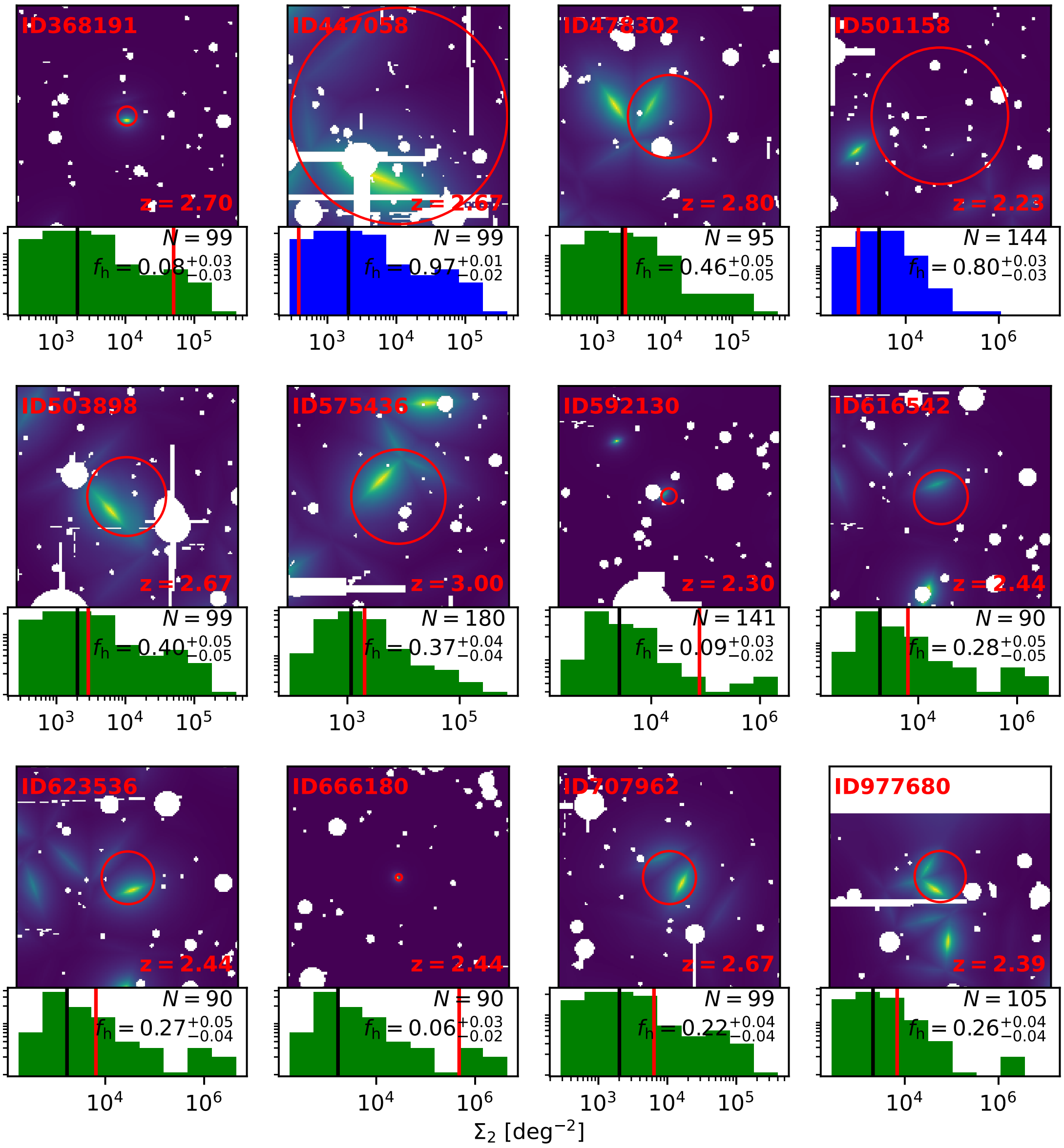

Figure 4.4: The second nearest neighbour density (Σ_2) map of massive galaxies as defined in Section 4.3, in portions of the COSMOS field around the studied quiescent targets. For each quiescent galaxy source (see Section 4.3) we show a pair of plots. *Upper panels:* cutout of Σ_2 maps with a size of 5 arcsec centered at the position of the quiescent galaxy and considering all $\log(M_\star/M_\odot) > 10.8$ galaxies in the photo-z range $z_{\rm spec} - 0.2 < z < z_{\rm spec} + 0.2$ as described in Section 4.3. Red circles show the distance to the second neighbour. *Lower panels:* Corresponding histograms of Σ_2 densities evaluated in the same photo-z range at the position of star-forming galaxies with photometric redshift within $z_{\rm spec} \pm 0.05$ from the target quiescent source. The density at the position of the studied quiescent targets is shown with the red vertical line, the average density at positions of star-forming galaxies with the black line. We also show the fraction $f_{\rm h}$ of star-forming galaxies right of the red line and the number N of galaxies contributing to the histogram. For visibility we colour histograms with a median density smaller then the density at the quiescent galaxy position with green, others with blue.

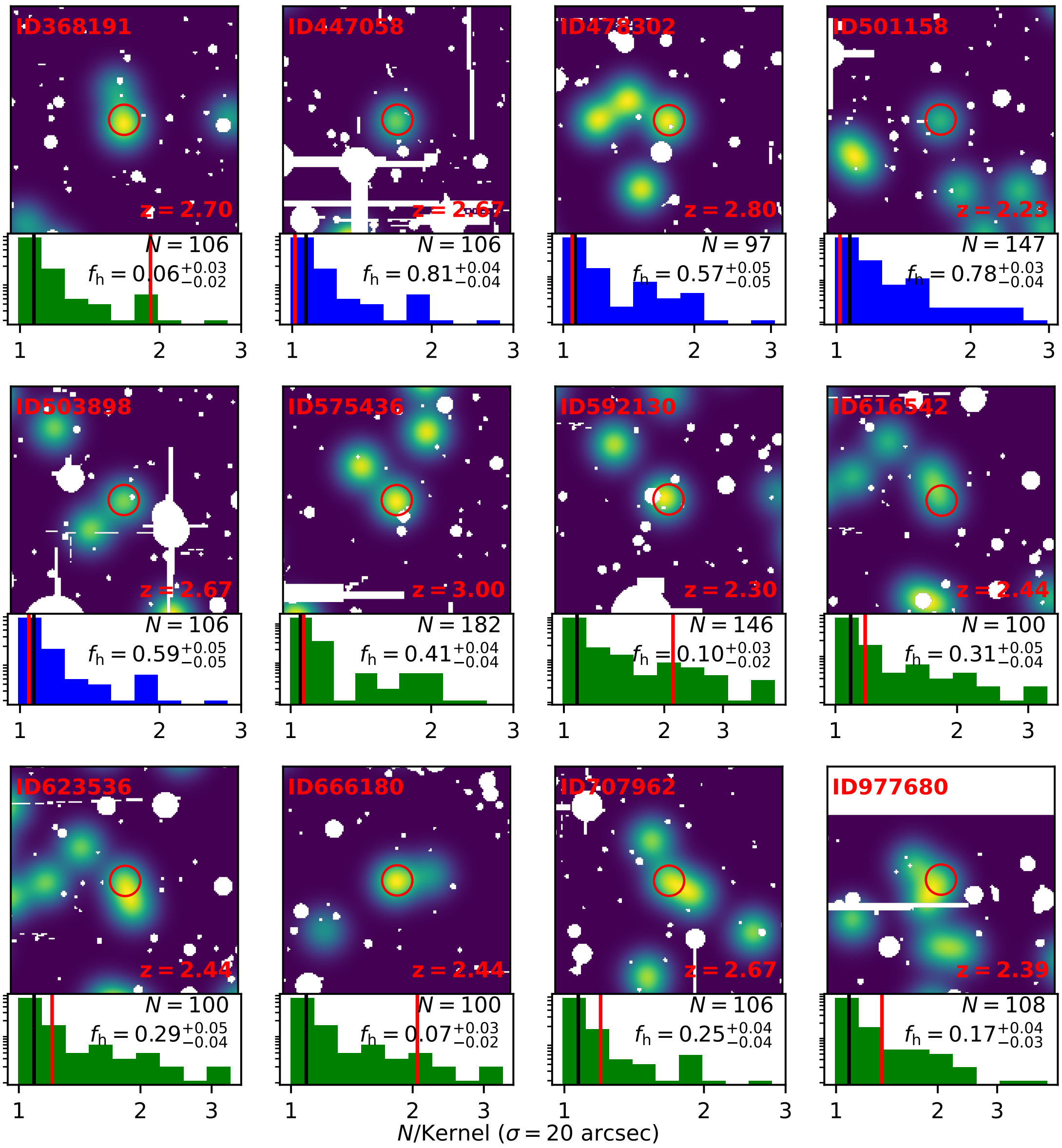

Figure 4.5: Like Figure 4.4, but source densities here are estimated by convolving positions of galaxies with a Gaussian kernel with a size of 20 arcsec (160 kpc at $z = 2.7$, see Section 4.3). Red circles shown in the maps have a radius of 20 arcsec.

To investigate the source density of $\log(M_\star/M_\odot) > 10.8$ galaxies in the COSMOS field we use two different estimators: the nearest neighbour density Σ_2 and the galaxy density convolved with a 20 arcsec Gaussian kernel (see Section 4.3). We compare the source density at positions of quiescent and star-forming galaxies, finding largely consistent results with both estimators. The majority of quiescent galaxies (8-10 out of 12) is located in overdense regions, although significant overdensities are only found at the position of three of the studied galaxies.

Due to the high stellar mass completeness threshold of $\log(M_\star/M_\odot) = 10.8$ our work is limited to the search for rare, massive galaxies in a proto-cluster core and is thus affected by statistical uncertainties that might lead one to miss the detection of some overdensities. This work is still in progress, and we are considering alternative ways to improve this aspect of our analysis. In this work we are relying on source detection and photometry from the COSMOS2015 catalog. Recently a new, deeper catalog of sources in the COSMOS field has been published (COSMOS2020, Weaver et al., 2022, see Figure 4.2). We are planning to repeat our analysis with this new catalog, potentially allowing us to derive more precise photo-z's for quiescent galaxies and to extend the estimates of local density to lower stellar mass galaxies. To improve the statistics of the used tracers and thus the significance of the overdensity detection we will also consider galaxies below the mass completeness threshold in our analysis, which we have avoided in the analysis presented here to limit biases in overdensity significance toward specific kinds of overdensities based on the stellar population properties of their host galaxies. We are also working on a spectroscopic analysis for the potential confirmation of the strongest overdensities where spectroscopic (including grism) data are already available. For this purpose we have also started to analyse Hubble Space Telescope grism observations from D'Eugenio et al. (2020, 2021), but will also consider targeted follow-up observations.

Furthermore, to date only few quiescent galaxies have been confirmed at $z \gtrsim 2$. We thus plan to include photometrically-selected quiescent galaxies in the above analysis to improve both its statistics and its representativeness with respect to the parent population of massive galaxies in the probed redshift range.

Chapter 5

Summary and outlook

In this thesis we have studied stellar population and structural properties of massive quiescent galaxies at high redshift by means of observations and hydrodynamical simulations.

We analyse galaxy morphologies of one of the first statistical samples of spectroscopically confirmed massive ($10.8 < \log(M_\star/M_\odot) < 11.3$) quiescent galaxies at $2.4 < z < 3.2$. Due to the intrisic rarity of these sources we rely on targeted imaging. An analysis of the representativeness of this sample with respect to the parent population of massive quiescent galaxies suggests a mild bias towards young ages (D'Eugenio et al., 2020; Lustig et al., 2021).

We find high Sérsic indices and axis ratios (medians ~ 4.5 and 0.73), suggesting that massive, quiescent galaxies are, already at high redshift, largely bulge dominated systems. The existence of a correlation between quiescence and morphology already at high redshift suggests that the morphological transformation from disk- to bulge-dominated structure either shortly precedes, is concomitant or happens shortly after quenching of star formation. We measure effective radii of the order of 1 kpc, in good agreement with the extrapolation to high stellar masses of previous determinations of the mass-size relation at similar redshift (e.g., van der Wel et al., 2014), and consistent with size evolution of massive, quiescent galaxies at fixed mass by nearly an order of magnitude since $z \sim 3$.

In a complementary analysis we focus on counterparts of massive ($\log(M_\star/M_\odot) > 11$) galaxies at $z \sim 2.7$ in the hydrodynamical simulations IllustrisTNG (boxes TNG100 and TNG300) and Magneticum (box 3). We find stellar mass functions in good agreement with observations at similar redshift, although with a ~ 2 times higher fraction of quiescent galaxies in IllustrisTNG. Quiescent galaxies in simulations are significantly older (by a factor of ~ 2) than their observed counterparts in spectroscopic studies at similar redshift. Besides intrinsically too old ages in simulations this might partly be explained through inaccuracies in estimating stellar ages from observations. We are currently analysing this further by generating spectro-photometric data for simulated galaxies, with the same characteristics as those in the compared observational studies, to estimate stellar ages with the same spectro-photometric modeling as adopted in observational studies, thus allowing a more direct estimate of the impact of observational methods on the observed stellar ages.

We further use simulations to investigate the performance at this redshift and for galaxies with high steller masses ($\log(M_\star/M_\odot) > 11$) of the routinely used UVJ restframe-color selection of quiescent galaxies, accounting for photometric scatter typical for current deep surveys. Applying standard UVJ selection criteria (Williams et al., 2009) we find evidence for significant contamination of quiescent samples (up to 60 percent) by star-forming galaxies entering the UVJ region typically populated by older quiescent systems. Furthermore, a significant fraction of young galaxies with already strongly suppressed star formation ($\log(\mathrm{sSFR} \times \mathrm{yr}) < -10$) has not yet entered the UVJ quiescent region, reducing the completeness of a UVJ selected quiescent sample by ~ 30 percent at these high masses.

We also investigate structural properties of simulated massive quiescent vs. star-forming galaxies at this redshift, finding that already at $z \sim 3$ the structural differences observed at lower redshifts between these two populations with respect to size, axis ratio, concentration and angular momentum have started to develop. However, quantitatively there remains tension between the observed and simulated results and the comparison is still hampered by poor statistics in both observations and simulations and unavoidable differences in their analysis procedures.

Because the most massive and old quiescent galaxies at lower redshift are found in galaxy clusters, we investigate the environment of massive quiescent galaxies at $2.2 < z < 3.5$ to search for over-densities that may potentially indicate the presence of a proto-cluster. To this aim we compare the source density at positions of quiescent vs. star-forming galaxies in the COSMOS field. Because photo-z's of high redshift quiescent galaxies are systematically underestimated in current photo-z catalogs, we improve for our analysis the quality of photo-z's for the specific population of very distant quiescent sources, by using spectroscopically confirmed quiescent galaxies in the same redshift range as a calibration set. We then estimate the density of massive galaxies around star-forming and quiescent galaxies and find that the majority of quiescent sources is located in marginally overdense environments with respect to star-forming analogs, and 3 out of 12 galaxies in the studied quiescent sample are located in significant overdensities that might evolve into massive clusters at lower redshift. We are also currently working on the possible spectroscopic confirmation of one of the strongest candidate overdensities from already available data.

As a counterpart to this work, we are currently designing an investigation on hydrodynamical simulations and semi-analytical models to probe the expected environments of high-redshift massive quiescent vs. star-forming galaxies. This analysis is expected in particular to investigate the association between early quenched, very massive sources and dense environments in proto-cluster regions, possibly proto-cluster cores, to investigate whether simulations predict that these first, massive, quiescent sources may be the progenitors of massive galaxies with high formation redshifts typically found in cluster cores at lower redshifts. In this context we are starting to explore this connection by probing likely descendant cluster environments in simulations at $z \sim 1.5$, investigating the comparison of the predicted properties of their massive galaxy populations with those observed in the most distant and massive clusters known.

For this analysis we use the box 2b of the Magneticum simulations with a comoving volume of $\sim$ 900 Mpc, large enough to contain massive clusters with $M_{500} > 2 \times 10^{14}\, M_\odot$[1] at $z \sim 1.5$ (14 clusters at $z = 1.3$ and 2 at $z = 1.7$). Dark matter and gas particles in this simulation have a mass of $9.8 \times 10^8\, M_\odot$ and $2 \times 10^8\, M_\odot$, respectively. Each gas particle spawns up to 4 stellar particles with an average mass

[1]We define R_{500} and R_{200} as the radii in which the mean density is 500 and 200 times, respectively, the critical density of the Universe at the cluster redshift. The mass contained within these radii is denoted M_{500} and M_{200}.

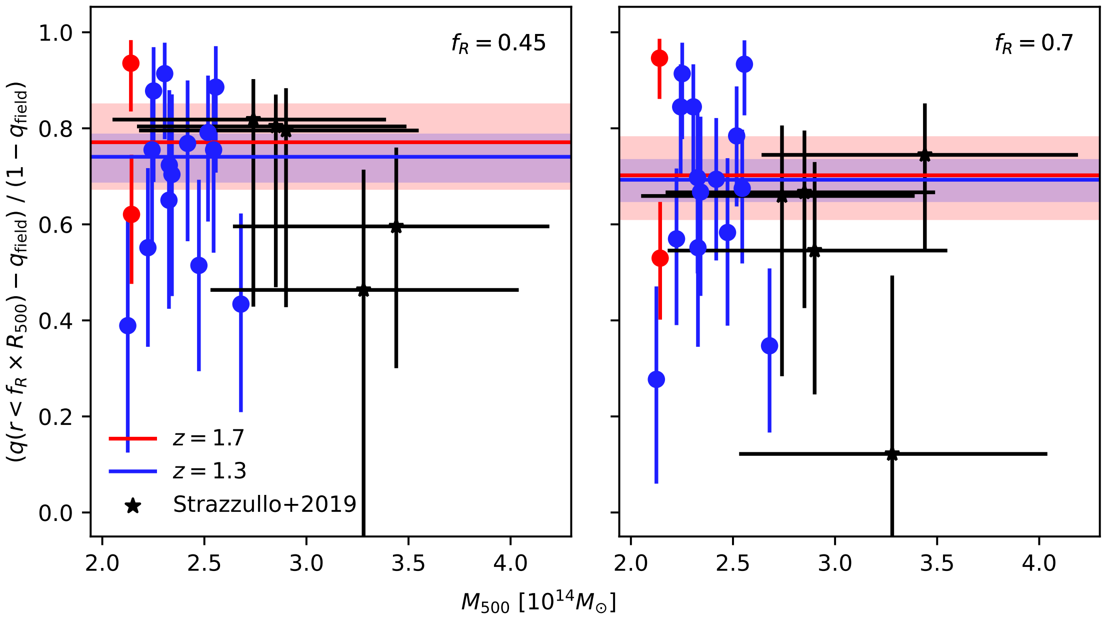

Figure 5.1: The environmental quenching efficiency in massive, high redshift galaxy clusters. The quenching efficiency within the central $0.45 \times R_{500}$ (left panel) and $0.7 \times R_{500}$ (right panel) is shown as a function of halo mass M_{500} for simulated clusters at $z = 1.7$ (red) and $z = 1.3$ (blue). Red and blue lines and shaded areas show the corresponding average and uncertainty across all $M_{500} > 2 \times 10^{14}\, M_\odot$ clusters. The average central quenching efficiency of all $M_{500} > 2 \times 10^{14}\, M_\odot$ clusters is shown with the horizontal lines. Black symbols show results from Strazzullo et al. (2019).

of $5 \times 10^7\, M_\odot$. For our analysis we consider all galaxies with $\log(M_\star/M_\odot) > 10.54$ for direct comparison with observational work with this stellar mass limit (see below).

In these rare, extreme environments in this simulation, we calculate the environmental quenching efficiency as a function of distance from the cluster center. This is defined as $q_{\rm eff}(r) = \frac{q(r) - q_{\rm field}}{1 - q_{\rm field}}$, where $q(r)$ is the quiescent fraction at clustercentric distance r and $q_{\rm field}$ the average quiescent fraction in the field (e.g., van den Bosch et al., 2008). The environmental quenching efficiency $q_{\rm eff}(r)$ thus represents the fraction of galaxies that would normally be star forming in the field which are instead quenched at clustercentric distance r in the cluster environment. By analogy with observational studies, with "field" we refer to all galaxies within a large volume (in this case the whole simulation box), regardless of the local density at their position.

In Figure 5.1 we compare simulation predictions with observational results in the central regions of a representative sample of five very massive clusters at $1.4 \lesssim z \lesssim 1.7$ (Strazzullo et al., 2019). We thus show the environmental quenching efficiency within the central 0.45 and $0.7 \times R_{500}$ for all clusters with $M_{500} > 2 \times 10^{14}\, M_\odot$, similar to what probed in these observations. The uncertainty on the quiescent fraction is calculated following Cameron (2011) and propagated to obtain the uncertainties on the quenching efficiency. We find that the average quenching efficiency in the central regions of massive clusters at this redshift predicted by the studied simulation is close to observations (~ 0.7 in the probed region, with no significant redshift dependence in the probed redshift range).

Observations to determine the quenching efficiency profile across the virial volume in such massive clusters at this redshift have only recently been acquired, and

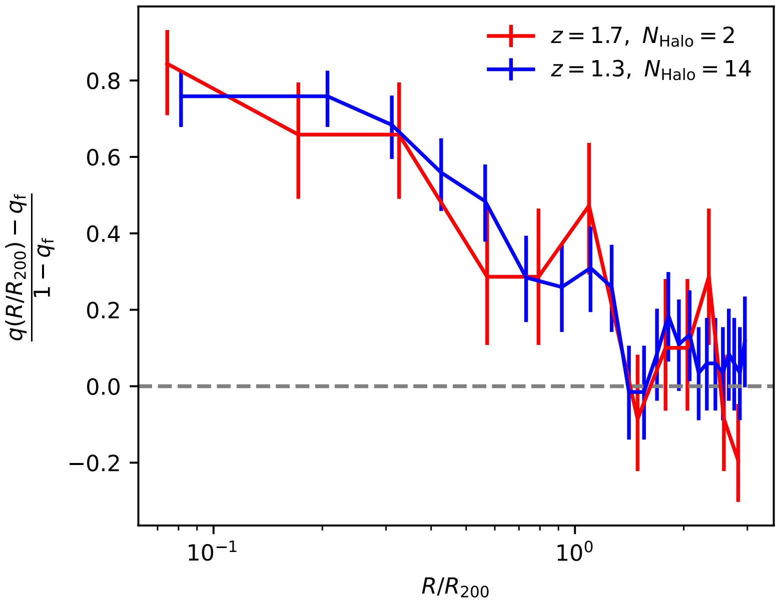

Figure 5.2: The environmental quenching efficiency as a function of clustercentric distance, averaged over all simulated $M_{500} > 2 \times 10^{14}\, M_{\odot}$ galaxy clusters at $z = 1.7$ (red) and $z = 1.3$ (blue).

are currently being analysed. The environmental quenching efficiency is expected to decrease with clustercentric distance, due to the correlation between clustercentric distance and galaxy infall time, and of the timescales of the relevant physical processes suppressing star formation in the cluster environment. In Figure 5.2 we show the quenching efficiency as a function of cluster-centric distance at $z = 1.3$ and $z = 1.7$, averaged over all $M_{500} > 2 \times 10^{14}\, M_{\odot}$ clusters. From the high environmental quenching efficiency in the central cluster regions discussed above, as expected the simulation shows a decreasing quenching efficiency at larger radii, with the quiescent galaxy fraction reaching the field level at $R \sim R_{200}$, independent of redshift. We are planning to compare these results with semianalytical models (Hirschmann, De Lucia, and Fontanot, 2016; Fontanot et al., 2020) and zoom-in hydrodynamical simulations (Bassini et al., 2019, 2020), both to investigate the impact of specific prescriptions on the simulation predictions, as well as to more effectively leverage the observational measurements to constrain actual physical processes affecting galaxy evolution in distant clusters and protocluster environments.

Bibliography

Licquia, Timothy C. and Jeffrey A. Newman (June 2015). "Improved Estimates of the Milky Way's Stellar Mass and Star Formation Rate from Hierarchical Bayesian Meta-Analysis". In: *ApJ* 806.1, 96, p. 96. DOI: 10.1088/0004-637X/806/1/96. arXiv: 1407.1078 [astro-ph.GA].

Bland-Hawthorn, Joss and Ortwin Gerhard (Sept. 2016). "The Galaxy in Context: Structural, Kinematic, and Integrated Properties". In: *ARA&A* 54, pp. 529–596. DOI: 10.1146/annurev-astro-081915-023441. arXiv: 1602.07702 [astro-ph.GA].

Kafle, Prajwal Raj et al. (Oct. 2014). "On the Shoulders of Giants: Properties of the Stellar Halo and the Milky Way Mass Distribution". In: *ApJ* 794.1, 59, p. 59. DOI: 10.1088/0004-637X/794/1/59. arXiv: 1408.1787 [astro-ph.GA].

McMillan, Paul J. (Feb. 2017). "The mass distribution and gravitational potential of the Milky Way". In: *MNRAS* 465.1, pp. 76–94. DOI: 10.1093/mnras/stw2759. arXiv: 1608.00971 [astro-ph.GA].

Mo, Houjun, Frank C. van den Bosch, and Simon White (2010). *Galaxy Formation and Evolution*.

Fukugita, Masataka and P. J. E. Peebles (Dec. 2004). "The Cosmic Energy Inventory". In: *ApJ* 616.2, pp. 643–668. DOI: 10.1086/425155. arXiv: astro-ph/0406095 [astro-ph].

Shull, J. Michael, Britton D. Smith, and Charles W. Danforth (Nov. 2012). "The Baryon Census in a Multiphase Intergalactic Medium: 30% of the Baryons May Still be Missing". In: *ApJ* 759.1, 23, p. 23. DOI: 10.1088/0004-637X/759/1/23. arXiv: 1112.2706 [astro-ph.CO].

Bluck, Asa F. L. et al. (Nov. 2020). "How do central and satellite galaxies quench? - Insights from spatially resolved spectroscopy in the MaNGA survey". In: *MNRAS* 499.1, pp. 230–268. DOI: 10.1093/mnras/staa2806. arXiv: 2009.05341 [astro-ph.GA].

Behroozi, Peter S., Risa H. Wechsler, and Charlie Conroy (Jan. 2013). "On the Lack of Evolution in Galaxy Star Formation Efficiency". In: *ApJ* 762.2, L31, p. L31. DOI: 10.1088/2041-8205/762/2/L31. arXiv: 1209.3013 [astro-ph.CO].

Dekel, A. and J. Silk (Apr. 1986). "The Origin of Dwarf Galaxies, Cold Dark Matter, and Biased Galaxy Formation". In: *ApJ* 303, p. 39. DOI: 10.1086/164050.

Ciotti, Luca et al. (Aug. 1991). "Winds, Outflows, and Inflows in X-Ray Elliptical Galaxies. I." In: *ApJ* 376, p. 380. DOI: 10.1086/170289.

Ciotti, Luca and Jeremiah P. Ostriker (Aug. 2007). "Radiative Feedback from Massive Black Holes in Elliptical Galaxies: AGN Flaring and Central Starburst Fueled by Recycled Gas". In: *ApJ* 665.2, pp. 1038–1056. DOI: 10.1086/519833. arXiv: astro-ph/0703057 [astro-ph].

Alexander, D. M. and R. C. Hickox (June 2012). "What drives the growth of black holes?" In: *New Astron. Rev.* 56.4, pp. 93–121. DOI: 10.1016/j.newar.2011.11.003. arXiv: 1112.1949 [astro-ph.GA].

Fabian, A. C. (Sept. 2012). "Observational Evidence of Active Galactic Nuclei Feedback". In: *ARA&A* 50, pp. 455–489. DOI: 10.1146/annurev-astro-081811-125521. arXiv: 1204.4114 [astro-ph.CO].

Madau, Piero and Mark Dickinson (Aug. 2014). "Cosmic Star-Formation History". In: *ARA&A* 52, pp. 415–486. DOI: 10.1146/annurev-astro-081811-125615. arXiv: 1403.0007 [astro-ph.CO].

Mancuso, C. et al. (Dec. 2016). "The Main Sequences of Star-forming Galaxies and Active Galactic Nuclei at High Redshift". In: *ApJ* 833.2, 152, p. 152. DOI: 10.3847/1538-4357/833/2/152. arXiv: 1610.05910 [astro-ph.GA].

Noeske, K. G. et al. (May 2007). "Star Formation in AEGIS Field Galaxies since z=1.1: The Dominance of Gradually Declining Star Formation, and the Main Sequence of Star-forming Galaxies". In: *ApJ* 660.1, pp. L43–L46. DOI: 10.1086/517926. arXiv: astro-ph/0701924 [astro-ph].

Daddi, E. et al. (Nov. 2007). "Multiwavelength Study of Massive Galaxies at $z \sim 2$. I. Star Formation and Galaxy Growth". In: *ApJ* 670.1, pp. 156–172. DOI: 10.1086/521818. arXiv: 0705.2831 [astro-ph].

Pannella, M. et al. (June 2009a). "Star Formation and Dust Obscuration at $z \approx 2$: Galaxies at the Dawn of Downsizing". In: *ApJ* 698.2, pp. L116–L120. DOI: 10.1088/0004-637X/698/2/L116. arXiv: 0905.1674 [astro-ph.CO].

Rodighiero, G. et al. (Oct. 2011). "The Lesser Role of Starbursts in Star Formation at z = 2". In: *ApJ* 739.2, L40, p. L40. DOI: 10.1088/2041-8205/739/2/L40. arXiv: 1108.0933 [astro-ph.CO].

Wuyts, Stijn et al. (Dec. 2011). "Galaxy Structure and Mode of Star Formation in the SFR-Mass Plane from $z \sim 2.5$ to $z \sim 0.1$". In: *ApJ* 742.2, 96, p. 96. DOI: 10.1088/0004-637X/742/2/96. arXiv: 1107.0317 [astro-ph.CO].

Schreiber, C. et al. (Mar. 2015). "The Herschel view of the dominant mode of galaxy growth from z = 4 to the present day". In: *A&A* 575, A74, A74. DOI: 10.1051/0004-6361/201425017. arXiv: 1409.5433 [astro-ph.GA].

Renzini, Alvio and Ying-jie Peng (Mar. 2015). "An Objective Definition for the Main Sequence of Star-forming Galaxies". In: *ApJ* 801.2, L29, p. L29. DOI: 10.1088/2041-8205/801/2/L29. arXiv: 1502.01027 [astro-ph.GA].

Tacchella, Sandro et al. (Apr. 2016b). "The confinement of star-forming galaxies into a main sequence through episodes of gas compaction, depletion and replenishment". In: *MNRAS* 457.3, pp. 2790–2813. DOI: 10.1093/mnras/stw131. arXiv: 1509.02529 [astro-ph.GA].

Whitaker, Katherine E. et al. (Aug. 2012b). "The Star Formation Mass Sequence Out to z = 2.5". In: *ApJ* 754.2, L29, p. L29. DOI: 10.1088/2041-8205/754/2/L29. arXiv: 1205.0547 [astro-ph.CO].

Speagle, J. S. et al. (Oct. 2014). "A Highly Consistent Framework for the Evolution of the Star-Forming Main Sequence from $z \sim 0 - 6$". In: *ApJS* 214.2, 15, p. 15. DOI: 10.1088/0067-0049/214/2/15. arXiv: 1405.2041 [astro-ph.GA].

Tomczak, Adam R. et al. (Feb. 2016). "The SFR-M_* Relation and Empirical Star-Formation Histories from ZFOURGE at $0.5 < z < 4$". In: *ApJ* 817.2, 118, p. 118. DOI: 10.3847/0004-637X/817/2/118. arXiv: 1510.06072 [astro-ph.GA].

Pearson, W. J. et al. (July 2018). “Main sequence of star forming galaxies beyond the Herschel confusion limit”. In: *A&A* 615, A146, A146. DOI: 10.1051/0004-6361/201832821. arXiv: 1804.03482 [astro-ph.GA].

Man, Allison and Sirio Belli (Sept. 2018). “Star formation quenching in massive galaxies”. In: *Nature Astronomy* 2, pp. 695–697. DOI: 10.1038/s41550-018-0558-1. arXiv: 1809.00722 [astro-ph.GA].

Feldmann, Robert and Lucio Mayer (Jan. 2015). “The Argo simulation - I. Quenching of massive galaxies at high redshift as a result of cosmological starvation”. In: *MNRAS* 446.2, pp. 1939–1956. DOI: 10.1093/mnras/stu2207. arXiv: 1404.3212 [astro-ph.GA].

Birnboim, Yuval and Avishai Dekel (Oct. 2003). “Virial shocks in galactic haloes?” In: *MNRAS* 345.1, pp. 349–364. DOI: 10.1046/j.1365-8711.2003.06955.x. arXiv: astro-ph/0302161 [astro-ph].

Dekel, Avishai and Yuval Birnboim (May 2006). “Galaxy bimodality due to cold flows and shock heating”. In: *MNRAS* 368.1, pp. 2–20. DOI: 10.1111/j.1365-2966.2006.10145.x. arXiv: astro-ph/0412300 [astro-ph].

Martig, Marie et al. (Dec. 2009). “Morphological Quenching of Star Formation: Making Early-Type Galaxies Red”. In: *ApJ* 707.1, pp. 250–267. DOI: 10.1088/0004-637X/707/1/250. arXiv: 0905.4669 [astro-ph.CO].

Khoperskov, S. et al. (Jan. 2018). “Bar quenching in gas-rich galaxies”. In: *A&A* 609, A60, A60. DOI: 10.1051/0004-6361/201731211. arXiv: 1709.03604 [astro-ph.GA].

Hubble, E. P. (Dec. 1926). “Extragalactic nebulae.” In: *ApJ* 64, pp. 321–369. DOI: 10.1086/143018.

Sandage, Allan, Kenneth C. Freeman, and N. R. Stokes (June 1970). “The Intrinsic Flattening of e, so, and Spiral Galaxies as Related to Galaxy Formation and Evolution”. In: *ApJ* 160, p. 831. DOI: 10.1086/150475.

de Vaucouleurs, Gerard (Jan. 1948). “Recherches sur les Nebuleuses Extragalactiques”. In: *Annales d’Astrophysique* 11, p. 247.

Sérsic, J. L. (Jan. 1963). “Influence of the atmospheric and instrumental dispersion on the brightness distribution in a galaxy”. In: *Boletin de la Asociacion Argentina de Astronomia La Plata Argentina* 6, p. 41.

— (1968). *Atlas de Galaxias Australes.*

Longair, Malcolm S. (2008). *Galaxy Formation.*

Loewenstein, Michael (Jan. 2004). “Chemical Composition of the Intracluster Medium”. In: *Origin and Evolution of the Elements*. Ed. by Andrew McWilliam and Michael Rauch, p. 422. arXiv: astro-ph/0310557 [astro-ph].

Sunyaev, R. A. and Ya. B. Zeldovich (Nov. 1972). “The Observations of Relic Radiation as a Test of the Nature of X-Ray Radiation from the Clusters of Galaxies”. In: *Comments on Astrophysics and Space Physics* 4, p. 173.

Hubble, Edwin and Milton L. Humason (July 1931). “The Velocity-Distance Relation among Extra-Galactic Nebulae”. In: *ApJ* 74, p. 43. DOI: 10.1086/143323.

Dressler, A. (Mar. 1980). “Galaxy morphology in rich clusters: implications for the formation and evolution of galaxies.” In: *ApJ* 236, pp. 351–365. DOI: 10.1086/157753.

Baldry, I. K. et al. (Dec. 2006). “Galaxy bimodality versus stellar mass and environment”. In: *MNRAS* 373.2, pp. 469–483. DOI: 10.1111/j.1365-2966.2006.11081.x. arXiv: astro-ph/0607648 [astro-ph].

Peng, Ying-jie et al. (Sept. 2010b). "Mass and Environment as Drivers of Galaxy Evolution in SDSS and zCOSMOS and the Origin of the Schechter Function". In: *ApJ* 721.1, pp. 193–221. DOI: 10.1088/0004-637X/721/1/193. arXiv: 1003.4747 [astro-ph.CO].

White, S. D. M. (July 1978). "Simulations of merging galaxies." In: *MNRAS* 184, pp. 185–203. DOI: 10.1093/mnras/184.2.185.

van der Wel, Arjen et al. (Nov. 2009a). "Major Merging: The Way to Make a Massive, Passive Galaxy". In: *ApJ* 706.1, pp. L120–L123. DOI: 10.1088/0004-637X/706/1/L120. arXiv: 0910.4018 [astro-ph.CO].

Khochfar, Sadegh and Joseph Silk (Sept. 2006). "A Simple Model for the Size Evolution of Elliptical Galaxies". In: *ApJ* 648.1, pp. L21–L24. DOI: 10.1086/507768. arXiv: astro-ph/0605436 [astro-ph].

Bell, Eric F. et al. (Mar. 2006). "Dry Mergers in GEMS: The Dynamical Evolution of Massive Early-Type Galaxies". In: *ApJ* 640.1, pp. 241–251. DOI: 10.1086/499931. arXiv: astro-ph/0506425 [astro-ph].

Naab, Thorsten, Sadegh Khochfar, and Andreas Burkert (Jan. 2006). "Properties of Early-Type, Dry Galaxy Mergers and the Origin of Massive Elliptical Galaxies". In: *ApJ* 636.2, pp. L81–L84. DOI: 10.1086/500205. arXiv: astro-ph/0509667 [astro-ph].

Mihos, J. Christopher and Lars Hernquist (June 1996). "Gasdynamics and Starbursts in Major Mergers". In: *ApJ* 464, p. 641. DOI: 10.1086/177353. arXiv: astro-ph/9512099 [astro-ph].

Draine, Bruce T. (2011). *Physics of the Interstellar and Intergalactic Medium.*

Salim, Samir and Desika Narayanan (Aug. 2020). "The Dust Attenuation Law in Galaxies". In: *ARA&A* 58, pp. 529–575. DOI: 10.1146/annurev-astro-032620-021933. arXiv: 2001.03181 [astro-ph.GA].

Bruzual, G. and S. Charlot (Oct. 2003). "Stellar population synthesis at the resolution of 2003". In: *MNRAS* 344.4, pp. 1000–1028. DOI: 10.1046/j.1365-8711.2003.06897.x. arXiv: astro-ph/0309134 [astro-ph].

Oke, J. B. (Feb. 1974). "Absolute Spectral Energy Distributions for White Dwarfs". In: *ApJS* 27, p. 21. DOI: 10.1086/190287.

Salpeter, Edwin E. (Jan. 1955). "The Luminosity Function and Stellar Evolution." In: *ApJ* 121, p. 161. DOI: 10.1086/145971.

Kroupa, Pavel (Apr. 2001). "On the variation of the initial mass function". In: *MNRAS* 322.2, pp. 231–246. DOI: 10.1046/j.1365-8711.2001.04022.x. arXiv: astro-ph/0009005 [astro-ph].

Chabrier, Gilles (July 2003). "Galactic Stellar and Substellar Initial Mass Function". In: *PASP* 115.809, pp. 763–795. DOI: 10.1086/376392. arXiv: astro-ph/0304382 [astro-ph].

Lejeune, T., F. Cuisinier, and R. Buser (Oct. 1997). "Standard stellar library for evolutionary synthesis. I. Calibration of theoretical spectra". In: *A&AS* 125, pp. 229–246. DOI: 10.1051/aas:1997373. arXiv: astro-ph/9701019 [astro-ph].

— (May 1998). "A standard stellar library for evolutionary synthesis. II. The M dwarf extension". In: *A&AS* 130, pp. 65–75. DOI: 10.1051/aas:1998405. arXiv: astro-ph/9710350 [astro-ph].

Girardi, L. et al. (Feb. 2000). "Evolutionary tracks and isochrones for low- and intermediate-mass stars: From 0.15 to 7 $M_\odot$, and from $Z = 0.0004$ to 0.03". In: *A&AS* 141, pp. 371–383. DOI: 10.1051/aas:2000126. arXiv: astro-ph/9910164 [astro-ph].

Tinsley, B. M. (Jan. 1980). “Evolution of the Stars and Gas in Galaxies”. In: *Fundamentals Cosmic Phys.* 5, pp. 287–388. DOI: 10.48550/arXiv.2203.02041. arXiv: 2203.02041 [astro-ph.GA].

Helou, George (Dec. 1986). “The IRAS Colors of Normal Galaxies”. In: *ApJ* 311, p. L33. DOI: 10.1086/184793.

Kennicutt Robert C., Jr. (Jan. 1998). “Star Formation in Galaxies Along the Hubble Sequence”. In: *ARA&A* 36, pp. 189–232. DOI: 10.1146/annurev.astro.36.1.189. arXiv: astro-ph/9807187 [astro-ph].

Kauffmann, Guinevere et al. (May 2003). “The dependence of star formation history and internal structure on stellar mass for 10^5 low-redshift galaxies”. In: *MNRAS* 341.1, pp. 54–69. DOI: 10.1046/j.1365-8711.2003.06292.x. arXiv: astro-ph/0205070 [astro-ph].

Daddi, E. et al. (Dec. 2004). “A New Photometric Technique for the Joint Selection of Star-forming and Passive Galaxies at $1.4 \lesssim z \lesssim 2.5$”. In: *ApJ* 617.2, pp. 746–764. DOI: 10.1086/425569. arXiv: astro-ph/0409041 [astro-ph].

Williams, Rik J. et al. (Feb. 2009). “Detection of Quiescent Galaxies in a Bicolor Sequence from $z = 0 - 2$”. In: *ApJ* 691.2, pp. 1879–1895. DOI: 10.1088/0004-637X/691/2/1879. arXiv: 0806.0625 [astro-ph].

Ilbert, O. et al. (Aug. 2013). “Mass assembly in quiescent and star-forming galaxies since $z \sim 4$ from UltraVISTA”. In: *A&A* 556, A55, A55. DOI: 10.1051/0004-6361/201321100. arXiv: 1301.3157 [astro-ph.CO].

Genel, Shy et al. (Nov. 2014). “Introducing the Illustris project: the evolution of galaxy populations across cosmic time”. In: *MNRAS* 445.1, pp. 175–200. DOI: 10.1093/mnras/stu1654. arXiv: 1405.3749 [astro-ph.CO].

Dehnen, Walter (June 2001). “Towards optimal softening in three-dimensional N-body codes - I. Minimizing the force error”. In: *MNRAS* 324.2, pp. 273–291. DOI: 10.1046/j.1365-8711.2001.04237.x. arXiv: astro-ph/0011568 [astro-ph].

Barnes, Josh and Piet Hut (Dec. 1986). “A hierarchical O(N log N) force-calculation algorithm”. In: *Nature* 324.6096, pp. 446–449. DOI: 10.1038/324446a0.

Klypin, Anatoly and Jon Holtzman (Dec. 1997). “Particle-Mesh code for cosmological simulations”. In: *arXiv e-prints*, astro-ph/9712217, astro–ph/9712217. arXiv: astro-ph/9712217 [astro-ph].

Dale, James E. (Oct. 2015). “The modelling of feedback in star formation simulations”. In: *New Astron. Rev.* 68, pp. 1–33. DOI: 10.1016/j.newar.2015.06.001. arXiv: 1508.06054 [astro-ph.GA].

Neistein, Eyal et al. (Apr. 2012). “Hydrodynamical simulations and semi-analytic models of galaxy formation: two sides of the same coin”. In: *MNRAS* 421.4, pp. 3579–3593. DOI: 10.1111/j.1365-2966.2012.20584.x. arXiv: 1109.4635 [astro-ph.CO].

Hou, Jun, Cedric G. Lacey, and Carlos S. Frenk (June 2019). “A comparison between semi-analytical gas cooling models and cosmological hydrodynamical simulations”. In: *MNRAS* 486.2, pp. 1691–1717. DOI: 10.1093/mnras/stz730. arXiv: 1803.01923 [astro-ph.GA].

Springel, Volker (Dec. 2005). “The cosmological simulation code GADGET-2”. In: *MNRAS* 364.4, pp. 1105–1134. DOI: 10.1111/j.1365-2966.2005.09655.x. arXiv: astro-ph/0505010 [astro-ph].

— (Jan. 2010). “E pur si muove: Galilean-invariant cosmological hydrodynamical simulations on a moving mesh”. In: *MNRAS* 401.2, pp. 791–851. DOI: 10.1111/j.1365-2966.2009.15715.x. arXiv: 0901.4107 [astro-ph.CO].

Baldry, Ivan K. et al. (Jan. 2004). "Quantifying the Bimodal Color-Magnitude Distribution of Galaxies". In: *ApJ* 600.2, pp. 681–694. DOI: 10.1086/380092. arXiv: astro-ph/0309710 [astro-ph].

Muzzin, Adam et al. (Nov. 2013b). "The Evolution of the Stellar Mass Functions of Star-forming and Quiescent Galaxies to z = 4 from the COSMOS/UltraVISTA Survey". In: *ApJ* 777.1, 18, p. 18. DOI: 10.1088/0004-637X/777/1/18. arXiv: 1303.4409 [astro-ph.CO].

Glazebrook, Karl et al. (Apr. 2017). "A massive, quiescent galaxy at a redshift of 3.717". In: *Nature* 544.7648, pp. 71–74. DOI: 10.1038/nature21680. arXiv: 1702.01751 [astro-ph.GA].

Oesch, P. A. et al. (Mar. 2016). "A Remarkably Luminous Galaxy at z=11.1 Measured with Hubble Space Telescope Grism Spectroscopy". In: *ApJ* 819.2, 129, p. 129. DOI: 10.3847/0004-637X/819/2/129. arXiv: 1603.00461 [astro-ph.GA].

van der Wel, A. et al. (June 2014). "3D-HST+CANDELS: The Evolution of the Galaxy Size-Mass Distribution since $z = 3$". In: *ApJ* 788.1, 28, p. 28. DOI: 10.1088/0004-637X/788/1/28. arXiv: 1404.2844 [astro-ph.GA].

Kubo, Mariko et al. (Nov. 2018). "The Rest-frame Optical Sizes of Massive Galaxies with Suppressed Star Formation at $z \sim 4$". In: *ApJ* 867.1, 1, p. 1. DOI: 10.3847/1538-4357/aae3e8. arXiv: 1810.00543 [astro-ph.GA].

Patel, Shannon G. et al. (Apr. 2017). "A Comparison of the Most Massive Quiescent Galaxies from $z \sim 3$ to the Present: Slow Evolution in Size, and spheroid-dominated". In: *ApJ* 839.2, 127, p. 127. DOI: 10.3847/1538-4357/aa6bf4. arXiv: 1704.01969 [astro-ph.GA].

Marsan, Z. Cemile et al. (Feb. 2019). "HST F160W Imaging of Very Massive Galaxies at $1.5 < z < 3.0$: Diversity of Structures and the Effect of Close Pairs on Number Density Estimates". In: *ApJ* 871.2, 201, p. 201. DOI: 10.3847/1538-4357/aaf808.

Cassata, P. et al. (Oct. 2013). "Constraining the Assembly of Normal and Compact Passively Evolving Galaxies from Redshift z = 3 to the Present with CANDELS". In: *ApJ* 775.2, 106, p. 106. DOI: 10.1088/0004-637X/775/2/106. arXiv: 1303.2689 [astro-ph.CO].

Carollo, C. M. et al. (Aug. 2013). "Newly Quenched Galaxies as the Cause for the Apparent Evolution in Average Size of the Population". In: *ApJ* 773.2, 112, p. 112. DOI: 10.1088/0004-637X/773/2/112. arXiv: 1302.5115 [astro-ph.CO].

Bell, Eric F. et al. (July 2012). "What Turns Galaxies Off? The Different Morphologies of Star-forming and Quiescent Galaxies since $z \sim 2$ from CANDELS". In: *ApJ* 753.2, 167, p. 167. DOI: 10.1088/0004-637X/753/2/167. arXiv: 1110.3786 [astro-ph.CO].

Mowla, Lamiya A. et al. (July 2019). "COSMOS-DASH: The Evolution of the Galaxy Size-Mass Relation since $z \sim 3$ from New Wide-field WFC3 Imaging Combined with CANDELS/3D-HST". In: *ApJ* 880.1, 57, p. 57. DOI: 10.3847/1538-4357/ab290a. arXiv: 1808.04379 [astro-ph.GA].

Esdaile, James et al. (Oct. 2020). "Confirmation of stellar masses and potential light IMF in massive quiescent galaxies at $3 < z < 4$ using velocity dispersions measurements with MOSFIRE". In: *arXiv e-prints*, arXiv:2010.09738, arXiv:2010.09738. arXiv: 2010.09738 [astro-ph.GA].

Stockton, Alan, Gabriela Canalizo, and Toshinori Maihara (Apr. 2004). "A Disk Galaxy of Old Stars at $z \sim 2.5$". In: *ApJ* 605.1, pp. 37–44. DOI: 10.1086/382235. arXiv: astro-ph/0312550 [astro-ph].

van Dokkum, Pieter G. et al. (Apr. 2008). "Confirmation of the Remarkable Compactness of Massive Quiescent Galaxies at $z \sim 2.3$: Early-Type Galaxies Did not Form in a Simple Monolithic Collapse". In: *ApJ* 677.1, p. L5. DOI: `10.1086/587874`. arXiv: `0802.4094 [astro-ph]`.

van der Wel, Arjen et al. (Mar. 2011). "The Majority of Compact Massive Galaxies at $z \sim 2$ are Disk Dominated". In: *ApJ* 730.1, 38, p. 38. DOI: `10.1088/0004-637X/730/1/38`. arXiv: `1101.2423 [astro-ph.CO]`.

Bezanson, Rachel et al. (May 2018). "Spatially Resolved Stellar Kinematics from LEGA-C: Increased Rotational Support in $z \sim 0.8$ Quiescent Galaxies". In: *ApJ* 858.1, 60, p. 60. DOI: `10.3847/1538-4357/aabc55`. arXiv: `1804.02402 [astro-ph.GA]`.

Hill, Allison R. et al. (Jan. 2019). "High-redshift Massive Quiescent Galaxies Are as Flat as Star-forming Galaxies: The Flattening of Galaxies and the Correlation with Structural Properties in CANDELS/3D-HST". In: *ApJ* 871.1, 76, p. 76. DOI: `10.3847/1538-4357/aaf50a`. arXiv: `1901.02009 [astro-ph.GA]`.

Shen, Shiyin et al. (Aug. 2003). "The size distribution of galaxies in the Sloan Digital Sky Survey". In: *MNRAS* 343.3, pp. 978–994. DOI: `10.1046/j.1365-8711.2003.06740.x`. arXiv: `astro-ph/0301527 [astro-ph]`.

Guo, Yicheng et al. (Sept. 2009). "Structural properties of central galaxies in groups and clusters". In: *MNRAS* 398.3, pp. 1129–1149. DOI: `10.1111/j.1365-2966.2009.15223.x`. arXiv: `0901.1150 [astro-ph.CO]`.

Holden, Bradford P. et al. (Apr. 2012). "A Constant Limiting Mass Scale for Flat Early-type Galaxies from $z \sim 1$ to $z = 0$: Density Evolves but Shapes Do Not". In: *ApJ* 749.2, 96, p. 96. DOI: `10.1088/0004-637X/749/2/96`. arXiv: `1108.6086 [astro-ph.CO]`.

Emsellem, Eric et al. (June 2011). "The ATLAS^{3D} project - III. A census of the stellar angular momentum within the effective radius of early-type galaxies: unveiling the distribution of fast and slow rotators". In: *MNRAS* 414.2, pp. 888–912. DOI: `10.1111/j.1365-2966.2011.18496.x`. arXiv: `1102.4444 [astro-ph.CO]`.

Cappellari, Michele (Sept. 2016). "Structure and Kinematics of Early-Type Galaxies from Integral Field Spectroscopy". In: *ARA&A* 54, pp. 597–665. DOI: `10.1146/annurev-astro-082214-122432`. arXiv: `1602.04267 [astro-ph.GA]`.

Stockton, Alan et al. (Jan. 2008). "Morphologies of Two Massive Old Galaxies at $z \sim 2.5$". In: *ApJ* 672.1, pp. 146–152. DOI: `10.1086/523789`. arXiv: `0710.0426 [astro-ph]`.

McGrath, Elizabeth J. et al. (July 2008). "Morphologies and Color Gradients of Luminous Evolved Galaxies at $z \sim 1.5$". In: *ApJ* 682.1, pp. 303–318. DOI: `10.1086/589631`. arXiv: `0707.1050 [astro-ph]`.

Bundy, Kevin et al. (Aug. 2010). "The Rise and Fall of Passive Disk Galaxies: Morphological Evolution Along the Red Sequence Revealed by COSMOS". In: *ApJ* 719.2, pp. 1969–1983. DOI: `10.1088/0004-637X/719/2/1969`. arXiv: `0912.1077 [astro-ph.CO]`.

Chang, Yu-Yen et al. (Aug. 2013). "Structural Evolution of Early-type Galaxies to z = 2.5 in CANDELS". In: *ApJ* 773.2, 149, p. 149. DOI: `10.1088/0004-637X/773/2/149`. arXiv: `1305.6931 [astro-ph.CO]`.

McLure, R. J. et al. (Jan. 2013). "The sizes, masses and specific star formation rates of massive galaxies at $1.3 < z < 1.5$: strong evidence in favour of evolution via minor mergers". In: *MNRAS* 428.2, pp. 1088–1106. DOI: `10.1093/mnras/sts092`. arXiv: `1205.4058 [astro-ph.CO]`.

Hsu, Li-Yen, Alan Stockton, and Hsin-Yi Shih (Dec. 2014). “Compact Quiescent Galaxies at Intermediate Redshifts”. In: *ApJ* 796.2, 92, p. 92. DOI: 10.1088/0004-637X/796/2/92. arXiv: 1401.7813 [astro-ph.GA].

Newman, Andrew B., Sirio Belli, and Richard S. Ellis (Nov. 2015). “Discovery of a Strongly Lensed Massive Quiescent Galaxy at z = 2.636: Spatially Resolved Spectroscopy and Indications of Rotation”. In: *ApJ* 813.1, L7, p. L7. DOI: 10.1088/2041-8205/813/1/L7. arXiv: 1509.04345 [astro-ph.GA].

Newman, Andrew B. et al. (Aug. 2018). “Resolving Quiescent Galaxies at $z \gtrsim 2$. II. Direct Measures of Rotational Support”. In: *ApJ* 862.2, 126, p. 126. DOI: 10.3847/1538-4357/aacd4f. arXiv: 1806.06815 [astro-ph.GA].

Toft, Sune et al. (June 2017). “A massive, dead disk galaxy in the early Universe”. In: *Nature* 546.7659, pp. 510–513. DOI: 10.1038/nature22388. arXiv: 1706.07030 [astro-ph.GA].

Lang, Philipp et al. (June 2014). “Bulge Growth and Quenching since z = 2.5 in CANDELS/3D-HST”. In: *ApJ* 788.1, 11, p. 11. DOI: 10.1088/0004-637X/788/1/11. arXiv: 1402.0866 [astro-ph.GA].

Tacchella, S. et al. (Apr. 2015). “Evidence for mature bulges and an inside-out quenching phase 3 billion years after the Big Bang”. In: *Science* 348.6232, pp. 314–317. DOI: 10.1126/science.1261094. arXiv: 1504.04021 [astro-ph.GA].

Brinchmann, J. et al. (July 2004). “The physical properties of star-forming galaxies in the low-redshift Universe”. In: *MNRAS* 351.4, pp. 1151–1179. DOI: 10.1111/j.1365-2966.2004.07881.x. arXiv: astro-ph/0311060 [astro-ph].

Franx, Marijn et al. (Dec. 2008). “Structure and Star Formation in Galaxies out to $z = 3$: Evidence for Surface Density Dependent Evolution and Upsizing”. In: *ApJ* 688.2, pp. 770–788. DOI: 10.1086/592431. arXiv: 0808.2642 [astro-ph].

van Dokkum, Pieter G. et al. (Nov. 2015). “Forming Compact Massive Galaxies”. In: *ApJ* 813.1, 23, p. 23. DOI: 10.1088/0004-637X/813/1/23. arXiv: 1506.03085 [astro-ph.GA].

Whitaker, Katherine E. et al. (Mar. 2017). “Predicting Quiescence: The Dependence of Specific Star Formation Rate on Galaxy Size and Central Density at $0.5 < z < 2.5$”. In: *ApJ* 838.1, 19, p. 19. DOI: 10.3847/1538-4357/aa6258. arXiv: 1607.03107 [astro-ph.GA].

Lilly, Simon J. and C. Marcella Carollo (Dec. 2016). “Surface Density Effects in Quenching: Cause or Effect?” In: *ApJ* 833.1, 1, p. 1. DOI: 10.3847/0004-637X/833/1/1. arXiv: 1604.06459 [astro-ph.GA].

Kereš, Dušan et al. (Oct. 2005a). “How do galaxies get their gas?” In: *MNRAS* 363.1, pp. 2–28. DOI: 10.1111/j.1365-2966.2005.09451.x. arXiv: astro-ph/0407095 [astro-ph].

Dekel, A. et al. (Jan. 2009). “Cold streams in early massive hot haloes as the main mode of galaxy formation”. In: *Nature* 457.7228, pp. 451–454. DOI: 10.1038/nature07648. arXiv: 0808.0553 [astro-ph].

Dekel, Avishai, Re’em Sari, and Daniel Ceverino (Sept. 2009). “Formation of Massive Galaxies at High Redshift: Cold Streams, Clumpy Disks, and Compact Spheroids”. In: *ApJ* 703.1, pp. 785–801. DOI: 10.1088/0004-637X/703/1/785. arXiv: 0901.2458 [astro-ph.GA].

Burkert, A. et al. (Dec. 2010). “High-redshift Star-forming Galaxies: Angular Momentum and Baryon Fraction, Turbulent Pressure Effects, and the Origin of Turbulence”. In: *ApJ* 725.2, pp. 2324–2332. DOI: 10.1088/0004-637X/725/2/2324. arXiv: 0907.4777 [astro-ph.CO].

Dekel, A. et al. (Oct. 2013). "Toy models for galaxy formation versus simulations". In: *MNRAS* 435.2, pp. 999–1019. DOI: 10.1093/mnras/stt1338. arXiv: 1303.3009 [astro-ph.CO].

Dekel, A. and A. Burkert (Feb. 2014). "Wet disc contraction to galactic blue nuggets and quenching to red nuggets". In: *MNRAS* 438.2, pp. 1870–1879. DOI: 10.1093/mnras/stt2331. arXiv: 1310.1074 [astro-ph.CO].

Zolotov, Adi et al. (July 2015). "Compaction and quenching of high-z galaxies in cosmological simulations: blue and red nuggets". In: *MNRAS* 450.3, pp. 2327–2353. DOI: 10.1093/mnras/stv740. arXiv: 1412.4783 [astro-ph.GA].

Gómez-Guijarro, C. et al. (Dec. 2019). "Compact Star-forming Galaxies as Old Starbursts Becoming Quiescent". In: *ApJ* 886.2, 88, p. 88. DOI: 10.3847/1538-4357/ab418b. arXiv: 1909.02572 [astro-ph.GA].

Wu, Po-Feng et al. (Jan. 2020). "The Colors and Sizes of Recently Quenched Galaxies: A Result of Compact Starburst before Quenching". In: *ApJ* 888.2, 77, p. 77. DOI: 10.3847/1538-4357/ab5fd9. arXiv: 1912.03683 [astro-ph.GA].

Dekel, Avishai and Yuval Birnboim (Jan. 2008). "Gravitational quenching in massive galaxies and clusters by clumpy accretion". In: *MNRAS* 383.1, pp. 119–138. DOI: 10.1111/j.1365-2966.2007.12569.x. arXiv: 0707.1214 [astro-ph].

Khochfar, Sadegh and Jeremiah P. Ostriker (June 2008). "Adding Environmental Gas Physics to the Semianalytic Method for Galaxy Formation: Gravitational Heating". In: *ApJ* 680.1, pp. 54–69. DOI: 10.1086/587470. arXiv: 0704.2418 [astro-ph].

Tacchella, Sandro et al. (May 2016a). "Evolution of density profiles in high-z galaxies: compaction and quenching inside-out". In: *MNRAS* 458.1, pp. 242–263. DOI: 10.1093/mnras/stw303. arXiv: 1509.00017 [astro-ph.GA].

Renzini, Alvio et al. (Aug. 2018). "The WFC3 Galactic Bulge Treasury Program: Relative Ages of Bulge Stars of High and Low Metallicity". In: *ApJ* 863.1, 16, p. 16. DOI: 10.3847/1538-4357/aad09b. arXiv: 1806.11556 [astro-ph.GA].

Daddi, E. et al. (June 2005). "Passively Evolving Early-Type Galaxies at $1.4 \lesssim z \lesssim 2.5$ in the Hubble Ultra Deep Field". In: *ApJ* 626.2, pp. 680–697. DOI: 10.1086/430104. arXiv: astro-ph/0503102 [astro-ph].

Trujillo, I. et al. (Nov. 2006). "Extremely compact massive galaxies at $z \sim 1.4$". In: *MNRAS* 373.1, pp. L36–L40. DOI: 10.1111/j.1745-3933.2006.00238.x. arXiv: astro-ph/0608657 [astro-ph].

Toft, S. et al. (Dec. 2007). "Hubble Space Telescope and Spitzer Imaging of Red and Blue Galaxies at $z \sim 2.5$: A Correlation between Size and Star Formation Activity from Compact Quiescent Galaxies to Extended Star-forming Galaxies". In: *ApJ* 671.1, pp. 285–302. DOI: 10.1086/521810. arXiv: 0707.4484 [astro-ph].

Cimatti, A. et al. (Apr. 2008). "GMASS ultradeep spectroscopy of galaxies at $z \sim 2$. II. Superdense passive galaxies: how did they form and evolve?" In: *A&A* 482.1, pp. 21–42. DOI: 10.1051/0004-6361:20078739. arXiv: 0801.1184 [astro-ph].

Cimatti, A., C. Nipoti, and P. Cassata (May 2012). "Fast evolving size of early-type galaxies at $z > 2$ and the role of dissipationless (dry) merging". In: *MNRAS* 422.1, pp. L62–L66. DOI: 10.1111/j.1745-3933.2012.01237.x. arXiv: 1202.5403 [astro-ph.CO].

Grogin, Norman A. et al. (Dec. 2011). "CANDELS: The Cosmic Assembly Near-infrared Deep Extragalactic Legacy Survey". In: *ApJS* 197.2, 35, p. 35. DOI: 10.1088/0067-0049/197/2/35. arXiv: 1105.3753 [astro-ph.CO].

Koekemoer, Anton M. et al. (Dec. 2011). "CANDELS: The Cosmic Assembly Near-infrared Deep Extragalactic Legacy Survey—The Hubble Space Telescope Observations, Imaging Data Products, and Mosaics". In: *ApJS* 197.2, 36, p. 36. DOI: 10.1088/0067-0049/197/2/36. arXiv: 1105.3754 [astro-ph.CO].

Momcheva, Ivelina G. et al. (Aug. 2016). "The 3D-HST Survey: Hubble Space Telescope WFC3/G141 Grism Spectra, Redshifts, and Emission Line Measurements for $\sim 100\,000$ Galaxies". In: *ApJS* 225.2, 27, p. 27. DOI: 10.3847/0067-0049/225/2/27. arXiv: 1510.02106 [astro-ph.GA].

Straatman, Caroline M. S. et al. (July 2015). "The Sizes of Massive Quiescent and Star-forming Galaxies at $z \sim 4$ with ZFOURGE and CANDELS". In: *ApJ* 808.1, L29, p. L29. DOI: 10.1088/2041-8205/808/1/L29. arXiv: 1506.01380 [astro-ph.GA].

Lin, Lihwai et al. (May 2007). "AEGIS: Enhancement of Dust-enshrouded Star Formation in Close Galaxy Pairs and Merging Galaxies up to $z \sim 1$". In: *ApJ* 660.1, pp. L51–L54. DOI: 10.1086/517919. arXiv: astro-ph/0607272 [astro-ph].

Lin, Lihwai et al. (July 2008). "The Redshift Evolution of Wet, Dry, and Mixed Galaxy Mergers from Close Galaxy Pairs in the DEEP2 Galaxy Redshift Survey". In: *ApJ* 681.1, pp. 232–243. DOI: 10.1086/587928. arXiv: 0802.3004 [astro-ph].

Perez, Josefa, Leo Michel-Dansac, and Patricia B. Tissera (Oct. 2011). "Chemical evolution during gas-rich galaxy interactions". In: *MNRAS* 417.1, pp. 580–590. DOI: 10.1111/j.1365-2966.2011.19300.x. arXiv: 1106.4556 [astro-ph.CO].

Athanassoula, E. et al. (Apr. 2016). "Forming Disk Galaxies in Wet Major Mergers. I. Three Fiducial Examples". In: *ApJ* 821.2, 90, p. 90. DOI: 10.3847/0004-637X/821/2/90. arXiv: 1602.03189 [astro-ph.GA].

Naab, Thorsten, Peter H. Johansson, and Jeremiah P. Ostriker (July 2009). "Minor Mergers and the Size Evolution of Elliptical Galaxies". In: *ApJ* 699.2, pp. L178–L182. DOI: 10.1088/0004-637X/699/2/L178. arXiv: 0903.1636 [astro-ph.CO].

Bezanson, Rachel et al. (June 2009). "The Relation Between Compact, Quiescent High-redshift Galaxies and Massive Nearby Elliptical Galaxies: Evidence for Hierarchical, Inside-Out Growth". In: *ApJ* 697.2, pp. 1290–1298. DOI: 10.1088/0004-637X/697/2/1290. arXiv: 0903.2044 [astro-ph.CO].

Oser, Ludwig et al. (Dec. 2010). "The Two Phases of Galaxy Formation". In: *ApJ* 725.2, pp. 2312–2323. DOI: 10.1088/0004-637X/725/2/2312. arXiv: 1010.1381 [astro-ph.CO].

Oser, Ludwig et al. (Jan. 2012). "The Cosmological Size and Velocity Dispersion Evolution of Massive Early-type Galaxies". In: *ApJ* 744.1, 63, p. 63. DOI: 10.1088/0004-637X/744/1/63. arXiv: 1106.5490 [astro-ph.CO].

Trujillo, Ignacio, Ignacio Ferreras, and Ignacio G. de La Rosa (Aug. 2011). "Dissecting the size evolution of elliptical galaxies since $z \sim 1$: puffing-up versus minor-merging scenarios". In: *MNRAS* 415.4, pp. 3903–3913. DOI: 10.1111/j.1365-2966.2011.19017.x. arXiv: 1102.3398 [astro-ph.CO].

Bédorf, J. and S. Portegies Zwart (May 2013). "The effect of many minor mergers on the size growth of compact quiescent galaxies". In: *MNRAS* 431.1, pp. 767–780. DOI: 10.1093/mnras/stt208. arXiv: 1301.6784 [astro-ph.GA].

van Dokkum, P. G. and M. Franx (Aug. 1996). "The Fundamental Plane in CL 0024 at z = 0.4: implications for the evolution of the mass-to-light ratio." In: *MNRAS* 281.3, pp. 985–1000. DOI: 10.1093/mnras/281.3.985. arXiv: astro-ph/9603063 [astro-ph].

van Dokkum, Pieter G. and Marijn Franx (May 2001). "Morphological Evolution and the Ages of Early-Type Galaxies in Clusters". In: *ApJ* 553.1, pp. 90–102. DOI: 10.1086/320645. arXiv: astro-ph/0501236 [astro-ph].

Poggianti, B. M. et al. (Jan. 2013). "Superdense Galaxies and the Mass-Size Relation at Low Redshift". In: *ApJ* 762.2, 77, p. 77. DOI: 10.1088/0004-637X/762/2/77. arXiv: 1211.1005 [astro-ph.CO].

Belli, Sirio, Andrew B. Newman, and Richard S. Ellis (Mar. 2014). "Velocity Dispersions and Dynamical Masses for a Large Sample of Quiescent Galaxies at $z > 1$: Improved Measures of the Growth in Mass and Size". In: *ApJ* 783.2, 117, p. 117. DOI: 10.1088/0004-637X/783/2/117. arXiv: 1311.3317 [astro-ph.CO].

Stockmann, Mikkel et al. (Jan. 2020). "X-shooter Spectroscopy and HST Imaging of 15 Massive Quiescent Galaxies at $z \gtrsim 2$". In: *ApJ* 888.1, 4, p. 4. DOI: 10.3847/1538-4357/ab5af4. arXiv: 1912.01619 [astro-ph.GA].

van der Wel, Arjen et al. (June 2009b). "On the Size and Comoving Mass Density Evolution of Early-Type Galaxies". In: *ApJ* 698.2, pp. 1232–1243. DOI: 10.1088/0004-637X/698/2/1232. arXiv: 0903.4857 [astro-ph.CO].

Bezanson, Rachel, Pieter van Dokkum, and Marijn Franx (Nov. 2012). "Evolution of Quiescent and Star-forming Galaxies since $z \sim 1.5$ as a Function of their Velocity Dispersions". In: *ApJ* 760.1, 62, p. 62. DOI: 10.1088/0004-637X/760/1/62. arXiv: 1210.0009 [astro-ph.CO].

Suess, Katherine A. et al. (June 2019a). "Half-mass Radii for ~ 7000 Galaxies at $1.0 \leq z \leq 2.5$: Most of the Evolution in the Mass-Size Relation Is Due to Color Gradients". In: *ApJ* 877.2, 103, p. 103. DOI: 10.3847/1538-4357/ab1bda. arXiv: 1904.10992 [astro-ph.GA].

— (Nov. 2019b). "Half-mass Radii of Quiescent and Star-forming Galaxies Evolve Slowly from $0 \lesssim z \leq 2.5$: Implications for Galaxy Assembly Histories". In: *ApJ* 885.1, L22, p. L22. DOI: 10.3847/2041-8213/ab4db3. arXiv: 1910.06984 [astro-ph.GA].

Labbé, Ivo et al. (May 2005). "IRAC Mid-Infrared Imaging of the Hubble Deep Field-South: Star Formation Histories and Stellar Masses of Red Galaxies at $z > 2$". In: *ApJ* 624.2, pp. L81–L84. DOI: 10.1086/430700. arXiv: astro-ph/0504219 [astro-ph].

Ilbert, O. et al. (Feb. 2010). "Galaxy Stellar Mass Assembly Between $0.2 < z < 2$ from the S-COSMOS Survey". In: *ApJ* 709.2, pp. 644–663. DOI: 10.1088/0004-637X/709/2/644. arXiv: 0903.0102 [astro-ph.CO].

Whitaker, Katherine E. et al. (Aug. 2010a). "The Age Spread of Quiescent Galaxies with the NEWFIRM Medium-band Survey: Identification of the Oldest Galaxies Out to $z \sim 2$". In: *ApJ* 719.2, pp. 1715–1732. DOI: 10.1088/0004-637X/719/2/1715. arXiv: 1006.5453 [astro-ph.CO].

Marchesini, Danilo et al. (Dec. 2010). "The Most Massive Galaxies at $3.0 \leq z < 4.0$ in the Newfirm Medium-band Survey: Properties and Improved Constraints on the Stellar Mass Function". In: *ApJ* 725.1, pp. 1277–1295. DOI: 10.1088/0004-637X/725/1/1277. arXiv: 1009.0269 [astro-ph.CO].

Brammer, Gabriel B. et al. (Sept. 2011a). "The Number Density and Mass Density of Star-forming and Quiescent Galaxies at $0.4 \leq z \leq 2.2$". In: *ApJ* 739.1, 24, p. 24. DOI: 10.1088/0004-637X/739/1/24. arXiv: 1104.2595 [astro-ph.CO].

Muzzin, Adam et al. (May 2013a). "A Public K_s -selected Catalog in the COSMOS/ULTRAVISTA Field: Photometry, Photometric Redshifts, and Stellar Population Parameters". In: *ApJS* 206.1, 8, p. 8. DOI: 10.1088/0067-0049/206/1/8. arXiv: 1303.4410 [astro-ph.CO].

Laigle, C. et al. (June 2016). "The COSMOS2015 Catalog: Exploring the $1 < z < 6$ Universe with Half a Million Galaxies". In: *ApJS* 224.2, 24, p. 24. DOI: 10.3847/0067-0049/224/2/24. arXiv: 1604.02350 [astro-ph.GA].

Glazebrook, Karl et al. (July 2004). "A high abundance of massive galaxies 3-6 billion years after the Big Bang". In: *Nature* 430.6996, pp. 181–184. DOI: 10.1038/nature02667. arXiv: astro-ph/0401037 [astro-ph].

Cimatti, A. et al. (July 2004). "Old galaxies in the young Universe". In: *Nature* 430.6996, pp. 184–187. DOI: 10.1038/nature02668. arXiv: astro-ph/0407131 [astro-ph].

Kriek, Mariska et al. (Oct. 2006). "Spectroscopic Identification of Massive Galaxies at $z \sim 2.3$ with Strongly Suppressed Star Formation". In: *ApJ* 649.2, pp. L71–L74. DOI: 10.1086/508371. arXiv: astro-ph/0608446 [astro-ph].

Gobat, R. et al. (Nov. 2012). "The Early Early Type: Discovery of a Passive Galaxy at $z_{\rm spec} \sim 3$". In: *ApJ* 759.2, L44, p. L44. DOI: 10.1088/2041-8205/759/2/L44. arXiv: 1210.4299 [astro-ph.CO].

Onodera, M. et al. (Aug. 2012). "Deep Near-infrared Spectroscopy of Passively Evolving Galaxies at $z \gtrsim 1.4$". In: *ApJ* 755.1, 26, p. 26. DOI: 10.1088/0004-637X/755/1/26. arXiv: 1206.1540 [astro-ph.CO].

Onodera, M. et al. (Aug. 2015). "The Ages, Metallicities, and Element Abundance Ratios of Massive Quenched Galaxies at $z \sim 1.6$". In: *ApJ* 808.2, 161, p. 161. DOI: 10.1088/0004-637X/808/2/161. arXiv: 1411.5023 [astro-ph.GA].

Marsan, Z. Cemile et al. (Mar. 2015). "Spectroscopic Confirmation of an Ultra Massive and Compact Galaxy at $z = 3.35$: a Detailed Look at an Early Progenitor of Local Giant Ellipticals". In: *ApJ* 801.2, 133, p. 133. DOI: 10.1088/0004-637X/801/2/133. arXiv: 1406.0002 [astro-ph.GA].

Hill, Allison. R. et al. (Mar. 2016). "A Stellar Velocity Dispersion for a Strongly-lensed, Intermediate-mass Quiescent Galaxy at $z = 2.8$". In: *ApJ* 819.1, 74, p. 74. DOI: 10.3847/0004-637X/819/1/74. arXiv: 1602.00007 [astro-ph.GA].

Marsan, Z. Cemile et al. (June 2017). "A Spectroscopic Follow-up Program of Very Massive Galaxies at $3 < z < 4$: Confirmation of Spectroscopic Redshifts, and a High Fraction of Powerful AGNs". In: *ApJ* 842.1, 21, p. 21. DOI: 10.3847/1538-4357/aa7206. arXiv: 1606.05350 [astro-ph.GA].

Gobat, R. et al. (Mar. 2017). "In and out star formation in $z \sim 1.5$ quiescent galaxies from rest-frame UV spectroscopy and the far-infrared". In: *A&A* 599, A95, A95. DOI: 10.1051/0004-6361/201629852. arXiv: 1612.06955 [astro-ph.GA].

Schreiber, C. et al. (Oct. 2018). "Near infrared spectroscopy and star-formation histories of $3 \leq z \leq 4$ quiescent galaxies". In: *A&A* 618, A85, A85. DOI: 10.1051/0004-6361/201833070. arXiv: 1807.02523 [astro-ph.GA].

Tanaka, Masayuki et al. (Nov. 2019). "Stellar Velocity Dispersion of a Massive Quenching Galaxy at z = 4.01". In: *ApJ* 885.2, L34, p. L34. DOI: 10.3847/2041-8213/ab4ff3. arXiv: 1909.10721 [astro-ph.GA].

Forrest, Ben et al. (Feb. 2020a). "An Extremely Massive Quiescent Galaxy at $z = 3.493$: Evidence of Insufficiently Rapid Quenching Mechanisms in Theoretical Models". In: *ApJ* 890.1, L1, p. L1. DOI: 10.3847/2041-8213/ab5b9f. arXiv: 1910.10158 [astro-ph.GA].

Forrest, Ben et al. (Nov. 2020b). "The Massive Ancient Galaxies at $z > 3$ NEar-infrared (MAGAZ3NE) Survey: Confirmation of Extremely Rapid Star Formation and Quenching Timescales for Massive Galaxies in the Early Universe". In: *ApJ* 903.1, 47, p. 47. DOI: `10.3847/1538-4357/abb819`. arXiv: `2009.07281 [astro-ph.GA]`.

Valentino, Francesco et al. (Feb. 2020). "Quiescent Galaxies 1.5 Billion Years after the Big Bang and Their Progenitors". In: *ApJ* 889.2, 93, p. 93. DOI: `10.3847/1538-4357/ab64dc`. arXiv: `1909.10540 [astro-ph.GA]`.

Belli, Sirio, Andrew B. Newman, and Richard S. Ellis (Jan. 2017). "MOSFIRE Spectroscopy of Quiescent Galaxies at $1.5 < z < 2.5$. I. Evolution of Structural and Dynamical Properties". In: *ApJ* 834.1, 18, p. 18. DOI: `10.3847/1538-4357/834/1/18`. arXiv: `1608.00608 [astro-ph.GA]`.

McCracken, H. J. et al. (Jan. 2010). "The COSMOS-WIRCam Near-Infrared Imaging Survey. I. BzK-Selected Passive and Star-Forming Galaxy Candidates at $z \gtrsim 1.4$". In: *ApJ* 708.1, pp. 202–217. DOI: `10.1088/0004-637X/708/1/202`. arXiv: `0910.2705 [astro-ph.CO]`.

Brammer, Gabriel B., Pieter G. van Dokkum, and Paolo Coppi (Oct. 2008). "EAZY: A Fast, Public Photometric Redshift Code". In: *ApJ* 686.2, pp. 1503–1513. DOI: `10.1086/591786`. arXiv: `0807.1533 [astro-ph]`.

Strazzullo, V. et al. (Apr. 2015a). "Passive galaxies as tracers of cluster environments at $z \sim 2$". In: *A&A* 576, L6, p. L6. DOI: `10.1051/0004-6361/201425038`. arXiv: `1501.05323 [astro-ph.CO]`.

Kriek, M. et al. (July 2009). "An Ultra-Deep Near-Infrared Spectrum of a Compact Quiescent Galaxy at $z = 2.2$". In: *ApJ* 700, pp. 221–231. DOI: `10.1088/0004-637X/700/1/221`. arXiv: `0905.1692 [astro-ph.CO]`.

Calzetti, Daniela (Dec. 2001). "The Dust Opacity of Star-forming Galaxies". In: *PASP* 113.790, pp. 1449–1485. DOI: `10.1086/324269`. arXiv: `astro-ph/0109035 [astro-ph]`.

Le Floc'h, Emeric et al. (Sept. 2009). "Deep Spitzer 24 µm COSMOS Imaging. I. The Evolution of Luminous Dusty Galaxies—Confronting the Models". In: *ApJ* 703.1, pp. 222–239. DOI: `10.1088/0004-637X/703/1/222`. arXiv: `0909.4303 [astro-ph.CO]`.

D'Eugenio, C. et al. (Mar. 2020). "The Typical Massive Quiescent Galaxy at $z \sim 3$ is a Post-starburst". In: *ApJ* 892.1, L2, p. L2. DOI: `10.3847/2041-8213/ab7a96`. arXiv: `2003.04342 [astro-ph.GA]`.

D'Eugenio, C. et al. (Sept. 2021). "HST grism spectroscopy of $z \sim 3$ massive quiescent galaxies. Approaching the metamorphosis". In: *A&A* 653, A32, A32. DOI: `10.1051/0004-6361/202040067`. arXiv: `2012.02767 [astro-ph.GA]`.

Maraston, C. et al. (Nov. 2006). "Evidence for TP-AGB Stars in High-Redshift Galaxies, and Their Effect on Deriving Stellar Population Parameters". In: *ApJ* 652.1, pp. 85–96. DOI: `10.1086/508143`. arXiv: `astro-ph/0604530 [astro-ph]`.

Longhetti, M. and P. Saracco (Apr. 2009). "Stellar mass estimates in early-type galaxies: procedures, uncertainties and models dependence". In: *MNRAS* 394.2, pp. 774–794. DOI: `10.1111/j.1365-2966.2008.14375.x`. arXiv: `0811.4041 [astro-ph]`.

Muzzin, Adam et al. (Nov. 2009). "How Massive are Massive Compact Galaxies?" In: *ApJ* 706.1, pp. L188–L191. DOI: `10.1088/0004-637X/706/1/L188`. arXiv: `0909.5182 [astro-ph.GA]`.

Conroy, Charlie (Aug. 2013). "Modeling the Panchromatic Spectral Energy Distributions of Galaxies". In: *ARA&A* 51.1, pp. 393–455. DOI: `10.1146/annurev-astro-082812-141017`. arXiv: `1301.7095 [astro-ph.CO]`.

Pacifici, Camilla et al. (Feb. 2015). "On the importance of using appropriate spectral models to derive physical properties of galaxies at $0.7 < z < 2.8$". In: *MNRAS* 447.1, pp. 786–805. DOI: 10.1093/mnras/stu2447. arXiv: 1411.5689 [astro-ph.GA].

Skelton, Rosalind E. et al. (Oct. 2014). "3D-HST WFC3-selected Photometric Catalogs in the Five CANDELS/3D-HST Fields: Photometry, Photometric Redshifts, and Stellar Masses". In: *ApJS* 214.2, 24, p. 24. DOI: 10.1088/0067-0049/214/2/24. arXiv: 1403.3689 [astro-ph.GA].

Saracco, P., M. Longhetti, and S. Andreon (Jan. 2009). "The population of early-type galaxies at $1 < z < 2$ - new clues on their formation and evolution". In: *MNRAS* 392.2, pp. 718–732. DOI: 10.1111/j.1365-2966.2008.14085.x. arXiv: 0810.2795 [astro-ph].

Belli, Sirio, Andrew B. Newman, and Richard S. Ellis (Feb. 2015). "Stellar Populations from Spectroscopy of a Large Sample of Quiescent Galaxies at $z > 1$: Measuring the Contribution of Progenitor Bias to Early Size Growth". In: *ApJ* 799.2, 206, p. 206. DOI: 10.1088/0004-637X/799/2/206. arXiv: 1409.7088 [astro-ph.GA].

Yano, Michael et al. (Feb. 2016). "The Relation between Galaxy Structure and Spectral Type: Implications for the Buildup of the Quiescent Galaxy Population at $0.5 < z < 2.0$". In: *ApJ* 817.2, L21, p. L21. DOI: 10.3847/2041-8205/817/2/L21. arXiv: 1601.02629 [astro-ph.GA].

Williams, Christina C. et al. (Apr. 2017). "Morphology Dependence of Stellar Age in Quenched Galaxies at Redshift ~ 1.2: Massive Compact Galaxies Are Older than More Extended Ones". In: *ApJ* 838.2, 94, p. 94. DOI: 10.3847/1538-4357/aa662f. arXiv: 1607.06089 [astro-ph.GA].

Zahid, H. Jabran and Margaret J. Geller (May 2017). "Velocity Dispersion, Size, Sérsic Index, and D $_n$4000: The Scaling of Stellar Mass with Dynamical Mass for Quiescent Galaxies". In: *ApJ* 841.1, 32, p. 32. DOI: 10.3847/1538-4357/aa7056. arXiv: 1701.01350 [astro-ph.GA].

Almaini, Omar et al. (Dec. 2017). "Massive post-starburst galaxies at $z > 1$ are compact proto-spheroids". In: *MNRAS* 472.2, pp. 1401–1412. DOI: 10.1093/mnras/stx1957. arXiv: 1708.00005 [astro-ph.GA].

Wu, Po-Feng et al. (Nov. 2018). "Fast and Slow Paths to Quiescence: Ages and Sizes of 400 Quiescent Galaxies from the LEGA-C Survey". In: *ApJ* 868.1, 37, p. 37. DOI: 10.3847/1538-4357/aae822. arXiv: 1809.01211 [astro-ph.GA].

Belli, Sirio, Andrew B. Newman, and Richard S. Ellis (Mar. 2019). "MOSFIRE Spectroscopy of Quiescent Galaxies at $1.5 < z < 2.5$. II. Star Formation Histories and Galaxy Quenching". In: *ApJ* 874.1, 17, p. 17. DOI: 10.3847/1538-4357/ab07af. arXiv: 1810.00008 [astro-ph.GA].

Whitaker, Katherine E. et al. (Feb. 2012a). "A Large Population of Massive Compact Post-starburst Galaxies at $z > 1$: Implications for the Size Evolution and Quenching Mechanism of Quiescent Galaxies". In: *ApJ* 745.2, 179, p. 179. DOI: 10.1088/0004-637X/745/2/179. arXiv: 1112.0313 [astro-ph.CO].

Marchesini, Danilo et al. (Oct. 2014). "The Progenitors of Local Ultra-massive Galaxies Across Cosmic Time: From Dusty Star-bursting to Quiescent Stellar Populations". In: *ApJ* 794.1, 65, p. 65. DOI: 10.1088/0004-637X/794/1/65. arXiv: 1402.0003 [astro-ph.GA].

Merlin, E. et al. (Jan. 2018). "Chasing passive galaxies in the early Universe: a critical analysis in CANDELS GOODS-South". In: *MNRAS* 473.2, pp. 2098–2123. DOI: 10.1093/mnras/stx2385. arXiv: 1709.00429 [astro-ph.GA].

Maltby, David T. et al. (Oct. 2018). "The structure of post-starburst galaxies at $0.5 < z < 2$: evidence for two distinct quenching routes at different epochs". In: *MNRAS* 480.1, pp. 381–401. DOI: 10.1093/mnras/sty1794. arXiv: 1807.01325 [astro-ph.GA].

Jin, Shuowen et al. (Sept. 2018). ""Super-deblended" Dust Emission in Galaxies. II. Far-IR to (Sub)millimeter Photometry and High-redshift Galaxy Candidates in the Full COSMOS Field". In: *ApJ* 864.1, 56, p. 56. DOI: 10.3847/1538-4357/aad4af. arXiv: 1807.04697 [astro-ph.GA].

Bertin, E. and S. Arnouts (June 1996). "SExtractor: Software for source extraction." In: *A&AS* 117, pp. 393–404. DOI: 10.1051/aas:1996164.

Bertin, E. et al. (2002). "The TERAPIX Pipeline". In: *Astronomical Data Analysis Software and Systems XI*. Ed. by D. A. Bohlender, D. Durand, and T. H. Handley. Vol. 281. Astronomical Society of the Pacific Conference Series, p. 228.

Brammer, Gabe (Jan. 2018). *Gbrammer/Grizli: Preliminary Release*. Version 0.4.0. DOI: 10.5281/zenodo.1146904.

Peng, C. Y. et al. (July 2002). "Detailed Structural Decomposition of Galaxy Images". In: *AJ* 124, pp. 266–293. DOI: 10.1086/340952. eprint: astro-ph/0204182.

— (June 2010a). "Detailed Decomposition of Galaxy Images. II. Beyond Axisymmetric Models". In: *AJ* 139, pp. 2097–2129. DOI: 10.1088/0004-6256/139/6/2097. arXiv: 0912.0731.

Koekemoer, A. M. et al. (Sept. 2007). "The COSMOS Survey: Hubble Space Telescope Advanced Camera for Surveys Observations and Data Processing". In: *ApJS* 172.1, pp. 196–202. DOI: 10.1086/520086. arXiv: astro-ph/0703095 [astro-ph].

Massey, Richard et al. (Jan. 2010). "Pixel-based correction for Charge Transfer Inefficiency in the Hubble Space Telescope Advanced Camera for Surveys". In: *MNRAS* 401.1, pp. 371–384. DOI: 10.1111/j.1365-2966.2009.15638.x. arXiv: 0909.0507 [astro-ph.CO].

Marchesi, S. et al. (Jan. 2016). "The Chandra COSMOS Legacy survey: optical/IR identifications". In: *ApJ* 817.1, 34, p. 34. DOI: 10.3847/0004-637X/817/1/34. arXiv: 1512.01105 [astro-ph.GA].

Marleau, Francine R. and Luc Simard (Nov. 1998). "Quantitative Morphology of Galaxies in the Hubble Deep Field". In: *ApJ* 507.2, pp. 585–600. DOI: 10.1086/306356. arXiv: astro-ph/9807223 [astro-ph].

Pignatelli, E., G. Fasano, and P. Cassata (Jan. 2006). "GASPHOT: a tool for Galaxy Automatic Surface PHOTometry". In: *A&A* 446.1, pp. 373–388. DOI: 10.1051/0004-6361:20041704.

Sargent, M. T. et al. (Sept. 2007). "The Evolution of the Number Density of Large Disk Galaxies in COSMOS". In: *ApJS* 172.1, pp. 434–455. DOI: 10.1086/516584. arXiv: astro-ph/0609042 [astro-ph].

Pannella, Maurilio et al. (Aug. 2009b). "The Evolution of Early- and Late-type Galaxies in the Cosmic Evolution Survey up to $z \approx 1.2$". In: *ApJ* 701.1, pp. 787–803. DOI: 10.1088/0004-637X/701/1/787. arXiv: 0906.2810 [astro-ph.CO].

Szomoru, Daniel et al. (July 2011). "Morphological Evolution of Galaxies from Ultra-deep Hubble Space Telescope Wide Field Camera 3 Imaging: The Hubble Sequence at $z \sim 2$”. In: *ApJ* 735.1, L22, p. L22. DOI: 10.1088/2041-8205/735/1/L22. arXiv: 1106.1641 [astro-ph.CO].

Wuyts, Stijn et al. (July 2012). “Smooth(er) Stellar Mass Maps in CANDELS: Constraints on the Longevity of Clumps in High-redshift Star-forming Galaxies”. In: *ApJ* 753.2, 114, p. 114. DOI: 10.1088/0004-637X/753/2/114. arXiv: 1203.2611 [astro-ph.CO].

van Dokkum, Pieter G. et al. (Aug. 2014). “Dense Cores in Galaxies Out to z = 2.5 in SDSS, UltraVISTA, and the Five 3D-HST/CANDELS Fields”. In: *ApJ* 791.1, 45, p. 45. DOI: 10.1088/0004-637X/791/1/45. arXiv: 1404.4874 [astro-ph.GA].

Kubo, M. et al. (Aug. 2017). “Bimodal morphologies of massive galaxies at the core of a protocluster at $z = 3.09$ and the strong size growth of a brightest cluster galaxy”. In: *MNRAS* 469.2, pp. 2235–2250. DOI: 10.1093/mnras/stx920. arXiv: 1704.05962 [astro-ph.GA].

Barro, Guillermo et al. (May 2017). “Structural and Star-forming Relations since $z \sim 3$: Connecting Compact Star-forming and Quiescent Galaxies”. In: *ApJ* 840.1, 47, p. 47. DOI: 10.3847/1538-4357/aa6b05. arXiv: 1509.00469 [astro-ph.GA].

Lilly, Simon J. et al. (June 1999). “The Canada-United Kingdom Deep Submillimeter Survey. II. First Identifications, Redshifts, and Implications for Galaxy Evolution”. In: *ApJ* 518.2, pp. 641–655. DOI: 10.1086/307310. arXiv: astro-ph/9901047 [astro-ph].

Genzel, Reinhard et al. (Feb. 2003). “Spatially Resolved Millimeter Interferometry of SMM J02399-0136: AVery Massive Galaxy at $z = 2.8$”. In: *ApJ* 584.2, pp. 633–642. DOI: 10.1086/345718. arXiv: astro-ph/0210449 [astro-ph].

Tacconi, L. J. et al. (June 2008b). “Submillimeter Galaxies at $z \sim 2$: Evidence for Major Mergers and Constraints on Lifetimes, IMF, and CO-H_2 Conversion Factor”. In: *ApJ* 680.1, pp. 246–262. DOI: 10.1086/587168. arXiv: 0801.3650 [astro-ph].

Simpson, J. M. et al. (June 2014). “An ALMA Survey of Submillimeter Galaxies in the Extended Chandra Deep Field South: The Redshift Distribution and Evolution of Submillimeter Galaxies”. In: *ApJ* 788.2, 125, p. 125. DOI: 10.1088/0004-637X/788/2/125. arXiv: 1310.6363 [astro-ph.CO].

Simpson, J. M. et al. (Apr. 2017). “The SCUBA-2 Cosmology Legacy Survey: Multiwavelength Properties of ALMA-identified Submillimeter Galaxies in UKIDSS UDS”. In: *ApJ* 839.1, 58, p. 58. DOI: 10.3847/1538-4357/aa65d0. arXiv: 1611.03084 [astro-ph.GA].

Toft, S. et al. (Feb. 2014). “Submillimeter Galaxies as Progenitors of Compact Quiescent Galaxies”. In: *ApJ* 782.2, 68, p. 68. DOI: 10.1088/0004-637X/782/2/68. arXiv: 1401.1510 [astro-ph.GA].

Oteo, I. et al. (Sept. 2017). “Witnessing the birth of the red sequence: the physical scale and morphology of dust emission in hyper-luminous starbursts in the early Universe”. In: *arXiv e-prints*, arXiv:1709.04191, arXiv:1709.04191. arXiv: 1709.04191 [astro-ph.GA].

Jin, S. et al. (Dec. 2019). “Discovery of Four Apparently Cold Dusty Galaxies at $z = 3.62 - 5.85$ in the COSMOS Field: Direct Evidence of Cosmic Microwave Background Impact on High-redshift Galaxy Observables”. In: *ApJ* 887.2, 144, p. 144. DOI: 10.3847/1538-4357/ab55d6. arXiv: 1906.00040 [astro-ph.GA].

Hopkins, Philip F. et al. (Apr. 2008). “A Cosmological Framework for the Co-Evolution of Quasars, Supermassive Black Holes, and Elliptical Galaxies. II. Formation of Red Ellipticals”. In: *ApJS* 175.2, pp. 390–422. DOI: 10.1086/524363. arXiv: 0706.1246 [astro-ph].

Wellons, Sarah et al. (May 2015). “The formation of massive, compact galaxies at z = 2 in the Illustris simulation”. In: *MNRAS* 449.1, pp. 361–372. DOI: 10.1093/mnras/stv303. arXiv: 1411.0667 [astro-ph.GA].

Lagos, Claudia del P. et al. (Sept. 2020). “Physical properties and evolution of (sub-)millimetre-selected galaxies in the galaxy formation simulation SHARK”. In: *MNRAS* 499.2, pp. 1948–1971. DOI: 10.1093/mnras/staa2861. arXiv: 2007.09853 [astro-ph.GA].

Hopkins, Philip F. et al. (Mar. 2006). “A Unified, Merger-driven Model of the Origin of Starbursts, Quasars, the Cosmic X-Ray Background, Supermassive Black Holes, and Galaxy Spheroids”. In: *ApJS* 163.1, pp. 1–49. DOI: 10.1086/499298. arXiv: astro-ph/0506398 [astro-ph].

Peng, Ying-jie and Alvio Renzini (Jan. 2020). “Disc growth and quenching”. In: *MNRAS* 491.1, pp. L51–L55. DOI: 10.1093/mnrasl/slz163. arXiv: 1910.10446 [astro-ph.GA].

Nelson, Erica et al. (Sept. 2014). “A massive galaxy in its core formation phase three billion years after the Big Bang”. In: *Nature* 513.7518, pp. 394–397. DOI: 10.1038/nature13616. arXiv: 1406.3350 [astro-ph.GA].

Gilli, R. et al. (Feb. 2014). “ALMA reveals a warm and compact starburst around a heavily obscured supermassive black hole at $z = 4.75$”. In: *A&A* 562, A67, A67. DOI: 10.1051/0004-6361/201322892. arXiv: 1312.1248 [astro-ph.GA].

Patel, Shannon G. et al. (Mar. 2013). “HST/WFC3 Confirmation of the Inside-out Growth of Massive Galaxies at $0 < z < 2$ and Identification of Their Star-forming Progenitors at $z \sim 3$”. In: *ApJ* 766.1, 15, p. 15. DOI: 10.1088/0004-637X/766/1/15. arXiv: 1208.0341 [astro-ph.CO].

Stefanon, Mauro et al. (May 2013). “What are the Progenitors of Compact, Massive, Quiescent Galaxies at $z = 2.3$? The Population of Massive Galaxies at $z > 3$ from NMBS and CANDELS”. In: *ApJ* 768.1, 92, p. 92. DOI: 10.1088/0004-637X/768/1/92. arXiv: 1301.7063 [astro-ph.CO].

Barro, Guillermo et al. (Mar. 2013). “CANDELS: The Progenitors of Compact Quiescent Galaxies at $z \sim 2$”. In: *ApJ* 765.2, 104, p. 104. DOI: 10.1088/0004-637X/765/2/104. arXiv: 1206.5000 [astro-ph.CO].

Barro, G. et al. (Aug. 2014a). “CANDELS+3D-HST: Compact SFGs at $z \sim 2-3$, the Progenitors of the First Quiescent Galaxies”. In: *ApJ* 791.1, 52, p. 52. DOI: 10.1088/0004-637X/791/1/52. arXiv: 1311.5559 [astro-ph.CO].

Barro, Guillermo et al. (Nov. 2014b). “Keck-I MOSFIRE Spectroscopy of Compact Star-forming Galaxies at $z \gtrsim 2$: High Velocity Dispersions in Progenitors of Compact Quiescent Galaxies”. In: *ApJ* 795.2, 145, p. 145. DOI: 10.1088/0004-637X/795/2/145. arXiv: 1405.7042 [astro-ph.GA].

Williams, Christina C. et al. (Feb. 2015). “The Interstellar Medium and Feedback in the Progenitors of the Compact Passive Galaxies at $z \sim 2$”. In: *ApJ* 800.1, 21, p. 21. DOI: 10.1088/0004-637X/800/1/21. arXiv: 1407.1834 [astro-ph.GA].

Martin, D. Christopher et al. (Jan. 2005). “The Galaxy Evolution Explorer: A Space Ultraviolet Survey Mission”. In: *ApJ* 619.1, pp. L1–L6. DOI: 10.1086/426387. arXiv: astro-ph/0411302 [astro-ph].

Capak, P. et al. (Sept. 2007). “The First Release COSMOS Optical and Near-IR Data and Catalog”. In: *ApJS* 172.1, pp. 99–116. DOI: 10.1086/519081. arXiv: 0704.2430 [astro-ph].

McCracken, H. J. et al. (Aug. 2012). "UltraVISTA: a new ultra-deep near-infrared survey in COSMOS". In: *A&A* 544, A156, A156. DOI: 10.1051/0004-6361/201219507. arXiv: 1204.6586 [astro-ph.CO].

Sanders, D. B. et al. (Sept. 2007). "S-COSMOS: The Spitzer Legacy Survey of the Hubble Space Telescope ACS 2 deg^2 COSMOS Field I: Survey Strategy and First Analysis". In: *ApJS* 172.1, pp. 86–98. DOI: 10.1086/517885. arXiv: astro-ph/0701318 [astro-ph].

Lilly, Simon J. et al. (Oct. 2009). "The zCOSMOS 10k-Bright Spectroscopic Sample". In: *ApJS* 184.2, pp. 218–229. DOI: 10.1088/0067-0049/184/2/218.

Krogager, J. K. et al. (Dec. 2014). "A Spectroscopic Sample of Massive, Quiescent $z \sim 2$ Galaxies: Implications for the Evolution of the Mass-Size Relation". In: *ApJ* 797.1, 17, p. 17. DOI: 10.1088/0004-637X/797/1/17. arXiv: 1309.6316 [astro-ph.CO].

Renzini, Alvio (Sept. 2006). "Stellar Population Diagnostics of Elliptical Galaxy Formation". In: *ARA&A* 44.1, pp. 141–192. DOI: 10.1146/annurev.astro.44.051905.092450. arXiv: astro-ph/0603479 [astro-ph].

Fall, S. M. (Jan. 1983). "Galaxy formation - Some comparisons between theory and observation". In: *Internal Kinematics and Dynamics of Galaxies*. Ed. by E. Athanassoula. Vol. 100. IAU Symposium, pp. 391–398.

Romanowsky, Aaron J. and S. Michael Fall (Dec. 2012). "Angular Momentum and Galaxy Formation Revisited". In: *ApJS* 203.2, 17, p. 17. DOI: 10.1088/0067-0049/203/2/17. arXiv: 1207.4189 [astro-ph.CO].

Fall, S. Michael and Aaron J. Romanowsky (Dec. 2018). "Angular Momentum and Galaxy Formation Revisited: Scaling Relations for Disks and Bulges". In: *ApJ* 868.2, 133, p. 133. DOI: 10.3847/1538-4357/aaeb27. arXiv: 1808.02525 [astro-ph.GA].

Martis, Nicholas S. et al. (Aug. 2016). "The Evolution of the Fractions of Quiescent and Star-forming Galaxies as a Function of Stellar Mass Since $z = 3$: Increasing Importance of Massive, Dusty Star-forming Galaxies in the Early Universe". In: *ApJ* 827.2, L25, p. L25. DOI: 10.3847/2041-8205/827/2/L25. arXiv: 1606.04090 [astro-ph.GA].

Davidzon, I. et al. (Sept. 2017). "The COSMOS2015 galaxy stellar mass function . Thirteen billion years of stellar mass assembly in ten snapshots". In: *A&A* 605, A70, A70. DOI: 10.1051/0004-6361/201730419. arXiv: 1701.02734 [astro-ph.GA].

Peebles, P. J. E. (Feb. 1969). "Origin of the Angular Momentum of Galaxies". In: *ApJ* 155, p. 393. DOI: 10.1086/149876.

Obreschkow, D. and K. Glazebrook (Mar. 2014). "Fundamental Mass-Spin-Morphology Relation Of Spiral Galaxies". In: *ApJ* 784.1, 26, p. 26. DOI: 10.1088/0004-637X/784/1/26. arXiv: 1312.4543 [astro-ph.GA].

Cortese, L. et al. (Nov. 2016). "The SAMI Galaxy Survey: the link between angular momentum and optical morphology". In: *MNRAS* 463.1, pp. 170–184. DOI: 10.1093/mnras/stw1891. arXiv: 1608.00291 [astro-ph.GA].

Barnes, Joshua and George Efstathiou (Aug. 1987). "Angular Momentum from Tidal Torques". In: *ApJ* 319, p. 575. DOI: 10.1086/165480.

Navarro, Julio F. and Simon D. M. White (Mar. 1994). "Simulations of dissipative galaxy formation in hierarchically clustering universes-2. Dynamics of the baryonic component in galactic haloes". In: *MNRAS* 267.2, pp. 401–412. DOI: 10.1093/mnras/267.2.401.

Heyl, Jeremy S., Lars Hernquist, and David N. Spergel (May 1996). "Structure of Merger Remnants. V. Kinematics". In: *ApJ* 463, p. 69. DOI: 10.1086/177223.

Zavala, Jesus, Takashi Okamoto, and Carlos S. Frenk (June 2008). "Bulges versus discs: the evolution of angular momentum in cosmological simulations of galaxy formation". In: *MNRAS* 387.1, pp. 364–370. DOI: 10.1111/j.1365-2966.2008.13243.x. arXiv: 0710.2901 [astro-ph].

Lagos, Claudia del P. et al. (Feb. 2018). "Quantifying the impact of mergers on the angular momentum of simulated galaxies". In: *MNRAS* 473.4, pp. 4956–4974. DOI: 10.1093/mnras/stx2667. arXiv: 1701.04407 [astro-ph.GA].

Lagos, Claudia del P. et al. (Feb. 2017). "Angular momentum evolution of galaxies in EAGLE". In: *MNRAS* 464.4, pp. 3850–3870. DOI: 10.1093/mnras/stw2610. arXiv: 1609.01739 [astro-ph.GA].

Obreschkow, Danail et al. (Dec. 2015). "Low Angular Momentum in Clumpy, Turbulent Disk Galaxies". In: *ApJ* 815.2, 97, p. 97. DOI: 10.1088/0004-637X/815/2/97. arXiv: 1508.04768 [astro-ph.GA].

Tacconi, Linda J., Reinhard Genzel, and Amiel Sternberg (Aug. 2020). "The Evolution of the Star-Forming Interstellar Medium Across Cosmic Time". In: *ARA&A* 58, pp. 157–203. DOI: 10.1146/annurev-astro-082812-141034. arXiv: 2003.06245 [astro-ph.GA].

Pan, Zhizheng, Xianzhong Zheng, and Xu Kong (Jan. 2017). "The Quenched Mass Portion of Star-forming Galaxies and the Origin of the Star Formation Sequence Slope". In: *ApJ* 834.1, 39, p. 39. DOI: 10.3847/1538-4357/834/1/39. arXiv: 1611.04698 [astro-ph.GA].

Johnston, Russell et al. (Nov. 2015). "The evolving relation between star formation rate and stellar mass in the VIDEO survey since $z = 3$". In: *MNRAS* 453.3, pp. 2540–2557. DOI: 10.1093/mnras/stv1715. arXiv: 1507.07503 [astro-ph.GA].

Tacconi, L. J. et al. (June 2008a). "Submillimeter Galaxies at $z \sim 2$: Evidence for Major Mergers and Constraints on Lifetimes, IMF, and CO-H_2 Conversion Factor". In: *ApJ* 680.1, pp. 246–262. DOI: 10.1086/587168. arXiv: 0801.3650 [astro-ph].

Dunne, L. et al. (Oct. 2011). "Herschel-ATLAS: rapid evolution of dust in galaxies over the last 5 billion years". In: *MNRAS* 417.2, pp. 1510–1533. DOI: 10.1111/j.1365-2966.2011.19363.x. arXiv: 1012.5186 [astro-ph.CO].

Genzel, R. et al. (Feb. 2015). "Combined CO and Dust Scaling Relations of Depletion Time and Molecular Gas Fractions with Cosmic Time, Specific Star-formation Rate, and Stellar Mass". In: *ApJ* 800.1, 20, p. 20. DOI: 10.1088/0004-637X/800/1/20. arXiv: 1409.1171 [astro-ph.GA].

Scoville, N. et al. (Apr. 2016). "ISM Masses and the Star formation Law at Z = 1 to 6: ALMA Observations of Dust Continuum in 145 Galaxies in the COSMOS Survey Field". In: *ApJ* 820.2, 83, p. 83. DOI: 10.3847/0004-637X/820/2/83. arXiv: 1511.05149 [astro-ph.GA].

Fontanot, Fabio et al. (Aug. 2009). "The many manifestations of downsizing: hierarchical galaxy formation models confront observations". In: *MNRAS* 397.4, pp. 1776–1790. DOI: 10.1111/j.1365-2966.2009.15058.x. arXiv: 0901.1130 [astro-ph.CO].

Arnouts, S. et al. (Oct. 2013). "Encoding of the infrared excess in the NUVrK color diagram for star-forming galaxies". In: *A&A* 558, A67, A67. DOI: 10.1051/0004-6361/201321768. arXiv: 1309.0008 [astro-ph.CO].

Lustig, Peter et al. (Feb. 2021). "Compact, bulge-dominated structures of spectroscopically confirmed quiescent galaxies at $z \sim 3$". In: *MNRAS* 501.2, pp. 2659–2676. DOI: 10.1093/mnras/staa3766. arXiv: 2012.02766 [astro-ph.GA].

Straatman, Caroline M. S. et al. (Mar. 2014). "A Substantial Population of Massive Quiescent Galaxies at $z \sim 4$ from ZFOURGE". In: *ApJ* 783.1, L14, p. L14. DOI: 10.1088/2041-8205/783/1/L14. arXiv: 1312.4952 [astro-ph.GA].

Merlin, E. et al. (Dec. 2019). "Red and dead CANDELS: massive passive galaxies at the dawn of the Universe". In: *MNRAS* 490.3, pp. 3309–3328. DOI: 10.1093/mnras/stz2615. arXiv: 1909.07996 [astro-ph.GA].

Guarnieri, Pierandrea et al. (Mar. 2019). "Candidate massive galaxies at $z \sim 4$ in the Dark Energy Survey". In: *MNRAS* 483.3, pp. 3060–3081. DOI: 10.1093/mnras/sty3305. arXiv: 1811.12422 [astro-ph.GA].

Alcalde Pampliega, Belén et al. (May 2019). "Optically Faint Massive Balmer Break Galaxies at $z > 3$ in the CANDELS/GOODS Fields". In: *ApJ* 876.2, 135, p. 135. DOI: 10.3847/1538-4357/ab14f2. arXiv: 1806.04152 [astro-ph.GA].

McCarthy, I. G. et al. (Apr. 2011). "Gas expulsion by quasar-driven winds as a solution to the overcooling problem in galaxy groups and clusters". In: *MNRAS* 412.3, pp. 1965–1984. DOI: 10.1111/j.1365-2966.2010.18033.x. arXiv: 1008.4799 [astro-ph.CO].

Dubois, Yohan et al. (Dec. 2016). "The HORIZON-AGN simulation: morphological diversity of galaxies promoted by AGN feedback". In: *MNRAS* 463.4, pp. 3948–3964. DOI: 10.1093/mnras/stw2265. arXiv: 1606.03086 [astro-ph.GA].

Remus, Rhea-Silvia et al. (Jan. 2017). "The co-evolution of total density profiles and central dark matter fractions in simulated early-type galaxies". In: *MNRAS* 464.3, pp. 3742–3756. DOI: 10.1093/mnras/stw2594. arXiv: 1603.01619 [astro-ph.GA].

Kaviraj, S. et al. (June 2017). "The Horizon-AGN simulation: evolution of galaxy properties over cosmic time". In: *MNRAS* 467.4, pp. 4739–4752. DOI: 10.1093/mnras/stx126. arXiv: 1605.09379 [astro-ph.GA].

Weinberger, Rainer et al. (Sept. 2018). "Supermassive black holes and their feedback effects in the IllustrisTNG simulation". In: *MNRAS* 479.3, pp. 4056–4072. DOI: 10.1093/mnras/sty1733. arXiv: 1710.04659 [astro-ph.GA].

Springel, Volker et al. (Mar. 2018). "First results from the IllustrisTNG simulations: matter and galaxy clustering". In: *MNRAS* 475.1, pp. 676–698. DOI: 10.1093/mnras/stx3304. arXiv: 1707.03397 [astro-ph.GA].

Nelson, Dylan et al. (Mar. 2018). "First results from the IllustrisTNG simulations: the galaxy colour bimodality". In: *MNRAS* 475.1, pp. 624–647. DOI: 10.1093/mnras/stx3040. arXiv: 1707.03395 [astro-ph.GA].

Marinacci, Federico et al. (Nov. 2018). "First results from the IllustrisTNG simulations: radio haloes and magnetic fields". In: *MNRAS* 480.4, pp. 5113–5139. DOI: 10.1093/mnras/sty2206. arXiv: 1707.03396 [astro-ph.CO].

Pillepich, Annalisa et al. (Mar. 2018a). "First results from the IllustrisTNG simulations: the stellar mass content of groups and clusters of galaxies". In: *MNRAS* 475.1, pp. 648–675. DOI: 10.1093/mnras/stx3112. arXiv: 1707.03406 [astro-ph.GA].

Naiman, Jill P. et al. (June 2018). "First results from the IllustrisTNG simulations: a tale of two elements - chemical evolution of magnesium and europium". In: *MNRAS* 477.1, pp. 1206–1224. DOI: 10.1093/mnras/sty618. arXiv: 1707.03401 [astro-ph.GA].

Nelson, Dylan et al. (May 2019). "The IllustrisTNG simulations: public data release". In: *Computational Astrophysics and Cosmology* 6.1, 2, p. 2. DOI: 10.1186/s40668-019-0028-x. arXiv: 1812.05609 [astro-ph.GA].

Planck Collaboration et al. (Sept. 2016). "Planck 2015 results. XIII. Cosmological parameters". In: *A&A* 594, A13, A13. DOI: 10.1051/0004-6361/201525830. arXiv: 1502.01589 [astro-ph.CO].

Weinberger, Rainer et al. (Mar. 2017). "Simulating galaxy formation with black hole driven thermal and kinetic feedback". In: *MNRAS* 465.3, pp. 3291–3308. DOI: 10.1093/mnras/stw2944. arXiv: 1607.03486 [astro-ph.GA].

Pillepich, Annalisa et al. (Jan. 2018b). "Simulating galaxy formation with the IllustrisTNG model". In: *MNRAS* 473.3, pp. 4077–4106. DOI: 10.1093/mnras/stx2656. arXiv: 1703.02970 [astro-ph.GA].

Hirschmann, Michaela et al. (Aug. 2014). "Cosmological simulations of black hole growth: AGN luminosities and downsizing". In: *MNRAS* 442.3, pp. 2304–2324. DOI: 10.1093/mnras/stu1023. arXiv: 1308.0333 [astro-ph.CO].

Teklu, Adelheid F. et al. (Oct. 2015). "Connecting Angular Momentum and Galactic Dynamics: The Complex Interplay between Spin, Mass, and Morphology". In: *ApJ* 812.1, 29, p. 29. DOI: 10.1088/0004-637X/812/1/29. arXiv: 1503.03501 [astro-ph.GA].

Steinborn, Lisa K. et al. (May 2016). "Origin and properties of dual and offset active galactic nuclei in a cosmological simulation at z=2". In: *MNRAS* 458.1, pp. 1013–1028. DOI: 10.1093/mnras/stw316. arXiv: 1510.08465 [astro-ph.GA].

Komatsu, E. et al. (Feb. 2011). "Seven-year Wilkinson Microwave Anisotropy Probe (WMAP) Observations: Cosmological Interpretation". In: *ApJS* 192.2, 18, p. 18. DOI: 10.1088/0067-0049/192/2/18. arXiv: 1001.4538 [astro-ph.CO].

Steinborn, Lisa K. et al. (Apr. 2015). "A refined sub-grid model for black hole accretion and AGN feedback in large cosmological simulations". In: *MNRAS* 448.2, pp. 1504–1525. DOI: 10.1093/mnras/stv072. arXiv: 1409.3221 [astro-ph.GA].

Sherman, Sydney et al. (Dec. 2020). "Investigating the growing population of massive quiescent galaxies at cosmic noon". In: *MNRAS* 499.3, pp. 4239–4260. DOI: 10.1093/mnras/staa3167. arXiv: 2010.04741 [astro-ph.GA].

Springel, Volker et al. (Dec. 2001). "Populating a cluster of galaxies - I. Results at $z = 0$". In: *MNRAS* 328.3, pp. 726–750. DOI: 10.1046/j.1365-8711.2001.04912.x. arXiv: astro-ph/0012055 [astro-ph].

Dolag, K. et al. (Oct. 2009). "Substructures in hydrodynamical cluster simulations". In: *MNRAS* 399.2, pp. 497–514. DOI: 10.1111/j.1365-2966.2009.15034.x. arXiv: 0808.3401 [astro-ph].

Genel, Shy et al. (Mar. 2018). "The size evolution of star-forming and quenched galaxies in the IllustrisTNG simulation". In: *MNRAS* 474.3, pp. 3976–3996. DOI: 10.1093/mnras/stx3078. arXiv: 1707.05327 [astro-ph.GA].

Donnari, Martina et al. (June 2019). "The star formation activity of IllustrisTNG galaxies: main sequence, UVJ diagram, quenched fractions, and systematics". In: *MNRAS* 485.4, pp. 4817–4840. DOI: 10.1093/mnras/stz712. arXiv: 1812.07584 [astro-ph.GA].

Donnari, Martina et al. (Oct. 2021). "Quenched fractions in the IllustrisTNG simulations: comparison with observations and other theoretical models". In: *MNRAS* 506.4, pp. 4760–4780. DOI: 10.1093/mnras/stab1950. arXiv: 2008.00004 [astro-ph.GA].

Noll, S. et al. (May 2009). "GMASS ultradeep spectroscopy of galaxies at $z \sim 2$. IV. The variety of dust populations". In: *A&A* 499.1, pp. 69–85. DOI: 10.1051/0004-6361/200811526. arXiv: 0903.3972 [astro-ph.CO].

Salim, Samir, Médéric Boquien, and Janice C. Lee (May 2018). "Dust Attenuation Curves in the Local Universe: Demographics and New Laws for Star-forming Galaxies and High-redshift Analogs". In: *ApJ* 859.1, 11, p. 11. DOI: 10.3847/1538-4357/aabf3c. arXiv: 1804.05850 [astro-ph.GA].

González Delgado, R. M. et al. (Sept. 2015). "The CALIFA survey across the Hubble sequence. Spatially resolved stellar population properties in galaxies". In: *A&A* 581, A103, A103. DOI: 10.1051/0004-6361/201525938. arXiv: 1506.04157 [astro-ph.GA].

McLure, R. J. et al. (May 2018). "Dust attenuation in $2 < z < 3$ star-forming galaxies from deep ALMA observations of the Hubble Ultra Deep Field". In: *MNRAS* 476.3, pp. 3991–4006. DOI: 10.1093/mnras/sty522. arXiv: 1709.06102 [astro-ph.GA].

Pannella, M. et al. (July 2015). "GOODS-Herschel: Star Formation, Dust Attenuation, and the FIR-radio Correlation on the Main Sequence of Star-forming Galaxies up to $z \approx 4$". In: *ApJ* 807.2, 141, p. 141. DOI: 10.1088/0004-637X/807/2/141. arXiv: 1407.5072 [astro-ph.GA].

Sargent, M. T. et al. (Sept. 2014). "Regularity Underlying Complexity: A Redshift-independent Description of the Continuous Variation of Galaxy-scale Molecular Gas Properties in the Mass-star Formation Rate Plane". In: *ApJ* 793.1, 19, p. 19. DOI: 10.1088/0004-637X/793/1/19. arXiv: 1303.4392 [astro-ph.CO].

Morselli, L. et al. (June 2019). "Spatial distribution of stellar mass and star formation activity at $0.2 < z < 1.2$ across and along the main sequence". In: *A&A* 626, A61, A61. DOI: 10.1051/0004-6361/201834559. arXiv: 1812.08561 [astro-ph.GA].

Lotz, Marcel et al. (Sept. 2021). "Rise and fall of post-starburst galaxies in Magneticum Pathfinder". In: *MNRAS* 506.3, pp. 4516–4542. DOI: 10.1093/mnras/stab2037. arXiv: 2011.06602 [astro-ph.GA].

Leja, Joel, Sandro Tacchella, and Charlie Conroy (July 2019). "Beyond UVJ: More Efficient Selection of Quiescent Galaxies with Ultraviolet/Mid-infrared Fluxes". In: *ApJ* 880.1, L9, p. L9. DOI: 10.3847/2041-8213/ab2f8c. arXiv: 1907.02970 [astro-ph.GA].

Cameron, Ewan (June 2011). "On the Estimation of Confidence Intervals for Binomial Population Proportions in Astronomy: The Simplicity and Superiority of the Bayesian Approach". In: *Publ. Astron. Soc. Australia* 28.2, pp. 128–139. DOI: 10.1071/AS10046. arXiv: 1012.0566 [astro-ph.IM].

Saracco, Paolo et al. (Dec. 2020). "The Rapid Buildup of Massive Early-type Galaxies: Supersolar Metallicity, High Velocity Dispersion, and Young Age for an Early-type Galaxy at z = 3.35". In: *ApJ* 905.1, 40, p. 40. DOI: 10.3847/1538-4357/abc7c4. arXiv: 2011.04657 [astro-ph.GA].

Carnall, A. C. et al. (July 2020). "Timing the earliest quenching events with a robust sample of massive quiescent galaxies at $2 < z < 5$". In: *MNRAS* 496.1, pp. 695–707. DOI: 10.1093/mnras/staa1535. arXiv: 2001.11975 [astro-ph.GA].

Kalita, Boris S. et al. (Aug. 2021). "An Ancient Massive Quiescent Galaxy Found in a Gas-rich $z \sim 3$ Group". In: *ApJ* 917.2, L17, p. L17. DOI: 10.3847/2041-8213/ac16dc. arXiv: 2107.13241 [astro-ph.GA].

Remus, Rhea-Silvia and Duncan A. Forbes (Jan. 2021). "Accreted or Not Accreted? The Fraction of Accreted Mass in Galaxies from Simulations and Observations". In: *arXiv e-prints*, arXiv:2101.12216, arXiv:2101.12216. arXiv: 2101.12216 [astro-ph.GA].

Kent, S. M. (Oct. 1985). "CCD surface photometry of field galaxies. II. Bulge/disk decompositions." In: *ApJS* 59, pp. 115–159. DOI: 10.1086/191066.

Swinbank, A. M. et al. (May 2017). "Angular momentum evolution of galaxies over the past 10 Gyr: a MUSE and KMOS dynamical survey of 400 star-forming galaxies from $z = 0.3$ to 1.7". In: *MNRAS* 467.3, pp. 3140–3159. DOI: 10.1093/mnras/stx201. arXiv: 1701.07448 [astro-ph.GA].

Brammer, Gabriel B. et al. (June 2012). "3D-HST: A Wide-field Grism Spectroscopic Survey with the Hubble Space Telescope". In: *ApJS* 200.2, 13, p. 13. DOI: 10.1088/0067-0049/200/2/13. arXiv: 1204.2829 [astro-ph.CO].

Bernardi, M. et al. (Sept. 2014). "Systematic effects on the size-luminosity relations of early- and late-type galaxies: dependence on model fitting and morphology". In: *MNRAS* 443.1, pp. 874–897. DOI: 10.1093/mnras/stu1106.

Teklu, A. F., R. S. Remus, and K. Dolag (June 2016). "Dynamical Properties of Galaxies with Different Morphological Types at z=0 and z=2". In: *The Interplay between Local and Global Processes in Galaxies,* ed. by S. F. Sanchez, C. Morisset, and G. Delgado-Inglada, 41, p. 41.

Santini, P. et al. (Aug. 2021). "The emergence of passive galaxies in the early Universe". In: *A&A* 652, A30, A30. DOI: 10.1051/0004-6361/202039738. arXiv: 2011.10584 [astro-ph.GA].

Tanaka, Masayuki et al. (Dec. 2004). "The Environmental Dependence of Galaxy Properties in the Local Universe: Dependences on Luminosity, Local Density, and System Richness". In: *AJ* 128.6, pp. 2677–2695. DOI: 10.1086/425529. arXiv: astro-ph/0411132 [astro-ph].

Postman, M. et al. (Apr. 2005). "The Morphology-Density Relation in $z \sim 1$ Clusters". In: *ApJ* 623.2, pp. 721–741. DOI: 10.1086/428881. arXiv: astro-ph/0501224 [astro-ph].

Cooper, Michael C. et al. (July 2006). "The DEEP2 Galaxy Redshift Survey: the relationship between galaxy properties and environment at $z \sim 1$". In: *MNRAS* 370.1, pp. 198–212. DOI: 10.1111/j.1365-2966.2006.10485.x. arXiv: astro-ph/0603177 [astro-ph].

Poggianti, Bianca M. et al. (Sept. 2008). "The Relation between Star Formation, Morphology, and Local Density in High-Redshift Clusters and Groups". In: *ApJ* 684.2, pp. 888–904. DOI: 10.1086/589936. arXiv: 0805.1145 [astro-ph].

Pannella, Maurilio et al. (Aug. 2009c). "The Evolution of Early- and Late-type Galaxies in the Cosmic Evolution Survey up to $z \approx 1.2$". In: *ApJ* 701.1, pp. 787–803. DOI: 10.1088/0004-637X/701/1/787. arXiv: 0906.2810 [astro-ph.CO].

Muzzin, Adam et al. (Feb. 2012). "The Gemini Cluster Astrophysics Spectroscopic Survey (GCLASS): The Role of Environment and Self-regulation in Galaxy Evolution at $z \sim 1$". In: *ApJ* 746.2, 188, p. 188. DOI: 10.1088/0004-637X/746/2/188. arXiv: 1112.3655 [astro-ph.CO].

Mok, Angus et al. (May 2013). "Efficient satellite quenching at $z \sim 1$ from the GEEC2 spectroscopic survey of galaxy groups". In: *MNRAS* 431.2, pp. 1090–1106. DOI: 10.1093/mnras/stt251. arXiv: 1302.2562 [astro-ph.CO].

Woo, Joanna et al. (Feb. 2013). "Dependence of galaxy quenching on halo mass and distance from its centre". In: *MNRAS* 428.4, pp. 3306–3326. DOI: 10.1093/mnras/sts274. arXiv: 1203.1625 [astro-ph.CO].

Kovač, K. et al. (Feb. 2014). "zCOSMOS 20k: satellite galaxies are the main drivers of environmental effects in the galaxy population at least to $z \sim 0.7$". In: *MNRAS* 438.1, pp. 717–738. DOI: 10.1093/mnras/stt2241. arXiv: 1307.4402 [astro-ph.CO].

Strazzullo, V. et al. (Feb. 2019). "Galaxy populations in the most distant SPT-SZ clusters. I. Environmental quenching in massive clusters at $1.4 \lesssim z \lesssim 1.7$". In: *A&A* 622, A117, A117. DOI: 10.1051/0004-6361/201833944. arXiv: 1807.09768 [astro-ph.GA].

Old, Lyndsay J. et al. (Apr. 2020). "The GOGREEN survey: the environmental dependence of the star-forming galaxy main sequence at $1.0 < z < 1.5$". In: *MNRAS* 493.4, pp. 5987–6000. DOI: 10.1093/mnras/staa579. arXiv: 2002.11735 [astro-ph.GA].

Larson, R. B., B. M. Tinsley, and C. N. Caldwell (May 1980). "The evolution of disk galaxies and the origin of S0 galaxies". In: *ApJ* 237, pp. 692–707. DOI: 10.1086/157917.

Balogh, Michael L. and Simon L. Morris (Nov. 2000). "Hα photometry of Abell 2390". In: *MNRAS* 318.3, pp. 703–714. DOI: 10.1046/j.1365-8711.2000.03826.x. arXiv: astro-ph/0007111 [astro-ph].

Balogh, Michael L., Julio F. Navarro, and Simon L. Morris (Sept. 2000). "The Origin of Star Formation Gradients in Rich Galaxy Clusters". In: *ApJ* 540.1, pp. 113–121. DOI: 10.1086/309323. arXiv: astro-ph/0004078 [astro-ph].

Kereš, Dušan et al. (Oct. 2005b). "How do galaxies get their gas?" In: *MNRAS* 363.1, pp. 2–28. DOI: 10.1111/j.1365-2966.2005.09451.x. arXiv: astro-ph/0407095 [astro-ph].

van den Bosch, Frank C. et al. (June 2008). "The importance of satellite quenching for the build-up of the red sequence of present-day galaxies". In: *MNRAS* 387.1, pp. 79–91. DOI: 10.1111/j.1365-2966.2008.13230.x. arXiv: 0710.3164 [astro-ph].

Peng, Y., R. Maiolino, and R. Cochrane (May 2015). "Strangulation as the primary mechanism for shutting down star formation in galaxies". In: *Nature* 521.7551, pp. 192–195. DOI: 10.1038/nature14439. arXiv: 1505.03143 [astro-ph.GA].

Gunn, James E. and III Gott J. Richard (Aug. 1972). "On the Infall of Matter Into Clusters of Galaxies and Some Effects on Their Evolution". In: *ApJ* 176, p. 1. DOI: 10.1086/151605.

Abadi, Mario G., Ben Moore, and Richard G. Bower (Oct. 1999). "Ram pressure stripping of spiral galaxies in clusters". In: *MNRAS* 308.4, pp. 947–954. DOI: 10.1046/j.1365-8711.1999.02715.x. arXiv: astro-ph/9903436 [astro-ph].

Quilis, Vicent, Ben Moore, and Richard Bower (June 2000). "Gone with the Wind: The Origin of S0 Galaxies in Clusters". In: *Science* 288.5471, pp. 1617–1620. DOI: 10.1126/science.288.5471.1617. arXiv: astro-ph/0006031 [astro-ph].

Werner, S. V. et al. (Feb. 2022). "Satellite quenching was not important for $z \sim 1$ clusters: most quenching occurred during infall". In: *MNRAS* 510.1, pp. 674–686. DOI: 10.1093/mnras/stab3484. arXiv: 2111.14624 [astro-ph.GA].

van der Burg, Remco F. J. et al. (June 2020). "The GOGREEN Survey: A deep stellar mass function of cluster galaxies at 1.0 ¡ z ¡ 1.4 and the complex nature of satellite quenching". In: *A&A* 638, A112, A112. DOI: 10.1051/0004-6361/202037754. arXiv: 2004.10757 [astro-ph.GA].

Andreon, S. et al. (Nov. 2009). "JKCS 041: a colour-detected galaxy cluster at $z_{\mathrm{phot}} \sim 1.9$ with deep potential well as confirmed by X-ray data". In: *A&A* 507.1, pp. 147–157. DOI: 10.1051/0004-6361/200912299. arXiv: 0812.1699 [astro-ph].

Henry, J. Patrick et al. (Dec. 2010). "An X-ray-selected Galaxy Cluster in the Lockman Hole at Redshift 1.753". In: *ApJ* 725.1, pp. 615–624. DOI: 10.1088/0004-637X/725/1/615. arXiv: 1010.0688 [astro-ph.CO].

Gobat, R. et al. (Feb. 2011). "A mature cluster with X-ray emission at $z = 2.07$". In: *A&A* 526, A133, A133. DOI: 10.1051/0004-6361/201016084. arXiv: 1011.1837 [astro-ph.CO].

Capak, Peter L. et al. (Feb. 2011). "A massive protocluster of galaxies at a redshift of $z \sim 5.3$". In: *Nature* 470.7333, pp. 233–235. DOI: 10.1038/nature09681. arXiv: 1101.3586 [astro-ph.CO].

Stanford, S. A. et al. (July 2012). "IDCS J1426.5+3508: Discovery of a Massive, Infrared-selected Galaxy Cluster at $z = 1.75$". In: *ApJ* 753.2, 164, p. 164. DOI: 10.1088/0004-637X/753/2/164. arXiv: 1205.3786 [astro-ph.CO].

Zeimann, Gregory R. et al. (Sept. 2012). "IDCS J1433.2+3306: An Infrared-selected Galaxy Cluster at $z = 1.89$". In: *ApJ* 756.2, 115, p. 115. DOI: 10.1088/0004-637X/756/2/115. arXiv: 1207.4793 [astro-ph.CO].

Yuan, Tiantian et al. (Nov. 2014). "Keck/MOSFIRE Spectroscopic Confirmation of a Virgo-like Cluster Ancestor at $z = 2.095$". In: *ApJ* 795.1, L20, p. L20. DOI: 10.1088/2041-8205/795/1/L20. arXiv: 1410.0690 [astro-ph.GA].

Newman, Andrew B. et al. (June 2014). "Spectroscopic Confirmation of the Rich $z = 1.80$ Galaxy Cluster JKCS 041 using the WFC3 Grism: Environmental Trends in the Ages and Structure of Quiescent Galaxies". In: *ApJ* 788.1, 51, p. 51. DOI: 10.1088/0004-637X/788/1/51. arXiv: 1310.6754 [astro-ph.CO].

Cucciati, O. et al. (Oct. 2014). "Discovery of a rich proto-cluster at $z = 2.9$ and associated diffuse cold gas in the VIMOS Ultra-Deep Survey (VUDS)". In: *A&A* 570, A16, A16. DOI: 10.1051/0004-6361/201423811. arXiv: 1403.3691 [astro-ph.CO].

Wang, Tao et al. (Sept. 2016). "Discovery of a Galaxy Cluster with a Violently Starbursting Core at $z = 2.506$". In: *ApJ* 828.1, 56, p. 56. DOI: 10.3847/0004-637X/828/1/56. arXiv: 1604.07404 [astro-ph.GA].

Mantz, A. B. et al. (Nov. 2018). "The XXL Survey. XVII. X-ray and Sunyaev-Zel'dovich properties of the redshift 2.0 galaxy cluster XLSSC 122". In: *A&A* 620, A2, A2. DOI: 10.1051/0004-6361/201630096. arXiv: 1703.08221 [astro-ph.CO].

Toshikawa, Jun et al. (Jan. 2020). "Discovery of Protoclusters at $z \sim 3.7$ and 4.9: Embedded in Primordial Superclusters". In: *ApJ* 888.2, 89, p. 89. DOI: 10.3847/1538-4357/ab5e85. arXiv: 1912.01625 [astro-ph.GA].

Shi, Ke et al. (Apr. 2021b). "Accelerated Galaxy Growth and Environmental Quenching in a Protocluster at $z = 3.24$". In: *ApJ* 911.1, 46, p. 46. DOI: 10.3847/1538-4357/abe62e. arXiv: 2102.06499 [astro-ph.GA].

Shi, Dong Dong et al. (July 2021a). "Spectroscopic Confirmation of Two Extremely Massive Protoclusters, BOSS1244 and BOSS1542, at $z = 2.24$". In: *ApJ* 915.1, 32, p. 32. DOI: 10.3847/1538-4357/abfec0. arXiv: 2105.02248 [astro-ph.GA].

Shen, Lu et al. (May 2021). "Implications of the Environments of Radio-detected Active Galactic Nuclei in a Complex Protostructure at $z \sim 3.3$". In: *ApJ* 912.1, 60, p. 60. DOI: 10.3847/1538-4357/abee75. arXiv: 2103.03441 [astro-ph.GA].

McConachie, Ian et al. (Sept. 2021). "Spectroscopic Confirmation of a Protocluster at $z = 3.37$ with a High Fraction of Quiescent Galaxies". In: *arXiv e-prints*, arXiv:2109.07696, arXiv:2109.07696. arXiv: 2109.07696 [astro-ph.GA].

Polletta, M. et al. (Oct. 2021). "Spectroscopic observations of PHz G237.01+42.50: A galaxy protocluster at $z = 2.16$ in the Cosmos field". In: *A&A* 654, A121, A121. DOI: 10.1051/0004-6361/202140612. arXiv: 2109.04396 [astro-ph.GA].

Calvi, Rosa et al. (Apr. 2021). "Probing the existence of a rich galaxy overdensity at $z = 5.2$". In: *MNRAS* 502.3, pp. 4558–4575. DOI: 10.1093/mnras/staa4037. arXiv: 2101.02747 [astro-ph.GA].

Foley, R. J. et al. (Apr. 2011). "Discovery and Cosmological Implications of SPT-CL J2106-5844, the Most Massive Known Cluster at $z > 1$". In: *ApJ* 731.2, 86, p. 86. DOI: 10.1088/0004-637X/731/2/86. arXiv: 1101.1286 [astro-ph.CO].

Bleem, L. E. et al. (Feb. 2015). "Galaxy Clusters Discovered via the Sunyaev-Zel'dovich Effect in the 2500-Square-Degree SPT-SZ Survey". In: *ApJS* 216.2, 27, p. 27. DOI: 10.1088/0067-0049/216/2/27. arXiv: 1409.0850 [astro-ph.CO].

Rosati, Piero et al. (July 1999). "An X-Ray-Selected Galaxy Cluster at $z = 1.26$". In: *AJ* 118.1, pp. 76–85. DOI: 10.1086/300934. arXiv: astro-ph/9903381 [astro-ph].

Adami, C. et al. (Feb. 2011). "The XMM-LSS survey: optical assessment and properties of different X-ray selected cluster classes". In: *A&A* 526, A18, A18. DOI: 10.1051/0004-6361/201015182. arXiv: 1010.6195 [astro-ph.CO].

Fassbender, R. et al. (Mar. 2011). "The X-ray luminous galaxy cluster XMMU J1007.4+1237 at $z = 1.56$. The dawn of starburst activity in cluster cores". In: *A&A* 527, L10, p. L10. DOI: 10.1051/0004-6361/201016169. arXiv: 1101.3313 [astro-ph.CO].

Klein, M. et al. (June 2021). "The eROSITA Final Equatorial-Depth Survey (eFEDS): Optical confirmation, redshifts, and properties of the cluster and group catalog". In: *arXiv e-prints*, arXiv:2106.14519, arXiv:2106.14519. arXiv: 2106.14519 [astro-ph.CO].

Bocquet, S. et al. (June 2019). "Cluster Cosmology Constraints from the 2500 deg^2 SPT-SZ Survey: Inclusion of Weak Gravitational Lensing Data from Magellan and the Hubble Space Telescope". In: *ApJ* 878.1, 55, p. 55. DOI: 10.3847/1538-4357/ab1f10. arXiv: 1812.01679 [astro-ph.CO].

Steidel, Charles C. et al. (Mar. 2000). "Lyα Imaging of a Proto-Cluster Region at $\langle z \rangle = 3.09$". In: *ApJ* 532.1, pp. 170–182. DOI: 10.1086/308568. arXiv: astro-ph/9910144 [astro-ph].

Ouchi, Masami et al. (Jan. 2003). "Subaru Deep Survey. II. Luminosity Functions and Clustering Properties of Lyα Emitters at $z = 4.86$ in the Subaru Deep Field". In: *ApJ* 582.1, pp. 60–68. DOI: 10.1086/344476. arXiv: astro-ph/0202204 [astro-ph].

Ouchi, Masami et al. (Feb. 2005). "The Discovery of Primeval Large-Scale Structures with Forming Clusters at Redshift 6". In: *ApJ* 620.1, pp. L1–L4. DOI: 10.1086/428499. arXiv: astro-ph/0412648 [astro-ph].

Lemaux, B. C. et al. (July 2009). "Serendipitous Discovery of an Overdensity of Lyα Emitters at $z \sim 4.8$ in the CL1604 Supercluster Field". In: *ApJ* 700.1, pp. 20–48. DOI: 10.1088/0004-637X/700/1/20. arXiv: 0905.2233 [astro-ph.CO].

Hatch, N. A. et al. (Aug. 2011). "Hα emitters in $z \sim 2$ protoclusters: evidence for faster evolution in dense environments". In: *MNRAS* 415.4, pp. 2993–3005. DOI: 10.1111/j.1365-2966.2011.18735.x. arXiv: 1103.4364 [astro-ph.CO].

Zheng, Xian Zhong et al. (Jan. 2021). "MAMMOTH: confirmation of two massive galaxy overdensities at $z = 2.24$ with Hα emitters". In: *MNRAS* 500.4, pp. 4354–4364. DOI: 10.1093/mnras/staa2882. arXiv: 2009.08068 [astro-ph.GA].

Kodama, Tadayuki et al. (June 2007). "The first appearance of the red sequence of galaxies in proto-clusters at $2 \lesssim z \lesssim 3$". In: *MNRAS* 377.4, pp. 1717–1725. DOI: 10.1111/j.1365-2966.2007.11739.x. arXiv: astro-ph/0703382 [astro-ph].

Spitler, Lee R. et al. (Apr. 2012). "First Results from Z -FOURGE: Discovery of a Candidate Cluster at $z = 2.2$ in COSMOS". In: *ApJ* 748.2, L21, p. L21. DOI: 10.1088/2041-8205/748/2/L21. arXiv: 1112.2691 [astro-ph.CO].

Castellano, M. et al. (Dec. 2007). "A Photometrically Detected Forming Cluster of Galaxies at Redshift 1.6 in the GOODS Field". In: *ApJ* 671.2, pp. 1497–1502. DOI: 10.1086/521595. arXiv: 0707.1783 [astro-ph].

Salimbeni, S. et al. (July 2009). "A comprehensive study of large-scale structures in the GOODS-SOUTH field up to $z \sim 2.5$". In: *A&A* 501.3, pp. 865–877. DOI: 10.1051/0004-6361/200811570. arXiv: 0903.3952 [astro-ph.CO].

Scoville, N. et al. (May 2013). "Evolution of Galaxies and Their Environments at $z = 0.1 - 3$ in COSMOS". In: *ApJS* 206.1, 3, p. 3. DOI: 10.1088/0067-0049/206/1/3. arXiv: 1303.6689 [astro-ph.CO].

Chiang, Yi-Kuan, Roderik Overzier, and Karl Gebhardt (Feb. 2014). "Discovery of a Large Number of Candidate Protoclusters Traced by ~ 15 Mpc-scale Galaxy Overdensities in COSMOS". In: *ApJ* 782.1, L3, p. L3. DOI: 10.1088/2041-8205/782/1/L3. arXiv: 1312.4747 [astro-ph.CO].

Strazzullo, V. et al. (Apr. 2015b). "Passive galaxies as tracers of cluster environments at $z \sim 2$". In: *A&A* 576, L6, p. L6. DOI: 10.1051/0004-6361/201425038. arXiv: 1501.05323 [astro-ph.CO].

Cucciati, O. et al. (Nov. 2018). "The progeny of a cosmic titan: a massive multi-component proto-supercluster in formation at $z = 2.45$ in VUDS". In: *A&A* 619, A49, A49. DOI: 10.1051/0004-6361/201833655. arXiv: 1806.06073 [astro-ph.CO].

Gladders, Michael D. and H. K. C. Yee (Oct. 2000). "A New Method For Galaxy Cluster Detection. I. The Algorithm". In: *AJ* 120.4, pp. 2148–2162. DOI: 10.1086/301557. arXiv: astro-ph/0004092 [astro-ph].

Eisenstein, Daniel J. et al. (Nov. 2001). "Spectroscopic Target Selection for the Sloan Digital Sky Survey: The Luminous Red Galaxy Sample". In: *AJ* 122.5, pp. 2267–2280. DOI: 10.1086/323717. arXiv: astro-ph/0108153 [astro-ph].

Padmanabhan, Nikhil et al. (May 2005). "Calibrating photometric redshifts of luminous red galaxies". In: *MNRAS* 359.1, pp. 237–250. DOI: 10.1111/j.1365-2966.2005.08915.x. arXiv: astro-ph/0407594 [astro-ph].

Barro, Guillermo et al. (Aug. 2019). "The CANDELS/SHARDS Multiwavelength Catalog in GOODS-N: Photometry, Photometric Redshifts, Stellar Masses, Emission-line Fluxes, and Star Formation Rates". In: *ApJS* 243.2, 22, p. 22. DOI: 10.3847/1538-4365/ab23f2. arXiv: 1908.00569 [astro-ph.GA].

Whitaker, Katherine E. et al. (Sept. 2019). "The Hubble Legacy Field GOODS-S Photometric Catalog". In: *ApJS* 244.1, 16, p. 16. DOI: 10.3847/1538-4365/ab3853. arXiv: 1908.05682 [astro-ph.GA].

Weaver, J. R. et al. (Jan. 2022). "COSMOS2020: A Panchromatic View of the Universe to $z \sim 10$ from Two Complementary Catalogs". In: *ApJS* 258.1, 11, p. 11. DOI: 10.3847/1538-4365/ac3078. arXiv: 2110.13923 [astro-ph.GA].

Arnouts, S. et al. (Dec. 1999). "Measuring and modelling the redshift evolution of clustering: the Hubble Deep Field North". In: *MNRAS* 310.2, pp. 540–556. DOI: 10.1046/j.1365-8711.1999.02978.x. arXiv: astro-ph/9902290 [astro-ph].

Bolzonella, M., J. M. Miralles, and R. Pelló (Nov. 2000). "Photometric redshifts based on standard SED fitting procedures". In: *A&A* 363, pp. 476–492. arXiv: astro-ph/0003380 [astro-ph].

Ilbert, O. et al. (Oct. 2006). "Accurate photometric redshifts for the CFHT legacy survey calibrated using the VIMOS VLT deep survey". In: *A&A* 457.3, pp. 841–856. DOI: 10.1051/0004-6361:20065138. arXiv: astro-ph/0603217 [astro-ph].

Feldmann, R. et al. (Oct. 2006). "The Zurich Extragalactic Bayesian Redshift Analyzer and its first application: COSMOS". In: *MNRAS* 372.2, pp. 565–577. DOI: 10.1111/j.1365-2966.2006.10930.x. arXiv: astro-ph/0609044 [astro-ph].

Tagliaferri, Roberto et al. (2003). "Neural Networks for Photometric Redshifts Evaluation". In: *Lecture Notes in Computer Science*. Vol. 2859, pp. 226–234. DOI: 10.1007/978-3-540-45216-4_26.

Collister, Adrian A. and Ofer Lahav (Apr. 2004). "ANNz: Estimating Photometric Redshifts Using Artificial Neural Networks". In: *PASP* 116.818, pp. 345–351. DOI: 10.1086/383254. arXiv: astro-ph/0311058 [astro-ph].

Hoyle, B. (July 2016). "Measuring photometric redshifts using galaxy images and Deep Neural Networks". In: *Astronomy and Computing* 16, pp. 34–40. DOI: 10.1016/j.ascom.2016.03.006. arXiv: 1504.07255 [astro-ph.IM].

Eriksen, M. et al. (Oct. 2020). "The PAU Survey: Photometric redshifts using transfer learning from simulations". In: *MNRAS* 497.4, pp. 4565–4579. DOI: 10.1093/mnras/staa2265. arXiv: 2004.07979 [astro-ph.GA].

Schmidt, S. J. et al. (Dec. 2020). "Evaluation of probabilistic photometric redshift estimation approaches for The Rubin Observatory Legacy Survey of Space and Time (LSST)". In: *MNRAS* 499.2, pp. 1587–1606. DOI: 10.1093/mnras/staa2799. arXiv: 2001.03621 [astro-ph.CO].

Schuldt, S. et al. (July 2021). "Photometric redshift estimation with a convolutional neural network: NetZ". In: *A&A* 651, A55, A55. DOI: 10.1051/0004-6361/202039945. arXiv: 2011.12312 [astro-ph.GA].

Brodwin, M. et al. (Jan. 2006). "The Canada-France Deep Fields Survey. III. Photometric Redshift Distribution to $I_{\rm AB} = 24$". In: *ApJS* 162.1, pp. 20–37. DOI: 10.1086/497990. arXiv: astro-ph/0310038 [astro-ph].

Scoville, N. et al. (Sept. 2007). "The Cosmic Evolution Survey (COSMOS): Overview". In: *ApJS* 172.1, pp. 1–8. DOI: 10.1086/516585. arXiv: astro-ph/0612305 [astro-ph].

Hoaglin, David C., Frederick Mosteller, and John W. Tukey (1983). *Understanding robust and exploratory data anlysis.*

Brammer, Gabriel B. et al. (Sept. 2011b). "The Number Density and Mass Density of Star-forming and Quiescent Galaxies at $0.4 \leq z \leq 2.2$". In: *ApJ* 739.1, 24, p. 24. DOI: 10.1088/0004-637X/739/1/24. arXiv: 1104.2595 [astro-ph.CO].

Whitaker, Katherine E. et al. (Aug. 2010b). "The Age Spread of Quiescent Galaxies with the NEWFIRM Medium-band Survey: Identification of the Oldest Galaxies Out to $z \sim 2$". In: *ApJ* 719.2, pp. 1715–1732. DOI: 10.1088/0004-637X/719/2/1715. arXiv: 1006.5453 [astro-ph.CO].

Whitaker, Katherine E. et al. (July 2011). "The NEWFIRM Medium-band Survey: Photometric Catalogs, Redshifts, and the Bimodal Color Distribution of Galaxies out to $z \sim 3$". In: *ApJ* 735.2, 86, p. 86. DOI: 10.1088/0004-637X/735/2/86. arXiv: 1105.4609 [astro-ph.CO].

Ilbert, O. et al. (Jan. 2009). "Cosmos Photometric Redshifts with 30-Bands for 2-deg^2". In: *ApJ* 690.2, pp. 1236–1249. DOI: 10.1088/0004-637X/690/2/1236. arXiv: 0809.2101 [astro-ph].

Daddi, E. et al. (Sept. 2017). "Radio Selection of the Most Distant Galaxy Clusters". In: *ApJ* 846.2, L31, p. L31. DOI: 10.3847/2041-8213/aa8808. arXiv: 1708.06910 [astro-ph.CO].

Oteo, I. et al. (Mar. 2018). "An Extreme Protocluster of Luminous Dusty Starbursts in the Early Universe". In: *ApJ* 856.1, 72, p. 72. DOI: 10.3847/1538-4357/aaa1f1. arXiv: 1709.02809 [astro-ph.GA].

Strazzullo, V. et al. (July 2018). "Deciphering the Activity and Quiescence of High-redshift Cluster Environments: ALMA Observations of Cl J1449+0856 at $z = 2$". In: *ApJ* 862.1, 64, p. 64. DOI: 10.3847/1538-4357/aacd10. arXiv: 1806.06856 [astro-ph.GA].

Willis, J. P. et al. (Jan. 2020). "Spectroscopic confirmation of a mature galaxy cluster at a redshift of 2". In: *Nature* 577.7788, pp. 39–41. DOI: 10.1038/s41586-019-1829-4. arXiv: 2001.00549 [astro-ph.GA].

Hirschmann, Michaela, Gabriella De Lucia, and Fabio Fontanot (Sept. 2016). "Galaxy assembly, stellar feedback and metal enrichment: the view from the GAEA model". In: *MNRAS* 461.2, pp. 1760–1785. DOI: 10.1093/mnras/stw1318. arXiv: 1512.04531 [astro-ph.GA].

Fontanot, Fabio et al. (Aug. 2020). "The rise of active galactic nuclei in the galaxy evolution and assembly semi-analytic model". In: *MNRAS* 496.3, pp. 3943–3960. DOI: 10.1093/mnras/staa1716. arXiv: 2002.10576 [astro-ph.CO].

Bassini, L. et al. (Oct. 2019). "Black hole mass of central galaxies and cluster mass correlation in cosmological hydro-dynamical simulations". In: *A&A* 630, A144, A144. DOI: 10.1051/0004-6361/201935383. arXiv: 1903.03142 [astro-ph.GA].

Bassini, L. et al. (Oct. 2020). "The DIANOGA simulations of galaxy clusters: characterising star formation in protoclusters". In: *A&A* 642, A37, A37. DOI: 10.1051/0004-6361/202038396. arXiv: 2006.13951 [astro-ph.GA].

Acknowledgements

First of all I want to thank my supervisors Joe Mohr and Veronica Strazzullo for having me as a student. You patiently taught me a lot about physics and motivated me for my work. Despite the distance to Italy Veronica's supervision could not have been better, you have always been there when I needed help for the project or was frustrated.

I thank our entire group for welcoming me and your input during our meetings, as well as my collaborators, in particular Chiara and Emanuele.

I want to thank all my office mates, especially Sebastian for our hikes and not very scientific conversations, Marco for all our inspiring discussions as well as Elena, Daniel, Aditya and Thomas for a lot of fun and many pranks. We see us for the next Music Monday!

I also want to thank all the fantastic people who are not in our group or office, in particular Stefan for many lunch breaks and the swim workouts together with Luca as well as Rhea and Jo for everything you taught me. I want to thank Arno and Matthias for the observation nights at the Wendelstein observatory that motivated me a lot, as well as Christian for his lessons in astrophotography. Furthermore I want to thank Tadziu for all the technical support and Gudrun, Nicola and Sabine for all their help.

Last but not least I want to thank my family and friends for all the support that I received.